Physical Aspects and Modelling of Turbulent MILD Combustion

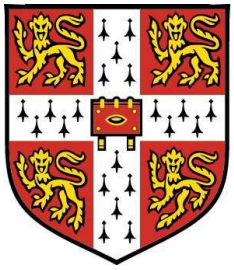

Yuki Minamoto – St John's College

Department of Engineering

University of Cambridge

A thesis submitted for the degree of

Doctor of Philosophy

16 December 2013

Declaration

This dissertation is the result of my own work and includes nothing which is the outcome of work done in collaboration except where specifically indicated in the text. It has not been submitted for another qualification to this or any other university. The dissertation contains approximately 42,000 words, 66 figures and 6 tables.

Yuki Minamoto

7th November 2013

To my grandfather.

Acknowledgements

Firstly, I would like to express my gratitude to my supervisor, Prof Swaminathan, for his continuous support and guidance regarding my research and career. Professor R. S. Cant provided helpful advice, especially on the numerical code SENGA2. I must thank two former researchers at Hopkinson laboratory. Dr T. D. Dunstan helped me kick start my PhD research, and gave extensive support for this thesis. Dr L. Teresa taught me Minkowski functionals in detail.

The financial supports of Nihon Keidanren, Cambridge Overseas Trust, EPSRC, Department of Engineering, St John's College, and Combustion Institute during my course and for conferences are also acknowledged. This work made use of the facilities of HECToR, the UK's national high-performance computing service, which is provided by UoE HPCx Ltd at the University of Edinburgh, Cray Inc and NAG Ltd, and funded by the Office of Science and Technology through EPSRCs High End Computing Programme. My huge workstation would not have lasted until now without the IT support of Mr Peter Benie.

I am grateful to members of Division A, both in past and present, for little technical and non-technical chats when I (we) got a little bored from work. In particular, Shaohong, Irufan, Zacharias, Jeng, Davide, Andrea, Rob, Fiona, Michael, Jenny, Hemanth, Tee, Larry, Dhiren, Antonio and the secretary Kate. Outside the department, I met some nice people who are keeping me smiling. In no particular order, Francis, Thomas, Echo, Neeraj, Kosta, Ivan, Kris, and Lucy who kindly read through and gave me suggestions for some of the chapters in this thesis. I also enjoyed sharing some time eating Baklava with her. I need to mention members of Aho-kai for making

my life less predictable. I am grateful for the support of my family, my grandmother, my parents, younger brother and sister.

Finally, special thanks to Ayako Henson for sending me imaginative and sophisticated cards from time to time, for reminding me to go to the laboratory every so often, and for many other things.

Abstract

Moderate or Intense Low-oxygen Dilution (MILD) combustion is one of combustion technologies which can improve efficiency and reduce emissions simultaneously. This combustion type is characterised by the highly preheated reactant temperature and the relatively small temperature rise during combustion due to the intense dilution of the reactant mixture. These unique combustion conditions give MILD combustion very attractive features such as high combustion efficiency, reduction of pollutant emissions, attenuation of combustion instabilities and flexibility of the flow field. However, our understanding of MILD combustion is not enough to employ the MILD combustion technology further for modern combustion devices.

In this thesis, Direct Numerical Simulation (DNS) has been carried out for turbulent MILD combustion under four MILD and classical premixed conditions. A two-phase strategy is employed in the DNS to include the effect of imperfect mixing between fresh and exhaust gases before intense chemical reactions start. In the simulated instantaneous MILD reaction rate fields, both thin and distributed reaction zones are observed. Thin reaction zones having flamelet like characteristics propagate until colliding with other thin reaction zones to produce distributed reaction zones. Also, the effect of such interacting reaction zones on scalar gradient has to be taken into account in flamelet approaches.

Morphological features of MILD reaction zones are investigated by employing Minkowski functionals and shapefinders. Although a few local reaction zones are classified as thin shape, the majority of local reaction zones have pancake or tube-like shapes. The representative

scales computed by the shapefinders also show a typical volume where intense reactions appear.

Given high temperature and existence of radicals in the diluted reactants, both reaction dominated and flame-propagation dominated regions are locally observed. These two phenomena are closely entangled under a high dilution condition. The favourable conditions for these phenomena are investigated by focusing on scalar fluxes and reaction rate.

A conditional Probability Density Function (PDF) is proposed to investigate flamelet/non-flamelet characteristics of MILD combustion. The PDF can be obtained by both numerically and experimentally. The PDF shows that MILD combustion still has the direct relationship between reaction rate and scalar gradient, although the tendency is statistically weak due to the distributed nature of MILD reaction zones.

Finally, based on the physical aspects of MILD combustion explained in this work, a representative model reactor for MILD combustion is developed. The model reactor is also used in conjunction with the presumed PDF for a mean and filtered reaction rate closure. The results show a good agreement between the modelled reaction rate and the DNS results.

Contents

List of Figures

List of Tables

Nomenclature

Roman Symbols

c_α	Molar concentration of species α
c_p	Mass specific heat capacity of mixture at constant pressure
$c_{p,\alpha}$	Mass specific heat capacity of species α at constant pressure
c_T	Reaction progress variable based on temperature
c_Y	Reaction progress variable based on fuel mass fraction
Da	Damköhler number
D_α	Diffusion coefficient of species α
E	Total energy
h_α	Total enthalpy of species α
Ka	Karlovitz number
k_m	Rate coefficient of backward reaction in the m-th reaction step
k_m	Rate coefficient of forward reaction in the m-th reaction step
k_m	Rate coefficient in the m-th reaction step
l_0	Longitudinal integral length scale of turbulence
Le_α	Lewis number of species α

L_x, L_y, L_z	Dimension of computational domain
N_c	Scalar dissipation rate of progress variable c
P	Stagnation pressure
p	Pressure
Pr	Prandtl number
$P(\xi)$	Probability density function of progress variable c
q_i	Heat flux component in x_i-direction
R^0	Universal gas constant
$\mathrm{Re}_{\mathrm{jet}}$	Reynolds number based on jet velocity and diameter of exit nozzle
Re_{l_0}	Reynolds number based on u' and l_0
Re_{λ}	Reynolds number based on u' and λ
S_c	Flame consumption speed
S_L	Laminar flame speed
T	Temperature
T_{ign}	Autoignition temperature of mixture
T_p	Product temperature
T_r	Reactant temperature
$\boldsymbol{u}$	Fluid velocity
u_i	Fluid velocity component in x_i-direction
u'	Root-mean-square turbulent velocity fluctuation
$V_{\alpha,i}$	Diffusion velocity component of species α in x_i-direction
W_α	Molar mass of species α

X_α Molar fraction of species α

Y_α Mass fraction of species α

Greek Symbols

δ_F Zeldovich thickness

ΔT Temperature increase during combustion, $T_p - T_r$

δ_{th} Flame thermal thickness

$\Gamma(\xi)$ Gamma function

λ Taylor microscale

λ_{th} Mixture thermal conductivity

μ Dynamic viscosity of mixture

$\nu'_{\alpha,m}$ Reactant stoichiometric coefficient of species α at m-th step reaction

$\nu''_{\alpha,m}$ Product stoichiometric coefficient of species α at m-th step reaction

ω_α Mass reaction rate of species α

ω_c Reaction rate of progress variable c

ϕ Equivalence ratio

ρ Mixture density

ρ_r Reactant mixture density

τ_D Mean convection time from inlet to outlet boundaries

τ_F Flame time scale

τ_{ign} Autoignition delay time

τ_{ij} Viscoss stress tensor

ξ Mixture fraction

ξ_{st} Stoichiometric mixture fraction

Chapter 1

Introduction

1.1 Importance of combustion technology

Over 80 % of world energy supply is provided by burning fossil fuels. Total world energy use has been predicted to increase linearly for the next 30 years, although energy use will be more efficient (U. S. Energy Information Administration, 2010). Figure 1.1 shows the history and projection of world marketed energy use by fuel type. Before 2007, about 85 % of energy consumption was supplied by the burnable fuels, while 15 % was made by nuclear and renewable sources. These proportions are predicted to change gradually to 80 % for fossil fuel and 20 % for nuclear and renewable energy by 2035. In the long-term, these projections are unlikely to significantly change after the Fukushima Daiichi accident in 2011; the IAEA argues that the accident has not led to a significant retraction in nuclear power programmes (World Energy Council, 2012). However, burning fossil fuels will still be the major source of energy supply for the next several decades, and the demands for the energy produced using combustion will linearly increase.

Electricity is a rapidly-growing end-use energy form: net electricity consumption is expected to rise by 2.3 percent every year until 2035, while total energy demand from all energy sources increases by 1.4 percent per year (U. S. Energy Information Administration, 2010). Although the proportions of electricity supply generated by renewable and nuclear resources will increase compared to the proportions in the total energy, combustion related electricity consists of about

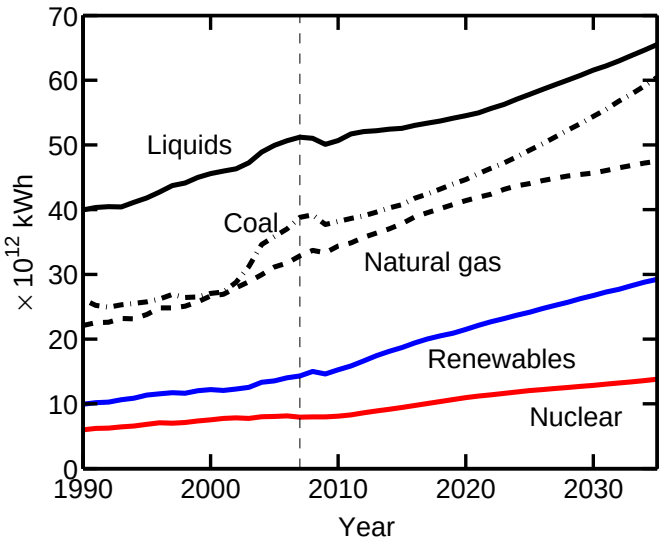

Figure 1.1: World marketed energy use by fuel type 1990–2035 (U. S. Energy Information Administration, 2010). Projections are shown from 2007 to 2035.

65 % of net electricity supply until 2035 (U. S. Energy Information Administration, 2010). Combustion related devices will also play a substantial role in the renewable energy market, for example through the use of synthesis gas (syngas) and biofuels. Thus, the demand for combustion systems — such as gas turbine engines for power generation, and automotive and aerospace engines — to improve efficiency and at the same time reduce pollutant emission will continue to grow.

1.2 Background – MILD combustion

Due to the significant demand for combustion systems — which are able to improve efficiency and reduce emissions simultaneously — alternative combustion technologies are being constantly explored to meet these requirements. Fuel lean premixed combustion is a potential method to meet these demands, but it is highly susceptible to thermo-acoustic instability. One method to avoid the instabilities is to preheat the reactant mixture by using recovered exhaust heat. This would also enhance the combustion efficiency in a system while improving

the combustion stability. However, preheating also increases the flame temperature, leading to an increase in thermal NO_x formation in conventional premixed combustion. This adverse effect of preheating on flame temperature and thus the subsequent reduction of thermal NO formation limits the potential for improvement of combustion efficiency by this method in a system employing conventional combustion techniques.

1.2.1 Fundamentals of MILD combustion

Combustion involving both preheating and dilution of the reactant mixture with burnt products is an important technology as it achieves high combustion efficiency with low emissions of pollutants, light and sound (Wünning & Wünning, 1997; Katsuki & Hasegawa, 1998; Cavaliere & de Joannon, 2004). This technology has already been applied mainly in furnaces (Wünning, 1991; Woelk & Wünning, 1993) and has predominantly employed internal recirculation of hot products to maintain combustion stability and the required oxygen dilution levels. This type of combustion is commonly known as "flameless" or MILD (Moderate or Intense Low-oxygen Dilution) combustion, which is characterised by highly preheated reactant mixtures and low temperature rise during combustion. Typically, the reactants are preheated to a temperature T_r, which is larger than the autoignition temperature T_{ign} of a given fuel, and the maximum temperature rise, $\Delta T = T_p - T_r$, is smaller than T_{ign}, where T_p is the product temperature (Cavaliere & de Joannon, 2004). The small temperature rise during the combustion process results from the combination of a high dilution level with the large amount of products and the low oxygen levels available for combustion. The products also contain chemically active radicals, which help to achieve stable combustion.

The combustion type diagram (Cavaliere & de Joannon, 2004) shown in figure 1.2 can be used to distinguish the MILD combustion condition from conventional premixed, pilot assisted, and high temperature air (HiTAC) combustion conditions. The diagram also shows one conventional premixed and three MILD combustion conditions simulated and considered in the present work, which are described in chapter 2. This diagram emphasises the small temperature rise during combustion under MILD conditions unlike conventional combustion con-

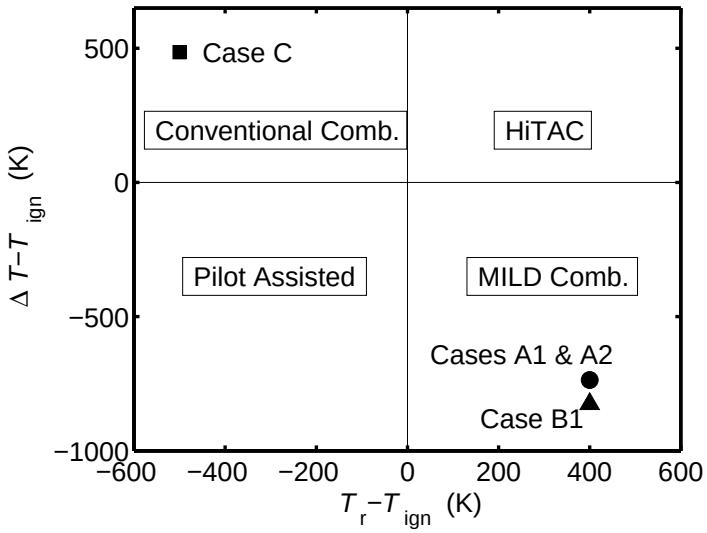

Figure 1.2: Combustion type diagram (Cavaliere & de Joannon, 2004).

ditions. This small temperature rise across the flame produces non-visible and uniform combustion as reported in previous experimental studies (de Joannon *et al.*, 2000; Özdemir & Peters, 2001; Krishnamurthy *et al.*, 2009). It is also reported that combustion under MILD conditions is governed by slower reactions compared to those in the conventional combustion regime (Plessing *et al.*, 1998; Christo & Dally, 2005; Awosope *et al.*, 2006; Galletti *et al.*, 2007; Lammel *et al.*, 2010; Parente *et al.*, 2011b).

These unique characteristics of MILD combustion offer a number of advantages. Firstly, combustion efficiency is enhanced due to the high preheating temperature using recovered exhaust heat (Wünning & Wünning, 1997; Katsuki & Hasegawa, 1998; Cavaliere & de Joannon, 2004). Secondly, thermal NO formation is suppressed significantly due to the low flame temperature and intense dilution (Wünning & Wünning, 1997; Katsuki & Hasegawa, 1998; Cavaliere & de Joannon, 2004; Mohamed *et al.*, 2009; Krishnamurthy *et al.*, 2009; Li & Mi, 2011). Typically, it takes a few seconds to produce a substantial level of thermal NO at around 1900 K, and this reduces to a few milliseconds when the temperature is about 2300 K (Wünning & Wünning, 1997). The maximum flame temperature is, however, typically much lower than 1900 K in MILD combustion with methane–

air mixtures (Wünning & Wünning, 1997; Cavaliere & de Joannon, 2004); thus the NO_x formation rate is usually very slow in MILD combustion. Also, because of the small temperature rise together with the high elevated reactant temperature, combustion noise and instabilities are suppressed even when the recirculation rate — the mass ratio between exhaust gas to fresh reactants — exceeds 30%, which is an upper limit for stable combustion in combustion systems with normal ambient air (Wünning & Wünning, 1997; Katsuki & Hasegawa, 1998). Thus, such combustion conditions which can enhance combustion efficiency and reduce pollutant emissions also help to avoid combustion instability which can cause serious problems during operation of modern combustion devices, such as gas turbine engines. This high preheating temperature condition also allows combustion to be maintained even in a high-velocity jet field without the need for internal recirculation zones (Wünning & Wünning, 1997; Cavaliere & de Joannon, 2004; Medwell, 2007). Therefore, the design of a MILD combustor would no longer be constrained by the requirements of recirculation zones or flame holders, which is advantageous for high-speed combustion. Furthermore, MILD conditions are achieved relatively straightforwardly in practical devices using conventional techniques such as exhaust or flue gas recirculation (EGR or FGR) or staged fuel injection (Wünning & Wünning, 1997; Cavaliere & de Joannon, 2004; Hayashi & Mizobuchi, 2011). There is renewed interest in these advantages of using MILD combustion as one of the "green" technologies for thermal power generation (Cavaliere & de Joannon, 2004; Awosope *et al.*, 2006; Lückerath *et al.*, 2008; Lammel *et al.*, 2010). However, the physics of MILD combustion in turbulent flows is not well understood.

1.2.2 Previous studies

As reported in previous studies (de Joannon *et al.*, 2000; Özdemir & Peters, 2001; Krishnamurthy *et al.*, 2009), thin reaction zones cannot be observed in direct photographs of MILD combustion, unlike in conventional premixed combustion. This in particular is the reason why MILD combustion is also called "flameless combustion" or "flameless oxidisation". Combustion under MILD conditions are indeed "flameless" by naked eyes, and these visual observations of MILD combustion are

basis of common knowledge of uniform and distributed nature of MILD reaction zones.

Based on these observations, theoretical analyses of methane oxidation under diluted conditions have been carried out assuming Perfectly Stirred Reactor (PSR) configurations for both premixed and non-premixed MILD combustion (Wünning & Wünning, 1997; de Joannon *et al.*, 2000; Cavaliere & de Joannon, 2004; de Joannon *et al.*, 2004, 2005; Sabia *et al.*, 2007). Although the sole use of a PSR might not be appropriate to model turbulent combustion under a practical MILD combustor, the colourless characteristics of MILD combustion is explained by addressing the two-staged evolution of the chemical reaction in a PSR. This two-staged oxidation does not seem to be unduly influenced by the residence time of a PSR for the temperature range of 500 - 2000 K (de Joannon *et al.*, 2000). Laboratory scale combustors have often been the subject of MILD combustion research in cooperation with numerical simulations based on the Reynolds averaged field. Most of such combustors apply a non-premixed combustion mode, where a cold fuel and a hot and diluted oxidiser are separately fed into a combustion chamber (Dally *et al.*, 2004; Oldenhof *et al.*, 2011; Medwell *et al.*, 2007, 2008; Duwig *et al.*, 2012), and such configuration is named Hot Oxidant-Diluted Oxidant (HODO). Alternatively, a hot fuel and a diluted oxidiser are also used in a configuration called Hot Fuel-Diluted Oxidant (HFDO) (Cavaliere & de Joannon, 2004). Several laboratory scale combustors apply another configuration where both diluted fuel and oxidiser are preheated by recovered exhaust heat and either fully premixed or partially premixed before entering a combustion chamber (Plessing *et al.*, 1998; Özdemir & Peters, 2001; de Joannon *et al.*, 2004, 2005; Sabia *et al.*, 2007; Mi *et al.*, 2009; Li & Mi, 2011).

In order to understand "invisible" reaction zones under MILD conditions, advanced laser diagnostics have been carried out in previous studies to measure instantaneous temperature and species fields (Plessing *et al.*, 1998; Özdemir & Peters, 2001; Dally *et al.*, 2004; Medwell *et al.*, 2007; Duwig *et al.*, 2012). Distributed reaction zones are observed under MILD conditions and compared with the conventional combustion cases in the laser thermometry images. The instant CH_2O field also suggests distributed reaction zones based on visual examinations of PLIF images (Medwell, 2007; Duwig *et al.*, 2012). The OH Planar Laser

Induced Fluorescence (PLIF) images, however, yield contradicting views: the instantaneous OH images show a clear gradient of OH concentration, suggesting existence of thin reaction zones (Plessing *et al.*, 1998; Özdemir & Peters, 2001; Medwell, 2007; Duwig *et al.*, 2012). MILD reaction zones are fairly distributed and show a patchy appearance in the temperature and OH PLIF images under the condition considered in Dally *et al.* (2004), although a bimodal Probability Density Function (PDF) is also reported in the same study.

Generally, OH PLIF is used in laser diagnostics of chemically reacting turbulent flows because of its high concentration and well understood spectroscopy characteristics (Hassel & Linow, 2000). Using OH PLIF alone, however, may be insufficient to investigate reaction zones in turbulent MILD combustion, because of the presence of OH radicals in the reactant mixture which come from exhaust gases used for dilution. Furthermore, the OH level inside reaction zones may not be significantly larger than that in the unburnt or burnt regions, especially when the oxygen level is near the lower end for MILD combustion. This issue may be addressed through careful calibration of the OH LIF system. However, a second marker would be required to identify the MILD reaction zones for a detailed analysis. These views clearly show that there need to be more investigations into reaction zones in MILD combustion numerically and experimentally.

Given highly elevated temperature conditions, autoignition is believed to play an important role in MILD combustion (Wünning & Wünning, 1997; Katsuki & Hasegawa, 1998; Cavaliere & de Joannon, 2004) in sustaining combustion even in high speed flows without recirculation zones. Autoignition characteristics in configurations employing diluted and/or hot reactants/coflow have been studied in the context of flame stabilisations (Mastorakos *et al.*, 1995; Arndt *et al.*, 2012). Such configurations are similar to MILD combustion with either HODO or HODF conditions. For MILD combustion, the part played by ignition in the flame stabilisation has been studied using a Jet in Hot Coflow (JHC) burner experimentally (Medwell, 2007; Medwell *et al.*, 2007, 2008) and numerically (van Oijen, 2013). The CH_2O PLIF images show that the heated coflow initiates the ignition of a mixture after localised extinction caused by cold surrounding air (Medwell *et al.*, 2007). Despite the interplay between extinction and ignition processes, presence of abundant hot exhaust gases ensures that the overall reac-

tion is sustained. Previous studies reviewed by Cavaliere & de Joannon (2004) emphasise the importance of the autoignition process in MILD combustion based on the analysis using a well-stirred MILD reactor. However, the existence of thin reaction zones observed based on OH PLIF images suggests the presence of propagating flame fronts (Plessing *et al.*, 1998; Özdemir & Peters, 2001; Medwell *et al.*, 2007; Duwig *et al.*, 2012). Probability density functions in Dally *et al.* (2004) also suggest that combustion occurring in the MILD combustion burner is due to flame propagation, rather than autoignition under the conditions considered. Thus, there is a possibility of the existence of competition between autoignition and flame propagation phenomena in MILD combustion (this is also suggested in Mastorakos (2009)), and this competition needs to be investigated to further our understanding of MILD reaction zones.

Lack of understanding of MILD reaction zones also calls into question the common use of both flamelet and non-flamelet based turbulent combustion models for MILD combustion for Reynolds Averaged Navier-Stokes (RANS) simulations (Weber *et al.*, 2000; Coelho & Peters, 2001; Orsino *et al.*, 2001; Dally *et al.*, 2004; Christo & Dally, 2005; Galletti *et al.*, 2007; Li & Mi, 2011; Aminian *et al.*, 2011) and for Large Eddy Simulations (LES) (Duwig *et al.*, 2008; Ihme & See, 2012). For flamelet type approaches, models assume that the flame length scales are typically smaller than the turbulence length scales so that the reaction zone structure is not unduly affected by turbulence. However, given experimental observations of uniform and distributed reaction zones, it has not yet been rigorously investigated whether this assumption is sufficiently valid. The RANS simulation results carried out by Coelho & Peters (2001) using the Eulerian particle flamelet model show a consistent trend with the experimental data in Özdemir & Peters (2001) in terms of the mean velocity. However, the predicted NO emission at the exhaust is about three times larger than the measured value. Dally *et al.* (2004) has carried out a RANS calculation using a similar turbulent combustion model. Although the trend of temperature is consistent with the experimental results, the simulated peak temperature differs up to 100 K. A presumed PDF is employed with a flamelet library for LES (Duwig *et al.*, 2008; Ihme & See, 2012). An Eddy Dissipation Concept (EDC) based model (Magnussen, 1981) is a non-flamelet model which is more widely used compared to flamelet type models

for MILD combustion. The model may be able to describe the distributed nature of MILD reaction zones (Weber *et al.*, 2000; Orsino *et al.*, 2001; Christo & Dally, 2005; Galletti *et al.*, 2007; Li & Mi, 2011; Aminian *et al.*, 2011). However, the assumption of homogeneous reaction within the fine structures of turbulence energy dissipation has not been verified for MILD combustion: distributed reaction zones instead seem to distribute in a larger area than the turbulence scale in the experimental images of temperature and species fields (Plessing *et al.*, 1998; Özdemir & Peters, 2001; Dally *et al.*, 2004; Medwell, 2007; Duwig *et al.*, 2012). Numerical simulation that has been carried out and reported in Christo & Dally (2005) using the EDC model shows reasonable agreement both quantitatively and qualitatively with the experimental results for the oxygen concentration of 9 % and 6 %. For the oxygen concentration of 3 %, however, the predicted peak temperature becomes lower by about 200 K at the upstream region and 600 K higher at the downstream region than the measured results. Similar deviation of temperature from the experimental results are also reported in other RANS simulation studies of MILD and HiTAC combustion (Orsino *et al.*, 2001; Kumar *et al.*, 2002; Galleti *et al.*, 2007; Aminian *et al.*, 2011), even though a qualitative agreement is seen. For MILD combustion, extra emphasis should be placed on an accurate prediction of temperature and heat release rate fields, since prediction of pollutant emissions is often associated with the computation of this "green" combustion, and it is shown that the prediction of minor species is sensitive to the temperature fluctuation in RANS (Aminian *et al.*, 2011).

1.2.3 Utilisation of exhaust gas

It is key for the MILD combustion technique to make use of both recovered exhaust gases and heat. A conventional technique such as EGR, FGR or staged fuel injection can be used to achieve high temperatures and diluted mixture conditions relatively straightforwardly (Cavaliere & de Joannon, 2004; Aida *et al.*, 2005; Swaminathan & Bray, 2011). In practice, it is common to inject fuel and air into either a recirculating flow or a stream containing hot products to achieve MILD combustion. Such configurations with high momentum jets have been applied to achieve a mixture for MILD combustion very quickly (Katsuki & Hasegawa, 1998;

Dally *et al.*, 2002; Cavaliere & de Joannon, 2004; Dally *et al.*, 2004; Awosope *et al.*, 2006; Galleti *et al.*, 2007; Li & Mi, 2011). In either of these configurations, there are possibilities for the fuel to be partly mixed, but not completely, with the products and air for a short mixing time; this thereby creates spatially and temporally non-uniform mixtures of exhaust and fresh gas pockets. The size of these pockets is random and determined by the turbulence conditions. Combustion that takes place in such a mixture field is considered to be complex compared to that in conventional premixed combustion. For instance, pockets of products and radicals, which are not well mixed before combustion, can lead to additional complexities such as reaction zone interactions. Also, given the high preheating temperature conditions together with the existence of chemically-active radicals, there is the possibility that autoignition or homogeneous-reactor-type reaction dominates in MILD combustion. On the other hand, local turbulence and mixture conditions can influence the residence time, thereby favouring flame propagation over autoignition. An investigation into these issues will help to understand reaction zones and the competing effects of turbulence and chemical reactions in MILD combustion. These effects related to the utilisation of exhaust gas and heat on the mean/filtered reaction rate prediction by turbulent combustion models have not been investigated and should be addressed in further findings and models of MILD combustion.

1.3 Computational approaches for turbulent reacting flows

Since the present work is intended to employ numerical approaches, general numerical approaches for turbulent reacting flows are briefly explained in this section. Computational fluid dynamics (CFD) of turbulent combustion can be classified in three levels based on time and spatial scales dealt with during simulations; Reynolds averaged Navier-Stokes (RANS) simulations, large eddy simulations (LES), and direct numerical simulations (DNS).

1.3.1 Reynolds averaged Navier-Stokes simulation

Reynolds averaged Navier-Stokes (RANS) simulations are the most available computations in practice, since they deal with only time-averaged balance equations and require the least computational resources among the three computational methods. The Reynolds/Favre (density-weighted) averaged balance equations for RANS simulations are obtained by averaging the instantaneous balance equations which are described in chapter 2. Due to the averaging operation, additional terms appear: Reynolds stress and turbulent flux terms. Thus, additional transport equations and models are required to close the averaged balance equations. Typically, a k-ϵ model is employed where transport equations for turbulent kinetic energy k and its dissipation rate ε are additionally solved to close Reynolds stress. The turbulent flux is commonly obtained assuming a gradient diffusion, although this assumption is not entirely valid in a flow with strong shear or dilatation (Veynante *et al.*, 1997; Frank *et al.*, 1999; Pope, 2000; Zimont & Biagioli, 2002; Pfadler *et al.*, 2009). For RANS simulations of reacting flows, the mean reaction rate also need to be modelled. Generally, the modelling of the mean reaction rate is most important in RANS simulations of turbulent combustion as it involves the coupling of turbulence and chemical reactions, which have strong non-linearity. Several approaches for turbulent combustion models have been thoroughly studied. Flamelet models (Bray *et al.*, 1985; Peters, 1986; Swaminathan & Bray, 2005) which are reviewed later (Peters, 2000; Veynante & Vervisch, 2002; Poinsot & Veynante, 2005) are often applied to combustion conditions with large Da numbers, where length scale of flame is smaller than that of turbulence eddies. For RANS simulations of MILD combustion, a flamelet approach is employed (Coelho & Peters, 2001; Dally *et al.*, 2004) using Eulerian Particle Flamelet Model (EPFM) (Barths *et al.*, 2000), where an additional transport equation of the probability of finding a flamelet particle is solved at each mesh point. Conditional moment closure (CMC) (Klimenko & Bilger, 1999; Bilger *et al.*, 1991) is another closure for non-premixed combustion and later applied to premixed combustion (Amzin *et al.*, 2012). In CMC, a transport equation of a conditional averaged quantity is solved, which is integrated with a presumed Probability Density Function (PDF). Kim *et al.* (2005) applied a CMC model

to study flame structure and NO formation of MILD combustion in a combustor which was experimentally studied and reported in Dally *et al.* (2002). The transported PDF model (Pope, 1985, 2000) is also a common choice for reaction rate closure. One of the advantages of this method is that the chemical source term in the transport equation for the PDF is closed; there is no assumption concerning the time scales of chemistry relative to the turbulence time scales. A mean reaction rate model based on EDC (Magnussen, 1981) is widely used for MILD combustion (Weber *et al.*, 2000; Orsino *et al.*, 2001; Christo & Dally, 2005; Li & Mi, 2011; Aminian *et al.*, 2011). In EDC, homogeneous combustion is assumed in a fine scale which is related to the size of turbulence energy dissipating regions, by solving PSR-combustion for an appropriate residence time, and so the complex chemistry can be used to describe finite rate chemistry. Although the computational requirement is less with the RANS approach, the validity of the solution is generally limited by the models, since the scales of turbulent motion are not explicitly solved and the turbulence effects on the chemical reaction are implicitly captured via turbulence models. However, commercial CFD codes are usually based on the RANS context including several closures and approaches (Cant & Mastorakos, 2008).

1.3.2 Large eddy simulation

Large eddy simulation (LES) is the next level of computational approach for turbulent reacting flows. In contrast to the RANS approach, LES deals with large scale motions of turbulence explicitly, whereas the effects of small scale turbulent motions are modelled using a subgrid scale (SGS) model. Large eddy simulations deal with instantaneous balance equations which are filtered in terms of space. Thus, LES can resolve instantaneous flame shapes and eddies in a large scale, but a subgrid model is still required to take into account the effects of small scale turbulent motions on mixing and chemical reaction. In practice, similar concepts for turbulent combustion modelling can be applied for both RANS and LES (Swaminathan & Bray, 2011), since the balance between the chemical reaction and the heat/species transport generally takes place on very small scales which are below the resolved length scale for both approaches (Pitsch, 2006; Cant &

Mastorakos, 2008). Since LES simulates the large scale time resolved motions explicitly, the computational cost is usually much higher than RANS simulations and SGS models are still required to take into account the effects of small scale turbulent motion on combustion (Poinsot & Veynante, 2005). For these reasons, LES is not widely used for practical purposes, although it is considered as a near-future industrial CFD tool (Swaminathan & Bray, 2011). For LES of MILD combustion, a presumed PDF approach with a flamelet library has been applied, where the PDF is modelled by using β or Dirac delta functions (Ihme & See, 2012), or top-hat PDF (Duwig *et al.*, 2008).

1.3.3 Direct numerical simulation

Direct numerical simulation (DNS) is the highest level of simulation for turbulent reacting flows, in which all the instantaneous fully-compressible Navier-Stokes equations are solved without using any models for turbulent motions. All-scale motions are explicitly solved and their effects on chemical reactions and mixing are captured, in contrast to RANS or LES simulations. On the other hand, DNS requires a large amount of computational resources; even with the latest high performance computing, simulations are limited to simple flow configurations with a small domain size (typically 1–2 cm cube).

Historically, DNS was first carried out for incompressible and non-reacting flows in 1980's (Poinsot & Veynante, 2005). In the early 1990's, fully-compressible and reactive flows were first solved in the two-dimensional domain using a one-step chemistry or a complex chemistry including the heat release effect (Rutland & Ferziger, 1991; Poinsot *et al.*, 1991; Baum *et al.*, 1994). However, given the three-dimensional nature of turbulence, it is not possible to capture the effects of turbulence on combustion without three-dimensional DNS. Three-dimensional combustion DNS started to be used in a few studies in the 1990's using single-step (Trouvé & Poinsot, 1994; Rutland & Cant, 1994; Cant, 1999), two-step (Swaminathan & Bilger, 1997) and complex mechanisms (Tanahashi *et al.*, 1999, 2000).

Given the computational difficulties, the flame configuration simulated by DNS is limited to relatively simple canonical combustion compared to the flames

observed in a practical combustor. The most common configuration for a turbulent premixed flame is a statistically one-dimensional planar flame (Poinsot *et al.*, 1991; Trouvé & Poinsot, 1994; Swaminathan & Bilger, 1997; Cant, 1999; Tanahashi *et al.*, 2000; Grout, 2007; Shim *et al.*, 2011), in which the flame propagates toward the upstream in a turbulent flow field. Therefore, the combustion in the turbulent planar flame is based on the balance between turbulence and the chemical reaction since the effect of configuration such as the mean shear does not exist. Only recently has DNS in relatively complicated configurations such as lifted, V, Bunsen, and swirl flames become possible (Mizobuchi *et al.*, 2002; Domingo *et al.*, 2005; Richardson *et al.*, 2010; Dunstan *et al.*, 2012; Minamoto *et al.*, 2011b; Tanaka *et al.*, 2011). In these flames, the presence of the mean shear on scalar mixing is not inevitable, and the modelling and investigation becomes more difficult due to this additional complexity, although models should be tested with such flame configurations as well. Since multiple chemical species equations can be solved in DNS, combustion DNS of stratified/partially premixed flames have also been carried out to study the effect of mixture composition on the turbulent flame speed (overall burning rate per unit area) (Hélie & Trouvé, 1998; Domingo & Vervisch, 2007; Grout *et al.*, 2009) and to extend a modelling approach for premixed flames to partially premixed flames (Malkeson & Chakraborty, 2010).

Today, DNS is considered as an important tool for the investigations of combustion physics and modelling; the results from this computational approach is used as much as experimental results. The DNS data is not only used to validate models in terms of *a priori* testing (Veynante & Vervisch, 2002; Mura *et al.*, 2008, 2009; Kolla *et al.*, 2009; Chakraborty & Swaminathan, 2010; Malkeson & Chakraborty, 2010; Yoshikawa *et al.*, 2013), but also studied in a very detailed manner to improve fundamental understanding of turbulent reacting flows (Tanahashi *et al.*, 2000; Chakraborty & Swaminathan, 2007; Malkeson & Chakraborty, 2010; Dunstan *et al.*, 2012; Minamoto *et al.*, 2011b), since all instantaneous quantities are available for all scales. Such simulations with multi-step chemical kinetics in three dimensional turbulence have been reviewed by Chen (2011).

1.4 Aims and objectives

The present work aims to study MILD combustion with an emphasis on detailed investigation into MILD reaction zones and their behaviour. Since a direct measurement of a reaction rate field is not particularly easy in general, the present investigations rely on numerical simulations. Zero-dimensional or one-dimensional computations of canonical MILD flames are not sufficient to address all the issues mentioned above. Thus, the numerical simulation to be performed should include effects of temporal and spatial inhomogeneity of diluted reactants in which mixtures autoignite or establish propagating flames. Although two-dimensional direct simulations have already been conducted (Minamoto *et al.*, 2011a; van Oijen, 2013), three-dimensionality of turbulence and reaction zone evolution and their interactions should not be neglected for detailed investigations. Thus, all the numerical simulation conducted in the present work is based on three-dimensional Direct Numerical Simulation (DNS) employing a skeletal mechanism for a methane-air mixture (Smooke & Giovangigli, 1991). The simulated DNS results are analysed and discussed specifically to answer the following questions based on the above literature review:

1. Are there thin reaction zones or flame fronts in MILD combustion? While combustion in MILD regime is believed to have no flame fronts (Li *et al.*, 2010; Aminian *et al.*, 2011), several PLIF images suggest their existence (Plessing *et al.*, 1998; Özdemir & Peters, 2001; Medwell, 2007; Duwig *et al.*, 2012). A visualisation of DNS results on par with the experimental direct photographs (de Joannon *et al.*, 2000; Özdemir & Peters, 2001; Krishnamurthy *et al.*, 2009) and PLIF images (Plessing *et al.*, 1998; Özdemir & Peters, 2001; Dally *et al.*, 2004; Medwell *et al.*, 2007; Duwig *et al.*, 2012) would be helpful.

2. If flame fronts exist, what is the reaction zone structure like? Are they represented adequately by a conventional canonical one-dimensional flame?

3. Can MILD combustion be modelled using flamelet? Coelho & Peters (2001) and Dally *et al.* (2004) have carried out RANS simulations of MILD combustion using a flamelet-type approach, while an EDC based model has

been extensively used in previous studies (Weber *et al.*, 2000; Orsino *et al.*, 2001; Christo & Dally, 2005; Galletti *et al.*, 2007; Li & Mi, 2011; Aminian *et al.*, 2011).

4. If no thin reaction zones exist, why are reaction zones distributed? Although the jet Reynolds number is likely to be a high value in order to enhance mixing in experiments, there may be other mechanisms which contribute to the uniform nature of MILD combustion.

5. Is there flame propagation, autoignition, or both in MILD combustion? The concept of MILD combustion clearly suggests a significant role played by autoignition, but the previous experimental studies suggest the existence of flame propagation in substantial regions (Plessing *et al.*, 1998; Özdemir & Peters, 2001; Dally *et al.*, 2004; Medwell *et al.*, 2007).

6. Considering the answers to all of the above questions, what is a representative canonical reactor for MILD combustion? Does an appropriate one-dimensional laminar flame work if flame propagation exists? Is a canonical PSR more appropriate? Also, can such a canonical reactors be used in conjunction with a conventional numerical approach to model reaction rate in a RANS or LES context?

These questions are tackled in this thesis after describing in detail the numerical methodology, configuration and conditions in chapter 2. General features of simulated MILD and conventional premixed combustion are discussed first, and then morphological characteristics of reaction zones are investigated in chapter 3. Afterwards, autoignition/flame-propagation behaviour, scalar gradient, and chemical markers in the MILD reaction zones are discussed in chapters 4 and 5. Based on the results presented in these chapters, a canonical model is proposed and a priori assessment is carried out using the canonical model and flamelets for RANS and LES in chapter 6. The conclusions are presented in chapter 7.

Chapter 2

Direct Numerical Simulation

A numerical code used for the present DNS is based on SENGA2 (Cant, 2012), which solves fully compressible equations for continuity, momentum, internal energy, and species mass fraction for turbulent reacting flows. All the governing equations are solved on a uniform mesh using a tenth order central difference scheme which gradually reduces to a fourth order scheme near boundaries. The integration in time is achieved using a third order Runge-Kutta scheme, although a fourth order scheme can be used in SENGA2. In this section, the numerical methodology, configuration and conditions used for the DNS are explained.

2.1 Governing equations

The governing equations to be solved in DNS are the partial differential equations for fully compressible reacting flows, consisting of equations for the mass conservation equation:

$$\frac{\partial}{\partial t}\rho + \frac{\partial}{\partial x_k}\left(\rho u_k\right) = 0, \tag{2.1}$$

the Navier-Stokes momentum equations:

$$\frac{\partial}{\partial t}\left(\rho u_i\right) + \frac{\partial}{\partial x_k}\left(\rho u_k u_i\right) = -\frac{\partial}{\partial x_i}p + \frac{\partial}{\partial x_k}\tau_{ki}, \tag{2.2}$$

the internal energy equation:

$$\frac{\partial}{\partial t}\left(\rho E\right)+\frac{\partial}{\partial x_k}\left(\rho u_k E\right)=-\frac{\partial}{\partial x_k}\left(p u_k\right)-\frac{\partial}{\partial x_k}q_k+\frac{\partial}{\partial x_k}\left(\tau_{km}u_m\right), \tag{2.3}$$

and the equation for the mass fraction of species α present in the reacting gas mixture:

$$\frac{\partial}{\partial t}\left(\rho Y_\alpha\right)+\frac{\partial}{\partial x_k}\left(\rho u_k Y_\alpha\right)=\omega_\alpha-\frac{\partial}{\partial x_k}\left(\rho V_{\alpha,k}Y_\alpha\right), \tag{2.4}$$

where $V_{\alpha,k}$ is the diffusion velocity of species α, and all other symbols have their usual meaning. The thermal equation of state for the mixture is:

$$p=\rho R^0 T\sum_{\alpha=1}^{N}\frac{Y_\alpha}{W_\alpha}, \tag{2.5}$$

where R^0 is the universal gas constant and N is the total number of species involved. The stagnation internal energy is defined as:

$$E=\sum_{\alpha=1}^{N}Y_\alpha h_\alpha-\frac{P}{\rho}+\frac{1}{2}u_k u_k, \tag{2.6}$$

where the enthalpy of species α is defined as:

$$h_\alpha=\int_{T_0}^{T}c_{p,\alpha}dT+h_\alpha^0. \tag{2.7}$$

The viscous stress tensor is given by:

$$\tau_{ki}=\mu\left(\frac{\partial u_k}{\partial x_i}+\frac{\partial u_i}{\partial x_k}\right)-\frac{2}{3}\mu\frac{\partial u_m}{\partial x_m}\delta_{ki}, \tag{2.8}$$

and the heat flux vector by:

$$q_k=-\lambda_{th}\frac{\partial T}{\partial x_k}+\sum_{\alpha=1}^{N}\rho V_{\alpha,k}Y_\alpha h_\alpha. \tag{2.9}$$

The species mass fractions and the diffusion velocities must satisfy following compatibility conditions:

$$\sum_{\alpha=1}^{N} Y_\alpha = 1, \tag{2.10}$$

and

$$\sum_{\alpha=1}^{N} V_{\alpha,k} Y_\alpha = 0. \tag{2.11}$$

For a reaction mechanism involving M steps of the form

$$\sum_{\alpha=1}^{N} \nu'_{\alpha,m} \mathcal{M}_\alpha \rightarrow \sum_{\alpha=1}^{N} \nu''_{\alpha,m} \mathcal{M}_\alpha, \quad m = 1, \ldots, M \tag{2.12}$$

the chemical production rate w_α for species α is expressed as

$$\omega_\alpha = W_\alpha \sum_{m=1}^{M} \left(\nu''_{\alpha,m} - \nu'_{\alpha,m}\right) k_m(T) \prod_{\beta=1}^{N} c_\beta^{\nu'_{\beta,m}}. \tag{2.13}$$

where the specific reaction rate coefficient $k_m(T)$ is given by the Arrhenius expression

$$k_m(T) = A_m T^{n_m} \exp\left(-\frac{E_m}{R^0 T}\right), \tag{2.14}$$

and the concentration c_β of species β is related to mass fraction by

$$c_\beta = \frac{\rho Y_\beta}{W_\beta}. \tag{2.15}$$

For the reaction rates the compatibility condition is

$$\sum_{\alpha=1}^{N} \omega_\alpha = 0. \tag{2.16}$$

2.2 Thermodynamic and transport properties

For a semi-perfect gas, the molar specific heat capacity at constant pressure, $\bar{c}_{p,\alpha}$, is known to depend on temperature (Poinsot & Veynante, 2005). This temper-

ature dependence is represented in an appropriate manner using a polynomial, where the polynomial degree is taken to be 5. The polynomial coefficients have different values for each species α in different temperature intervals. SENGA2 employs the CHEMKIN database format, in which polynomials of degree 5 are used for two different temperature intervals: for most species the intervals are $0 < T < 1000$ K and $1000 < T < 3000$ K (Cant, 2012).

The molecular transport coefficients are represented using the relationship

$$\frac{\lambda_{th}}{c_p} = A_\lambda \left(\frac{T}{T_0}\right)^r, \tag{2.17}$$

where A_λ, r and T_0 are constants and λ_{th} is the thermal conductivity. Then the mixture dynamic viscosity is given by:

$$\mu = \frac{\lambda_{th}}{c_p}\mathrm{Pr}, \tag{2.18}$$

where the mixture Prandtl number, Pr, taken as a constant value of 0.7. The diffusive mass flux for species α may be represented using Fick's law as:

$$\rho V_{\alpha,k} Y_\alpha = -\rho D_\alpha \frac{\partial Y_\alpha}{\partial x_k}, \tag{2.19}$$

where the diffusion coefficient, D_α, for each species is given by:

$$D_\alpha = \frac{\lambda_{th}}{\rho c_p Le_\alpha}, \tag{2.20}$$

where the Lewis number, Le_α, is assumed as constant, and differs for each species. Applying this Fick's law does not guarantee that the continuity equation will be recovered when all N species mass fraction equations are summed. Substituting equation 2.19 into equation 2.4 and summing over all species yields

$$\frac{\partial}{\partial t}\rho + \frac{\partial}{\partial x_k}\rho u_k = \sum_{\alpha=1}^{N} \frac{\partial}{\partial x_k}\rho D_\alpha \frac{\partial Y_\alpha}{\partial x_k}, \tag{2.21}$$

where the compatibility conditions have been applied as in equations 2.10, 2.11 and 2.16 for the species mass fraction, the diffusion velocities and reaction rates,

respectively. Clearly, by comparison with the continuity equation (2.1), the quantity on the right hand side is an error term. This term can be removed by making a slight modification to Fick's law according to

$$\rho V_{\alpha,k} Y_\alpha = -\rho D_\alpha \frac{\partial Y_\alpha}{\partial x_k} + \rho V_k^{(c)} Y_\alpha, \tag{2.22}$$

where the correction velocity, $V_k^{(c)}$, is given by:

$$\rho V_k^{(c)} = \sum_{\alpha=1}^{N} \frac{\partial}{\partial x_k} \rho D_\alpha \frac{\partial Y_\alpha}{\partial x_k}. \tag{2.23}$$

2.3 Reaction rate

The chemical production rate, ω_α, for species mass fraction is evaluated using equations 2.13–2.15. The reaction rate of species α is obtained by summation over all steps in the reaction mechanism as:

$$\omega_\alpha = W_\alpha \sum_{m=1}^{M} \bar{\omega}_{\alpha,m}, \quad m = 1, \ldots, M. \tag{2.24}$$

Each step in the reaction mechanism may involve one of several possible special cases.

A forward and backward reaction step is expressed by:

$$\sum_{\alpha=1}^{N} \nu'_{\alpha,m} \mathcal{M}_\alpha \rightleftharpoons \sum_{\alpha=1}^{N} \nu''_{\alpha,m} \mathcal{M}_\alpha, \tag{2.25}$$

and the molar production rate, $\bar{\omega}_{\alpha,m}$, is given by:

$$\bar{\omega}_{\alpha,m} = \left(\nu''_{\alpha,m} - \nu'_{\alpha,m}\right) \left[k_{f,m}(T) \prod_{\beta=1}^{N} c_\beta^{\nu'_{\beta,m}} - k_{b,m}(T) \prod_{\beta=1}^{N} c_\beta^{\nu''_{\beta,m}} \right], \tag{2.26}$$

where $k_{f,m}$ and $k_{b,m}$ are respectively the rate coefficients of forward and backward reactions, given by equation 2.14, and c_β is the molar concentration given by equation 2.15. This is the simplest and most common type of reaction step which

includes forward and backward reactions.

In the cases where a reaction step, m, is of the form

$$\sum_{\alpha=1}^{N} \nu'_{\alpha,m} \mathcal{M}_\alpha + M \rightarrow \sum_{\alpha=1}^{N} \nu''_{\alpha,m} \mathcal{M}_\alpha + M, \tag{2.27}$$

the molar production rate for a species α is given by:

$$\bar{\omega}_{\alpha,m} = \left(\nu''_{\alpha,m} - \nu'_{\alpha,m}\right) k_m(T) c_M \prod_{\beta=1}^{N} c_\beta^{\nu'_{\beta,m}}, \tag{2.28}$$

where the molar concentration of the third body, M, is given by:

$$c_M = \sum_{\alpha=1}^{N} \eta_{\alpha,M} c_\alpha, \tag{2.29}$$

where the coefficients $\eta_{\alpha,M}$ are the third-body efficiencies for M.

Certain reaction steps may have a fall-off reaction. In the low-pressure limit, the reaction takes place through:

$$\sum_{\alpha=1}^{N} \nu'_{\alpha,m} \mathcal{M}_\alpha + M \rightarrow \sum_{\alpha=1}^{N} \nu''_{\alpha,m} \mathcal{M}_\alpha + M, \tag{2.30}$$

where a third-body collision is required to provide the energy necessary to maintain the reaction. However, in the high-pressure limit, the reaction process is taken over by the alternate reaction as:

$$\sum_{\alpha=1}^{N} \nu'_{\alpha,m} \mathcal{M}_\alpha \rightarrow \sum_{\alpha=1}^{N} \nu''_{\alpha,m} \mathcal{M}_\alpha. \tag{2.31}$$

In either pressure limit, the description of reaction rate depends on temperature alone. However, for pressures somewhere between the limits the rate expressions must depend on pressure as well. This pressure regime is called the fall-off region. In this case, $(+M)$ is used rather than $+M$ to formally indicate that a reaction

is pressure-dependent as:

$$\sum_{\alpha=1}^{N} \nu'_{\alpha,m} \mathcal{M}_\alpha (+M) \rightarrow \sum_{\alpha=1}^{N} \nu''_{\alpha,m} \mathcal{M}_\alpha (+M), \tag{2.32}$$

One formulation of a pressure-dependent reaction rate is Lindemann. In Lindemann form, both the high (k_∞) and the low (k_0) pressure limiting rate constant are taken to be of the Arrhenius form. For pressures, p, in the fall-off regime, rate constants, $k_L(T)$, are expressed by the curve-fit as:

$$k_L(T) = \frac{k_\infty}{1 + k_{fall}/c_M}, \tag{2.33}$$

where k_{fall} is the fall-off rate coefficient written as $k_{fall} = f_\infty / k_0$ and c_M is the third-body concentration.

For MILD combustion, the existence of intermediate species and radicals, and differential diffusion effects are important (Aminian *et al.*, 2011; van Oijen, 2013). Therefore, the chemical kinetics of methane-air combustion are modelled using a skeletal mechanism (Smooke & Giovangigli, 1991) including non-unity Lewis number effects. The Lewis number of each species and elementary reactions are listed in tables 1 and 2 in Appendix A. The skeletal mechanism contains 10 reversible and 15 irreversible reactions with 15 reactive species (+ N_2). The skeletal mechanism has also been validated against GRI-3.0 mechanism (Smith *et al.*) in several flame conditions including MILD conditions, using a commercial software Cosilab. Basic flame parameters obtained from the skeletal mechanism are comparable with the solutions calculated using the GRI-3.0 mechanism. The laminar unstrained flame speed and the peak temperature, for instance, respectively differ less than 10% and 3% from GRI-3.0 results for all cases tested. The autoignition delay time obtained from homogeneous reactor calculation has a maximum difference of 25% between GRI-3.0 and the skeletal mechanism under the conditions considered in this work.

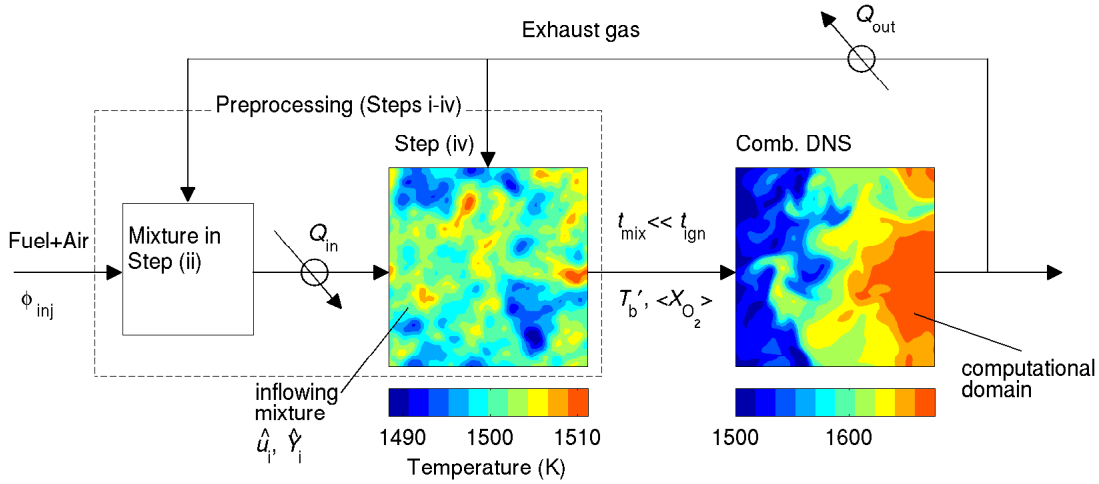

Figure 2.1: Schematic illustration of the present two-phase strategy. Characteristics of initial and inflowing mixture at the end of Step (iv) explained in section 2.5.1.

2.4 Configuration and boundary conditions

In practice, it is common to inject fuel and air into either a recirculating flow or a stream containing products to achieve MILD combustion (Wünning & Wünning, 1997; Katsuki & Hasegawa, 1998; Cavaliere & de Joannon, 2004). The diluted mixture may be preheated significantly using recovered exhaust heat employing recuperative or regenerative heat exchangers (Suzukawa *et al.*, 1997; Plessing *et al.*, 1998). Such configurations with high momentum jets have been applied to achieve an appropriate mixture for MILD combustion in a limited mixing time (Katsuki & Hasegawa, 1998; Plessing *et al.*, 1998; Özdemir & Peters, 2001; Dally *et al.*, 2002; Cavaliere & de Joannon, 2004; Dally *et al.*, 2004; Awosope *et al.*, 2006; Galleti *et al.*, 2007; Li & Mi, 2011). Although the high jet momentum typically used in MILD combustors can enhance mixing, a limited mixing time may result in a spatially and temporally inhomogeneous mixture consisting of fresh and exhaust gases. The size of these pockets is random and determined by the turbulence conditions. This inhomogeneous mixture then either autoignites or establishes a propagating flame depending on the local turbulence and ther-

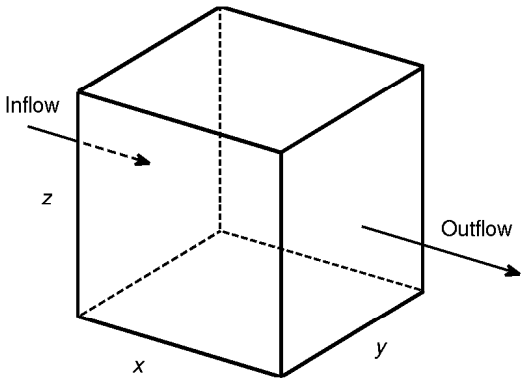

Figure 2.2: Numerical configuration of combustion DNS.

mochemical conditions. Such processes of MILD combustion in EGR-type configuration are schematically illustrated in figure 2.1. These processes and the mixture inhomogeneity effect have to be taken into account in the combustion DNS for investigations into MILD reaction zones. However, DNS of a complete MILD combustion system employing such a configuration is not yet feasible because of the heavy computational cost involved. Thus, the simulation is split into two phases to mimic the physical processes involved in MILD combustion, under the assumptions explained above. The first phase, namely mixing DNS, consists of the construction of a non-uniform mixture field which is consistent with the required turbulence and MILD combustion condition. The second phase, combustion DNS, is turbulent MILD combustion in a computational domain. The non-uniform mixture field generated in the mixing DNS is fed into the combustion DNS domain. These two phases considered in the present DNS are pictorially shown in figure 2.1 and Steps (ii) and (iv) noted are discussed in the next section. Note that the present study considers premixed combustion mode, although the vast majority of applications are non-premixed.

The computational domain considered for combustion DNS (the second phase) is shown in figure 2.2; this domain has an inflow and non-reflecting outflow boundary conditions in the x-direction, and periodic conditions in the y and z-directions. The non-reflecting boundary conditions are specified according to

the Navier-Stokes Characteristic Boundary Condition (NSCBC) formalism with Local One-Dimensional Inviscid (LODI) approximation (Poinsot & Lele, 1992; Jenkins & Cant, 1999). The initial mixture field inside the cubic computational domain and the mixture flowing into this domain are carefully preprocessed to include the mixture inhomogeneity effect based on the physical process explained in the previous paragraph. Such mixture fields are constructed using a method explained in section 2.5 for MILD cases. The preprocessed mixture field containing pockets of exhaust and fresh gases is fed at an average velocity of U_{in} from the inflow boundary located at $x = 0$ of the computational domain. On the inflow boundary, turbulent velocity $\boldsymbol{u}$, mass fractions Y_i of species i and temperature T are specified using preprocessed fields, $\hat{\boldsymbol{u}}$, $\hat{Y}_i$ and $\hat{T}$, for MILD combustion cases as:

$$\boldsymbol{u}(x = 0, y, z, t) = \hat{\boldsymbol{u}}[\underline{x}(t), y, z] + U_{in}, \tag{2.34}$$

$$Y_i(x = 0, y, z, t) = \hat{Y}_i[\underline{x}(t), y, z], \tag{2.35}$$

$$T(x = 0, y, z, t) = \hat{T}[\underline{x}(t), y, z], \tag{2.36}$$

where $\underline{x}(t)$ denotes the x location of a scanning plane at time t; this scanning plane is moving at a velocity of U_{in} through the preprocessed fields. The method to construct these preprocessed fields is described in the next section. For the DNS of conventional turbulent premixed combustion, only the turbulent velocity field $\boldsymbol{u}$ is preprocessed, and the species mass fraction and temperature at the inflow boundary are set to be constant values, as in a standard practice. These constant values correspond to the initial mixture composition.

2.5 Preprocessing of initial and inflow fields

2.5.1 MILD combustion

The desired inhomogeneous fields, $\hat{\boldsymbol{u}}$, $\hat{Y}_i$ and $\hat{T}$, are obtained for DNS of MILD combustion following the steps given below.

Step (i) A turbulent velocity field is generated in a preliminary DNS of freely decaying, homogeneous isotropic turbulence in a periodic domain.

The flow field is first initialised based on an energy spectrum (Batchelor & Townsend, 1948) as in (Rogallo, 1981). After the initialisation, the simulation is continued until the velocity derivative skewness reaches an approximately constant value of -0.5 representing a fully developed turbulence field and desirable turbulence intensity is achieved.

Step (ii) A one-dimensional laminar flame freely propagating into a reactant mixture of a desired MILD condition is calculated using the skeletal mechanism (Smooke & Giovangigli, 1991). The reactants are diluted with products of fully burnt mixture ($X_{H_2O} : X_{CO_2} = 2 : 1$), and the molar fraction of O_2 in the reactant mixture $X_{O_2,r}$ is matched with the desired dilution level. Thermochemical properties of these laminar flames are described in section 2.6.

Step (iii) An initial artificial inhomogeneous scalar field is obtained by specifying a scalar-energy spectrum function as in Eswaran & Pope (1987). A technique similar to this is also used in a previous study (Sankaran *et al.*, 2005). This field is taken as the initial reaction progress variable, defined as $c_Y = 1 - Y_{CH_4}/Y_{CH_4,r}$, taking values between 0 and 1. The same c_Y field shown in figure 2.5a is used for all the MILD cases. The fuel (CH_4) mass fraction is Y_{CH_4} and the subscript, r, denotes the reactant mixture. The flame solution from Step (ii) is then mapped to this c_Y field to obtain the inhomogeneous species mass fraction fields, and the elevated temperature is set to a constant value of T_m to be specified later. Note that under this assumption, the enthalpy is not conserved during the mixing DNS. However, such nearly-constant temperature and fluctuating species fields before combustion may be observed in MILD combustor employing recuperative or regenerative heat exchangers to heat up a mixture between exhaust gases, air, and fuel (Plessing *et al.*, 1998; Özdemir & Peters, 2001). The fluctuations in these species mass fraction fields do not yet have any correlation with the turbulence obtained in Step (i).

Step (iv) These species mass fraction and turbulence fields are then allowed to evolve in a periodic domain to mimic the EGR-mixing without any chemical reaction. This mixing DNS — allowing the scalar fields to develop correlations with the turbulence — is run for about one large eddy time, ℓ_0/v', which is much shorter than the autoignition delay time for the respective mixture summarised in table 2.1 in the next section. The root-mean-square (RMS) of the turbulent fluctuations obtained in Step (i) is v' and its integral length scale is ℓ_0. The internal energy equation is also solved in this step to mimic the evolution of temperature during the mixing process; this creates a maximum temperature fluctuation of about 2% of the mean value, T_m, for the cases considered in this work. The detailed mixture conditions and features of the preprocessed field are respectively explained in sections 2.6 and 2.7. Note that the species in exhaust gas pockets are not in chemical equilibrium in these steps to simplify the problem of the present work.

2.5.2 Conventional Premixed combustion

The initial scalar field for the conventional premixed combustion DNS is constructed by mapping a laminar flamelet solution onto the DNS domain, where x-direction is the coordinate normal to the flame. The laminar flamelet used for the conventional premixed combustion case is explained in section 2.6. The initial turbulent velocity field is preprocessed using the same method as in Step (i), explained in section 2.5.1 for MILD combustion DNS. The turbulent velocity field is then mapped onto the DNS domain by assuming constant mass flux through the flame (Cant, 2012).

2.6 Simulation conditions

2.6.1 Introduction of Flames and MILD Flame Elements

The one-dimensional unstrained laminar flames used in the initial field construction described in section 2.5 are named Flames A and B for MILD cases, and Flame C for the conventional premixed case. Their temperature profiles are shown in Figure 2.3, and thermochemical properties are summarised in Table 2.1. The mole fraction of the species α in reactants $X_{\alpha,r}$ shows the dilution level of the mixture. The laminar flame speed S_L is based on the integral of the burning rate across the flame brush (Poinsot & Veynante, 2005):

$$S_L = -\frac{1}{\rho_r Y_{\mathrm{CH_4},r}} \int_{-\infty}^{+\infty} \omega_{\mathrm{CH_4}} dx. \tag{2.37}$$

The laminar flame speed is a few metres per second because of the high reactant temperature for MILD conditions. The flame thermal thickness δ_{th} is calculated as $\delta_{th} = (T_p - T_r)/|\nabla T|_{\max}$.

These flame quantities are computed using 1D version of SENGA2 and these values are close to those obtained using the PREMIX code (Kee *et al.*, 1985) and Cosilab (COSILAB, 2007). When the reactant temperature is larger than its autoignition temperature the value of S_L may depend on the computational domain size, and the values in table 2.1 are computed using a domain size of 10 mm, which is the largest length employed for the DNS computations (see next subsection). These laminar flames are also computed using a 40 mm domain, but the difference between the results of 10 and 40 mm domains in S_L and δ_{th} is around 5% of the values in table 2.1. Since S_L may not be unique (Habisreuther *et al.*, 2013) for $T_r > T_{ign}$, retaining the computational domain size allows one to have a basis for a meaningful analyses. For these reasons, S_L given in table 2.1 for reactants with $T_r > T_{ign}$ must be read with caution. The autoignition delay time τ_{ign} given in table 2.1 is computed using a zero-dimensional, constant pressure homogeneous reactor and employing the maximum temperature gradient criterion. The presence of turbulence can alter the balance among unsteady evolution, reaction and diffusion processes locally leading to a change in ignition

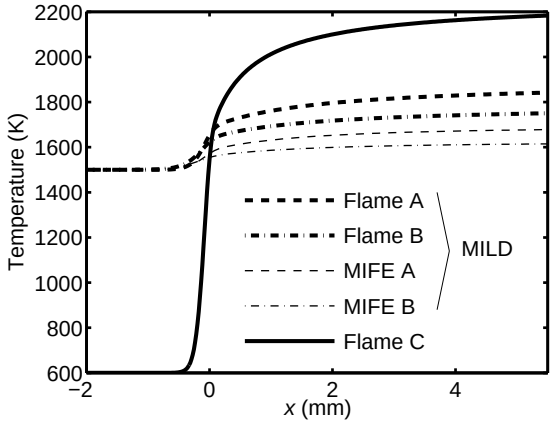

Figure 2.3: One-dimensional flames for the MILD and conventional premixed combustion cases.

Table 2.1: Summary of laminar flame properties. Units are Kelvin (K), meters/second (m/s), millimetres (mm) and milliseconds (ms).

	$X_{\mathrm{CH_4},r}$	$X_{\mathrm{O_2},r}$	$X_{\mathrm{H_2O},r}$	$X_{\mathrm{CO_2},r}$	T_r	T_p	S_L	δ_{th}	τ_{ign}
Flame A	0.019	0.048	0.121	0.061	1500	1865	3.20	0.69	4.968
Flame B	0.014	0.035	0.132	0.066	1500	1775	2.15	0.94	6.710
Flame C	0.078	0.194	0.0	0.0	600	2179	1.18	0.37	-
MIFE A	0.0095	0.0349	0.136	0.064	1500	1692	2.62	1.00	5.420
MIFE B	0.0060	0.0248	0.143	0.068	1500	1624	1.66	1.29	6.960

delay time compared to the PSR model value. This is not considered here and thus the value of τ_{ign} given in table 2.1 is only for guidance purposes, and one must use a partially stirred reactor (PaSR) model to include turbulence effects. The PaSR will obviously introduce some uncertainties due to modelling involved in that approach.

Flame C is a classical premixed flame, which is indicated by the large temperature rise seen in figure 2.3 and the reactant mole fractions listed in table 2.1. In contrast, the temperature rise across the laminar flames with the diluted and preheated mixtures is observed to be relatively small, about 370 K for the Flame A and 290 K for the Flame B. This is typical of MILD combustion.

Spatial variations of species mass fraction in the inflowing mixture fields are

inevitable when the MILD combustion occurs in three dimensions, and it is not possible to represent this spatial variation in a representative 1D laminar flame. Indeed, the effect of the additional dilution resulting from the spatial variation reduces the burnt mixture temperature in the turbulent cases by almost 150 K compared to the respective laminar Flames A and B. To account for the dilution effect even for laminar flames, the mass fractions of major species in the reactant mixture are computed based on the volume average of the respective species in the preprocessed DNS initial field obtained in Step (iv) described in section 2.5.1. A laminar flame having these reactant mixtures is named MILD Flame Element (MIFE) in this study. As one would expect, this averaging yields significantly smaller oxygen mole fraction values as noted in Table 2.1 for MIFEs A and B compared to the Flames A and B. Also, the burnt mixture temperature, T_p, is only about 27 K larger than the DNS values (this is the maximum difference observed). A detailed analysis of MIFE is performed in Appendix B. For these reasons, MIFEs are taken to be representative canonical candidates for the MILD combustion cases investigated in this study, and their thermochemical attributes listed in Table 2.1 are used to normalise the respective DNS results. For example, length, gradient of reaction progress variable and reaction rate are respectively normalised using δ_{th}, $1/\delta_{th}$ and $\rho_r S_L/\delta_{th}$. The normalised quantities are denoted using a superscript "+".

2.6.2 Turbulence and thermochemical conditions

The velocity and scalar fields, preprocessed as described in the previous subsection, are used as the initial and inflow fields in the three-dimensional combustion DNS. Three cases having MILD conditions (Cases A1, A2 and B1) and one having a conventional premixed condition (Case C) are considered for this study as summarised in Table 2.2. The preprocessed mixture for Cases A1 and A2 is based on Flame A, and that for Case B1 is based on Flame B. Thus, Case A1 and Case A2 have the same dilution level. Also turbulence level for Cases A1 and B1 is very close, since the identical turbulent velocity field generated in Step (i) in section 2.5 is used for the preprocessing for these two cases. All of these combustion conditions have an equivalence ratio of $\phi = 0.8$ under atmospheric pressure.

The iginition temperature is 1100 K for this lean methane-air mixture, which is obtained based on PSR calculations with 1 s residence time. The inlet and initial mixture temperatures are set to be $T_m \approx 1500$ K for the MILD combustion cases, which is comparable to that used in the previous study (Suzukawa *et al.*, 1997). This inlet temperature and the dilution level used in the present DNS show that the combustion conditions for Cases A1–B1 are strictly in the MILD regime as shown in figure 1.2. The reactant temperature for the conventional turbulent premixed combustion, Case C, is set to be 600 K. The maximum $X_{O_2,r}^{max}$ and averaged $\langle X_{O_2,r} \rangle$ molar fractions of oxygen in the reactant mixtures given for the MILD cases show that they are nearly an order of magnitude smaller than for the conventional premixed case, Case C, indicating high dilution level. The dilution level for MILD cases is comparable with the previous studies (Katsuki & Hasegawa, 1998; de Joannon *et al.*, 2000; Cavaliere & de Joannon, 2004). The Zel'dovich thickness is obtained as:

$$\delta_F = \frac{\lambda_{th,r}}{\rho_r c_{p,r}} \frac{1}{S_L}, \tag{2.38}$$

where $\lambda_{th,r}$ and $c_{p,r}$ are respectively the thermal conductivity and specific heat capacity at constant pressure in the reactant mixture. The mean $\langle \xi \rangle$ and stoichiometric ξ_{st} mixture fraction values for the different cases are also given in table 2.2. The RMS turbulent velocity fluctuations and the integral length scale of the initial turbulence field are denoted respectively as u' and l_0 in table 2.2.

The Reynolds numbers based on the longitudinal integral length scale Re_{l_0} and Taylor microscale Re_λ are varied respectively from 67 to 96 and from 25 to 33 for the MILD cases, where the RMS turbulent velocity fluctuation u' is used as a characteristic velocity scale. In the previous experimental studies of MILD combustion, only jet Reynolds number $\mathrm{Re}_{\mathrm{jet}}$ is reported and ranges between 2500–8800 (Oldenhof *et al.*, 2011), about 9300 (Duwig *et al.*, 2012), and 5000–15000 (Medwell, 2007). However, both Re_{l_0} and $\mathrm{Re}_{\mathrm{jet}}$ are reported or can be calculated for several jet flame experiments (not MILD), and their relation is shown in figure 2.4a. Based on these reported values, Re_{l_0} for typical laboratory scale MILD combustors is estimated, and they are comparable to Re_{l_0} of the present DNS conditions for MILD combustion. For Cases A1 and B1, there is a strong

Table 2.2: turbulent combustion conditions.

	$X_{O_2,r}^{max}$	$\langle X_{O_2,r} \rangle$	$\langle \xi \rangle$	ξ_{st}	U_{in}/S_L	u'/S_L	l_0/δ_F	l_0/δ_{th}	$Re_{l_0\,(\lambda)}$	Da	Ka
Case A1	0.048	0.035	0.011	0.014	9.6	6.26	10.8	1.48	96.2 (32.6)	1.72	4.78
Case A2	0.048	0.035	0.011	0.014	9.6	3.80	12.3	1.70	67.0 (25.6)	3.25	2.11
Case B1	0.035	0.025	0.008	0.010	15.1	9.88	6.8	1.15	96.1 (32.6)	0.69	11.9
Case C	0.194	0.194	0.044	0.055	3.0	2.19	12.3	2.11	38.5 (17.6)	5.64	0.92

possibility that local reacting mixtures are convected towards outside the inlet boundary since $U_{in} \sim u'$ as in table 2.2. However, the results described in the later chapters are unduly influenced by this effect which is assessed by comparing the results of lower turbulence case (Case A2) and the other MILD cases. Note that the turbulence level for the conventional premixed combustion case is deliberately set to be a small value. This is due to the intention to compare MILD combustion and conventional premixed combustion with large Damköhler and small Karlovitz number conditions (Peters, 2000). The Damköhler and Karlovitz numbers are defined as $\mathrm{Da} = (l_0/\delta_F)/(u'/S_L)$ and $\mathrm{Ka} \approx (u'/S_L)^{3/2}(l_0/\delta_F)^{-1/2}$ respectively. Using the classical turbulent combustion regime diagram (Peters, 2000), the first three cases, Cases A1, A2 and B1, are in the thin-reaction zones regime, and Case C is near the border between the thin-reaction zones and corrugated flamelets regimes. Note that the regime diagram for MILD combustion might not be as representative as for conventional premixed combustion, due to the presence of autoignition and the distributed nature that do not necessarily require very high turbulent flows for generation of distributed reaction zones. Case A1 and Case A2 have the same dilution level but differ in the turbulence conditions of the inflowing mixture. The turbulence Reynolds numbers for Case A1 and Case B1 are almost the same but these cases have different dilution levels.

The computational domain has dimensions of $L_x \times L_y \times L_z = 10.0 \times 10.0 \times 10.0\,\mathrm{mm}^3$ for Cases A1, A2 and B1, and $L_x \times L_y \times L_z = 10.0 \times 5.0 \times 5.0\,\mathrm{mm}^3$ for the conventional premixed flame, Case C. If the computational domain is normalised using δ_{th} of the respective laminar flame, $L_x^+ \times L_y^+ \times L_z^+ = 10.0^3$ for Cases A1 and A2, 7.7^3 for Case B1, and $26.7 \times 13.4 \times 13.4$ for Case C. These domains are discretised using $512 \times 512 \times 512$ mesh points for Cases A1 and A2, $384 \times 384 \times 384$ mesh points for Case B1, and $512 \times 256 \times 256$ mesh points for Case C. These meshes ensure that there are at least 15 mesh points inside the thermal thickness, δ_{th}, and at least 2 mesh points inside the Kolmogorov length scale.

The simulations of the MILD cases were run for 1.5 flow-through times before collecting data for statistical analysis. This ensured that the initial transients had left the domain. The flow-through time τ_D is defined as the mean convection time, L_x/U_{in}, from the inflow to the outflow boundary. The simulations were

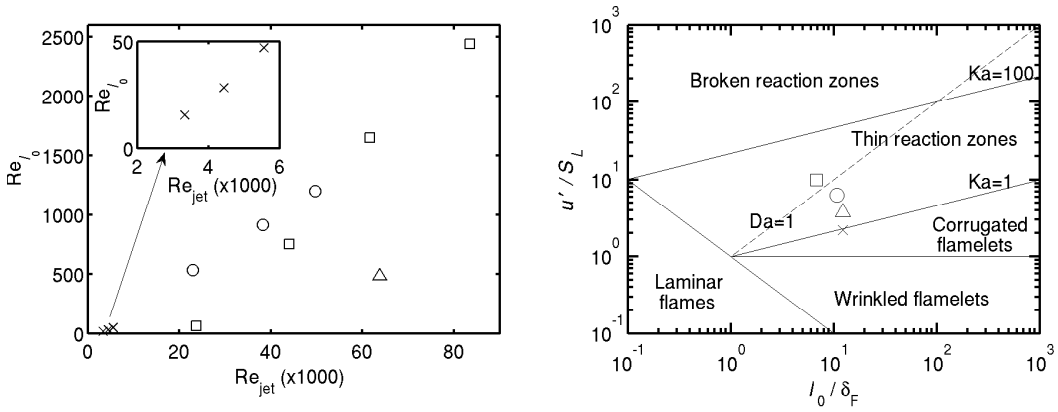

(a) (b)

Figure 2.4: (a) Turbulence conditions in the past experimental studies of jet flames. ◯ : Chen *et al.* (1996), △ : Duwig *et al.* (2007), □ : Buschmann *et al.* (1996), and × : Pfadler *et al.* (2008). (b) Turbulent combustion regime diagram (Peters, 2000). ◯ : Case A1, △ : Case A2, □ : Case B1, and × : Case C.

then continued for one additional flow-through time and 80 data sets (all the primitive variables) were collected. For the Case C, 93 data sets were collected over a time of $0.56\tau_D$ after allowing one flow-through time for initial transients to exit the computational domain. These simulations have been run on Cray XE6 systems using 4096 cores with a wall-clock time of about 120 hours for Case A1 and Case A2, which have the largest number of mesh points in MILD cases, and using 16384 cores with 80 hours of wall-clock time for Case C.

2.7 Results of preprocessed fields

Spatial variation of c_Y field obtained from the scalar energy spectrum in Step (iii) and its PDF (red dashed line) are shown in figure 2.5. It is clearly shown that the c_Y field has a typical bimodal distribution at this stage, because variation of mixture composition is based on the respective laminar flame solution. The PDF of c_Y in the preprocessed field obtained in Step (iv) is shown in figure 2.5b for Case A1 (solid line), Case A2 (dashed line), and Case B1 (dash-dotted line). Although the PDF of the progress variable c_Y field obtained in Step (iii) shows

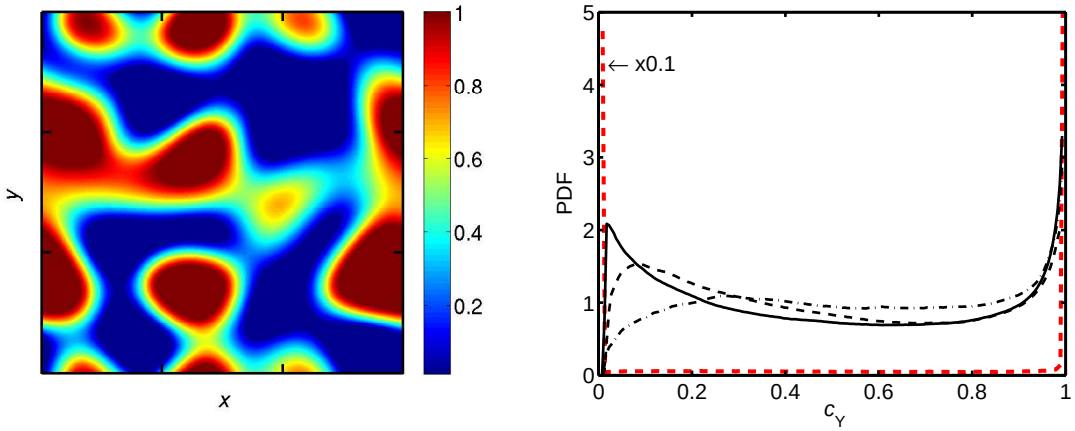

(a) (b)

Figure 2.5: (a) Spatial variation of c_Y field at a mid x-y plane obtained in Step (iii). (b) PDF of c_Y field. Red dashed line: initial field of mixing DNS obtained in Step (iii), solid line: preprocessed inhomogeneous field to be used for Case A1, dashed line: Case A2, and dash-dotted line: Case B1. Note that the PDF of initial mixing DNS field (red dashed line) is multiplied by a factor of 0.1.

a typical bimodal shape, the turbulent mixing and molecular diffusion processes that have occurred during Step (iv) yield samples with intermediate values, $0 < c_Y < 1$. The PDFs of the c_Y field obtained in Step (iv) show that a substantial portion of mixture is well mixed after these procedures, while there are local mixture pockets which still have either fresh or exhaust gases.

Spatial variations of the scalar fields obtained at the end of Step (iv) are also shown for c_Y, $\hat{Y}_{O_2}$, $\hat{Y}_{H_2O}$, and $\hat{Y}_{OH}$ in figures 2.6, 2.7 and 2.8, to be used respectively for Cases A1, A2 and B1. The species have evolved with the turbulence during the mixing DNS resulting in an inhomogeneous mixture of reactants and products. Radicals and intermediate species also exist and are partially mixed in the domain to represent an EGR-type mixture. It is clearly shown in the preprocessed fields that the mass fraction of O_2 is lower than the H_2O mass fraction accordingly to the dilution level summarised in table 2.2. Despite the use of the same shape of initial c_Y field obtained in Step (iii), two turbulence velocity fields yield different inhomogeneous mixture fields as shown in a comparison of the pre-

processed c_Y field for Cases A1 (figure 2.6a) and A2 (figure 2.7a). A comparison of the preprocessed field between Cases A1 (figure 2.6) and B1 (figure 2.8) shows that the dilution level also affects the mixing process.

After the preprocessing procedures described in section 2.5, the mean and variance of the preprocessed c_Y field are respectively $\langle c_Y \rangle \approx 0.50$ and $\langle c_Y'^2 \rangle \approx 0.09$ for all MILD cases considered for this study. In the preprocessed mixture field, the Bilger's mixture fraction (Bilger *et al.*, 1990) has a variation of around $\pm 5\%$ of the mean value, $\langle \xi \rangle$. The equivalence ratio — obtained using $\phi = (1-\xi_{st})\xi/[(1-\xi)\xi_{st}]$, where ξ_{st} is the stoichiometric mixture fraction — gives a mean value of $\langle \phi \rangle = 0.8$ for all the cases considered in this study. The calculation of the mixture fraction is based on a boundary condition in which the air diluted with products to a desired level of oxygen is fed from the air stream, while pure fuel is fed from the fuel stream. The preprocessed partially premixed mixture fields of fresh and exhaust gases are essential to simulate a MILD combustion field on a par with those observed in laboratory scale MILD combustors.

From the following chapters, the data sets from the DNS are analysed to address the objectives of this thesis outlined in the introduction.

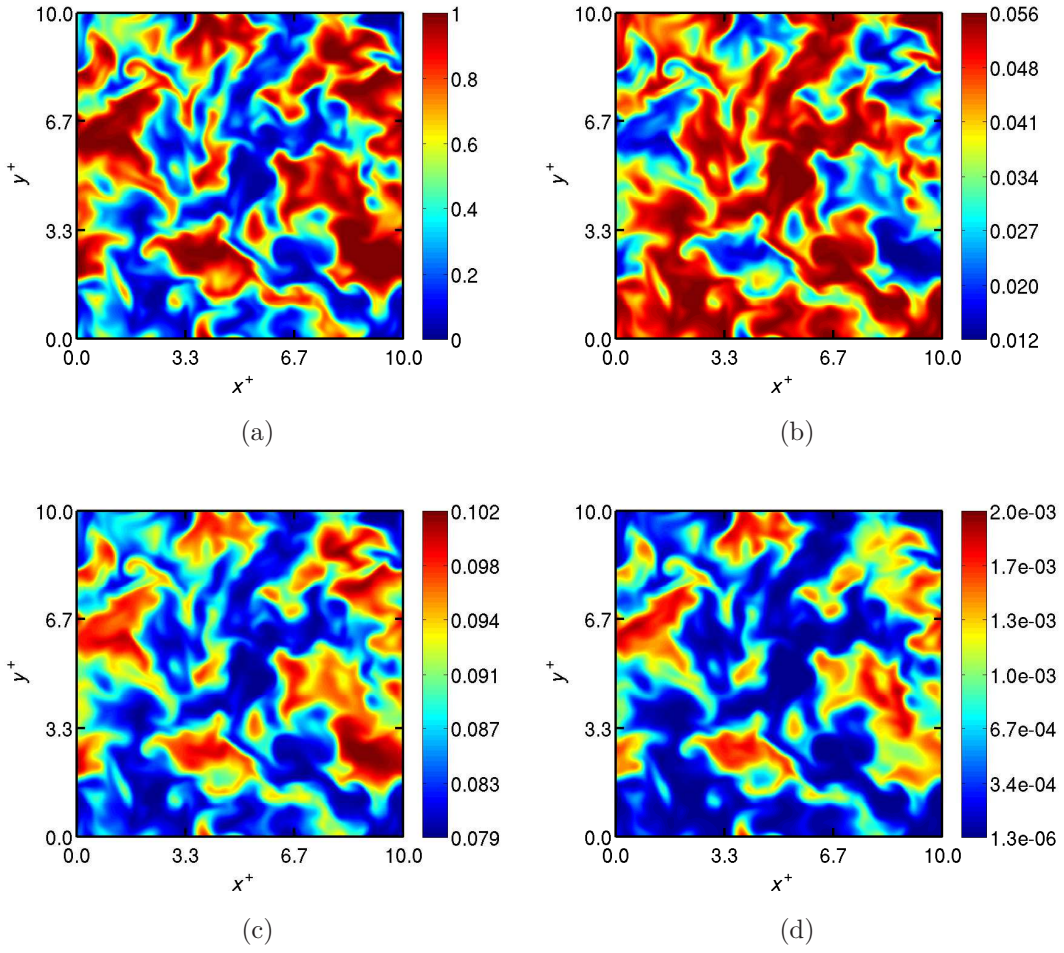

Figure 2.6: Spatial variations of initial field (a) c_Y, (b) $\hat{Y}_{O_2}$, (c) $\hat{Y}_{H_2O}$, and (d) $\hat{Y}_{OH}$ at the mid x-y plane obtained in Step (iv) for Case A1.

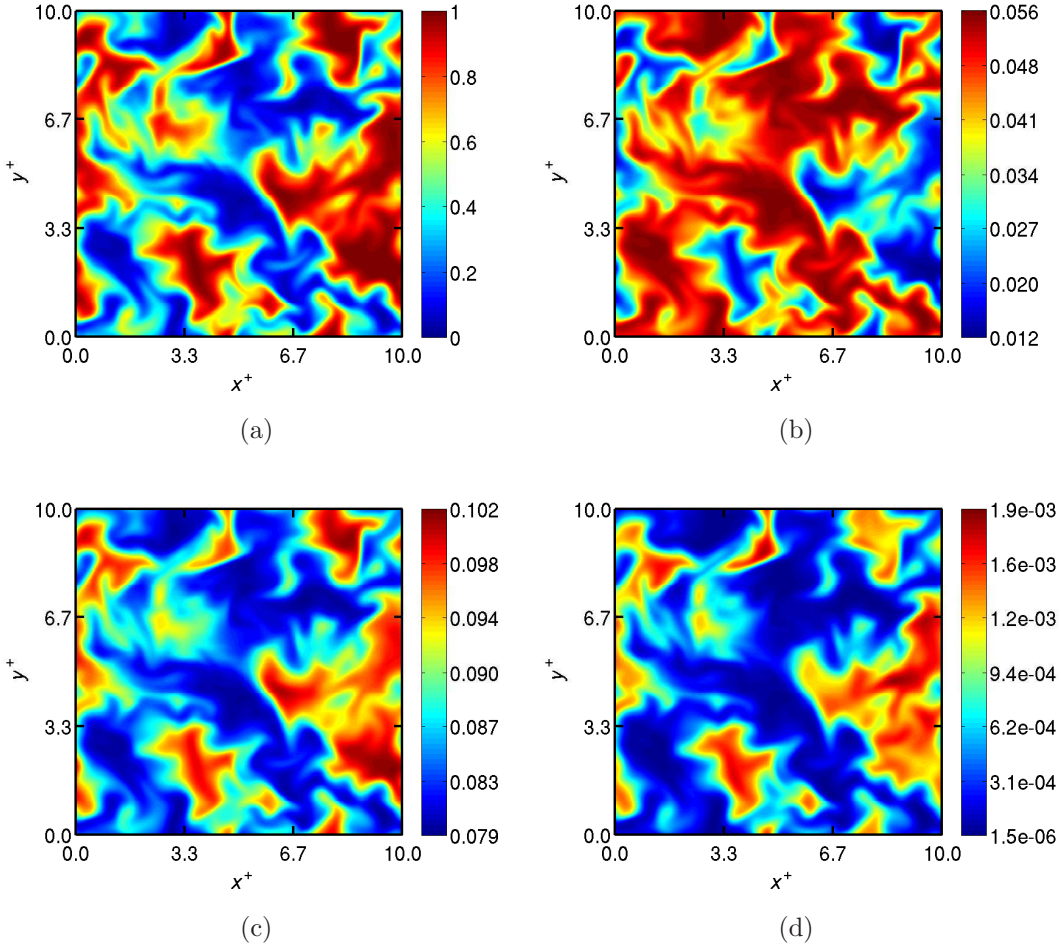

Figure 2.7: Spatial variations of initial field (a) c_Y, (b) $\hat{Y}_{O_2}$, (c) $\hat{Y}_{H_2O}$, and (d) $\hat{Y}_{OH}$ at the mid x-y plane obtained in Step (iv) for Case A2.

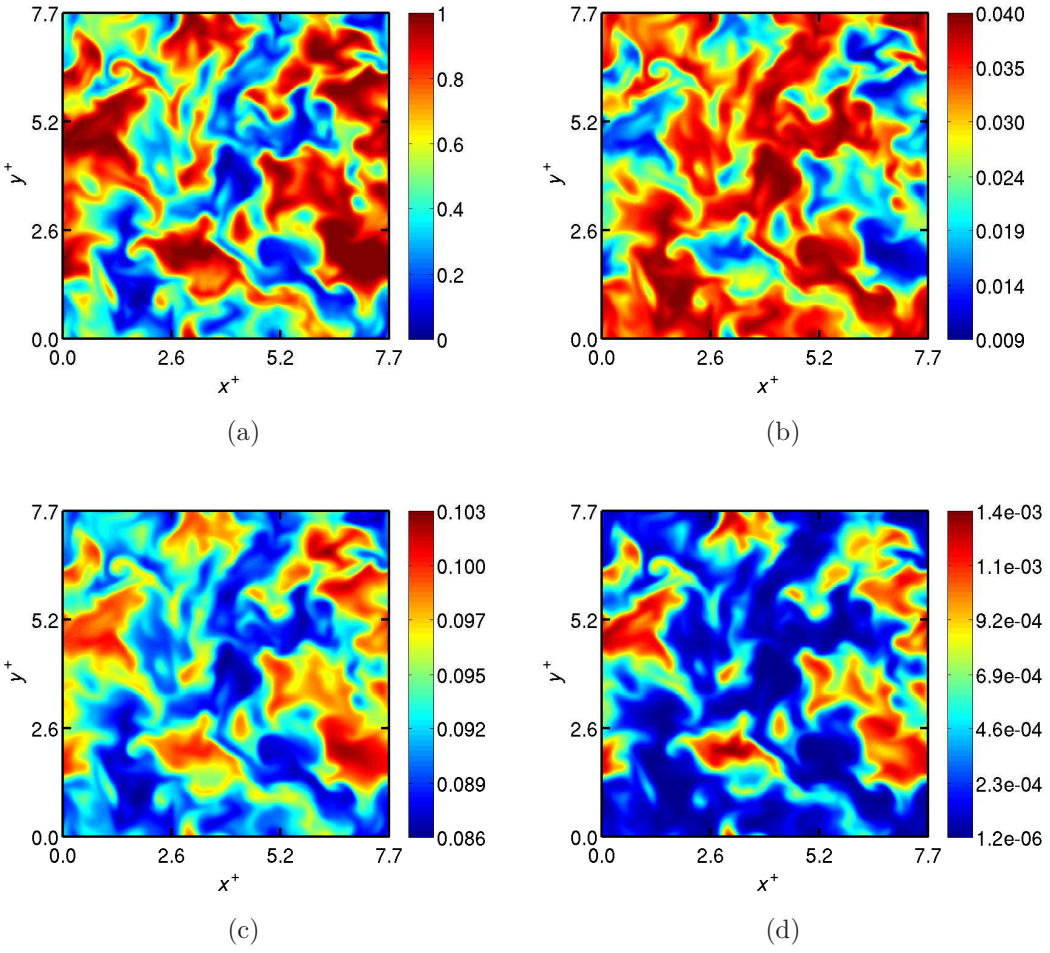

Figure 2.8: Spatial variations of initial field (a) c_Y, (b) $\hat{Y}_{O_2}$, (c) $\hat{Y}_{H_2O}$, and (d) $\hat{Y}_{OH}$ at the mid x-y plane obtained in Step (iv) for Case B1.

Chapter 3

Structure and Morphology of MILD Reaction Zones

Through understanding of reaction zones evolving in turbulence is necessary for turbulent combustion modelling. In this chapter, reaction zone structure, morphology of reaction zones as well as general features of the simulated MILD combustion are discussed for further investigations which are followed afterwards.

3.1 General features of MILD combustion

Volume rendered temperature fields for the simulated conventional premixed combustion (Case C) and MILD combustion (Case B1) cases are shown in figure 3.1. These snap shots are taken at $t = 1.5\tau_D$ looking through the z-direction. Here, since the same colour map and opacity are used, the two images may be compared directly as is often done for direct photographs of turbulent flames. As shown in figure 3.1a, flame fronts are observed in the conventional premixed combustion case, clearly suggesting a strong gradient across the flame. However, there is no visible flame front observed in MILD combustion as in figure 3.1b. Similar observations based on direct photographs have been reported in previous studies (de Joannon *et al.*, 2000; Özdemir & Peters, 2001; Krishnamurthy *et al.*, 2009). Such "colourless" combustion is the reason why MILD combustion is often referred to as "flameless" combustion. The comparison of the simulated combus-

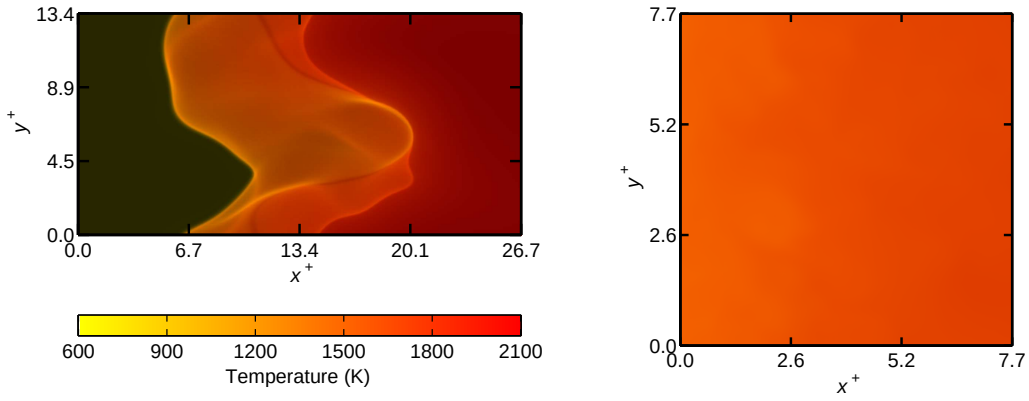

(a) (b)

Figure 3.1: Comparison of volume rendered temperature field of (a) conventional turbulent premixed and (b) MILD combustion from the present DNS cases.

tion modes seems to support the non-appearance of thin flame fronts in MILD combustion.

Probability Density Functions (PDF) of reaction progress variable, $c_T = (T - T_r)/(T_p - T_r)$, are shown in figure 3.2. The sampling locations, $x^+ = 7.48$, 17.5 and 25.9, respectively correspond to $\tilde{c}_T = 0.07$, 0.66 and 0.94. The PDFs for Case C in figure 3.2a show typical bimodal behaviour of progress variable in conventional premixed combustion. The PDFs have sharp peaks at $c_T \sim 0$ and/or $c_T \sim 1$, and the probability of finding intermediate values is close to zero for all the x-locations, ensuring thin reaction zones with a strong scalar gradient. However, the PDFs for the MILD cases shown in figures 3.2b–3.2d reveal neither such sharp peaks nor bimodal behaviour in most streamwise locations. The PDF at $x^+ = 0.30$, which is near the inlet boundary, shows a relatively sharp peak at around $c_T = 0.05$, indicating that the unburnt gas is predominant at this region. At $x^+ = 2.9$ in Case B1, the PDF shows a plateau at $0.2 \leq c_T \leq 0.7$, suggesting distributed combustion, which may be very hard to model using a flamelet type approach. As the sampling location goes further down-stream, the probability of finding burnt gases becomes high, although the PDF distribution is still relatively broad compared to the PDF for the conventional premixed case.

The PDFs of c_T are represented reasonably well by using a presumed PDF

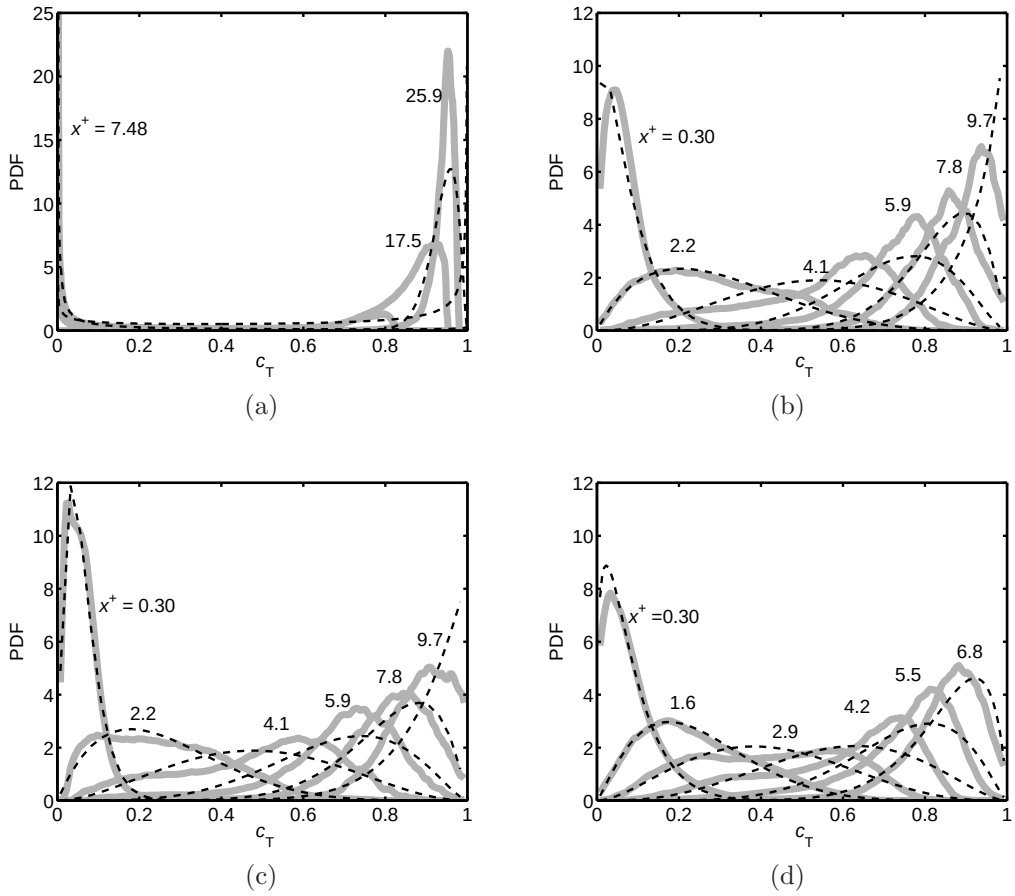

Figure 3.2: PDF of reaction progress variable (thick grey line) based on temperature at various x^+ locations for (a) Case C, (b) Case A1, (c) Case A2, and (d) Case B1. The PDF calculated based on the β-function is also shown (dashed line).

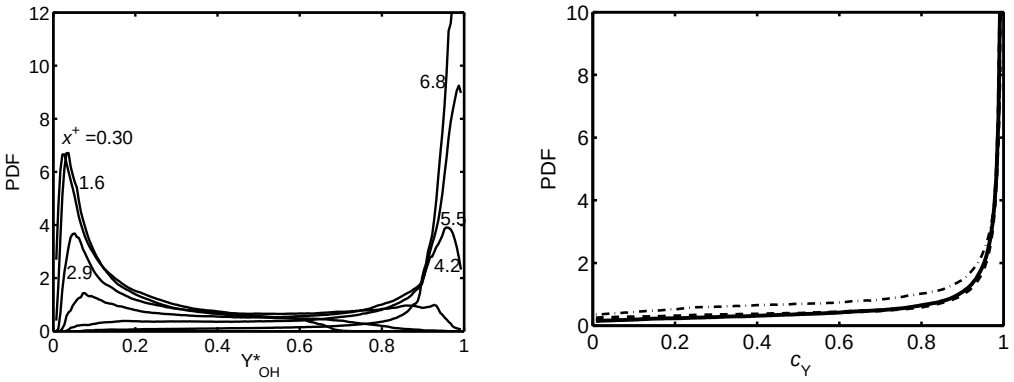

(a) (b)

Figure 3.3: (a) Typical PDF of normalised OH mass fraction Y^*_{OH} at various x^+ locations for Case B1. (b) Typical PDF of c_T for Case A1 (solid line), Case A2 (dashed line), and Case B1 (dash-dotted line). The sampling locations are $x^+ = 4.1$ for Cases A1 and A2, and $x^+ = 2.9$ for Case B1.

based on the β-function as shown in figures 3.2a–3.2d for both the conventional and MILD cases. Here, the presumed PDF $P(\xi)$ is constructed as:

$$P(\xi) = \frac{\xi^{r-1}(1-\xi)^{s-1}}{I_b}, \tag{3.1}$$

$$I_b = \int_0^1 \xi^{r-1}(1-\xi)^{s-1} d\xi = \frac{\Gamma(r)\Gamma(s)}{\Gamma(r+s)}, \tag{3.2}$$

$$r = \tilde{c}_T \left(\tilde{c}_T \frac{1-\tilde{c}_T}{\widetilde{c''^2_T}} - 1 \right), \quad s = r\frac{1-\tilde{c}_T}{\tilde{c}_T}, \tag{3.3}$$

where $\tilde{c}_T$ is Favre average of c_T, and c''_T is its fluctuation. The Reynolds and Favre averages of any field f are respectively denoted as $\bar{f}$ and $\tilde{f}$, which are calculated as:

$$\bar{f}(x) = \frac{1}{N_t N_y N_z} \sum_{n=1}^{N_t} \sum_{j=1}^{N_y} \sum_{k=1}^{N_z} f(x; j, k, n), \tag{3.4}$$

and

$$\tilde{f} = \frac{\overline{\rho f}}{\bar{\rho}}, \tag{3.5}$$

where N_t is the number of data sets collected over the sampling period. The presumed PDF is discussed and applied in section 6.3.1.

The PDF of normalised OH mass fraction, $Y^*_{\mathrm{OH}} = (Y_{\mathrm{OH}} - Y_{\mathrm{OH,min}})/(Y_{\mathrm{OH,max}} - Y_{\mathrm{OH,min}})$, is shown for Case B1 in figure 3.3a. Compared with the PDF of c_T for the same case, the OH mass fraction field exhibits relatively bimodal distribution. The sharp PDF peaks and a small probability density for intermediate values show that the spatial extent of the regions where OH production is intense is very small, which suggests the existence of thin reaction zones for the MILD case. Thin and distributed natures of MILD reaction zones are discussed in section 3.5 later in this chapter.

The statistical behaviour observed for $c_Y = 1 - Y_{\mathrm{CH_4}}/Y_{\mathrm{CH_4},r}$ is quite different from c_T, as in figure 3.3b. The PDF shows large probability density of the finding burnt gas, although the chosen sampling locations are in the middle of the domain where the temperature is still not close to T_p statistically (see figure 3.2). The sharp PDF peak for c_Y suggests that CH_4 is consumed quickly, due to the existence of chemically-active radicals and the low CH_4 level. The sharp peak and the small probability of finding intermediate values imply that the c_Y field has larger gradients than c_T at reaction zones, which is discussed in section 5.2.

3.2 Instantaneous fields

Iso-surfaces of normalised reaction rate $\omega^+_{c_T}$ of c_T, calculated as $\omega_{c_T} = \dot{Q}/c_p(T_r - T_p)$, is shown in figure 3.4, where $\dot{Q}$ is the heat release rate and c_p is the specific heat capacity of the mixture. As clearly shown in figure 3.4a, the intense reaction rate regions are bounded by the two iso-surfaces narrowly one another for the conventional combustion case. This suggests thin sheet reaction zones, which are typical for conventional premixed flames under high Da conditions, and are the basis of flamelet approaches (Peters, 2000). The reaction rate iso-surfaces in figure 3.4 show the length scales of the fluctuations, although the relatively uniform combustion nature with no evident gradient is suggested in the previous and present studies (de Joannon *et al.* (2000); Özdemir & Peters (2001); Krishnamurthy *et al.* (2009) and figure 3.1b). The MILD reaction zones shown in figure 3.4 are generally highly convoluted, and they seem to spread out

in a substantial volume of the domain, unlike the conventional combustion case. Although the Da number for the present conventional case is higher than the MILD cases, conventional planar premixed turbulent flames under comparable Da $(= (l_0/u')/(\delta_F/S_L))$ conditions to the present MILD cases show thin sheet like reaction zones with occasional interactions (Trouvé & Poinsot, 1994). The degree of iso-surface wrinkling observed in the MILD combustion cases shown in figures 3.4b–3.4d suggests the existence of frequent reaction zones interactions. The mixture reacts as soon as it enters the domain in the MILD case due to the high temperature inlet condition, and this is signified by the high iso-surface density near the inflow boundary as seen in figures 3.4b–3.4d. The iso-surface becomes more sparse towards the outflow boundary.

In order to carry out visual examinations of reaction zones in detail, the variation of the reaction rate ω_{cT}^{+} is shown in 2D slices (x-y and y-z planes) for the conventional premixed case (left column in figure 3.5), Cases A1 and A2 (figure 3.6), and Case B1 (figure 3.7). For the conventional premixed case, the reaction zones (eg. coloured area) are generally thin, giving a typical thickness of about δ_{th} as shown in figure 3.5. Due to the corrugated flame shape and flame displacement, reaction zones interact occasionally as shown in figure 3.5d. Such reaction zone behaviour is typical for conventional turbulent premixed combustion under large Da conditions (Trouvé & Poinsot, 1994).

Frequent reaction zone interactions are observed in the 2D slices of the reaction rate contours shown in figures 3.6 and 3.7 for the MILD cases. Interacting reaction zones have a typical thickness of about 2–3 δ_{th}, while reaction zones with a thickness of about δ_{th} are also observed in non-interacting regions. The x-y slices of the reaction rate field show that the intense reaction rate regions occupy a substantial volume at relatively upstream regions ($x \leq 0.5L_x$) for the MILD cases. The volume seems to decrease in the downstream regions for Cases A1 and A2. However, figure 3.7a shows that the convoluted reaction zones in Case B1 reach the downstream boundary frequently, ensuring volumetric combustion spreading out a larger portion of the domain under the high dilution condition.

The composition of a local mixture affects local propagation characteristics and ignitability of the mixture, and non-uniformity of the mixture composition eventually causes convolutions of reaction zones unlike in conventional combus-

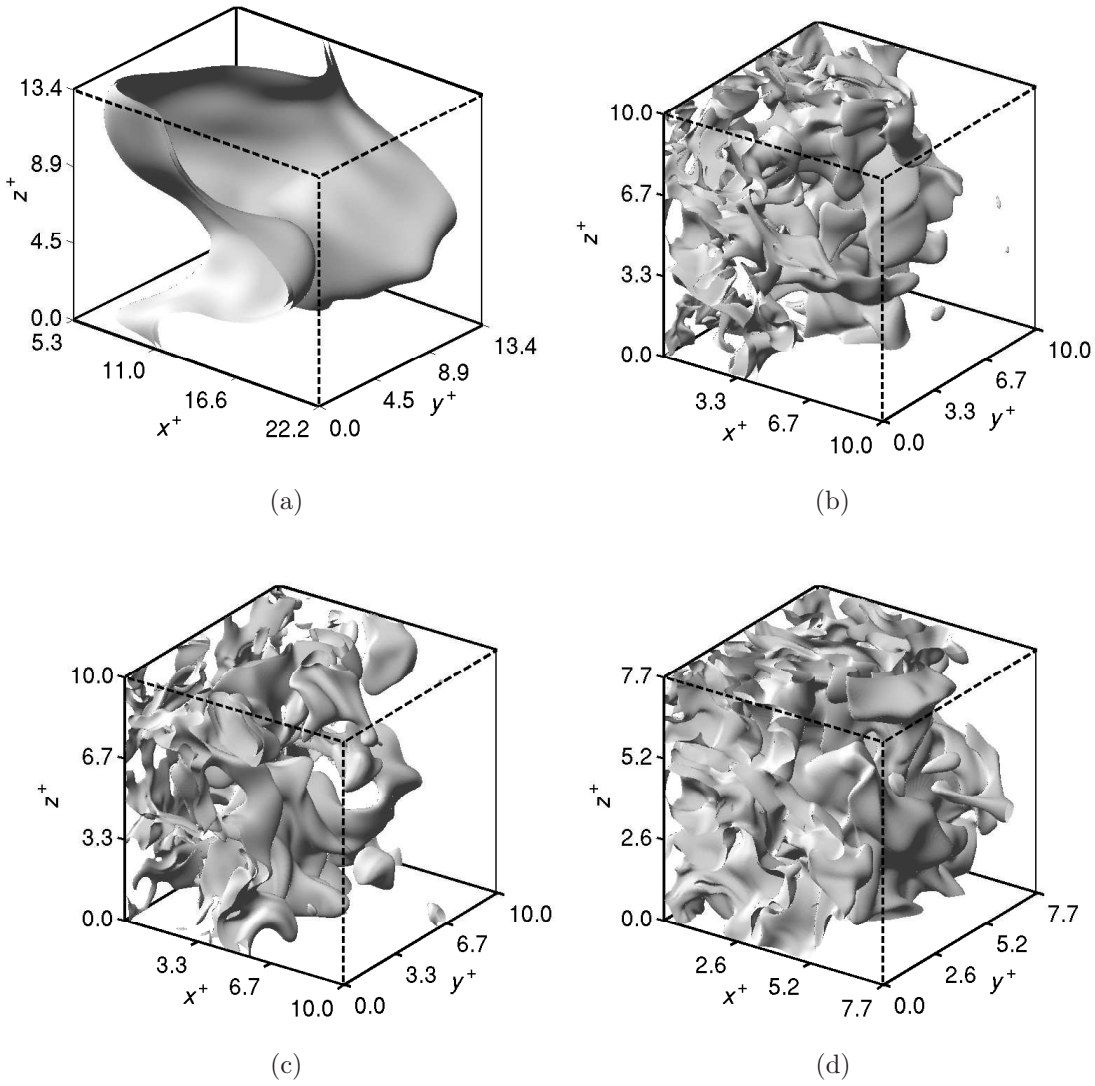

Figure 3.4: Reaction rate iso-surface of $\omega^+_{c_T} = 1.0$ for the conventional premixed case (a), and $\omega^+_{c_T} = 2.0$ for the MILD cases: (b) Case A1, (c) Case A2, and (d) Case B1. Note that only $5.3 \leq x^+ \leq 22.2$ of the computational domain is shown for Case C. All snapshots are taken at $t = 1.5\tau_D$.

tion. A comparison between the conventional and one MILD combustion cases, Cases C and A2, shows that the MILD reaction zones are highly convoluted, despite that the Da conditions are relatively similar one another. This suggests that reaction zone convolutions observed in the MILD case are not caused solely by interactions between strong turbulence and reaction zones, but also by the non-uniformity of a mixture and subsequent interactions between reaction zones. Importance of the mixture non-uniformity effect is also suggested in a comparison of Cases A1 and A2, whose dilution levels are the same but different turbulence conditions. The degrees of overall reaction zone convolutions do not seem to differ significantly between the two cases.

The effect of turbulence and reaction zone interactions is also shown by a comparison of Cases A1 and B1. As mentioned in section 2.6, the identical turbulent velocity field is used in the mixing DNS for Cases A1 and B1, but Case B1 has the higher dilution condition. As a result, Case B1 has higher Da and lower Ka than Case A1. The reaction zones in Case B1 (figures 3.7a, 3.7d and 3.7g) seem to have the highest degree of reaction zone convolutions among the MILD combustion cases, due to the low Da condition. Thus, interactions between turbulence and reaction zones are still important for MILD combustion, although reaction zone interactions are emphasized above.

The progress variables, c_T and c_Y, are also shown in the same slices in figures 3.5–3.7. For the conventional premixed case, both c_T and c_Y fields show typical thin reaction zones with a rapid increase of the progress variable across the flame in figure 3.4a. Among them, the gradient of c_Y seems to be larger than gradient of c_T. This is partly due to the effect of non-unity Lewis numbers; heat release is distributed among many species, and so is more spread out in space because of differential diffusion compared to the single species CH_4.

For the MILD cases, both c_T and c_Y fields seem to reflect the convolutions of reaction zones. Due to the size of computational domain and the moderate c_T increase suggested by the PDF of c_T in figure 3.2, the temperature continues to increase at the outflow boundary. However, CH_4 is quickly consumed to yield $c_Y = 1$ at downstream regions (eg. $x \geq 0.5L_x$) due to the existence of chemically-active radicals and the low CH_4 level available for combustion. Such behaviour of c_Y is ensured by the PDF of c_Y shown in figure 3.3b. For these reasons, the slope

of c_T is smaller than that of c_Y throughout the computational domain. Behaviour of c_T and c_Y gradients is discussed in detail in section 5.2.

A comparison of the progress variable fields between the conventional premixed case and MILD cases shows that the gradients of c_T and c_Y in the MILD cases do not seem as large as those in the conventional premixed case, where the regions of rapid production of c_T and c_Y are confined in very narrow regions. Although a detailed analysis on scalar gradient behaviour is carried out in chapter 5, these results based on the visual examination of instantaneous fields show the significant differences in reaction zones between the conventional premixed and MILD cases.

The variations of species mass fractions, Y_{H_2O}, Y_{CO_2} and Y_{OH}, are also shown in the same slices only for Case B1 in figure 3.8. The product mass fraction Y_{H_2O} variation seem to be qualitatively similar to c_Y (figures 3.7c, 3.7f and 3.7i). The other product mass fraction field Y_{CO_2}, however, shows a patchy appearance of high Y_{CO_2} regions as in figures 3.8e and 3.8h, compared to Y_{H_2O} field. The difference of behaviours between two product species mass fraction fields may be due to the effect of non-unity Lewis numbers and the use of complex chemistry in the DNS. The 2D slices of Y_{OH} show that the regions where Y_{OH} increases rapidly ($Y_{OH} \sim 7.3 \times 10^{-4}$, green colour) exist in relatively narrow area (compare figures 3.7b and 3.8a) (Plessing *et al.*, 1998; Özdemir & Peters, 2001; Dally *et al.*, 2004; Medwell, 2007; Duwig *et al.*, 2012), as suggested in figure 3.3a. This shows thin reaction zones unlike the temperature field in the same plane, as reported in previous experimental studies (Plessing *et al.*, 1998; Özdemir & Peters, 2001). Two y-z slices of Y_{OH} shown in figures 3.8f and 3.8i suggest a patchy appearance of OH radicals, which also has been observed in the OH PLIF images in a previous study (Dally *et al.*, 2004). However, such visual examinations are not sufficient to draw conclusions on reaction zone structures, especially to answer whether the reaction zones are still flamelet or non-flamelet like. More rigorous analysis on this issue is carried out in sections 3.4 and 5.3.

Contours of c_T and $\omega^+_{c_T}$ are shown together in figure 3.9 to gain closer understanding of the temperature and heat release rate fields. For the conventional premixed case, the $c_T = 0.6$ contour bounded closely by the two iso-contours of $\omega^+_{c_T} = 1.0$ indicates that the heat release rate always peaks at around $c_T = 0.6$.

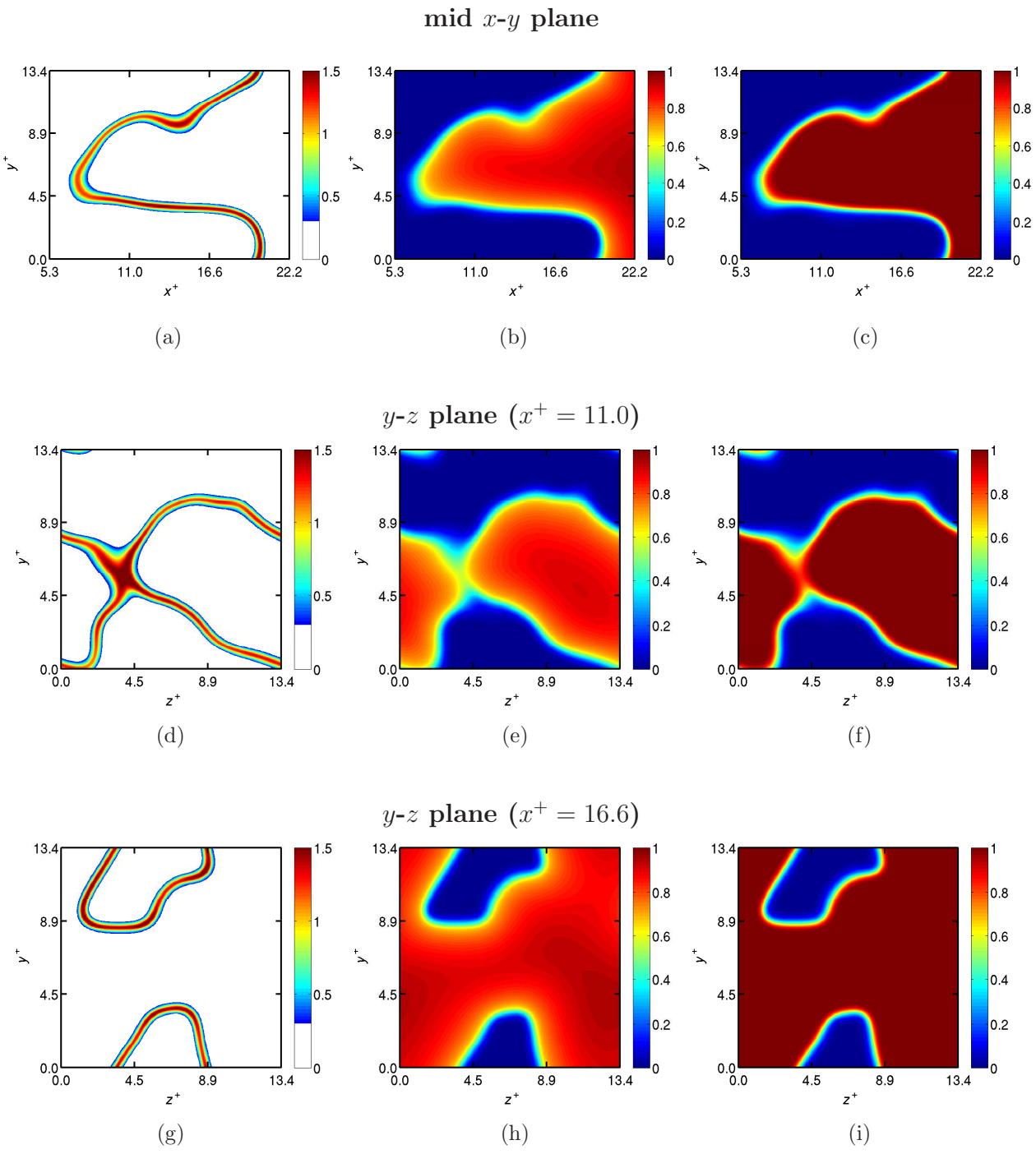

Figure 3.5: Spatial variations of $\omega^+_{c_T}$ (a, d, g), c_T (b, e, h) and c_Y (c, f, i) in a mid x-y plane (a–c), and a y-z plane at $x^+ = 11.0$ (d–f) and $x^+ = 16.6$ (g–i). Snapshots are taken at $t = 1.5\tau_D$ for Case C.

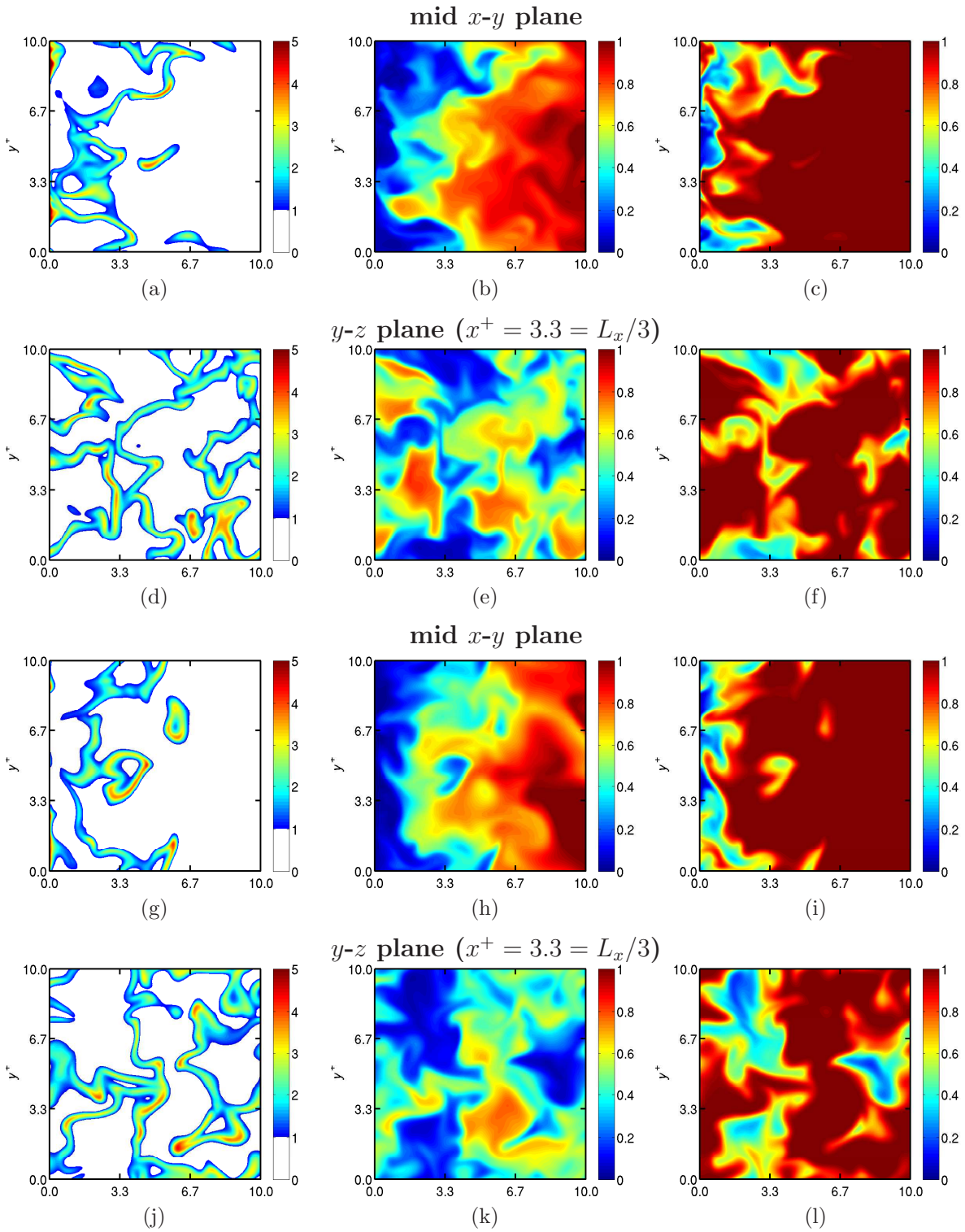

Figure 3.6: Spatial variations of $\omega^+_{c_T}$ (a, d, g, j), c_T (b, e, h, k) and c_Y (c, f, i, l) in a mid x-y plane (a–c, g–i), and y-z plane at $x^+ = 3.3$ (d–f, j–l) for Case A1 (a–f) and Case A2 (g–l). Snapshots are taken at $t = 1.5\tau_D$.

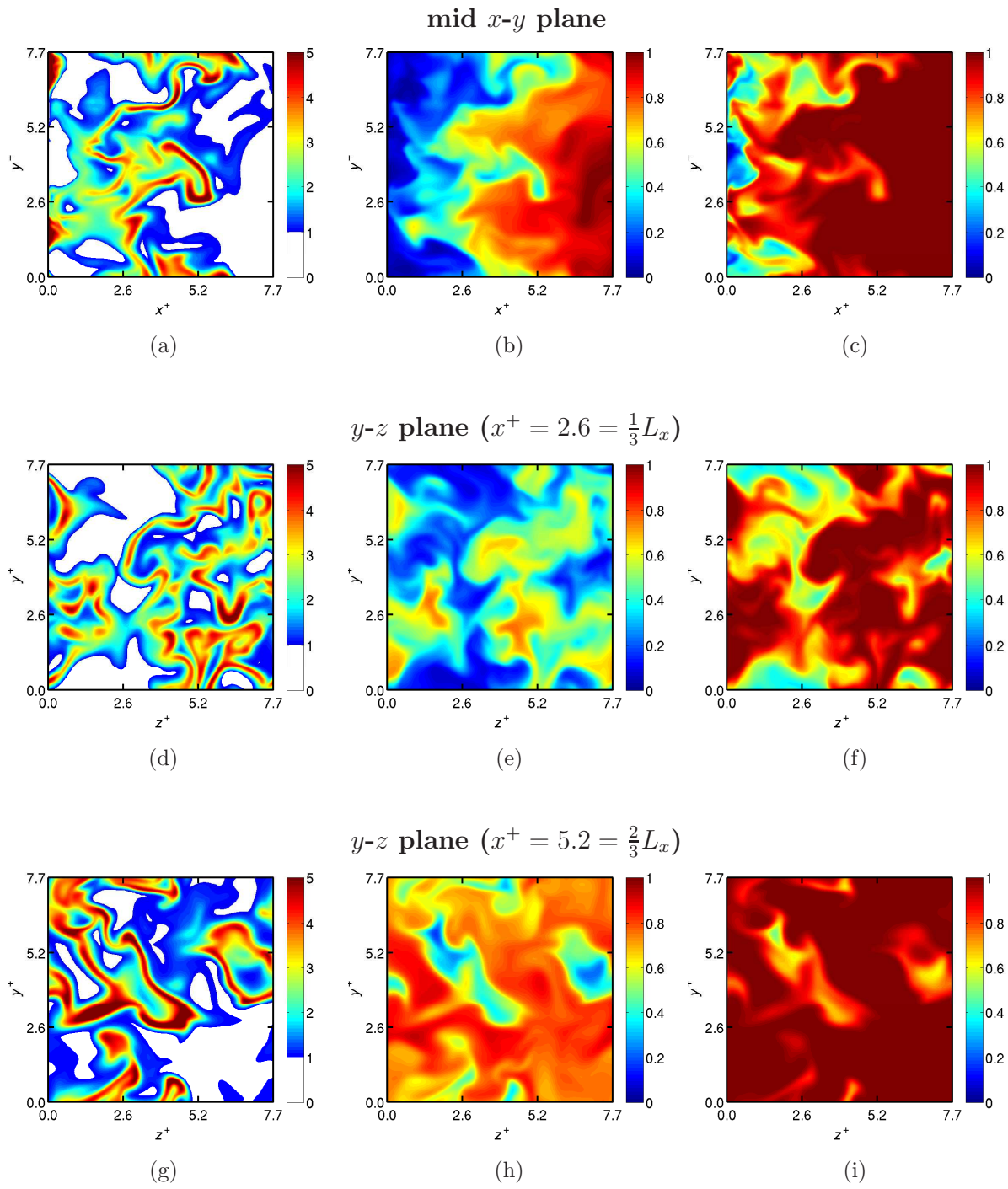

Figure 3.7: Spatial variations of $\omega^+_{c_T}$ (a, d, g), c_T (b, e, h) and c_Y (c, f, i) in a mid x-y plane (a–c), and y-z planes at $x^+ = 2.6$ (d–f) and 5.2 (g–i). Snapshots are taken at $t = 1.5\tau_D$ for Case B1.

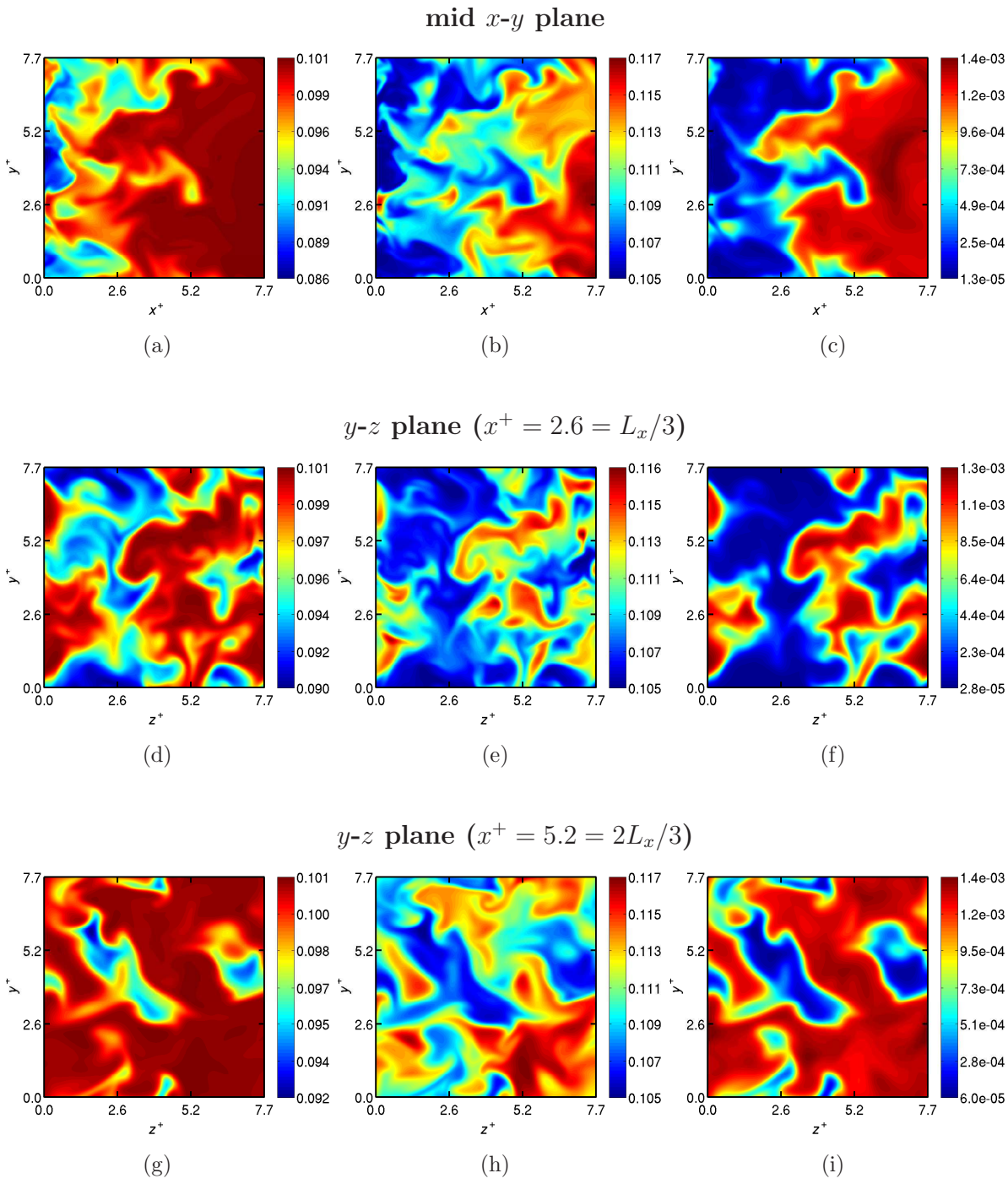

Figure 3.8: Spatial variations of Y_{H_2O} (a, d, g), Y_{CO_2} (b, e, h) and Y_{OH} (c, f, i) in a mid x-y plane (a–c), and y-z planes at $x^+ = 2.6$ (d–f) and 5.2 (g–i). Snapshots are taken at $t = 1.5\tau_D$ for Case B1.

A previous study reports that the reaction rate reaches to a maximum value at $c_T \approx 0.6$ for CH_4-air laminar flame, when a multi-step mechanism is considered in simulations (Swaminathan *et al.*, 2001). The conventional premixed flame considered here clearly exhibits the one of flamelet combustion characteristics.

For the MILD cases, the contours do not show such a consistent trend of the correlation between c_T and $\omega^+_{c_T}$. The intense reaction rate regions (eg. those surrounded by the $\omega^+_{c_T} = 2.0$ contours for Cases A1 and A2, and by the $\omega^+_{c_T} = 3.5$ contours for Cases B1) locate at any c_T. These regions are locally thin but disconnected caused by the convolution, revealing a patchy appearance of reaction zones. A similar reaction zone behaviour is implied in a previous laser diagnostics (Dally *et al.*, 2004). Despite this patchy appearance of reaction zones, the temperature contours are relatively smooth and do not show as many hot or cold islands as the reaction rate contours. Instead, the distance between the contour lines shows that the temperature increase seems to be relatively moderate, which is also shown in the PDF of c_T in figure 3.2 for MILD cases. These results suggest that the heat generated in the patchy reaction zones is conducted quickly away to non-burning regions containing relatively cooler recovered exhaust gas. Such heat conduction tends to level the temperature throughout the combustion field. Thus, convoluted reaction zones and the heat conduction effect are some of the reasons for the apparently uniform combustion shown in figure 3.1b and in the previous studies (de Joannon *et al.*, 2000; Özdemir & Peters, 2001; Krishnamurthy *et al.*, 2009).

3.3 Reaction zone interactions

In the previous subsection, occasional and frequent interactions between reaction zones are suggested respectively for the conventional premixed and MILD cases. For conventional turbulent premixed flames, flame-flame interactions have been studied previously with the aim of attenuating combustion noise and instabilities, since they are susceptible to heat release and temperature fluctuations which may be caused by the interactions (Burluka *et al.*, 1997; Schuller *et al.*, 2003; Dunstan *et al.*, 2013b). In MILD combustion, however, combustion instabilities are less susceptible to such interactions due to the elevated temperature as explained in

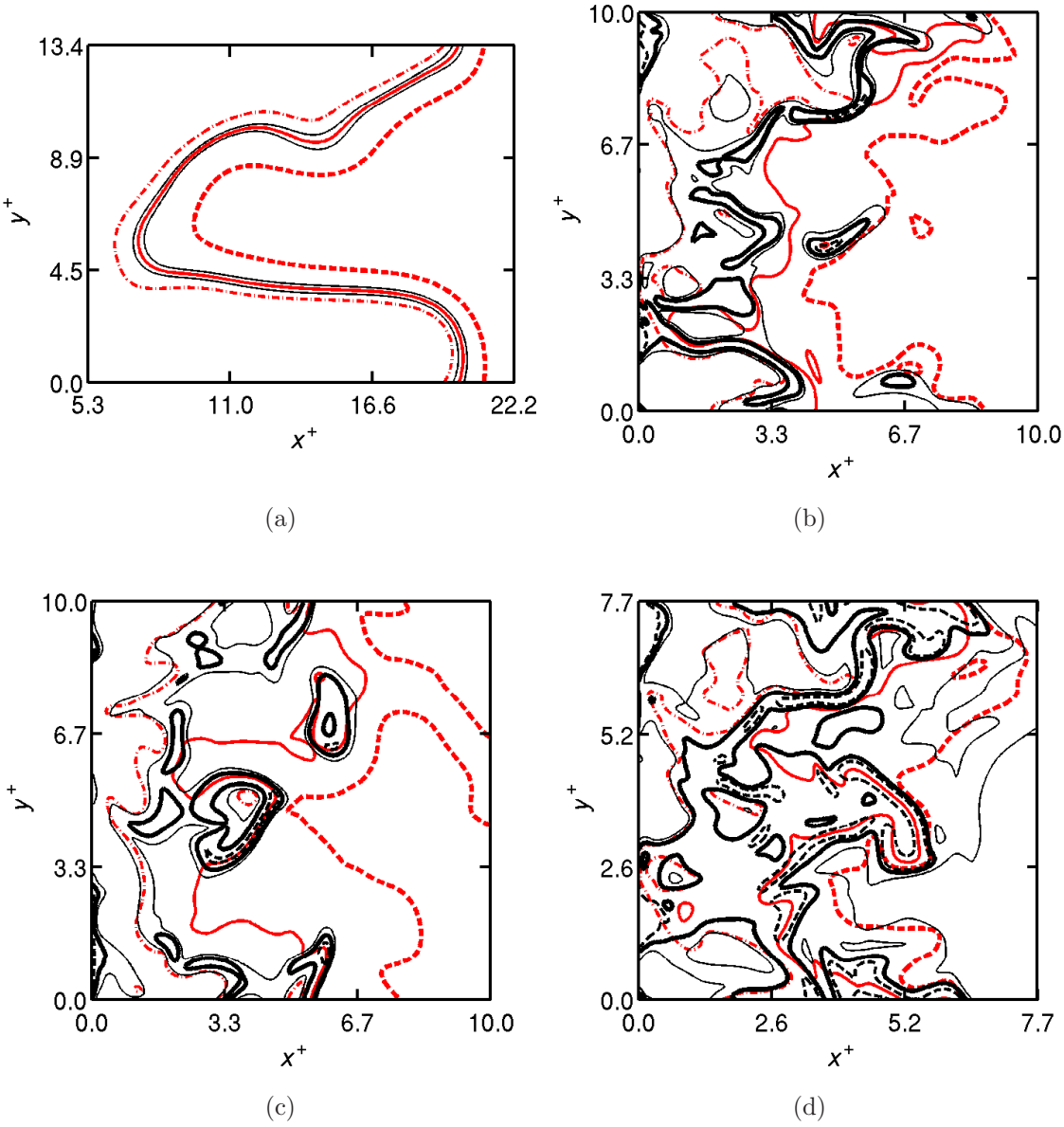

Figure 3.9: Contours of c_T and $\omega^+_{c_T}$ in the mid x-y planes for (a) Case C, (b) Case A1, (c) Case A2, and (d) Case B1. Dash-dotted red line: $c_T = 0.2$, solid red line: $c_T = 0.6$, and dashed red line: $c_T = 0.8$. Thin solid black line: $\omega^+_{c_T} = 1.0$, thick solid black line: $\omega^+_{c_T} = 2.0$, and dashed black line: $\omega^+_{c_T} = 3.5$. Note that only $5.3 \leq x^+ \leq 22.2$ of the computational domain is shown for Case C. Snapshots are taken at $t = 1.5\tau_D$.

the introduction (Wünning & Wünning, 1997; Katsuki & Hasegawa, 1998; Cavaliere & de Joannon, 2004). Another aspect of flame interactions with adjacent flames is that local flame elements do not follow the flamelet structure, due to generation of highly curved cusps at the initial interaction stage (Chen *et al.*, 1999). These processes have a relatively short time scale compared to a flame time scale (Chen *et al.*, 1999; Dunstan *et al.*, 2013b). Although the occurrence is not so frequent in the conventional premixed case, interacting reaction zones in MILD combustion occupy a substantial volume in the domain, and they may have a significant effect on turbulent combustion modelling from a flamelet view point. In this subsection, reaction zone interactions in MILD combustion are investigated and the effect on turbulent combustion modelling is discussed. First, an interaction event in the conventional combustion Case C is chosen to study fundamental behaviour of interacting reaction zones.

In the conventional premixed case, reaction zone interactions happen occasionally. Successive snapshots of one of the typical interaction events are shown in figure 3.10 in the y-z planes for the conventional premixed case. The x^+-location of each y-z plane changes with time, depending on the local fluid velocity at the circle shown in the figure. This circle shows the location of the respective Lagrangian particle considered in the figure. The black solid line moving with the particle corresponds to the c_T normal direction $\boldsymbol{n}$ at the particle location during the interaction. It should be noted that the duration between figures 3.10c and 3.10d, which corresponds to the initial interacting stage, is about $0.06\tau_F$, where τ_F is the flame time scale defined as δ_{th}/S_L. Thus, the interaction event happens in a relatively short time scale as reported in previous DNS studies for conventional premixed flames (Chen *et al.*, 1999; Dunstan *et al.*, 2013b).

The subset figure shows variations of $\omega^*_{c_T}$ (thick solid line), $|\nabla c_T|^*$ (dashed line) and c_T (dash-dotted line) along $\boldsymbol{n}^+$. The superscript "*" denotes a normalisation using a global maximum value in the three-dimensional domain. Here, another quantity Ψ is introduced and its variation is shown in the subset to study interacting regions:

$$\Psi \equiv \frac{|\nabla c_T|^*}{\omega^*_{c_T}}. \tag{3.6}$$

The value Ψ would be (i) very large, very small or unity in chemically non-

active regions ($\omega^*_{c_T} \ll 1$) depending on the balance between ∇c^*_T and $\omega^*_{c_T}$, or (ii) approximately unity at flame front locations ($\omega^*_{c_T} \sim 1$) for conventional turbulent premixed combustion without flame interactions. This is based on the insight from the relationship:

$$\langle \omega_{c_T} \rangle = \rho_r s_c \Sigma, \tag{3.7}$$

where $\langle\rangle$ denotes an appropriate averaging or filtering operation, s_c is the average flame consumption speed, and Σ is the flame surface density defined as $\langle |\nabla c| \rangle$ using a progress variable c (Veynante & Vervisch, 2002; Poinsot & Veynante, 2005).

In a sequence of the interaction event captured in figure 3.10, two local flames having a thickness of $\sim \delta_{th}$ approach from both sides, collide, and merge into one flame as follows.

1. Figure 3.10a shows two local flames before the interaction begins. These fronts are almost separated having relatively large reaction rates and large c_T gradients. As a result, $\Psi \sim 0.8$ at the flame fronts. Thus, these two flames have the characteristics as in the scenario (ii) above.

2. Figure 3.10b may be considered as the beginning of the interaction, as the normalised reaction rate at $n^+ = 0$ bounded by the two flames slightly increased. The reaction rate, scalar gradient, and Ψ at the flame fronts have similar values as in the previous instant. Also, Ψ is still much larger than unity at $n^+ = 0$. This shows that the chemical activity is not yet intense and non-zero scalar gradient at $n^+ = 0$ is due to preheating from both flame fronts.

3. At $t = 1.50\tau_D$ shown in figure 3.10c, two flame fronts start to collide. The reaction rate and scalar gradient at $n^+ = 0$ rapidly increase from the previous instant. The peak reaction rate is slightly higher than that in the previous instants, and $\Psi \sim 0.8$ at the merging two flame fronts. Thus, these two flames still have the characteristics (ii) explained using equation 3.7 above. Also, the thickness of reaction zones (eg. $\omega^*_{c_T} \sim 0.4$) is about $2\delta_{th}$ due to the process of the collision. Thus, distributed reaction zone can be caused by a partial collisions of propagating flames.

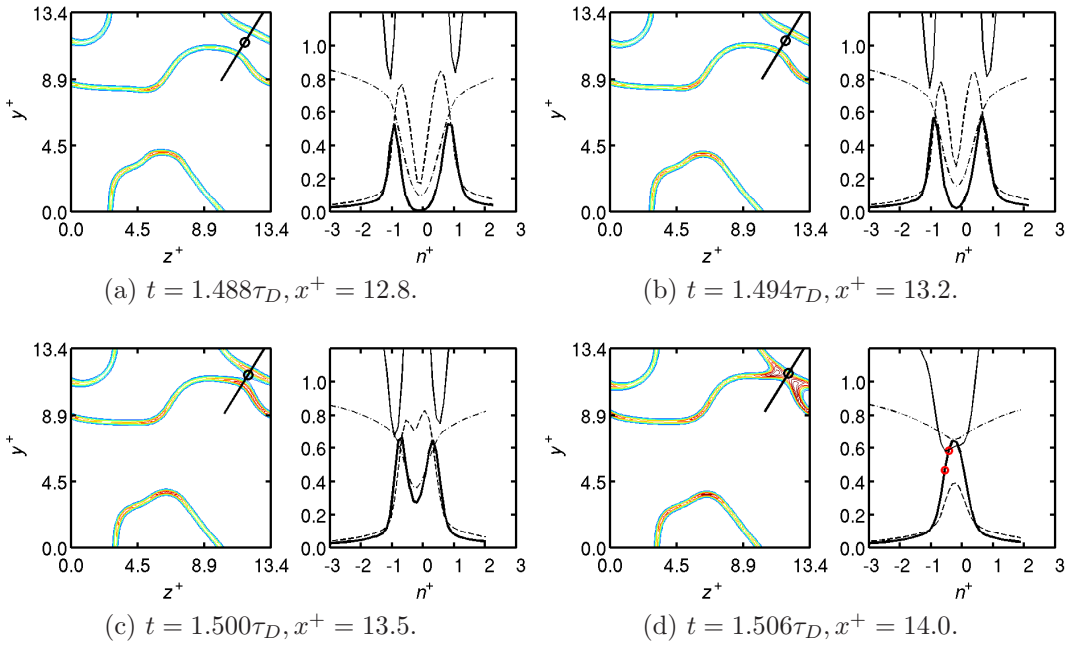

(a) $t = 1.488\tau_D, x^+ = 12.8$. (b) $t = 1.494\tau_D, x^+ = 13.2$.

(c) $t = 1.500\tau_D, x^+ = 13.5$. (d) $t = 1.506\tau_D, x^+ = 14.0$.

Figure 3.10: Contours of successive reaction rate field in y-z slices for the conventional premixed case. Level of contours are $\omega^*_{c_T} = 0.30, 0.35, \cdots 0.90$. A Lagrangian particle is shown as a circle and a black solid line corresponds to $\boldsymbol{n}^+$. Variations along $\boldsymbol{n}^+$ are shown in the subset for $\omega^*_{c_T}$ (thick solid line), Ψ (thin solid line), $|\nabla c_T|^*$ (dashed line), and c_T (dash-dotted line). The location of the Lagrangian particle corresponds to $n^+ = 0$. Red dots indicate interacting reaction zones identified by equation 3.8.

4. By the next instant shown in figure 3.10d, two flame fronts merge into one completely. The peak scalar gradient quickly decreases from 0.8 to 0.4, while the peak reaction rate is as high as that in the previous instants. Similar scalar gradient behaviour during interaction is reported based on unsteady RANS calculations (Darbyshire, 2011). Because of the small scalar gradient and large reaction rate, Ψ at the flame front ($n^+ \sim 0$) decreases to about 0.60, which is much smaller than that in the previous instant. Such behaviour of Ψ is found to be typical for interacting regions, where the reaction rate increases without a large scalar gradient.

Typically, $\omega_{c_T} \sim \rho_r S_L/\delta_{th}$ and $|\nabla c_T| \sim 1/\delta_{th}$ at flame fronts in flamelet combustion, using the corresponding laminar flame values. The ratio of these two quantities is the dimensional Ψ, defined as $\Psi_{\text{dim}} \equiv |\nabla c_T|/\omega_{c_T}$. Without a reaction zone interaction, $\Psi_{\text{dim}} \sim (\rho_r S_L)^{-1}$ at flame fronts. At interacting regions, $\Psi_{\text{dim}} \leq (\rho_r S_L)^{-1}$ while ω_{c_T} remains $\sim \rho_r S_L/\delta_{th}$ since only the scalar gradient decreases as shown in figures 3.10a–3.10d. Such interacting reaction zones are denoted by red circles in the subset shown in figure 3.10d. Here, interacting reaction zones for the conventional premixed case are identified using two markers, $\omega^*_{c_T}$ and Ψ, as:

$$\omega^*_{c_T} \geq 0.4, \text{ and } \Psi \leq 0.6. \tag{3.8}$$

The local mixture identified by using equation 3.8 locates at interacting regions near $\boldsymbol{n}^+ = 0$ in figure 3.10d. The figure shows that the identified interacting region locally generates a thin reaction zone with a relatively small temperature gradient. The c_Y field is also computed (not shown) to identify interacting regions using the same criteria as in equation 3.8, and it showed the choice of progress variable does not unduly affect the location or shape of identified interacting regions.

As indicated in equation 3.8, the heat generated in the interacting reaction zones cannot be described adequately by using conventional flamelet approaches, where combustion models are often based on flame surface density (equation 3.7) (Veynante & Vervisch, 2002; Poinsot & Veynante, 2005), or scalar dissipation rate, $N_c = D_c \nabla c \cdot \nabla c$, (Bray, 1979; Dunstan *et al.*, 2013a) as:

$$\langle \omega \rangle = \frac{2\langle \rho \rangle}{2C_m - 1} \langle N_c \rangle. \tag{3.9}$$

Here, D_c is the diffusion coefficient of c, and C_m is the model parameter (Bray, 1979). In conventional combustion, the effect of reaction zone interactions on combustion modelling is generally confined in a relatively small volume, since reaction zone interactions identified by equation 3.8 occur occasionally. Thus, clear flame fronts exist in an average sense (the direct photograph or volume rendered temperature field), and so the effect of reaction zone interactions may be negligible. However, reaction zone interactions seem to occur in a much larger

volume in MILD combustion, due to the highly convoluted reaction zones caused by the mixture non-uniformity. Thus, unlike conventional combustion, the effect of the frequent interactions on MILD combustion modelling can be significant and so it needs to be investigated.

Interacting reaction zones at arbitrary chosen locations are shown in figure 3.11 for Cases A1 and B1. A typical sequence of an interacting event experienced by a Lagrangian particle for Case A1 is clearly shown in figures 3.11a–3.11d, and the behaviour of $\omega^*_{c_T}$ and Ψ during the interacting event is similar to that observed in the conventional premixed case. Despite the nature of relatively uniform combustion, the same criteria as in equation 3.8 work appropriately to identify interacting reaction zones in MILD combustion. However, not only the location of the particle ($n^+ = 0$), but also its neighbouring reaction zones experience interactions at the same time. Similar behaviour is observed in an interacting event in Case B1 as in figures 3.11e–3.11h, although this interacting event seems to appear in a broader volume than that in Case A1. As a result of the frequent interactions, MILD reaction zones are broader and scalar gradient is smaller than the conventional premixed case. The durations from figure 3.11a to figure 3.11d and figure 3.11e to figure 3.11h are respectively $0.08\tau_F$ and $0.06\tau_F$. Thus, interactions in MILD combustion have a short time scale compared to the flame time scale as well.

Due to the nature of equation 3.8, the spatial extent of identified interacting regions represents the effect of interactions on flamelet combustion modelling. Interacting reaction zones identified by using equation 3.8 are shown in three-dimensional iso-surface of the reaction rate field for all the cases considered in figure 3.12. The surfaces with the purple colour are interacting reaction zones, and the light blue colour denotes non-interacting reaction zones having $\omega^*_{c_T} \geq 0.4$, which is a part of equation 3.8. These iso-surfaces clearly show the large spatial extent of interacting regions in MILD combustion, and so the possibility of the significant effect on combustion modelling. The effect of reaction zone interactions is investigated more quantitatively by computing the spatial ratio of interacting reaction zones to the total reaction zones. By denoting the volume of interacting reaction zones as V_{int}, the ratio $V_{\text{int}}/V_{\text{tot}}$ is 1.1% for Case C, 79% for Case A1, 64% for Case A2, and 88% for Case B1, where V_{tot} is the total volume

of reaction zones (local mixtures which have $\omega^*_{c_T} \geq 0.4$). Thus, contribution of reaction zone interaction in a unit volume of reaction zones increases because of (1) inhomogeneity of mixture field and (2) higher dilution level (lower Da and higher Ka conditions).

To summarise, the frequent occurrence of interacting events in MILD combustion reduces the scalar gradient as shown in the PDF discussed in sections 3.1. Also, distributed reaction zones are generated in the process of an interaction event, which are shown in section 3.2. The non-bimodality of the PDF becomes more obvious with an increase of $V_{\text{int}}/V_{\text{tot}}$ (compare with figure 3.2). These results show that the effect of reaction zone interactions on combustion modelling is so small for the conventional premixed combustion case. However, from a MILD combustion modelling view point, appropriate treatments for reaction zone interactions are clearly necessary.

3.4 Reaction zone structure

The frequent interactions and distributed reaction zones discussed in the previous sections can change the reaction zone structure in MILD combustion. The reaction zone structure is best understood by studying variations of instantaneous species mass fractions with temperature. Typical species mass fractions variations in the MILD Cases A1 and B1 are shown in figure 3.13 as scatter plots. The conditional average mass fractions $\langle Y_i|T\rangle$ constructed using the samples collected over the entire sampling period are also shown in figure 3.13. Furthermore, the results of the laminar Flames A and B, and MIFEs are also included for comparison purposes.

There is a large scatter in Y_i for lower temperature because of inflowing mixture inhomogeneity containing pockets of exhaust and fresh mixtures. This large scatter is consistent with the field shown in figure 2.6 for Case A1 and figure 2.8 for Case B1. The scatter in Y_i reduces as the temperature increases, because of the combined effects of combustion, molecular diffusion and turbulent mixing. This mixing process reduces the inhomogeneity in the mixture leading to reduced scatter as T increases. As combustion consumes CH_4 forming products such as H_2O, the temperature increases and this trend is shown clearly by the conditional

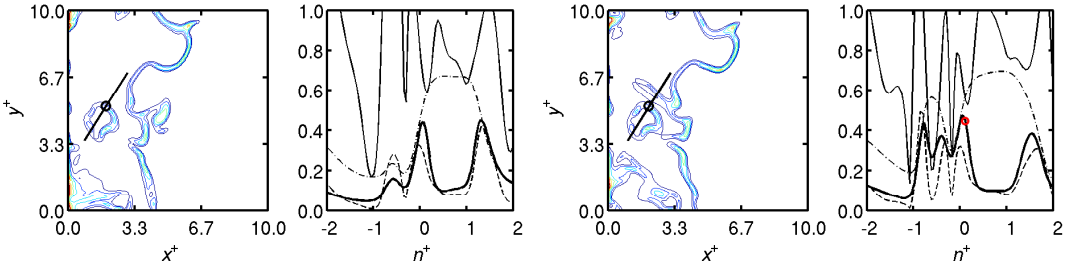

(a) $t = 1.51\tau_D, z^+ = 4.1$.

(b) $t = 1.54\tau_D, z^+ = 4.3$.

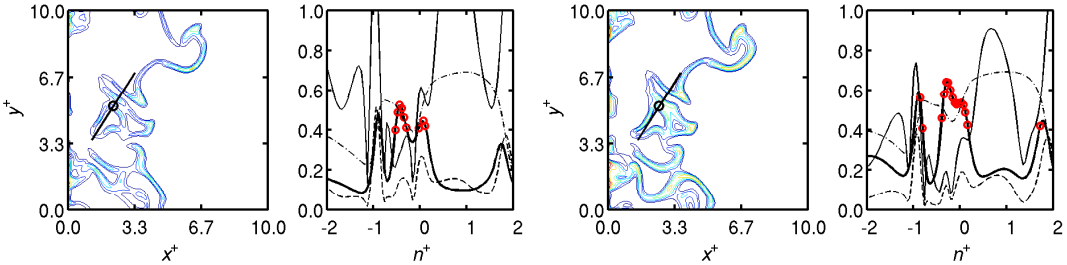

(c) $t = 1.56\tau_D, z^+ = 4.5$.

(d) $t = 1.59\tau_D, z^+ = 4.8$.

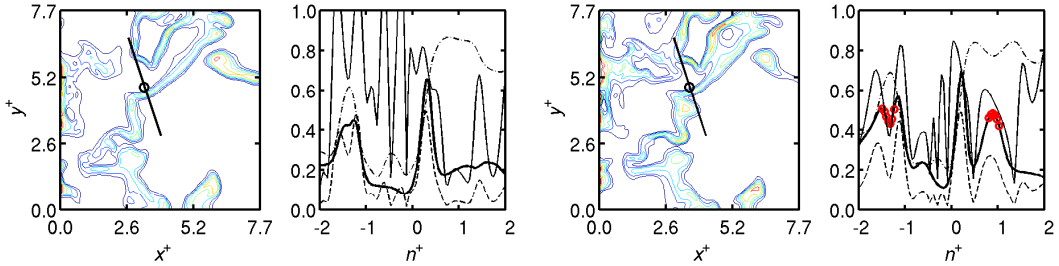

(e) $t = 1.89\tau_D, z^+ = 3.1$.

(f) $t = 1.93\tau_D, z^+ = 3.3$.

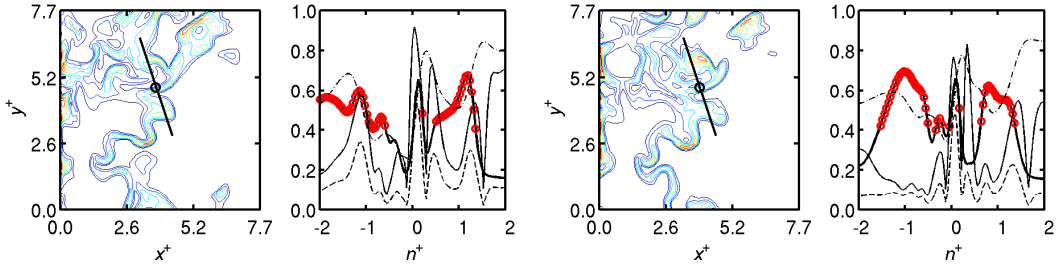

(g) $t = 1.96\tau_D, z^+ = 3.4$.

(h) $t = 2.00\tau_D, z^+ = 3.6$.

Figure 3.11: Contours of successive reaction rate field in x-y slices for Case A1 (a–d) and Case B1 (e–h). Level of contours are $\omega^*_{c_T} = 0.30, 0.35, \cdots 0.90$. A Lagrangian particle is shown as a circle and a black solid line corresponds to $\boldsymbol{n}^+$. Variations along $\boldsymbol{n}^+$ are shown in the subset for $\omega^*_{c_T}$ (thick solid line), Ψ (thin solid line), $|\nabla c_T|^*$ (dashed line), and c_T (dash-dotted line). The location of the Lagrangian particle corresponds to $n^+ = 0$. Red dots indicate interacting reaction zones.

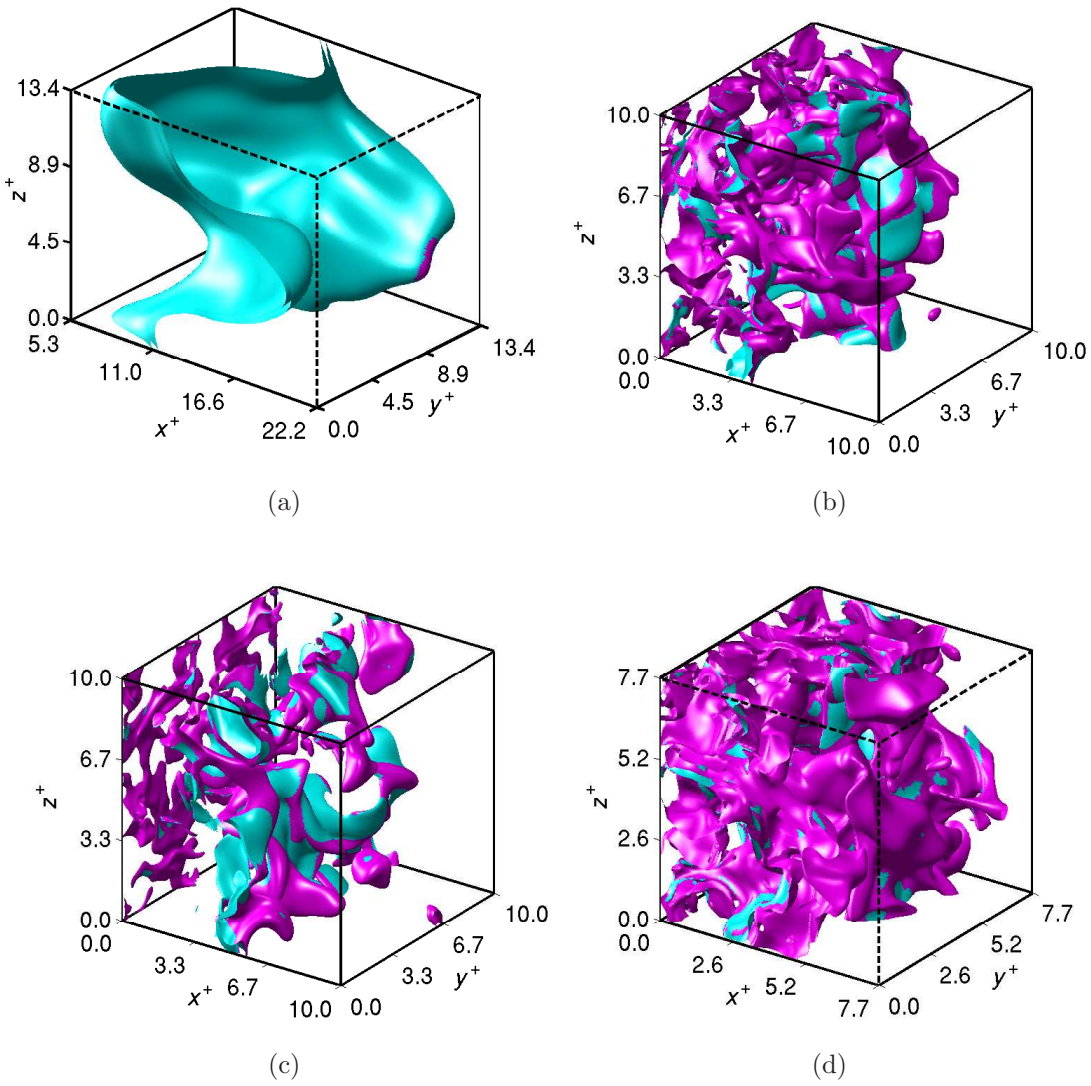

Figure 3.12: Reaction rate iso-surface of $\omega^*_{c_T} = 0.4$ for (a) the conventional premixed case, (b) Case A1, (c) Case A2, and (d) Case B1 at $t = 1.5\tau_D$. Interacting and non-interacting local reaction zones are respectively denoted by purple and light blue colours. Note that only $5.3 \leq x^+ \leq 22.2$ of the computational domain is shown for Case C.

averages, $\langle Y_{CH4}|T\rangle$ and $\langle Y_{H2O}|T\rangle$, plotted in figure 3.13.

As noted in section 2.6.1, the reactant mixtures for Flames A and B do not include the effect of additional dilution due to exhaust gas pockets, and the oxygen mole fraction is larger than the average value in the respective DNS cases (compare tables 2.1 and 2.2). Thus, the product temperature in these laminar flames is larger than that in the respective DNS as noted in section 2.6.1. Also, the variations of mass fractions with T in these laminar flames are not representative of the variations in the MILD combustion DNS. In contrast, the flamelet structure, at least for many major species (not all of them are shown here) in the MIFEs seems to be representative of the MILD reaction zones structure. The poor agreement shown for the minor species such as OH is because the reactant mixture for the MIFEs does not include intermediate species which are present in the initial inhomogeneous mixture for the DNS. However, the agreement for minor species in figure 3.13 is improved for MIFEs compared to Flames A and B, because the additional dilution effect is included in the reactant mixture in the MIFEs as explained in section 2.6.1.

Figure 3.14 shows the variation of $\omega^+_{c_T}$ with c_T for the three MILD cases considered in this study. The results for the classical premixed case, Case C, are also included for comparison. The data for the scatter plots is taken at $t = 1.5\tau_D$, and the conditionally averaged values are constructed using samples collected over the entire sampling period as has been done for figure 3.13. The maximum value of $\omega^+_{c_T}$ observed over the entire sampling period for a given c_T is also shown in figure 3.14. The scatter in $\omega^+_{c_T}$ for the conventional premixed case is smaller compared to the MILD cases and has a peak at $c_T \approx 0.6$. The conditionally averaged reaction rate suggests that the peak reaction rate occurs at smaller c_T in the MILD cases compared to the conventional premixed case. This behaviour of $\langle \omega^+_{c_T}|c_T\rangle$ is because the temperature rise in MILD combustion is gradual partly due to heat conduction to non-burning regions containing relatively cooler products.

The solution for the respective MIFE is also shown using a dash-dotted line in figure 3.14 and the results of Flame A and B are not shown, since they deviate significantly from the DNS and MIFE results as discussed in figure 3.13. Although the trends in the variations of $\omega^+_{c_T}$ with c_T are similar to the DNS results, the

quantitative agreement is not as good as that for the major species mass fractions shown in figure 3.13. The peak value of $\langle \omega^+_{c_T} | c_T \rangle$ in the MILD case is higher than the respective MIFE values. The difference of the peak $\langle \omega^+_{c_T} | c_T \rangle$ values in the DNS and the respective MIFE solution is 0.56 for Case A1, 0.40 for Case A2, and 1.65 for Case B1, increasing with the dilution and turbulence levels as shown in figure 3.14. Also, there is substantial reaction rate in the DNS for $c_T = 0$ as indicated by the conditional reaction rate, and this is not captured in the MIFE result. The reduced reaction rate in the MIFE is because its solution includes only a part of the effects of the presence of exhaust gas pockets in the initial/inflowing mixtures. Specifically, the presence of radicals is not captured. Also, a MIFE has a thin propagating reaction zone as in a classical laminar premixed flame. As the dilution level increases in MILD combustion, the presence of individual reaction zones influenced only by turbulence-chemistry interaction becomes less clear, due to the interaction of reaction zones as noted in section 3.3. Thus, a fully representative canonical candidate for turbulent MILD combustion needs to include effects of locally homogeneous combustion resulting from interactions and collisions of reaction zones and inhomogeneous combustion, creating spatial gradients, resulting in thin reaction zones. A fully representative canonical flame is discussed in chapter 6.

3.5 Morphology of reaction zones

The instantaneous reaction rate field in MILD combustion shown in figures 3.6 and 3.7 exhibits both thin and distributed reaction zones. In this subsection, shapefinders for reaction zones are proposed to investigate morphological features of MILD reaction zones, and the results are compared with the conventional combustion result.

3.5.1 Minkowski functional and shapefinders

The morphology of reaction zones is investigated using Minkowski functionals which help to define shapefinders (Minkowski, 1903). The shapefinders are characteristic scales for length, L, width, W, and thickness, T, of an object of interest.

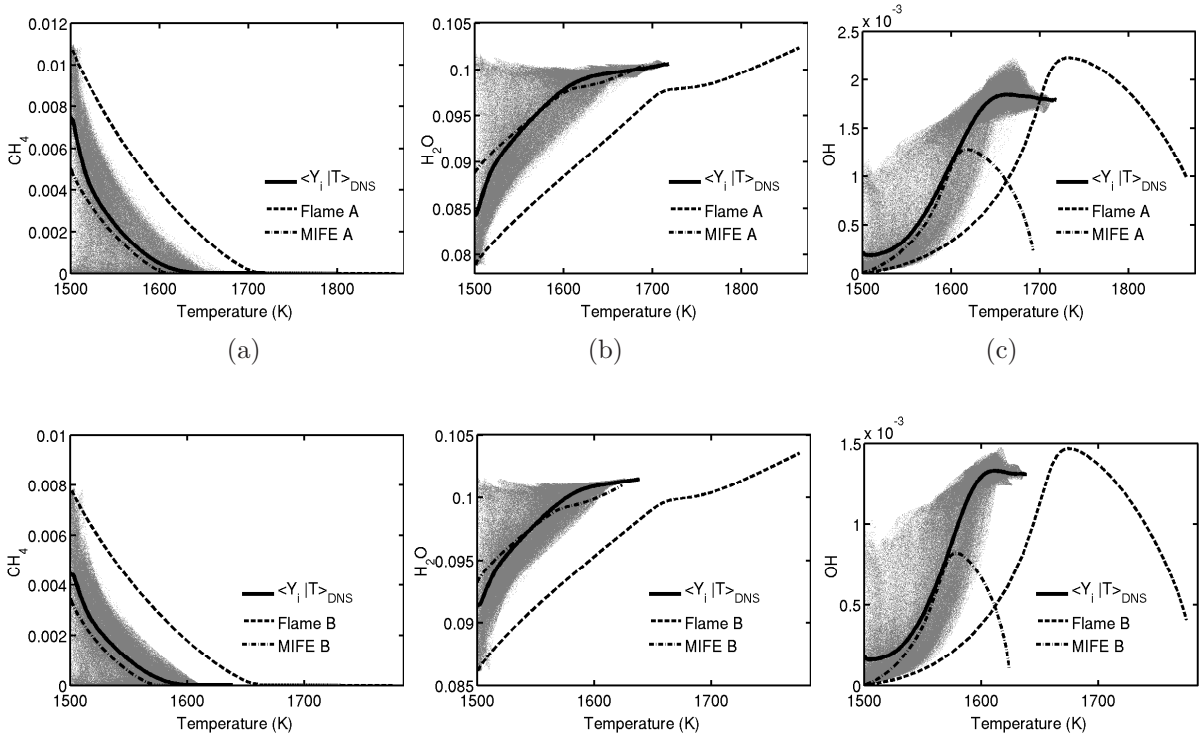

Figure 3.13: Variations of species mass fraction, CH_4 (a, d), H_2O (b,e), and OH (c,f) with temperature for the MILD combustion DNS results (scatter), Case A1 (a–c) and Case B1 (d–f). The solid line is the conditional average $\langle Y_i|T\rangle$ of the DNS results, dashed line is the laminar flame used in Step (ii) of section 2.5, and dash-dotted line is the respective MIFE solution.

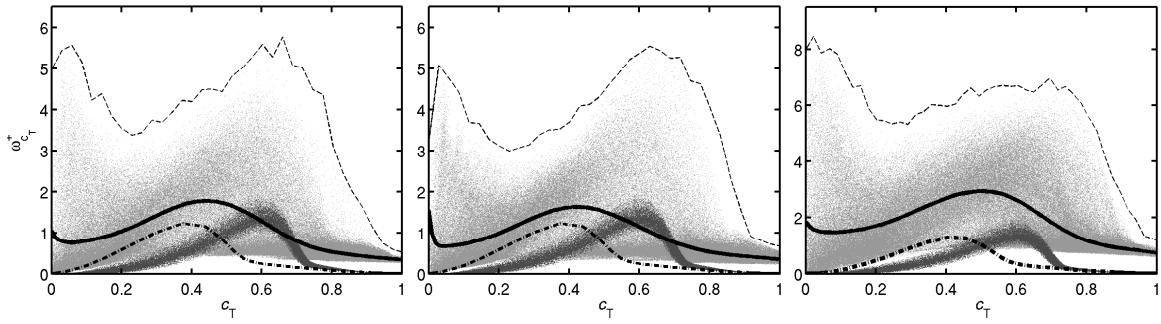

Figure 3.14: Normalised reaction rate $\omega^+_{c_T}$ for Cases A1 (a), A2 (b), and B1 (c) with reaction progress variable c_T in the MILD combustion DNS (light grey points) and the conventional premixed case (dark grey points). The points are taken from $t = 1.5\tau_D$, and the thin dashed line is the maximum value of each MILD case from the entire sampling period. The solid line is the conditional average $\langle \omega^+_{c_T} | c_T \rangle$, and the dash-dotted line is the respective MIFE solution.

These functionals have been used to quantify iso-density structures in cosmology (Mecke *et al.*, 1994; Kerscher *et al.*, 1997; Schmalzing & Buchert, 1997; Sahni *et al.*, 1998; Schmalzing *et al.*, 1999; Sheth *et al.*, 2003; Shandarin *et al.*, 2004; Sheth & Sahni, 2005; Einasto *et al.*, 2007), magnetic field structures in magneto-hydrodynamics (Wilkin *et al.*, 2007) and turbulence structures (Leung *et al.*, 2012). There are four Minkowski functionals for three-dimensional objects which are given as (Sahni *et al.*, 1998; Einasto *et al.*, 2007)

$$V_0 = \mathcal{V}, \quad V_1 = \frac{\mathcal{S}}{6}, \quad V_2 = \frac{1}{3\pi}\int_S \frac{\kappa_1 + \kappa_2}{2}\, dS, \quad V_3 = \frac{1}{2\pi}\int_S (\kappa_1\kappa_2)\, dS, \qquad (3.10)$$

where $\mathcal{V}$ is the volume enclosed by the surface, S, with the surface area $\mathcal{S}$, and κ_1 and κ_2 ($\kappa_1 \geq \kappa_2$) are the two principal curvatures of S. It is apparent that the mean and Gaussian curvatures integrated over the entire surface are involved, and local values of these curvatures are used in many turbulent combustion models. The integrated Gaussian curvature V_3 is the Euler characteristic χ, which is a topological invariant of the object. These four functionals defined above are Galilean invariant morphological properties of a three-dimensional object. In

this section, the Minkowski functionals are computed for each isolated object constructed by iso-surfaces of reaction rate by using a grid cell counting method (Schmalzing & Buchert, 1997; Schmalzing *et al.*, 1999). The spatial resolution required for this method is explained in Appendix C. As described later, the iso-value used here is relatively large, yielding a enclosed surface rather than two iso-surfaces for each flame element.

The three characteristic length scales can be obtained from the four functionals as (Sahni *et al.*, 1998):

$$\text{Thickness, } T \equiv \frac{V_0}{2V_1}, \quad \text{Width, } W \equiv \frac{2V_1}{\pi V_2}, \quad \text{Length, } L \equiv \frac{3V_2}{2V_3}. \tag{3.11}$$

and they satisfy $L \geq W \geq T$ for any convex body (Schmalzing *et al.*, 1999). Also this inequality holds for closed partially concave objects since Minkowski functionals are additive (Schmalzing *et al.*, 1999; Leung *et al.*, 2012). As clearly indicated, the Minkowski functionals have to be positive to obtain meaningful shapefinders using equation 3.11. However, V_3 can be positive, negative or zero in general, because V_3 is related to the three-dimensional genus as $G = 1 - 0.5\chi$. In short, the genus, which is defined as the number of cuts that can be made along a curve on an object without splitting it, corresponds to the number of the holes in a three-dimensional object. Therefore, $V_3 = 2\,(G = 0)$ for a closed surface (an object without hole), $V_3 = 0(G = 1)$ for a torus, and $V_3 = -4(G = 3)$ for a pretzel. Thus, for structures with a hole, $V_3 = 0$ and L is singular (see equation 3.11). More extensive definition of L is written for objects with non-zero G as (Sheth *et al.*, 2003):

$$L \equiv \frac{3V_2}{4(G+1)}. \tag{3.12}$$

For objects without hole, $G = 0$ and L in equations 3.11 and 3.12 are identical. For objects with $G > 0$, the scale L quantifies the characteristic length between holes. The scale L corresponds to the representative radius of a circular torus when $G = 1$ (Leung *et al.*, 2012). In special cases, equations 3.10–3.12 can be verified: $T = W = L = r$ when equations 3.10 and 3.11 are applied to a sphere of radius r; for an infinitely long cylinder with radius r_1, these shapefinders are $(T, W, L) = (1.5r_1, 2r_1, \infty)$; for an infinitely large thin circular disk of thickness

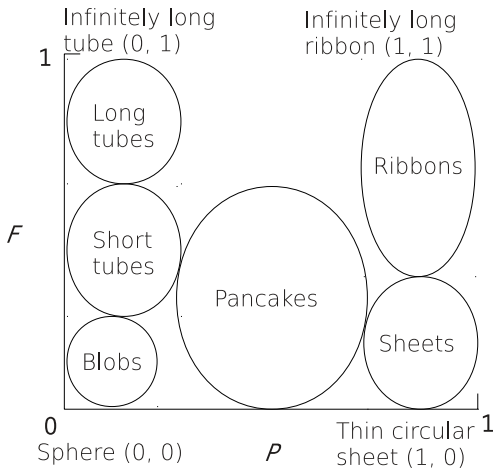

Figure 3.15: A map of shapefinders using Minkowski functionals (Leung *et al.*, 2012).

δ, they are $(T, W, L) = (1.5\delta, \infty, \infty)$. Thus, the shapefinders yield representative scales for the spatial extent of a structure and do not give the exact dimensions except for a sphere.

Dimensionless shapefinders can also be defined as (Sahni *et al.*, 1998):

$$\text{Planarity, } P \equiv \frac{W-T}{W+T}, \qquad \text{Filamentarity, } F \equiv \frac{L-W}{L+W}. \tag{3.13}$$

These two quantities allow a convenient visual representation of the geometry for a group of objects in a two-dimensional (P, F) space. They vary from 0 to 1 when the inequality $L \geq W \geq T$ is met. The filamentarity approaches to 1 when L is very large compared to W and T. The planarity is close to 1 when $W \gg T$. Thus, an infinitely long tube has $F \sim 1$ and $P \sim 0$ while a thin circular sheet has $F \sim 0$ and $P \sim 1$. It is obvious that $(P, F) = (0, 0)$ for a spherical object. Typical shapes are marked in the shapefinder map (P, F) shown in figure 3.15.

3.5.2 Shape of reaction zones

The reaction zones are identified first using a threshold for $\omega^+_{c_T}$ to compute the shapefinders. However, as shown in earlier in this chapter, the MILD reaction zones are spatially distributed in a broader volume, and so there can be a sub-

jectivity depending on the threshold value used. A constant threshold value for all the cases does not identify regions with similar reaction rate magnitudes since the normalising factor $\rho_r s_L/\delta_{th}$ is not the same for all the cases considered in this study. Additionally, it is not yet confirmed that the normalising factor is appropriate, because the quantities are based on MIFE, which is not fully representative as discussed in section 3.4. To remove these ambiguities, a threshold value is calculated for each case based on the conditional average the of reaction rate weighted by the scalar dissipation rate and surface area, rather than using an arbitrary chosen value. Here, the conditional average is defined as $\mathcal{Z}(\xi) \equiv \langle \Delta S N_c \ \omega_{c_T} | \omega_{c_T} = \xi \rangle$, where the scalar dissipation rate is calculated as $N_c = D_c(\nabla c_T \cdot \nabla c_T)$ and ΔS is the surface area identified using $\omega_{c_T} = \xi$.

The variation of $(\mathcal{Z}(\xi)/\mathcal{Z}_{\max})$ with ξ^+ is plotted in figure 3.16a and the value of $\xi^+ = \omega^+_{cT}$ corresponding to the $(\mathcal{Z}(\xi)/\mathcal{Z}_{\max}) = 1$ is chosen as the threshold value to identify reaction zone iso-surfaces for each case. Such surfaces have a reasonably large reaction rate and scalar dissipation rate, and occupy a relatively large area at the same time. Also, this helps to exclude reaction zones with the effect of strong interactions in an average sense, since the interacting regions have large ω_{c_T} and small N_c. This ensures that the statistics of the MILD reaction zones and the comparison to a conventional premixed reaction zone are not unduly influenced by the interactions or possibly autoignition.

It is found that these surfaces enclose about top 50% of the reaction rate in each case, and the enclosed surfaces represent regions with intense chemical activities. Thus, the present morphological analysis looks at the shape of intense reaction rate regions which is expected to be thin in classical premixed combustion. It has also been verified that when a threshold value changed by -20 % from the value used in this work, the statistics of shapefinders do not change significantly, although this affects the number of holes existing in the identified objects. Furthermore, the use of c_Y and its reaction rate does not unduly change the conclusions either. There were objects interacting with inflow/outflow boundaries yielding unclosed surfaces (two separated surfaces for one object) and they were excluded from further consideration, since the Minskowski functionals require closed objects.

Using the threshold value shown in figure 3.16a, the surface average of $\kappa_1\kappa_2$

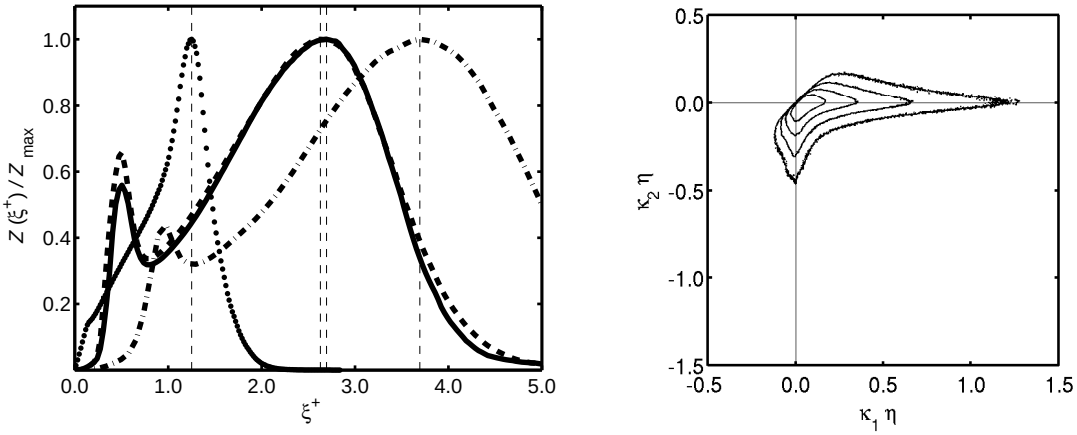

(a) (b)

Figure 3.16: (a) The variation of $\mathcal{Z}(\xi)/\mathcal{Z}_{\max}$ with ξ^+ in Case A1 (solid line), Case A2 (dashed), Case B1 (dash-dotted) and Case C (dotted). (b) Typical joint PDF of $\kappa_1\eta$ and $\kappa_2\eta$ for Case A1. Level of the PDF is 0.25, 1, 4, 16.

of all sample objects is positive for all the cases, suggesting $V_3 > 0$ for most of the entities of interest. However, the joint PDF of κ_1 and κ_2 of reaction rate structures shown in figure 3.16b suggests the possibilities to find negative principal curvature(s) locally. Thus, the structures are locally concave objects possibly with holes, although they are made of convex surface in an integral sense. Therefore, in the present analysis, equation 3.12 is used to compute L. Also, because of convoluted shape and interactions of reaction zones, less than 15 % of the structures defined from reaction rate used in the present analysis have holes, implying that they are multiply connected structures.

Two arbitrary chosen objects with holes are shown in figure 3.17 for MILD cases. As clearly shown, these objects are of partially concave with the negative principal curvatures observed locally, and the object in figure 3.17a presents five holes, meaning $V_3 \ll 0$. The dimensional shapefinders, however, show that the inequality $L \geq W \geq T$ is strictly met, suggesting robustness of this method. These objects are typical examples to address the limitation of visual examinations to determine whether reaction zones are thin or not; the results of such examinations for these reaction zone shapes would end up with subjective conclusions. Based

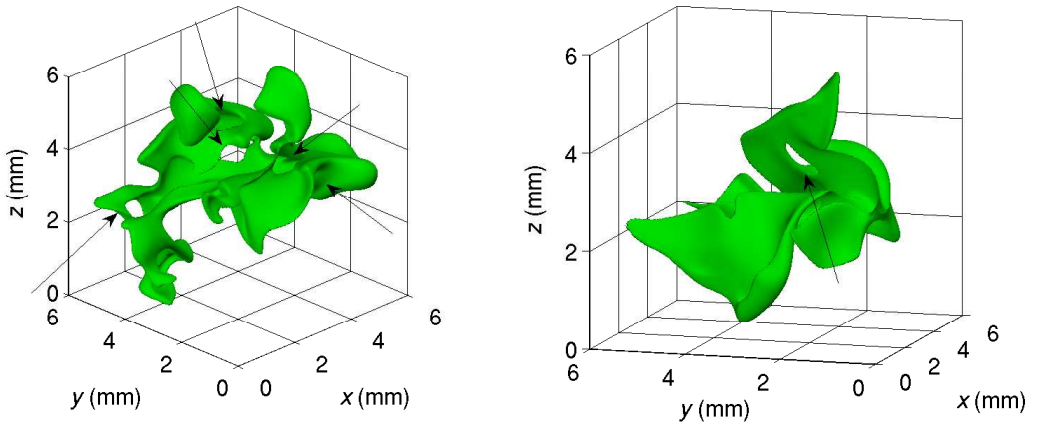

(a) (b)

Figure 3.17: Arbitrary chosen objects and the parameters. Unit: volume (mm^3), area (mm^2), and length (mm). Arrows indicate the locations of holes. (a): found in Case A1, $V_0 = 8.1$, $V_1 = 14.5$, $V_2 = 11.0$, $V_3 = -8.0$ ($G = 5$), $T = 0.28$, $W = 0.84$, $L = 1.4$, $P = 0.50$, $F = 0.25$. (b): found in Case A2, $V_0 = 4.6$, $V_1 = 9.1$, $V_2 = 6.7$, $V_3 = 0.0$ ($G = 1$), $T = 0.26$, $W = 0.87$, $L = 2.5$, $P = 0.54$, $F = 0.49$.

on Minkowski functionals and shapefinders, such morphological characteristics of reaction zones are quantitatively shown, and statistical analysis is also possible.

Figure 3.18 shows arbitrarily chosen shapes of reaction zones, along with their dimensionless shapefinders (P, F) observed in the MILD and conventional premixed cases considered here. The Minkowski functionals and shapefinders are computed for the half of the data sets mentioned in section 2.6, and there are 510 objects for Case A1, 328 for Case A2, 272 for Case B1, and 42 for the conventional premixed case. Since the relatively large reaction rate is used as an iso-value, even the statistically planar premixed flame case has sufficiently small closed surfaces which do not interact with boundaries. The reaction zones are sheet-like as in figures 3.18p–3.18t for the conventional premixed case, and the reaction zone shapes are varied, complex and multiply connected for the MILD combustion cases.

Figure 3.19 shows the three length scales normalised using the respective δ_{th}

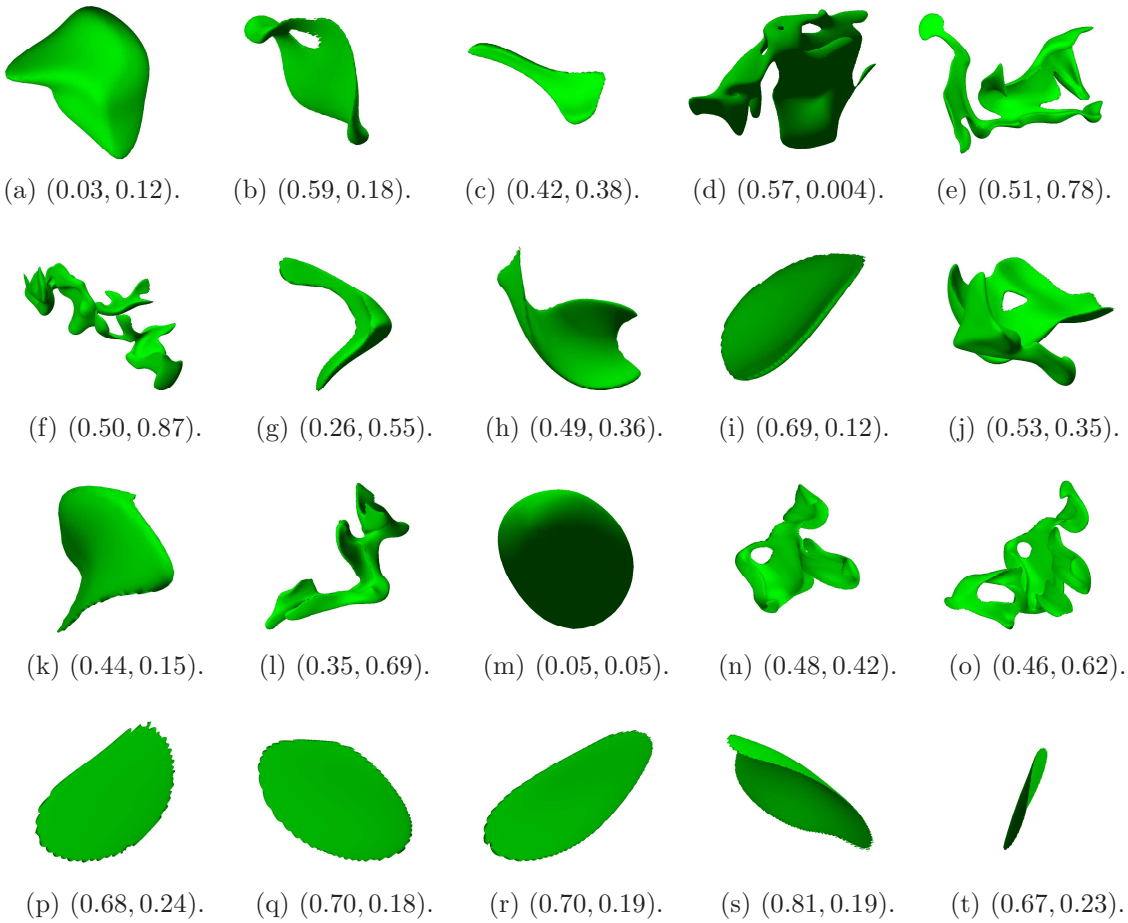

(a) $(0.03, 0.12)$. (b) $(0.59, 0.18)$. (c) $(0.42, 0.38)$. (d) $(0.57, 0.004)$. (e) $(0.51, 0.78)$.

(f) $(0.50, 0.87)$. (g) $(0.26, 0.55)$. (h) $(0.49, 0.36)$. (i) $(0.69, 0.12)$. (j) $(0.53, 0.35)$.

(k) $(0.44, 0.15)$. (l) $(0.35, 0.69)$. (m) $(0.05, 0.05)$. (n) $(0.48, 0.42)$. (o) $(0.46, 0.62)$.

(p) $(0.68, 0.24)$. (q) $(0.70, 0.18)$. (r) $(0.70, 0.19)$. (s) $(0.81, 0.19)$. (t) $(0.67, 0.23)$.

Figure 3.18: Sample reaction zone shapes and their shapefinders, (P, F), extracted from the DNS of the Case A1 (a–e), Case A2 (f–j), Case B1 (k–o) and Case C (p–t) at an arbitrary time and position.

for the MILD cases and conventional combustion case given in table 2.2. The black solid lines denoting $W^+ = T^+$ and $L^+ = W^+$ are shown to verify whether the inequality $T^+ \leq W^+ \leq L^+$ is met by the computed results. This inequality is satisfied predominantly, but there are some samples violating this inequality (ie., $L^+ < W^+$) due to numerical errors as noted in Appendix C. This violation yields non-physical negative shapefinders, P and F. A thorough analysis of the data sets, however, showed that there are only a small percentage, 1.8% for Case A1, 1.2% for Case A2, 0.37% for Case B1 and none for Case C, of such objects to impart statistical influence on the results discussed in this section.

The characteristic width W is much larger than the thickness T and is comparable to the length L for the conventional combustion case suggesting a thin sheet like shape. The scatter shows that characteristic thickness vary from $0.05 \leq T^+ \leq 0.15$, which is relatively narrow compared to the other length scales. The characteristic length and width, however, vary equally widely as shown in figure 3.19b. The scatter follows the $W = L$ line closely, suggesting thin-circular sheet. The distributions are wider in the MILD combustion; the characteristic thickness is $0.09 \leq T^+ \leq 0.5$ for all the MILD cases. This is because of the non-uniform mixture in MILD combustion, where the reaction zones thickness is not only influenced by global quantities such as the equivalence ratio and inlet temperature, but also by convolutions and interactions of reaction zones led by the non-uniformity of mixtures as shown in figures 3.6 and 3.7. The relation of W and L in MILD combustion is no longer expected by the $W = L$ line unlike in the conventional premixed case.

The results shown in figure 3.19 are used to calculate P and F through equation 3.13. A scatter plot of P and F are shown in figure 3.20. The results of the conventional premixed case reside in a narrow region mostly confined to the (P, F) regions for "sheets" shapes, but the MILD reaction zones have broad distribution; P ranges from about 0.01 to 0.7 and F from about 0.01 to 0.8. A comparison of this result to figure 3.15 suggests that the MILD reaction zone shapes range from blobs (small P and F) to pancakes (intermediate P and F). There are also short tubes. The pocket burnouts would give blob-like shapes, which are represented by the points close to (0, 0) in figure 3.20.

The marginal PDF of P and F constructed using 20 bins for the MILD cases

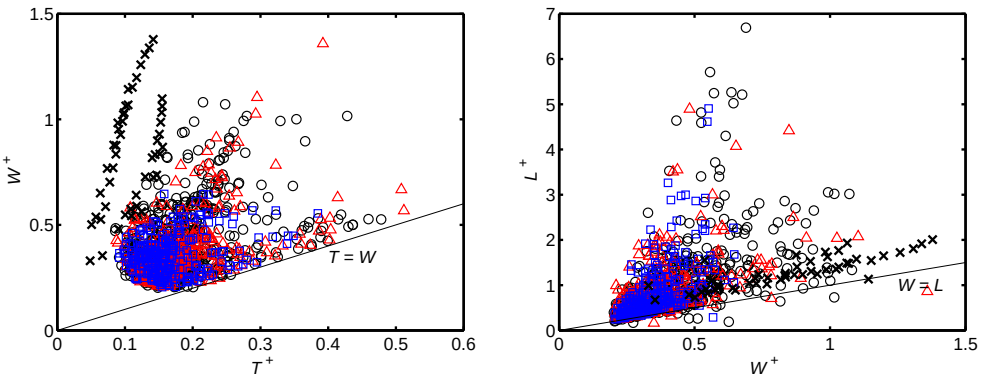

(a) (b)

Figure 3.19: The three length scales, calculated using equations. 3.11, for the reaction zones in Case A1 (black ∘), Case A2 (red △), Case B1 (blue □) and Case C (black ×).

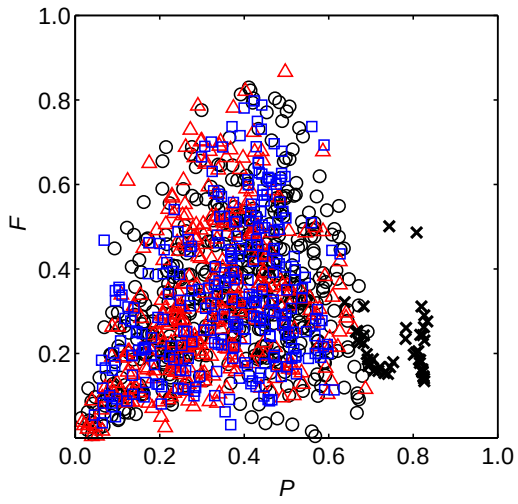

Figure 3.20: Shapefinder, P and F, values in Case A1 (black ∘), Case A2 (red △), Case B1 (blue □), and Case C (black ×).

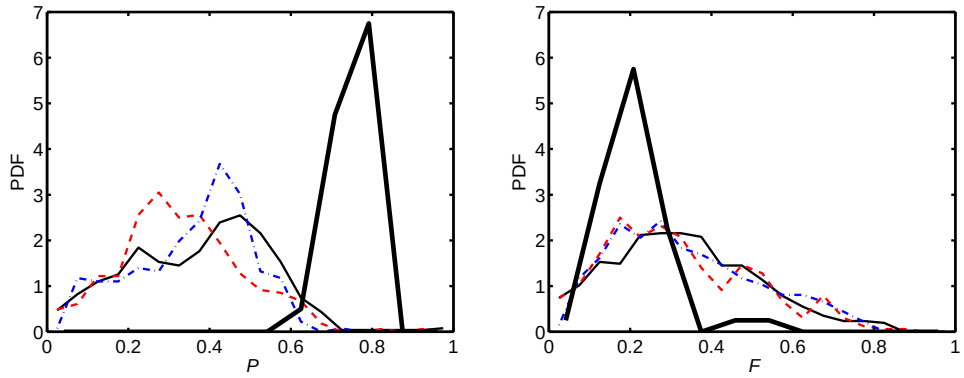

(a) (b)

Figure 3.21: PDF of (a) planarity and (b) filamentarity for Case A1 (black thin-solid), Case A2 (red dashed), Case B1 (blue dash-dotted), and Case C (black thick solid).

and 12 bins for the conventional premixed case shown in figure 3.21 suggests that P and F are distributed from 0 to about 0.8 for the MILD cases as discussed in above. However, for the conventional premixed case, their ranges are $0.6 \leq P \leq 0.9$ and $0.1 \leq F \leq 0.4$, with the sharp peaks in the PDFs. The data in this figure suggests that the most probable (P, F) is (0.79, 0.2) for the conventional premixed case. The most probable value of P varies between 0.3 to 0.5 and F is about 0.2 for the MILD cases considered. These values show that the most probable shape for the MILD reaction zone is pancake like. Such reaction zone shapes may be caused by autoigniting mixtures or interacting flames, which do not necessarily create thin flame fronts unlike propagating flames. Also, Da conditions do not have significant effects on reaction zone shape statistically (Da of Cases A2 and B1 differs almost 5 times). The pancake like reaction zones have a typical volume $\mathcal{V}$ of $\sim \delta_{th}^3$ as shown in table 3.1. The average and most probable values of $\mathcal{V}$ and the three characteristic length scales used in the above analyses are given in table 3.1. These values are normalised using the respective δ_{th} given in the same table. The mean and most probable normalised thickness T^+ of the reaction zones show a very weak sensitivity to Da, although the dimensional thickness increases with dilution level since δ_{th} increases. This implies that the popularly-

used EDC models, where the characteristic residence time of reactants in the fine structure is considered as $\sim (\nu/\varepsilon)^{0.5}$, may need to include the effect of dilution level on the size of such structures. The values of W^+_{mean} and L^+_{mean} also show this insensitivity in the MILD cases. Generally L^+_{mean} is larger than W^+_{mean} and the ratio $L^+_{\mathrm{mean}}/W^+_{\mathrm{mean}}$ is about 2.3 for the MILD cases and 1.5 for the conventional premixed case. The ratio $W^+_{\mathrm{mean}}/T^+_{\mathrm{mean}}$ is also about 2.1 for the MILD cases, but it is 7.6 for the conventional premixed case. These values clearly agree with the above observation on the reaction zone morphology even in an average sense.

Table 3.1: Average and most probable values of $\mathcal{V}$ and the three characteristic length scales (equations 3.11 and 3.12).

	δ_{th} (mm)	Da	Ka	$\mathcal{V}^+_{\text{mean}}$	T^+_{mean}	W^+_{mean}	L^+_{mean}	$\mathcal{V}^+_{\text{prob}}$	T^+_{prob}	W^+_{prob}	L^+_{prob}
Case A1	1.00	1.72	4.78	0.93	0.19	0.44	1.00	0.07	0.15	0.26	0.46
Case A2	1.00	3.25	2.11	0.42	0.19	0.38	0.87	0.07	0.18	0.29	0.45
Case B1	1.29	0.69	11.9	0.30	0.17	0.36	0.85	0.12	0.16	0.36	0.63
Case C	0.37	5.64	0.92	0.56	0.11	0.84	1.27	0.22	0.15	0.83	1.23

Chapter 4

Autoignition and Flame Propagation in MILD Combustion

4.1 Background and objectives

Given the high elevated temperature conditions and the presence of chemically active radicals in the inlet mixture, autoignition plays an important role in MILD combustion to maintain combustion even in a high speed flow without recirculation zones (Wünning & Wünning, 1997; Katsuki & Hasegawa, 1998; Cavaliere & de Joannon, 2004). The analysis in chapter 3, section 3.5 showed that MILD reaction zones have statistically pancake-like shapes. Since propagating flames are usually associated with thin sheet-like structures, these pancake-like shapes are also suggestive of autoignition events in MILD combustion. Ignition characteristics in configurations employing diluted and/or hot reactants/coflow have been studied in the context of flame stabilisation (Mastorakos *et al.*, 1995; Markides & Mastorakos, 2005; Oldenhof *et al.*, 2010; Arndt *et al.*, 2012). Such configurations are similar to MILD combustion with either HODO or HODF conditions. For MILD combustion, roles played by ignition for flame stabilisation has been studied using a Jet-in-Hot-Coflow (JHC) burner experimentally (Medwell, 2007; Medwell *et al.*, 2007, 2008) and numerically (van Oijen, 2013). The CH_2O PLIF

imgaes show that the heated coflow initiates ignition of mixture after localised extinction caused by cold surrounding air (Medwell *et al.*, 2007). Despite this interplay between extinction and ignition processes, the presence of abundant hot exhaust gas ensures to sustain the overall reaction in MILD combustion. At the same time, the results discussed in the previous sections also suggest that there are thin reaction zones with thickness of about δ_{th} in MILD combustion, while "distributed" reaction zones are caused predominantly by interactions between propagating reaction zones. Such thin reaction zones may be represented reasonably well using appropriately constructed laminar flame elements MIFE, where the local reaction zones propagate toward reactants at the speed of $\sim S_L$. Probability density functions of a temperature field in Dally *et al.* (2004) suggest that combustion observed in their MILD combustion burner is due to the flame propagation, rather than autoignition in the conditions considered. Thus, there is a strong possibility of the existence of a competition between autoignition and flame propagation in MILD combustion, which is also suggested in Mastorakos (2009).

Generally, autoignition is sensitive to the local mixture composition, which is influenced by a balance of turbulent mixing, molecular diffusion and chemical reactions, as well as the local temperature (Cavaliere & de Joannon, 2004; Markides & Mastorakos, 2005; Oldenhof *et al.*, 2011; Arndt *et al.*, 2012). Especially, turbulent mixing can directly affect the autoignition delay time (Markides & Mastorakos, 2005). In the present DNS configuration, the inlet mixture is imperfectly mixed due to the inclusion of the EGR-type mixing procedure, where not only the turbulence conditions, but also the mass fractions of chemically active radicals have variations spatially and temporary. Thus, the autoignition delay time spatially varies as well. Also, the local turbulence condition affects the local residence time of the mixture, thereby favouring flame propagation over autoignition, or other way around. Effects of the global mixture composition on autoignition has been studied for MILD combustion (Parente *et al.*, 2011a). However, the competing effects of the local turbulence and mixture composition on autoignition/flame propagation characteristics have not studied thoroughly, although such characteristics directly influence MILD combustion modelling.

The objectives in this chapter are to investigate whether there is autoigni-

tion, flame propagation or both, and to find under which condition autoignition or flame propagation is favoured in MILD combustion. An effect of the presence of such reaction zones on conventional flamelet modelling is also discussed. The identification of the two combustion phenomena is based on the transport equation of a reaction progress variable. The physical background and identification method are explained first, and then the reaction dominated and flame-propagation dominated regions are identified. After that, favourable conditions for these two activities are discussed.

4.2 Balance of convection, diffusion and chemical reaction rate

Turbulent combustion phenomena consist of a competition between turbulence and chemical reactions, which is therefore a balance of the convection, diffusion and chemical source terms of a transported quantity. The instantaneous transport equation of a reaction progress variable c is written in conservation form as:

$$\frac{\partial \rho\, c}{\partial t} \underbrace{+ \frac{\partial \rho\, u_i\, c}{\partial x_i}}_{\mathscr{C}\text{: convection}} = \underbrace{\frac{\partial}{\partial x_j}\left(\rho D_c \frac{\partial c}{\partial x_j}\right)}_{\mathscr{D}\text{: diffusion}} + \underbrace{\omega_c}_{\mathscr{R}\text{: reaction}}, \tag{4.1}$$

where u_i is the fluid velocity in direction x_i and D_c is the diffusivity of c. The balance between these predominant terms, $\mathscr{C}$, $\mathscr{D}$ and $\mathscr{R}$, is assessed by using a quantity $\mathscr{B}$ defined as:

$$\mathscr{B} \equiv |\mathscr{C} - \mathscr{D}| - |\mathscr{R}|. \tag{4.2}$$

For homogeneous transient combustion in a fixed-mass constant pressure reactor, the equation 4.1 is dominated by the chemical source $\mathscr{R}$ and unsteady terms, giving $\mathscr{B} = -|\mathscr{R}| \ll 0$. This situation is also regarded as combustion in a Perfectly Stirred Reactor (PSR) with the volume V and the mass flow rate $\dot{m}_{in}$, since its governing equation for c is written as:

$$\frac{dc}{dt} = -\frac{c}{\tau_R} + \frac{\omega_c}{\rho}, \tag{4.3}$$

where τ_R is the residence time of a reactor defined as $\tau_R = \rho V/\dot{m}_{in}$. Thus, for a canonical configuration such as a homogeneous reactor or PSR, regions with $\mathscr{B} \ll 0$ signify autoignition events. Although it may not be adequate to assume an entire MILD combustion field as a homogeneous reactor or a PSR, the elevated temperature conditions and distributed reaction zones shown in section 3.2 may locally generate reaction zones with $\mathscr{B} \ll 0$. In the present MILD cases, not only autoigniting mixtures, but flame interacting regions can also have a small $\mathscr{C}$ and $\mathscr{D}$ yielding a negative $\mathscr{B}$ as explained in section 3.3. Thus, local regions having negative $\mathscr{B}$ are called Reaction Dominated (RD) regions in this work. Clearly, such RD regions cannot be modelled based on scalar gradient or scalar dissipation rate flamelet approaches since the direct relation between reaction rate and scalar gradient no longer holds. Also, the insight based on these canonical configurations ensures adequacy of previous investigation into premixed MILD combustion using PSR or homogeneous type reactors (de Joannon *et al.*, 2004, 2005; Sabia *et al.*, 2007).

Another canonical situation of equation 4.1 is a steady one-dimensional conventional premixed flame with the inlet mixture velocity of S_L. In this case, a balance between the three terms gives $\mathscr{B} = 0$. In turbulent premixed combustion, however, there are large velocity fluctuations leading to local displacement of flames. Thus, large $\mathscr{C}$ and $\mathscr{R} \sim \rho_u S_L/\delta_{th}$ are observed near flame fronts, yielding $\mathscr{B} \gg 0$. Such reaction zones are called Flame-propagation Dominated (FD) regions in this work. Based on these insights, RD and FD regions are identified respectively as mixtures having $\mathscr{B} \ll 0$ and $\mathscr{B} \gg 0$.

Spatial variations of $|\mathscr{C} - \mathscr{D}|$ and $|\mathscr{R}|$ are analysed first. Figure 4.1 shows typical contours of $|\mathscr{C}^+ - \mathscr{D}^+| = 1.0$ and $|R^+| = 1.0$ in y-z planes at two different x^+-locations for the conventional premixed case. Although the contour of $|\mathscr{C}^+ - \mathscr{D}^+| = 1.0$ and $|R^+| = 1.0$ are not identical to one another, the intense reaction rate regions are well correlated with the $|\mathscr{C}^+ - \mathscr{D}^+| = 1.0$ contours. The variations of $\mathscr{C}^+$, $\mathscr{D}^+$ and $\mathscr{R}^+$ across the local flame are also shown in figures 4.1c and 4.1d. This suggests that intense chemical reaction always occurs near regions of large diffusion for the conventional premixed case. As a result, the predominant terms, $\mathscr{C}$, $\mathscr{D}$ and $\mathscr{R}$, are more or less balanced in an average sense, although $\mathscr{B}$ varies locally.

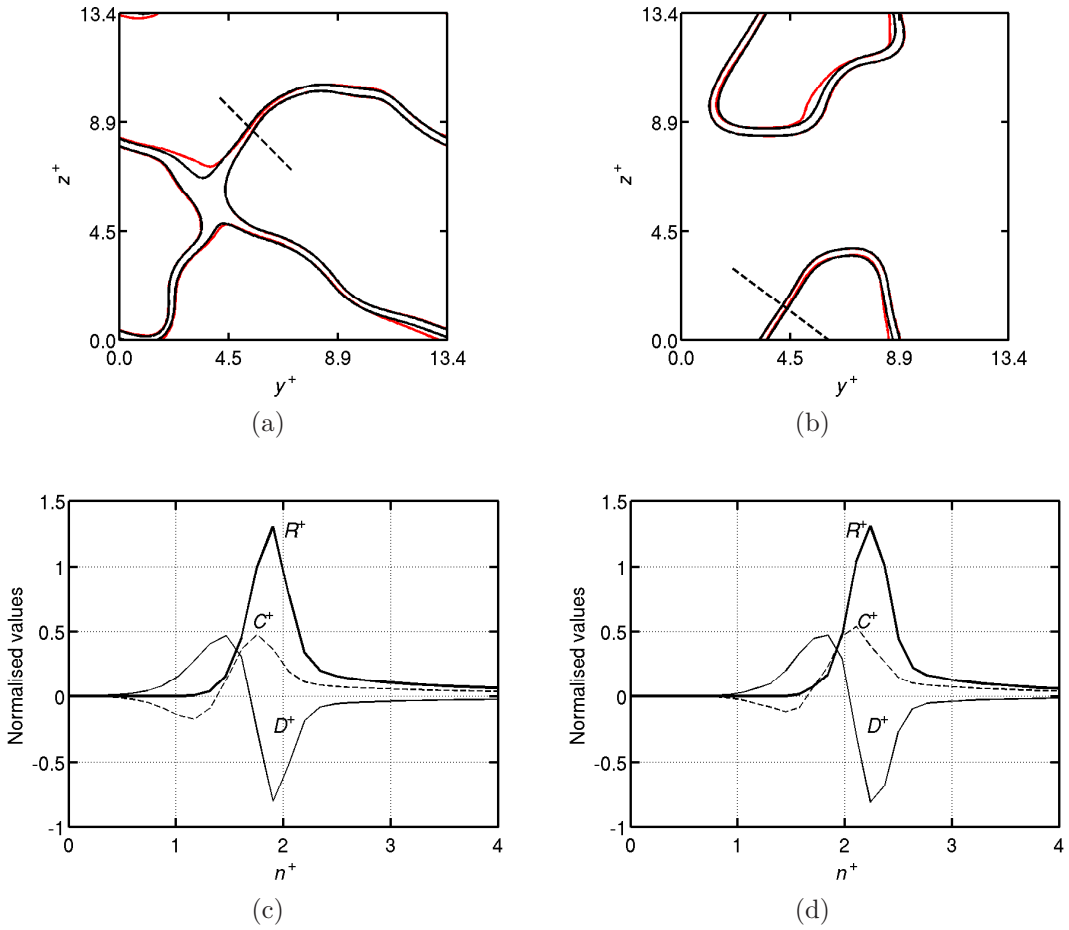

Figure 4.1: (a, b) Typical contours of $|\mathscr{C}^+ - \mathscr{D}^+| = 1.0$ (red) and $|R^+| = 1.0$ (black) in y-z planes at $x^+ = 11.0$ (a) and 16.6 (b) at $t = 1.5\tau_D$. Note that contours are shown on the same planes as in figure 3.5. (c, d) Variations of $\mathscr{C}^+$, $\mathscr{D}^+$ and $\mathscr{R}^+$ in equation 4.1 along the dashed line in (a) and (b). (c): extracted from (a), (d): extracted from (b). Note that $\boldsymbol{n}^+$ orients towards the burnt side.

In MILD combustion, the correlation between $|\mathscr{C}-\mathscr{D}|$ and $|\mathscr{R}|$ depends on x^+-locations and their behaviours are more complicated in general. Figures 4.2a–4.2c show contours of $|\mathscr{C}^+ - \mathscr{D}^+| = 1.5$ and $|\mathscr{R}^+| = 1.5$ in a y-z plane at $x^+ = 0$ (one point inside the domain) for the MILD Cases A1, A2 and B1. For combustion with the lowest dilution and lowest turbulence condition, Case A2 in figure 4.2b, these two contours are almost identical to one another, like those in the conventional premixed case shown in figure 4.1. With an increase of turbulence level (compare Cases A1 and B1 in figures 4.2a and 4.2c), the $|\mathscr{C}^+ - \mathscr{D}^+| = 1.5$ contours (red lines) become more wrinkled compared to the $|R^+| = 1.5$ contours, reflecting the stronger turbulence level and smaller length scale. However, both $|\mathscr{C}^+-\mathscr{D}^+| = 1.5$ and $|\mathscr{R}^+| = 1.5$ contours cluster at similar locations for all the MILD cases, suggesting not much progress of heat release, turbulent mixing and diffusion are made at this location since the mixture experienced turbulence for only one large eddy turnover time as explained in section 2.5.

Figures 4.2d–4.2f show contours of $|\mathscr{C}^+ - \mathscr{D}^+| = 1.5$ and $|R^+| = 1.5$ at $x = L_x/3$, where strong convolutions and frequent interactions of reaction zones are observed for the MILD cases as shown in section 3.2. Because of the progress of turbulent combustion, the contours of these two fields exhibit quite different behaviour to one another. Therefore, strong spatial variations for the unsteady term in equation 4.1 exists. Contours of the same level are shown for the 2D slice at a downstream location ($x = 2L_x/3$) in figures 4.2g–4.2i. These contours are not highly convoluted compared to those observed in the middle of the computational domain ($x = L_x/3$) for Cases A1 and A2, because of the progress of heat releasing, turbulent mixing and diffusion, which generates relatively uniform c_T field close to unity at downstream regions. However, a relatively strong convolutions of the contours are still observed for Case B1 at this location, due to the relatively slow chemical process that is caused by the high dilution condition. This result agrees with the visual examination of the reaction rate field in figure 3.7.

The local dominance of flame propagation or reaction phenomena is studied by investigating the spatial variation of $\mathscr{B}^+$. Typical spatial variation of this quantity along with ω_{cT}^+ is shown in figures 4.3–4.5 for Cases A1, A2 and B1. The RD regions are signified by $\mathscr{B}^+ \leq -1.5$ and such regions are denoted by the black contour lines. The FD regions, $\mathscr{B}^+ \geq 1.5$, are represented by the

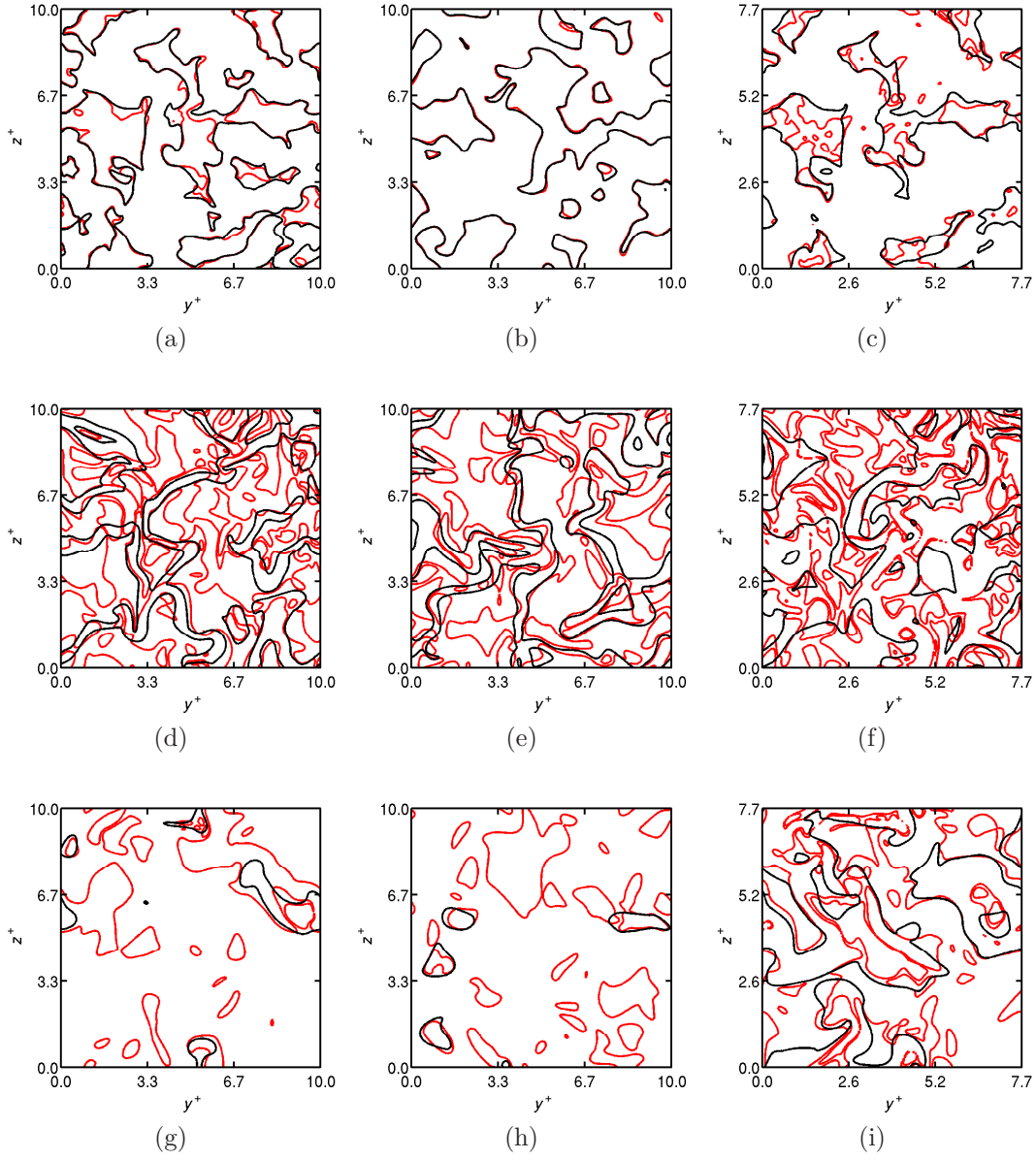

Figure 4.2: Contours of $|\mathscr{C}^+ - \mathscr{D}^+| = 1.5$ (red) and $|R^+| = 1.5$ (black) in a y-z plane for Case A1 (a, d, g), Case A2 (b, e, h), and Case B1 (c, f, i) at $t = 1.5\tau_D$. The slices are shown at one grid point from the inlet boundary (a–c), $x = L_x/3$ (d–f) and $x = 2L_x/3$ (g–i).

white contour lines in this figure. The thin reaction zones tend to have $\mathscr{B}^+ > 1.5$ due to the turbulence, and one such region is marked by a white box (also enlarged) as an example for each case. As clearly seen, the FD regions exist in a substantial volume, especially for Cases A1 and A2. Regions with relatively thick and distributed-like reaction zones typically tend to have$\mathscr{B}^+ < -1.5$ as expected, and an example for this is marked using a black box with a solid line (also enlarged) for Cases A1 and B1. However, there are many continuous reaction zones having $\mathscr{B}^+ > 1.5$ for some parts and $\mathscr{B}^+ < -1.5$ for the rest. Several such regions are marked using black boxes with dashed lines (some of them are also enlarged) for all the MILD cases.

For Case B1 shown in figure 4.5, the RD and FD regions are entangled locally, where RD events are closely followed by FD phenomena. The central region marked using a box with black-dot-dashed lines (also enlarged) in figure 4.5 is a good example of the entangled RD and FD regions. These $\mathscr{B}^+$ variations clearly show that both RD and FD regions coexist in the MILD combustion. Also, the intense reaction in this region can result from the collision of multiple flame elements propagating towards one another. These collision or interaction events are very quick and have a time scale of about one tenth of the corresponding laminar flame element time scale (Chen *et al.*, 1999; Dunstan *et al.*, 2013b), and thus the unsteady term will be very large to yield large $|\mathscr{B}^+|$.

The statistical nature of the coexistence can be investigated using the PDF of $\mathscr{B}^+$. Figure 4.6 shows such PDFs at various streamwise positions for Cases A1–B1, and the conventional premixed case result is also shown at $x^+ = 10.2$ for a comparison. The inset shows the variation of the most probable and averaged $\mathscr{B}^+$ with x^+. The average is obtained as $\int \mathscr{B}^+ P(\mathscr{B}^+) d\mathscr{B}^+$ at x^+ of interest.

The behaviour of $P(\mathscr{B}^+)$ for the conventional premixed case shows that the PDF of $\mathscr{B}^+$ peaks at close to zero signifying the balance among convection, diffusion and reaction in an average sense. The PDF has a broader distribution for the MILD cases and it varies depending on the streamwise position. At upstream regions, the PDF has long positive and negative tails with non-zero probability density, suggesting the existence of both RD and FD regions which may have a wide range of scales. At downstream regions, however, only the positive $\mathscr{B}^+$ tail with non-zero probability density is long, and the probability

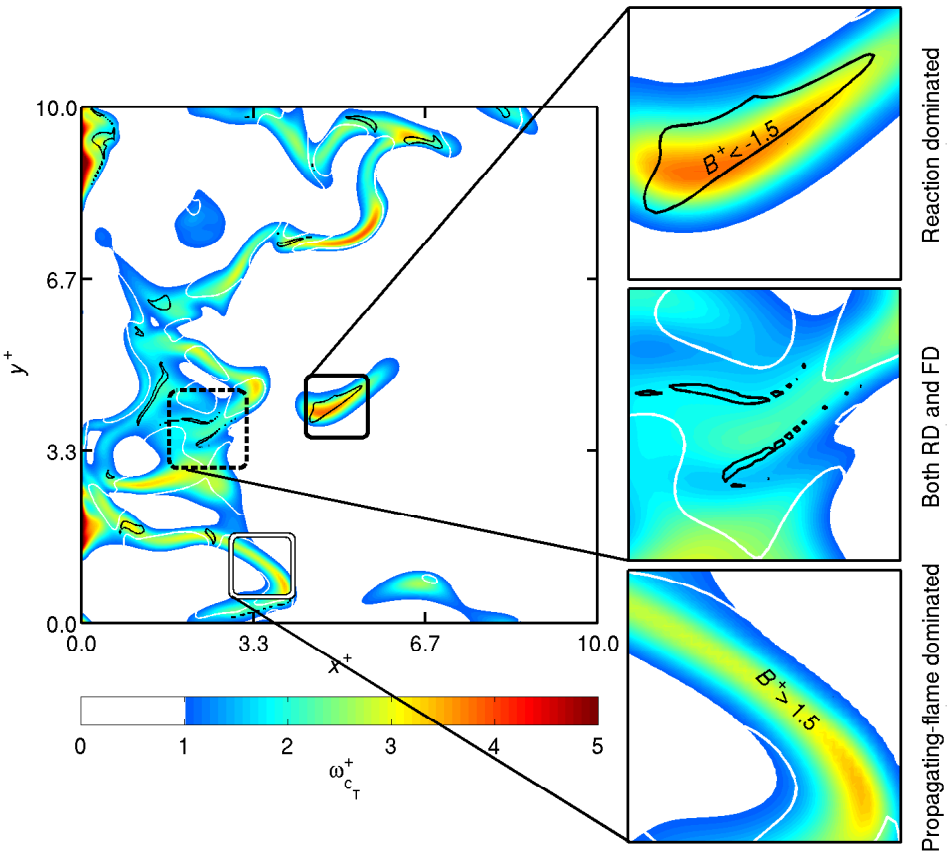

Figure 4.3: Typical contours of $\omega^+_{c_T}$ (colour map) are shown along with propagating-flame dominated ($\mathscr{B}^+ = 1.5$, white contour lines) and reaction dominated ($\mathscr{B}^+ = -1.5$, black contour lines) regions for Case A1 in the same x-y plane as in figure 3.6a. Typical reaction dominated and propagating-flame dominated regions are marked respectively by a black box and a white box with solid lines, and they are enlarged in top right and bottom right. A continuous reaction zone having both reaction and propagating-flame dominated phenomena is marked using black boxes with dashed lines, and enlarged in middle right.

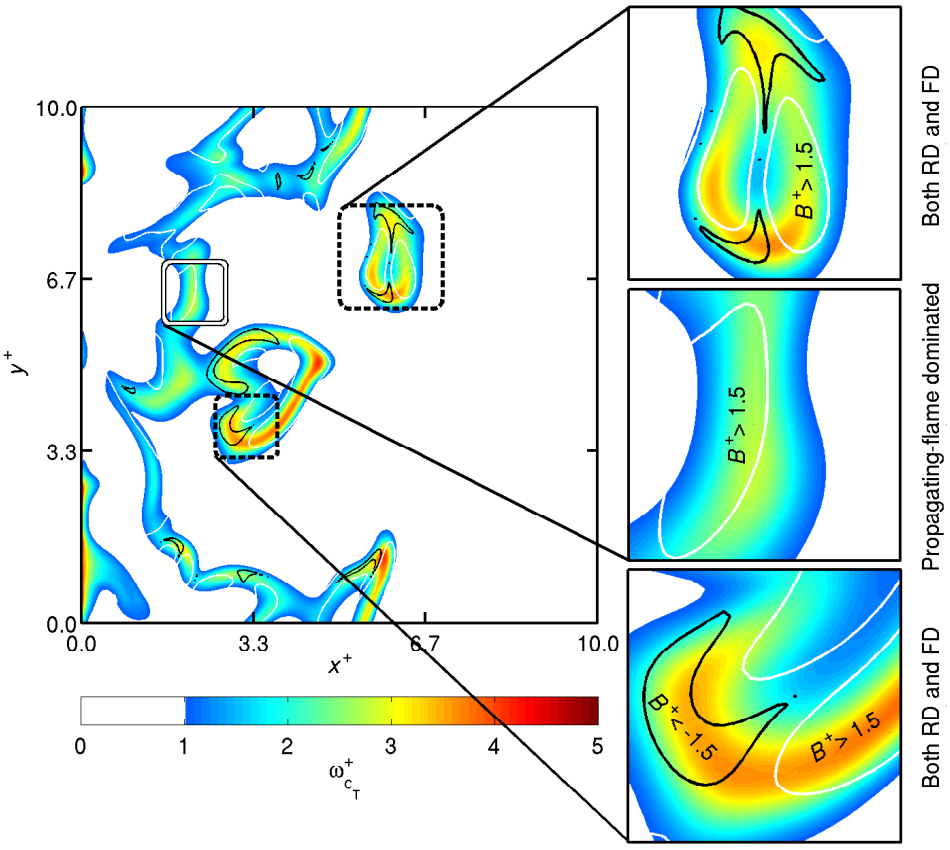

Figure 4.4: Typical contours of $\omega^+_{c_T}$ (colour map) are shown along with propagating-flame dominated ($\mathscr{B}^+ = 1.5$, white contour lines) and reaction dominated ($\mathscr{B}^+ = -1.5$, black contour lines) regions for Case A2 in the same x-y plane as in figure 3.6g. A typical propagating-flame dominated region is marked a white box with solid lines, and enlarged in middle right. Several continuous reaction zones having both reaction and propagating-flame dominated phenomena are marked using black boxes with dashed lines and enlarged in top right and bottom right.

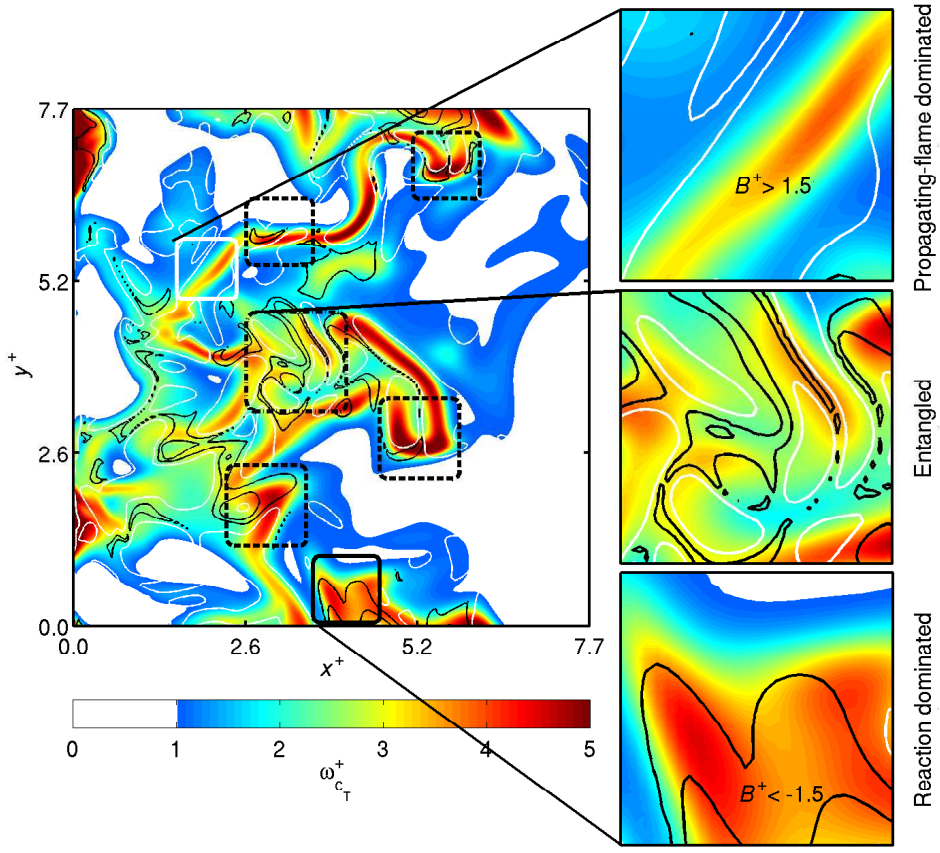

Figure 4.5: Typical contours of $\omega^+_{c_T}$ (colour map) are shown along with propagating-flame dominated ($\mathscr{B}^+ = 1.5$, white contour lines) and reaction dominated ($\mathscr{B}^+ = -1.5$, black contour lines) regions for Case B1 in the same x-y plane as in figure 3.7a. Typical reaction dominated and propagating-flame dominated regions are marked respectively by a black box and a white box with solid lines, and they are enlarged in bottom right and top right. Several continuous reaction zones having both reaction and propagating-flame dominated phenomena are marked using black boxes with dashed lines. The box with dash-dotted lines in the center denotes a region where the two phenomena are closely entangled, which is also enlarged in middle right.

density quickly decreases for the negative $\mathscr{B}^+$. This shows that FD combustion is more active in downstream regions, although the reaction rate at these regions decreases with the x^+ distance due to consumption of the fuel in general.

The peak of $P(\mathscr{B}^+)$ locates at close to $\mathscr{B}^+ \approx 0$ in the upstream positions for all MILD cases. The peak location shifts to negative $\mathscr{B}^+$ and then moves back towards positive $\mathscr{B}^+$ as the sampling position moves downstream. These changes are gradual as seen in the insets of figure 4.6. The most probable $\mathscr{B}^+$ stays in the negative side as shown in the inset, while the averaged $\mathscr{B}^+$ is positive for all streamwise positions. Therefore, the MILD combustion is dominated by strong unsteady flame propagation phenomena in a volume average sense, although a homogeneous-reactor type events are common for the conditions considered in this study.

While such a consistent trend of $\mathscr{B}^+$ is observed for all the MILD cases considered, turbulent combustion conditions for these cases influence the shape of the PDF. A comparison of the PDF near the inlet boundary shows that the peak value is 0.80 for Case A1, 1.79 for Case A2 and 0.30 for Case B1, clearly reflecting the effect of turbulence level on mixing during the mixing process in section 2.5. As shown in the inset, the peak value of the averaged $\mathscr{B}^+$ variations for Cases A2 is 1.1, which is smaller than 1.5 observed for Case A1 (see the insets), because of the lower turbulence condition, yielding smaller $\mathscr{C}$. Also, the probability density for Case B1 is generally small compared to other MILD cases, having no sharp peak near $\mathscr{B}^+ = 0$ at any x^+ locations. This suggests that the reaction zones in Case B1 tend to have a wider range variations than the other MILD cases, due to the high dilution and turbulence condition.

Similar PDFs of $\mathscr{B}^+$ computed using progress variables, c_Y, $c_{\mathrm{H_2O}}$ and $c_{\mathrm{CO_2}}$, are shown in figure 4.7. Here, $c_{\mathrm{H_2O}} = (Y_{\mathrm{H_2O}} - Y_{\mathrm{H_2O,r}})/(Y_{\mathrm{H_2O,p}} - Y_{\mathrm{H_2O,r}})$ and $c_{\mathrm{CO_2}} = (Y_{\mathrm{CO_2}} - Y_{\mathrm{CO_2,r}})/(Y_{\mathrm{CO_2,p}} - Y_{\mathrm{CO_2,r}})$. As clearly shown in the figure, behaviour of the most probable and mean of $\mathscr{B}^+$ is different depending on which progress variable is used. This difference may show the effect of non-unity Lewis numbers and complex chemistry, since c_Y, $c_{\mathrm{H_2O}}$ and $c_{\mathrm{CO_2}}$ would behave the same as c_T if unity Lewis number and a single step chemistry were used. However, fundamental reaction/flame-propagation characteristics do not rely on the choice of progress variable. A broader distribution of $P(\mathscr{B}^+)$ in the MILD combustion signifies the

importance of strong local unsteady effects and the coexistence of RD and FD phenomena.

The gradient of a progress variable field — relating to the convection term $\mathscr{C}$ and scalar dissipation rate which plays important role for both premixed and non-premixed combustion — is shown in figure 4.8 with contours of $\mathscr{B}^+ = 1.5$ (white) and $\mathscr{B}^+ = -1.5$ (black) as in figures 4.3–4.5. The scalar gradient field is only shown for the regions of high reaction rate, $\omega^+_{c_T} \geq 1.0$. As expected from the discussion in section 3.3, the figure shows that these high reaction rate regions are not necessarily associated with a large scalar gradient, unlike conventional combustion (Bray, 1979; Swaminathan & Bray, 2011).

As clearly shown in the figures, most of large scalar gradient regions are enclosed by white lines, which denotes flame-propagation dominated regions. Some flame-propagation dominated local mixtures appear in small scalar gradient regions, but the proportion of such mixtures to the total of flame-propagation dominated mixtures seems to be negligible in these instantaneous shots for all the MILD combustion cases. In contrast, substantial regions of reaction dominated mixtures (black lines) exist at relatively small scalar gradient regions. One regions showing reaction/flame-propagation dominated behaviour is shown at about $(x^+, y^+) = (6.5, 6.7)$ in figure 4.8b; the high scalar gradient regions occupy two closed white lines representing flame-propagation dominated mixtures, and the rest of island is enclosed by two black lines, denoting reaction dominated mixtures. Similar behaviour is located as well in figures 4.8a and 4.8c.

In conventional premixed combustion, intense heat release rate is associated with a large scalar dissipation rate, which is directly related to scalar gradient (Bray, 1979; Swaminathan & Bray, 2011). Thus, regions with large scalar gradient are likely to establish flames, which propagates until they collide with other locally propagating flames (section 3.3). In contrast, high scalar dissipation rate delays the autoignition due to the heat and species loss for non-premixed combustion (Mastorakos, 2009), and this may occur in the present cases as well. The establishment of propagating flames is not fast enough in small scalar gradient regions, which are then taken over by reaction dominated events. Similar selective features of reaction dominated events have been reported for non-premixed and partially-premixed combustion with hot air (Mastorakos *et al.*, 1997; Hilbert

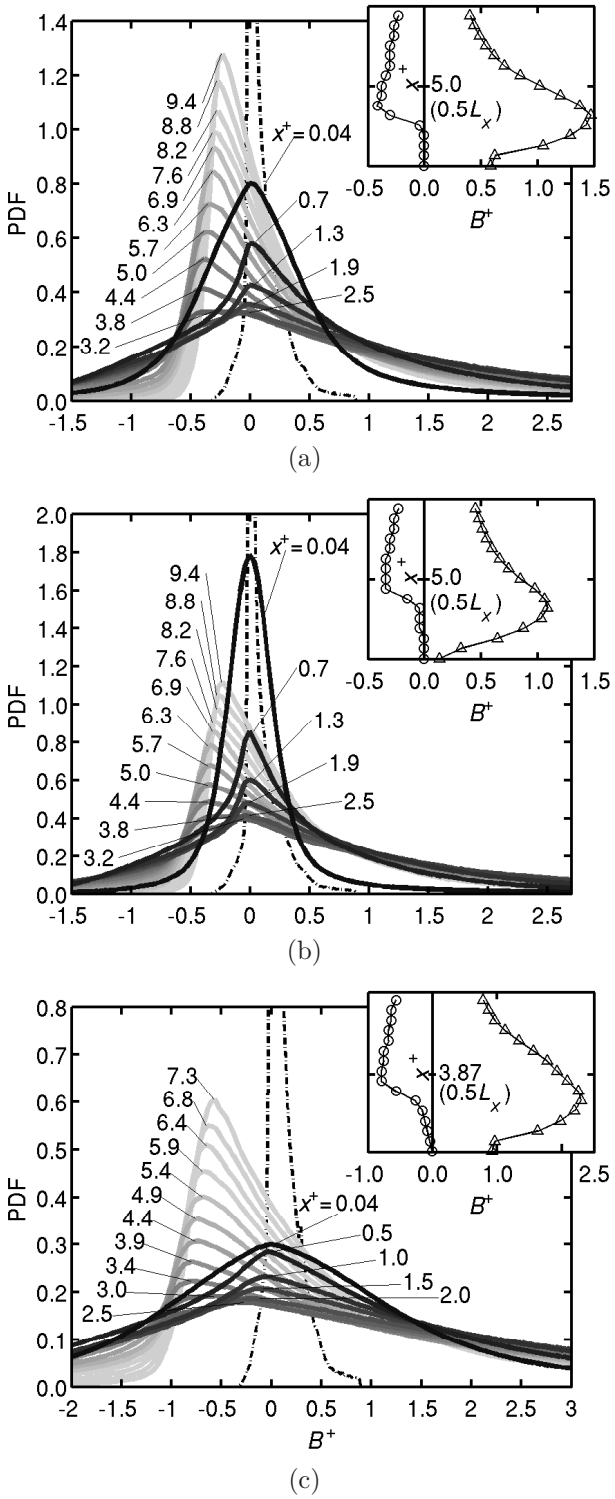

Figure 4.6: PDF of $\mathscr{B}^+$ at various x^+ positions as marked for (a) Case A1, (b) Case A2 and (c) Case B1. The PDF is also shown for the conventional premixed case at $x^+ = 10.2$ (dash-dotted line). The inset shows the variation of the most probable ($\circ$) and averaged ($\triangle$) values along x^+.

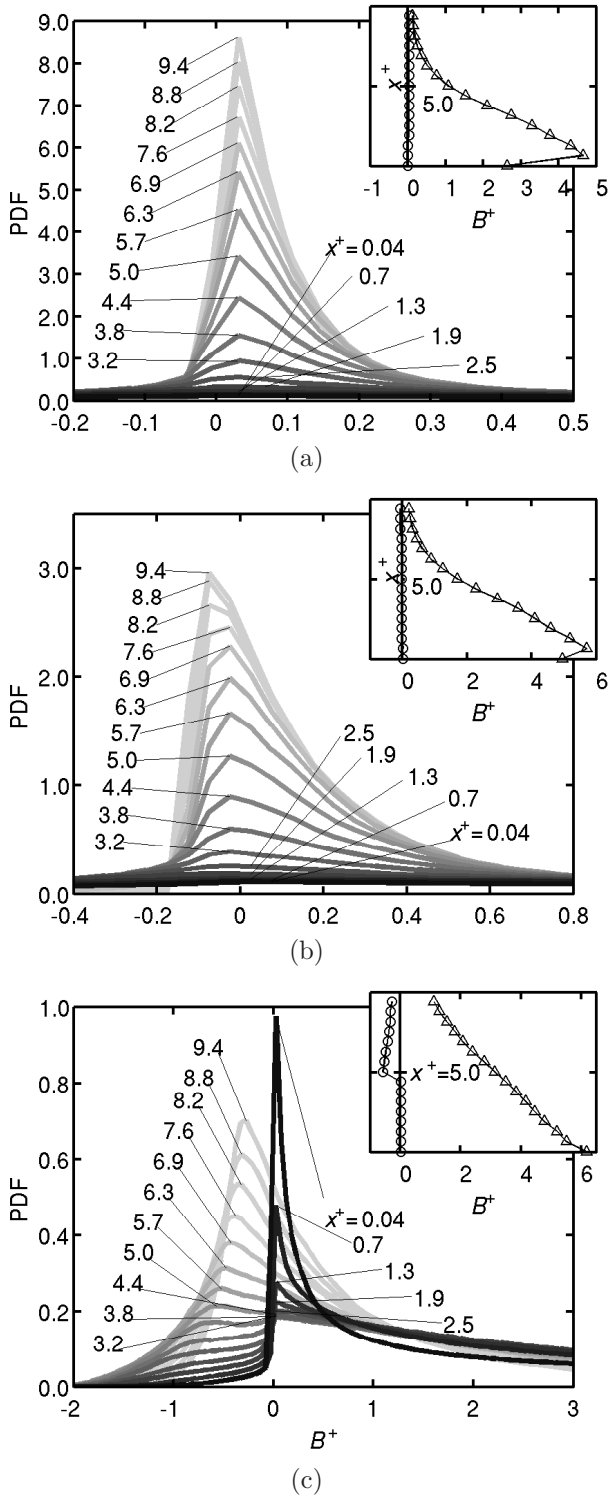

Figure 4.7: Typical PDF of $\mathscr{B}^+$ calculated using (a) c_Y, (b) c_{H_2O}, and (c) c_{CO_2} at various x^+ positions as marked for Case A1. The inset shows the variation of the most probable (○) and averaged (△) values along x^+.

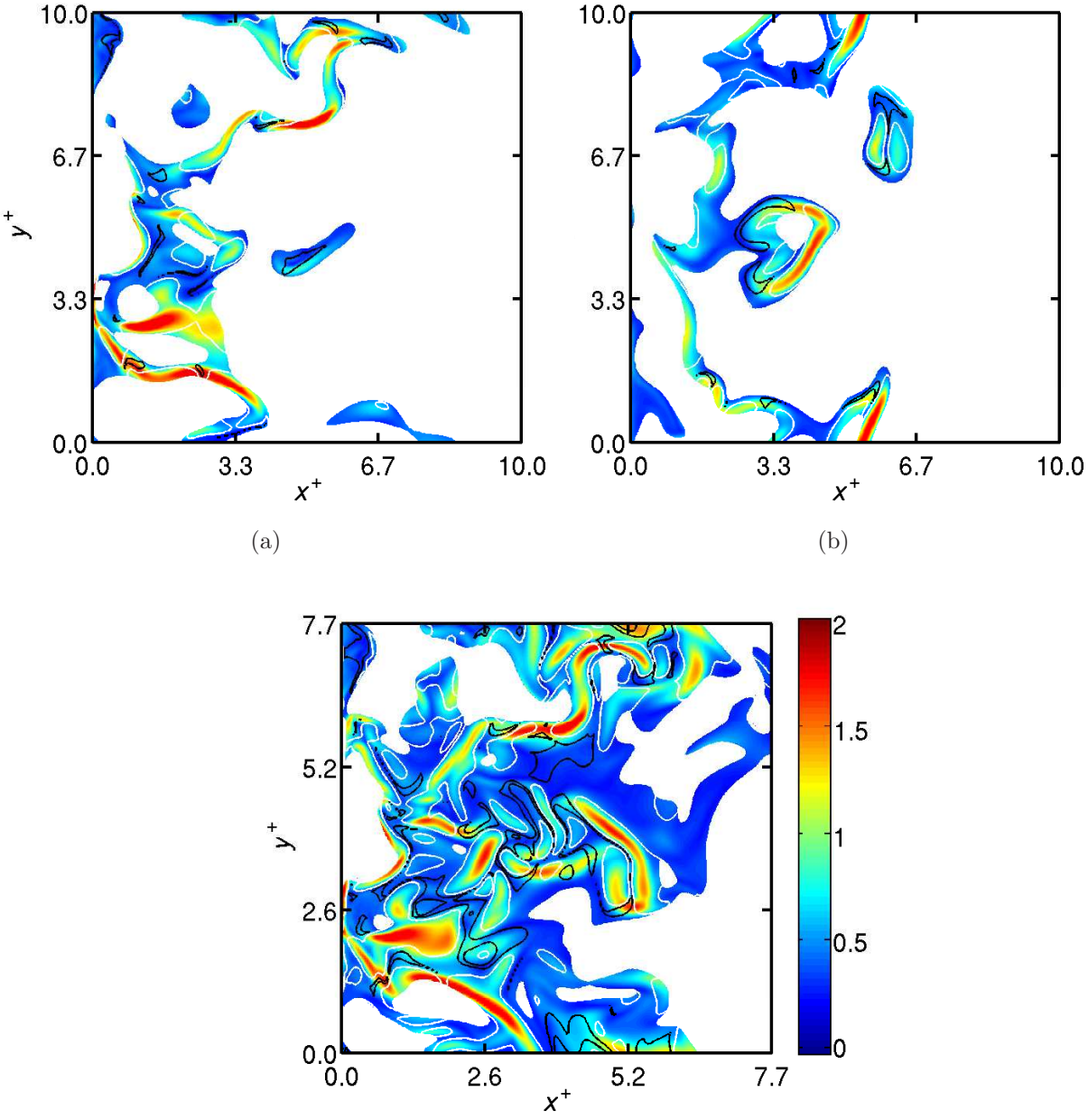

Figure 4.8: Typical contours of $|\nabla c_T|^+$ (colour map) are shown along with propagating-flame dominated ($\mathscr{B}^+ = 1.5$, white contour lines) and reaction dominated ($\mathscr{B}^+ = -1.5$, black contour lines) regions for (a) Case A1, (b) Case A2 and (c) Case B1 in the mid x-y plane at $t = 1.5\tau_D$. Regions with $\omega^+_{c_T} \leq 1.0$ are masked using white colour in the same way as in figures 4.3, 4.4 and 4.5.

& Thévenin, 2002; Zheng *et al.*, 2004; Arndt *et al.*, 2012). The configuration of these burners is similar to MILD burners having HODO or HODF conditions, and such laboratory scale MILD burners have been used intensively in previous studies (Plessing *et al.*, 1998; Dally *et al.*, 2004; Oldenhof *et al.*, 2011; Medwell *et al.*, 2007).

Such selective features of reaction/flame-propagation dominated regions can be studied statistically by using the PDF of reaction rate and scalar gradient calculated for the mixtures dominated either by reaction ($\mathscr{B}^+ \leq -1.5$) or by flame propagation ($\mathscr{B}^+ \geq 1.5$) using the samples from the entire domain and the entire sampling period. The PDFs are shown in figure 4.9 at the various x^+ positions for all the MILD cases.

The PDFs of reaction rate in figures 4.9a, 4.9c and 4.9e show that a range of reaction rates exists in both RD and FD mixtures. However, the PDFs clearly show separation of the reaction rates favoured by RD and FD regions. It seems propagating flames are active at around $\omega_{c_T} = 0.5$ for Cases A1 and A2, and $\omega^+_{c_T} = 1.0$ for Case B1. Thus, flames in FD regions have the reaction rate similar to the one in MIFE. The PDF peak value grows sharply with x^+ distance, but its location moves to slightly smaller $\omega^+_{c_T}$, because the fuel is consumed at downstream regions. For RD regions, however, the PDF is more evenly distributed in a broad $\omega^+_{c_T}$, but $\omega^+_{c_T} \geq 1.5$ because of the condition, $\mathscr{B}^+ \leq -1.5$. The PDF peak value decreases with x^+ distance, but the range of $\omega^+_{c_T}$ having non-zero probability increases. This suggests the reaction dominated events involve a spectrum of reaction rates, depending of the local mixture composition, and this trend is strong at downstream regions.

The statistical behaviour of scalar gradient in RD/FD regions is shown in figures 4.9b, 4.9d and 4.9f. Although the separation of the PDF between the two regions is not as significant as the PDF of reaction rate, there seems to be some preferred scalar gradient values for each of RD and FD regions. The reason of less significant separation may be due to the local mixtures which have both FD and RD characteristics. The most probable scalar gradients in RD regions are generally smaller than that in FD regions, clearly supporting the above discussion on the relation between RD/FD regions and scalar gradient.

For Case A1 shown in figure 4.9b, the peak PDF of $|\nabla c_T|^+$ first decreases

in the upstream regions and then increases again in the down stream regions with x^+ distance. The location of transition from the decrease to increase is at $x^+ = 4.4$ for RD regions, and $x^+ = 3.2$ for FD regions. Similar behaviour is shown for Case B1, but not for Case A2, where the PDF peak value continues to decrease. The x^+-locations of such turn-around appearance correspond more or less to the locations where the peak of the PDF of $\mathscr{B}^+$ stops decreasing and starts increasing, as shown in figures 4.6a. Frequent reaction zone interactions, which keep the local scalar gradient from increasing as discussed in section 3.3, are also observed around these locations. Thus, RD scalar transport is not only caused by inhomogeneous mixture field due to initial incomplete premixing, but also by the reaction zone interactions during combustion. A similar trend is observed in the PDF of Case B1 shown in figure 4.9f.

To summarise this chapter, both RD and FD activities coexist in MILD combustion under the conditions considered in this work. Although these two kinds of activities are entangled in a complex way, scalar gradient behaviour is correlated with local RD or FD activities. In addition, frequent reaction zone interactions also affects these characteristics, creating small scalar dissipation and large reaction rate regions, which are governed by the unsteady and chemical source terms.

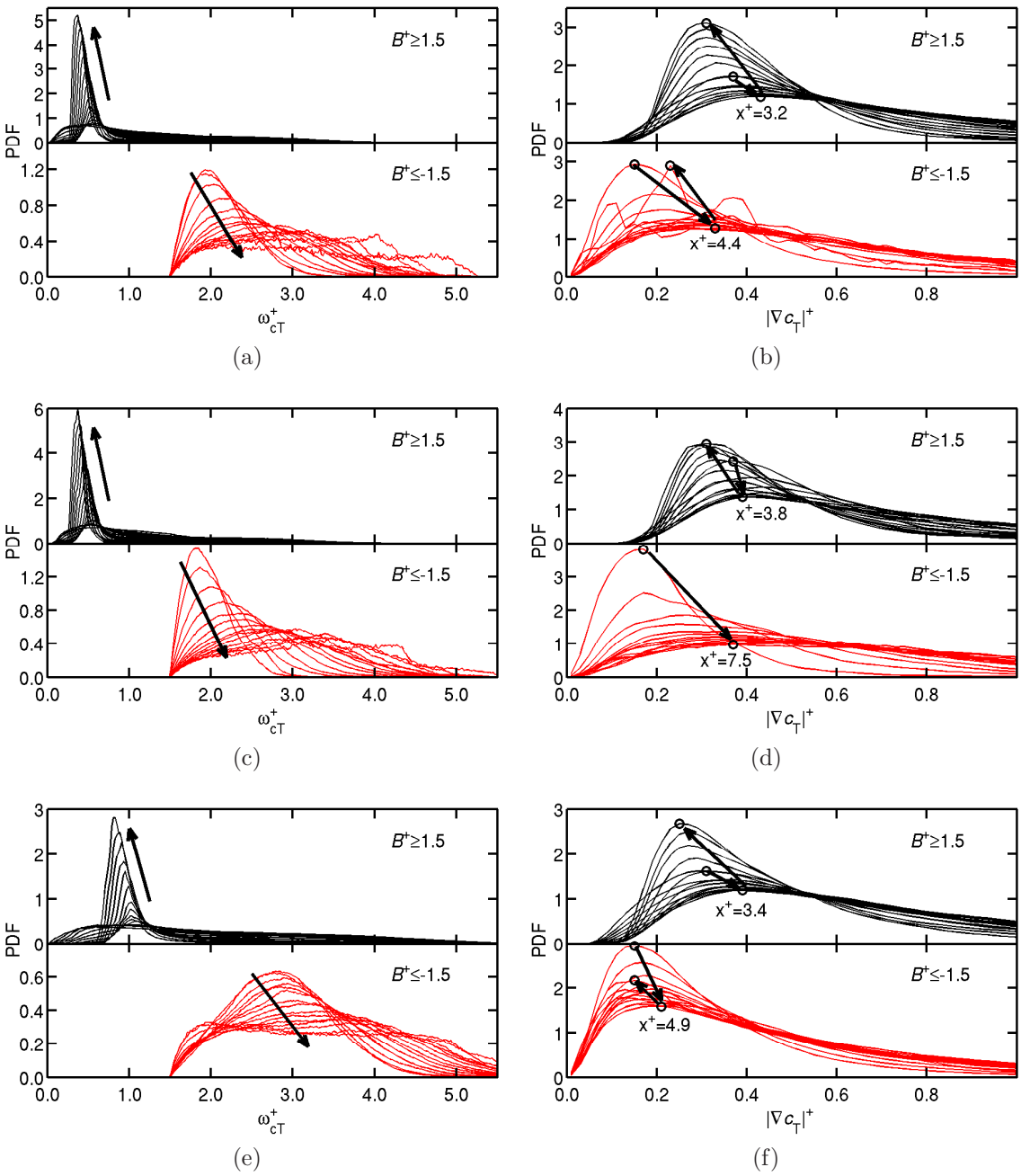

Figure 4.9: PDF of $|\nabla c_T|^+$ (a, c, e) and $\omega^+_{c_T}$ (b, d, f) at flame-propagation dominated regions ($\mathscr{B}^+ \geq 1.5$, black lines) and reaction dominated regions ($\mathscr{B}^+ \leq -1.5$, red lines) at the various x^+ positions used in figure 4.6 for Cases A1 (a, b), A2 (c, d) and B1 (e, f). Arrows show general transition of the PDF peak location with x^+, and circles in (b, d, f) are the PDF peaks at the nearest-inlet sampling location, the turn-around point, and the nearest-outlet sampling location. The PDFs are constracted using the all data sets.

Chapter 5

Scalar Gradients in MILD Reaction Zones

5.1 Background and objectives

In chapters 3 and 4, propagating, interacting, and autoigniting reaction zones are observed in MILD combustion. These phenomena in MILD combustion are found to be closely correlated with the local scalar gradient.

Strong scalar gradient due to the intense chemical activity within thin regions characterises flamelet-like combustion. The effect of such scalar gradient behaviour on the reaction rate is described through the scalar dissipation rate of a progress variable c in the context of Reynolds average (Bray, 1979). Thus, studying the relationship between the mean scalar dissipation rate and reaction rate would help to investigate flamelet or non-flamelet behaviour of MILD combustion.

Also in flamelet combustion, the flame normal component of the scalar gradient is statistically large compared to the tangential component when the reaction rate is intense. Hence, the relationship between the normal component of the scalar gradient and reaction rate in conventional turbulent premixed flame would be similar to that of the respective laminar flame solution locally. The characteristics of such relationship can be understood by investigating the PDF of the scalar gradient conditioned on the reaction rate, which is discussed in this

chapter.

The objective in this chapter is to investigate flamelet or non-flamelet behaviour of MILD combustion in a statistical sense using the above insights. First approach is to study the relation between the mean scalar dissipation rate and reaction rate by using conventional combustion modelling, which is discussed in the next section. The second approach is to use the PDF briefly mentioned above, and the results are discussed in section 5.3.

5.2 Relation between mean reaction rate and scalar dissipation rate

The Reynolds averaged equations are often solved in turbulent flow simulations. The mean reaction rate $\bar{\omega}_c^+$ and scalar dissipation rate $\tilde{N}_c^+$ variations based on c_T and c_Y are shown in figure 5.1 for all the cases. The results in figure 5.1a show typical mean variations for conventional premixed combustion. The variation of $\tilde{N}_{c_Y}^+$ is larger than $\tilde{N}_{c_T}^+$ by a factor of around 2, suggesting the effects of non-unity Lewis numbers and the use of complex chemistry, since c_Y would behave the same as c_T if unity Lewis number and a single step chemistry were used. However, the variations of $\tilde{N}_{c_Y}^+$ and $\tilde{N}_{c_T}^+$ look qualitatively similar one another.

The variations of $\bar{\omega}_c^+$ and $\tilde{N}_c^+$ for the MILD cases are different from the conventional premixed case. Both $\bar{\omega}_{c_T}^+$ (red-solid) and $\bar{\omega}_{c_Y}^+$ (red-dashed) are relatively large near the inlet boundary. This shows that the mixture reacts as soon as it enters the combustion domain with recovered exhaust gases, due to the elevated temperature and the presence of chemically active radicals. Apart from these large reaction rate near inlet boundary, the mean reaction rate peaks at $x^+ \sim 4$ for both $\bar{\omega}_{c_T}^+$ and $\bar{\omega}_{c_Y}^+$. However, in the downstream regions, $\bar{\omega}_{c_Y}^+$ decreases quickly to yield $\bar{\omega}_{c_Y}^+ \sim 0$ at the outlet boundary, while $\bar{\omega}_{c_T}^+$ decreases slowly. The mixture continues to generate heat even at downstream regions, due to the slow chemical reactions under MILD conditions.

The two mean scalar dissipation rates, $\tilde{N}_{c_T}^+$ (black-solid) and $\tilde{N}_{c_Y}^+$ (black-dashed) show a different trend to one another. Because of the partially premixed condition of the mixture field, $\tilde{N}_{c_Y}^+$ tends to be large near the inlet boundary. The

mean scalar dissipation rate of c_Y then continues to decreases with x^+-distance because of turbulent mixing, molecular diffusion and consumption of the species due to chemical reactions. For c_T, the scalar dissipation rate $\tilde{N}^+_{c_T}$ is not as large as $\tilde{N}^+_{c_Y}$ at the inlet boundary because of the condition of preheating using the recovered exhaust heat. The $\tilde{N}^+_{c_T}$ peaks at $x^+ \sim 4$ where reaction zones are highly convoluted. The non-zero values of $\tilde{N}^+_{c_T}$ at the outflow boundary are because of the limited size of domain and non-zero $\bar{\omega}^+_{c_T}$, and both $\tilde{N}^+_{c_T}$ and $\bar{\omega}^+_{c_T}$ would approach to zero if a larger computational domain was used. Although these mean variations give images of the Reynolds averaged fields of conventional premixed and MILD combustion, it is not yet clear if the MILD combustion considered in the present work is flamelet or non-flamelet like.

The Reynolds averaged reaction rate for a progress variable is written for $\mathrm{Da} \gg 1$ and $Ka \ll 1$ limit using the mean scalar dissipation rate N_c as (Bray, 1979):

$$\bar{\omega}_c = \frac{2\bar{\rho}}{2C_m - 1}\tilde{N}_c, \tag{5.1}$$

where the model parameter C_m is written as:

$$C_m = \frac{\int_0^1 c\,\omega_L(c)P(c)dc}{\int_0^1 \omega_L(c)P(c)dc}, \tag{5.2}$$

for turbulent premixed combustion having PDF of c, $P(c)$, and the reaction rate variation across the respective laminar flame solution $\omega_L(c)$. It has been reported that $0 \leq C_m \leq 1$ for various PDF shapes, and $C_m \sim 0.7$ is typical for combustion having bimodal distribution of a c field (Bray, 1979). A comparison of the parameter C_m calculated from equations 5.1 and 5.2 would be useful to study flamelet/non-flamelet behaviour in MILD combustion. For flamelet combustion, the parameters C_m from both equations would be similar one another and almost constant inside flame brush (Bray, 1979). Also, equation 5.2 reveals whether the respective laminar flame, MIFE, is fully representative for MILD combustion or not, and whether the c field is flamelet like, since the equation includes a laminar flame solution and a PDF of c.

Figure 5.2 shows variation of C_m with $\tilde{c}$. The parameter is calculated using equations 5.1 and 5.2 for c_T and c_Y. As clearly shown, the parameter C_m based

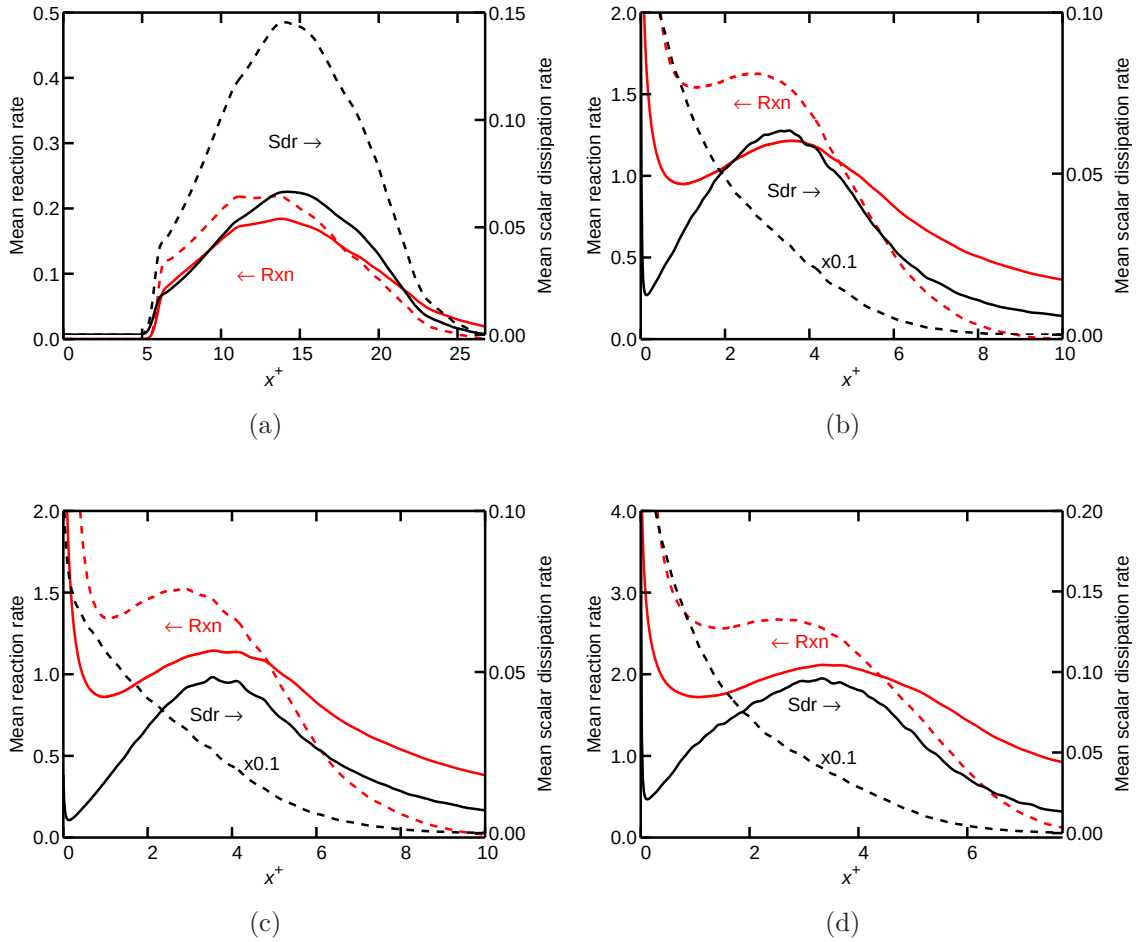

Figure 5.1: Reynolds average of normalised reaction rate (red lines) and scalar dissipation rate (black lines) for (a) Case C, (b) Case A1, (c) Case A2, and (d) Case B1. Solid lines: values based on c_T, and dashed lines: values based on c_Y. The scalar dissipation rate of c_Y for MILD cases are multiplied by a factor of 0.1 for visibility.

on c_Y is generally larger than that based on c_T, since $\tilde{N}_{c_T} < \tilde{N}_{c_Y}$ and $\bar{\omega}_{c_T} \sim \bar{\omega}_{c_T}$ in general for these cases. For the conventional premixed case, the parameter calculated using equation 5.1 shows a very large value at $\tilde{c} \leq 0.05$ due to the singularity in equation 5.1 for $\bar{\omega}_{c_T} \sim 0$. For $0.2 \leq \tilde{c} \leq 0.8$ which corresponds to inside the flame brush, the parameters C_m — obtained using both equations 5.1 and 5.2 — are almost constant and close one another. Thus, the conventional premixed case considered in this study is adequately modelled using the flamelet model in equation 5.1 as in previous studies (Swaminathan & Bray, 2005; Kolla *et al.*, 2009, 2010).

In MILD combustion, the behaviour of the parameter C_m is different from that observed for the conventional premixed case. The variation C_m for c_T obtained from equation 5.1 (solid line) shows a constant variation for all the MILD cases, while that for c_Y does not. Such behaviour of C_m for c_Y is because of large mean scalar dissipation rate near upstream regions as shown in figure 5.1, which is due to imperfect mixing of the mixture. Thus, the mean reaction rate ω_{c_Y} cannot be modelled for MILD combustion using this C_m value because equation 5.1 no longer holds for c_Y.

The parameters calculated based on equation 5.2 (symbols) do not seem consistent with the ones obtained from equation 5.1, unlike the conventional premixed case. Such behaviour of the parameter is because of the non-bimodal PDF (figure 3.2) and MIFE (figure 3.14) which is partly representative of the present MILD combustion cases. The parameter C_m for c_Y obtained using equation 5.2 also shows unsatisfactory results, although the PDF distribution of c_Y is relatively sharp as discussed in figure 3.3b. These results show the possibility that the flamelet approach is used for c_T for the present MILD cases, although an appropriate flamelet library needs to be developed to systematically determine C_m.

5.3 Conditional PDF of scalar gradient

In this section, the conditional PDF of scalar gradient is used to understand flamelet or non-flamelet behaviour of MILD reaction zones. After the construction method is explained, the PDF is discussed for the conventional premixed case.

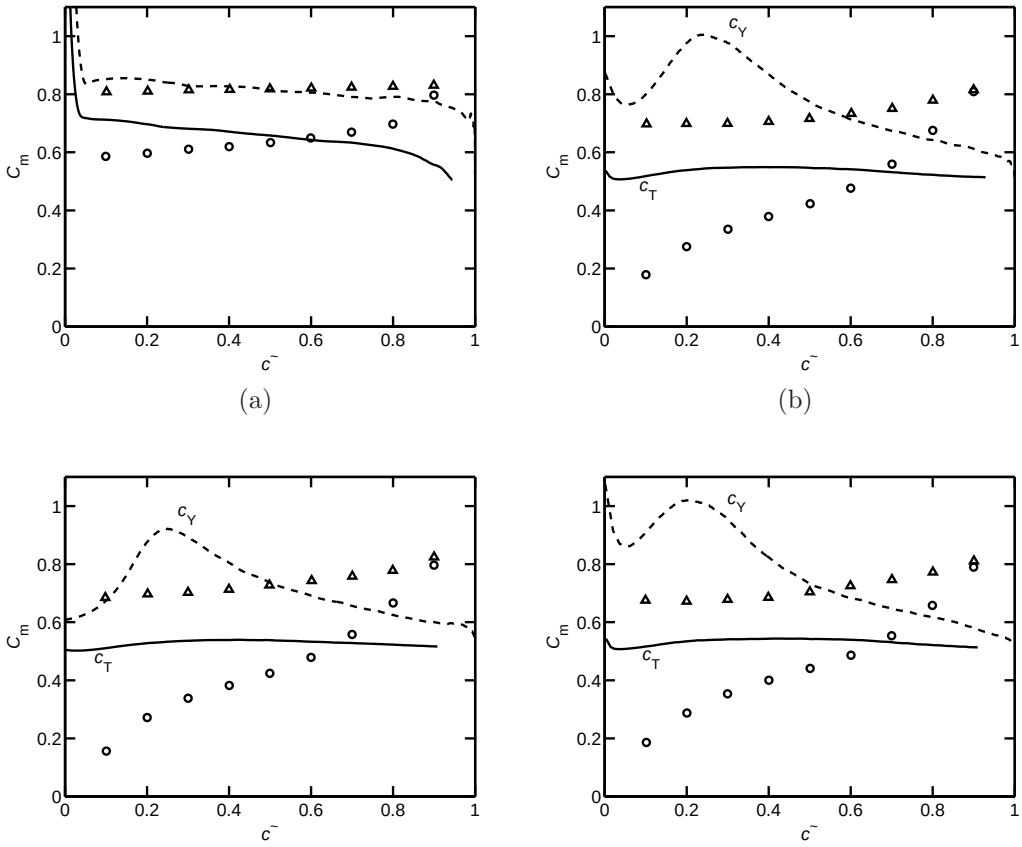

Figure 5.2: The model parameter C_m directly calculated from equations 5.1 (lines) and 5.2 (Symbol) for (a) Case C, (b) Case A1, (c) Case A2, and (d) Case B1. The parameter C_m is based on c_T (solid line and $\circ$), and c_Y (dashed line and $\triangle$).

The PDF is also directly compared with the respective laminar flame solution. The result for the conventional premixed case is used for comparative purposes in a discussion for the MILD cases. The method to construct the conditional PDF of scalar gradient based on the three-dimensional fields of the reaction rate and scalar gradient involves five steps given below.

1. The three-dimensional gradient of progress variable ∇c_T is computed using the same numerical scheme employed for the DNS.

2. The flame surface is identified using the local minimum value of $\nabla\omega_{c_T}^+$ subject to $\omega_{c_T}^+ \geq 0.5\omega_{c_T,\max}^+$, where $\omega_{c_T,\max}^+$ is the global maximum value of $\omega_{c_T}^+$. The identified surface is then expressed locally as $(f_x(s), f_y(s))$ for x-y, and $(f_x(s), f_z(s))$ for x-z planes, where s is a local coordinate along the surface.

3. The normal vectors, $\boldsymbol{n}_{1,xy}$ and $\boldsymbol{n}_{1,xz}$, of the surfaces are calculated in every 2D plane as $\boldsymbol{n}_{1,xy} = (-df_y/ds, df_x/ds)$ for x-y and $\boldsymbol{n}_{1,xz} = (-df_z/ds, df_x/ds)$ for x-z planes. Similar procedure is followed to obtain the tangential vectors, $\boldsymbol{n}_{2,xy}$ and $\boldsymbol{n}_{2,xz}$, in the corresponding planes.

4. The flame normal and one of its two tangential vectors at every point on the surface is then constructed using the respective 2D vectors obtained in the previous step. The second tangential vector is calculated using the vector cross product rule. The normal and tangential components of ∇c_T are then computed as $\nabla c_T \cdot \boldsymbol{n_i}$, where $i = 1$, 2 and 3 denote respectively the normal and two tangential directions.

5. The samples for constructing PDF are collected in the normal and tangential directions over a length of $2\delta_{th}$ on either side of the point of interest. These samples obtained from the entire computational domain are used to construct joint, $P(\psi_i^+, \omega_{c_T}^+)$, and marginal, $P(\omega_{c_T}^+)$, PDFs, where the symbol ψ_i^+ denotes $\ln(|\nabla^+ c_T \cdot \boldsymbol{n}_i|)$. The conditional PDF is then obtained using the Bayes theorem: $P(\psi_i^+|\omega_{c_T}^+) = P(\psi_i^+, \omega_{c_T}^+)/P(\omega_{c_T}^+)$.

The above procedure identifies the locations of local maximum reaction rate as the reaction zone surfaces. Thus, any subjectivity, which arises when a particular

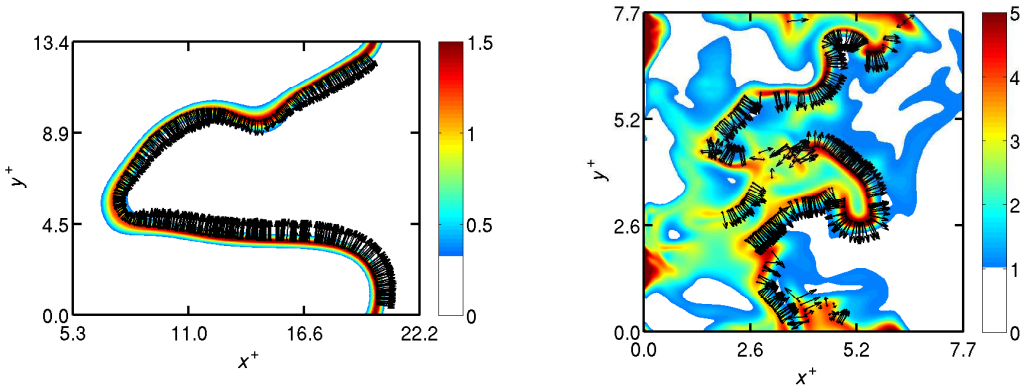

(a) (b)

Figure 5.3: Typical reaction rate variation (colour), and reaction zone normal vectors computed as in Steps (2–4) for (a) the conventional premixed case and (b) Case B1.

threshold value is used, can be generally avoided. Also, this method helps to avoid effects of multiply connected surfaces, which would also result if a threshold is used, especially in the MILD cases (see figure 3.9). Typical normal vectors $\boldsymbol{n}_1$ are shown in figure 5.3 for Cases B1 and C. Note the vectors point the out-of-plane directions in general which makes some of these vectors look shorter than unity. As shown in the figure, the vectors are calculated at local maximum reaction rate locations, and multiply connected surfaces do not seem to affect the normal directions in the MILD case using this method. The normal vectors computed using a threshold value are also shown for a comparison in figure 5.4, where two typical threshold values are tested. As clearly shown, the choice of threshold value has a significant effect on the reaction zone surface and its normal directions. Also, the multiply connected surfaces alter the normal directions of the surfaces if threshold is used.

Figure 5.5 shows the conditional PDF constructed using the above steps. Contours of the PDF are shown for the normal (ψ_1, thick black line) and one of the tangential components (ψ_2, thin-dashed lines), since the behaviour of $P(\psi_3|\omega_{c_T}^+)$ is similar $P(\psi_2|\omega_{c_T}^+)$. The variation of $(\psi, \omega_{c_T}^+)$ obtained from the respective laminar flame is also shown in the figure for a comparison (grey line).

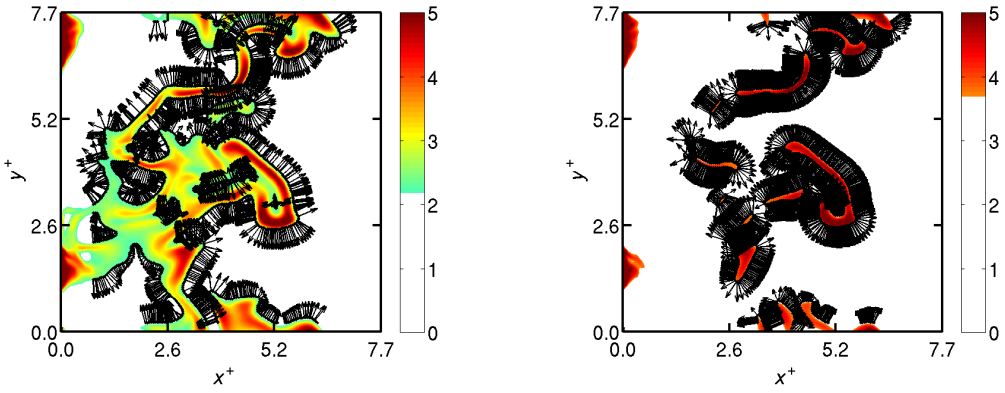

(a) (b)

Figure 5.4: Typical reaction rate variation (colour), and reaction zone normal vectors computed by using a threshold, instead of using a local minimum $\nabla\omega^+_{c_T}$ location as in Steps (2–4). The threshold is (a) 30%, and (b) 50% of the global maximum reaction rate $\omega^+_{c_T,\max}$. Note that only half of computed vectors are shown for visibility in (a).

First, the conventional premixed case shown in figure 5.5a is discussed. The most probable normal component of the scalar gradient ψ^+_1 is larger than that of the tangential component in general. Such behaviour of the normal and tangential components is typical for flamelet combustion. The normal component PDF shows that the scalar gradient increases with the reaction rate, which is well described by equations 3.7 and 5.1. In contrast, the large $P(\psi_2|\omega^+_{c_T})$ exists at very small ψ_2 irrespective of $\omega^+_{c_T}$. The most probable normal gradient of the conventional premixed case closely agrees with the respective laminar flame solution denoted by a grey line. The two branches seen for the conditional PDF (also for the laminar flame solution) for $\omega^+_{c_T} \leq 1$ are due to the typical variation of ∇c_T and ω_{cT} in c_T space. The upper branch (larger gradient with small reaction rate) corresponds to the flame front thermal region. These results are consistent with the expected behaviour for conventional premixed combustion.

The behaviour of the normal gradient component in the MILD cases is quite different from that for the conventional premixed case as shown in figures 5.5b–5.5d. The PDF of the normal component is more distributed than in the con-

ventional premixed case, and suggests that MILD combustion does not have a strong trend of scalar gradient behaviour. Such broad distribution of the PDF results from the reaction zone interactions and reaction-dominated scalar transport discussed in sections 3.3 and 4.2. However, despite the broad distribution of the normal component PDF, the scalar normal gradient tends to increase with an increase of the reaction rate. Such behaviour seems flamelet like, and is due to the presence of thin reaction zones observed locally in figure 3.9. Similar partial flamelet characteristics are also observed in figure 5.2 for MILD cases.

A comparison of the normal and tangential components in the MILD cases shows that the PDF of the tangential component is as broad as that of the normal component. For small reaction rate, the PDFs of the normal and tangential components are almost identical. The PDF contours of the tangential component start to deviate from the normal component at $\omega_{c_T}^+ \sim 0.05$ for Case C, $\omega_{c_T}^+ \sim 1$ for Cases A1 and A2, and $\omega_{c_T}^+ \sim 2$ for Case B1, due to the heat release effect. In intense reaction rate regions, the normal component is generally larger than the tangential component of scalar gradient, which is interpreted as flamelet characteristics. However, by comparing the $P(\psi_1|\omega_{c_T}^+) = 0.3$ and $P(\psi_2|\omega_{c_T}^+) = 0.3$ contours, the difference of the normal and tangential components seems to be smaller in the MILD cases than in the conventional premixed case. Such behaviour suggests that the scalar gradient behaviour in MILD combustion is less directional compared to conventional premixed combustion. Thus, the MILD combustion cases considered in the present work has flamelet characteristics, but the tendency is relatively weak.

In figure 5.6, the marginal PDF of ψ_i^+ is extracted from the conditional PDF at $\omega_{c_T}^+ = \omega_1$ and ω_2 to study the scalar gradient behaviour in detail. Here, ω_1 is $0.1\omega_2$ and ω_2 is a half of $\omega_{c_T,\max}^+$. For the high reaction rate region $\omega_{cT}^+ = \omega_2$, the PDF shows that the locations of the PDF peaks differ between the normal (thick lines) and tangential (thin lines) components by 2.4 for Case C, 1.2 for Case A1, 1.3 for Case A2, and 0.8 for Case B1. The difference is largest for the conventional premixed case as shown earlier. Amongst the MILD cases, the difference is largest in Case A2 (largest Da) and smallest in Case B1 (smallest Da). This implies that the difference between the normal and tangential gradients diminishes progressively as Da decreases or the dilution level increases. For

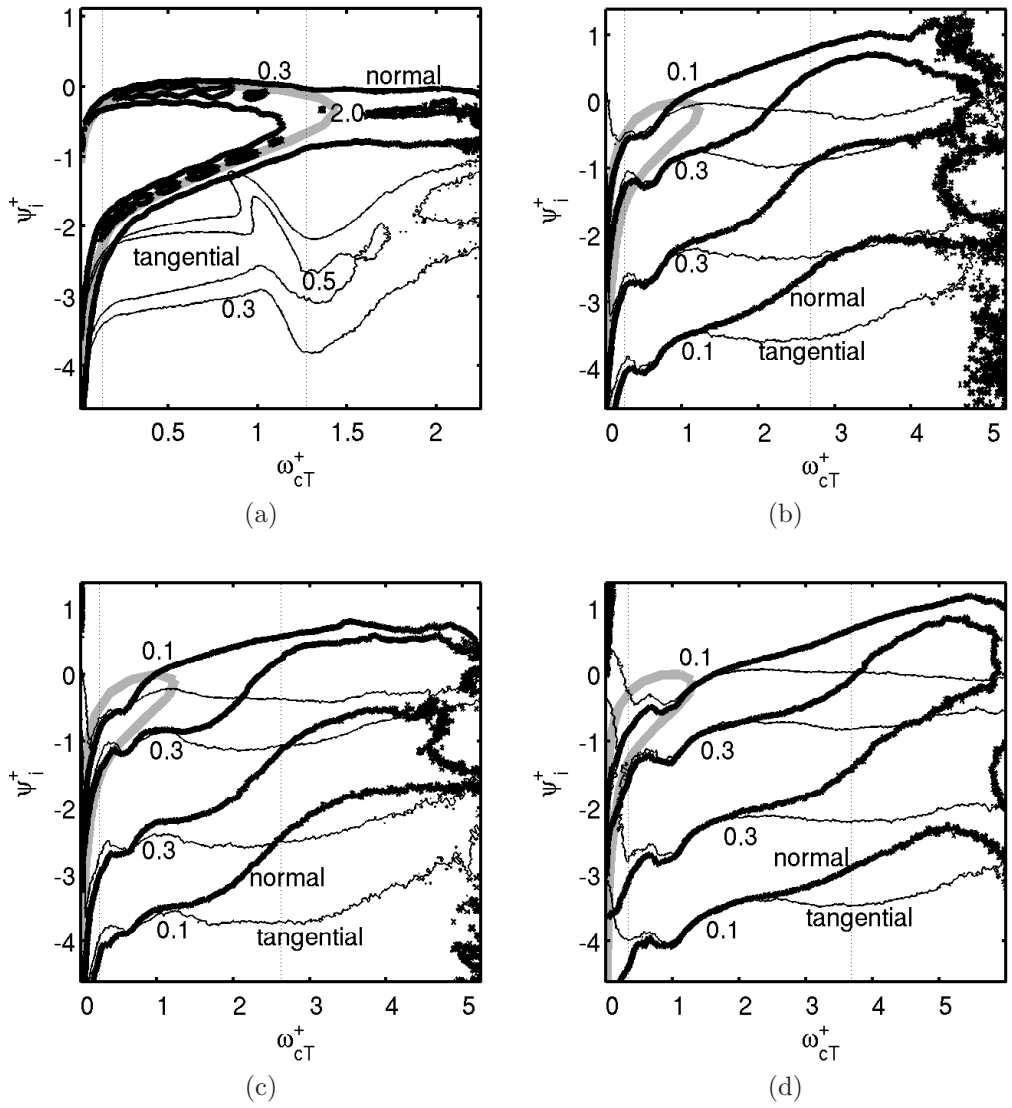

Figure 5.5: Conditional PDF of ψ_1 (thick lines) and ψ_2 (thin lines) conditioned on normalised reaction rate $\omega_{c_T}^+$ for (a) Case C, (b) Case A1, (c) Case A2, and (d) Case B1. The grey line is the respective laminar flame solutions of MIFEs A and B (for Cases A1–B1) and Flame C (for Case C).

low reaction rate $\omega_{cT}^{+} = \omega_1$, the difference in the PDFs between the normal and tangential components is negligible because of the small heat release rate. Therefore, the scalar gradient behaviour is less flamelet like when the dilution level and turbulence level are high, although there is still a direct relation between scalar gradient and reaction rate.

5.4 Chemical Markers for MILD Reaction Zones

Although this chapter explains chemical markers which is not the prime objective of the present work, it is included here as a main content of the thesis, since it can be used to extend the PDF described in the previous section. The OH PLIF measurements have been performed for MILD combustion (Plessing *et al.*, 1998; Özdemir & Peters, 2001; Medwell, 2007; Duwig *et al.*, 2012) to study MILD reaction zones because OH LIF signal S_{OH} appears in the burnt regions and it has a good signal-to-noise ratio. However, identifying reaction zones using iso-contours of S_{OH} might be subjective as the choice of a threshold value affects the shape of distributed reaction zones. Non-uniformity of the MILD mixture field also affects the shape of reaction zones identified using this method. For these reasons, observations of MILD reaction zones relying on S_{OH} show only part of their behaviour.

Many previous studies on turbulent premixed flames used a LIF signal of particular species, such as CH and CHO, and the products of LIF signals of two species such as $S_{\mathrm{OH}} \times S_{\mathrm{CH_2O}}$, to identify heat releasing regions (Nguyen & Paul, 1996; Paul & Najm, 1998; Balachandran *et al.*, 2005; Fayoux *et al.*, 2005; Tanahashi *et al.*, 2005, 2008; Kiefer *et al.*, 2009; Richter *et al.*, 2005; Li *et al.*, 2010; Röder *et al.*, 2013). The choice of these scalars are fuel mixture specific (Paul & Najm, 1998; Najm *et al.*, 1998b,a), and they have been tested and used for stoichiometric and lean premixed methane-air flames previously. The chemical marker CH has reasonable correlation with heat release only for undiluted reactant mixture with equivalence ratio of around 0.8-1.2 (Kiefer *et al.*, 2009). Thus, this marker may not be a suitable choice for the MILD combustion. The signal-to-noise ratio for CHO LIF signal is generally low compared to OH and formaldehyde (Paul & Najm, 1998), although Kiefer *et al.* (2009) measured

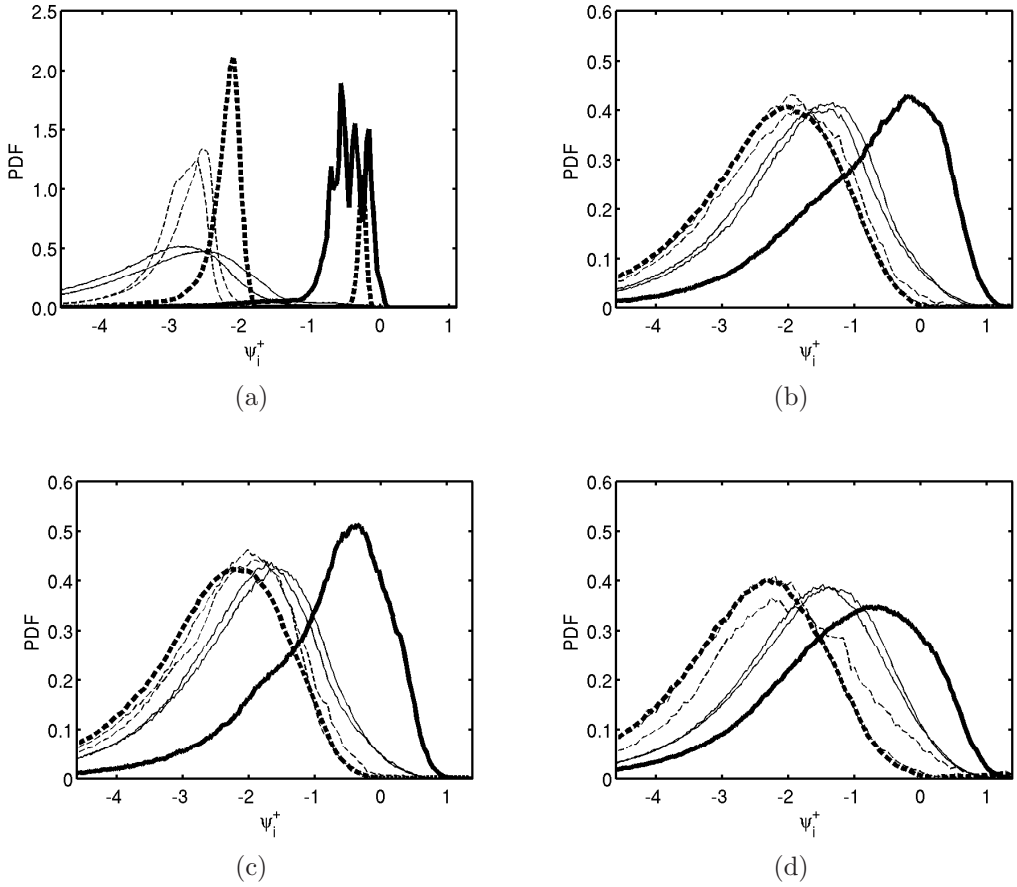

Figure 5.6: PDF of ψ_1 (thick lines), and ψ_2 and ψ_3 (thin lines) for (a) Case C, (b) Case A1, (c) Case A2 and (d) Case B1. The PDF is at $\omega_{c_T}^+ = \omega_1$ (dashed lines) and $\omega_{c_T}^+ = \omega_2$ (solid lines), where ω_1 is $0.1\omega_2$ and ω_2 is a half of global maximum $\omega_{c_T}^+$ in the entire domain except the upstream boundary. The PDF is extracted from figure 5.5, and these two $\omega_{c_T}^+$ values are indicated using dotted lines in figure 5.5.

CHO LIF images with a sufficient signal-to-noise ratio using multimode lasers .

The PLIF measurements of OH and CH_2O have been conducted for MILD combustion in past studies (Duwig *et al.*, 2012; Medwell, 2007) with decent signal-to-ratio. However, thorough and direct investigation into the applicability of these chemical markers to estimate heat release rate has not been carried out for MILD combustion, and effects of dilution and mixture non-uniformity on this ability are not yet clear. Thus, it is useful to test whether the above chemical markers to identify heat releasing zones work for the MILD combustion. This is the prime motive in this section. The representative LIF signals of the markers, OH, CH_2O and CHO, are deduced using the DNS data of turbulent MILD combustion first. These signals are then used to evaluate the adequacy of these chemical markers by comparing with the heat releasing regions from the DNS data. The second objective is to develop an alternative method to construct a conditional PDF similar to the one obtained in section 5.3, using only experimentally available quantities. The developed method is used to obtain the PDF using the deduced LIF signals and discussed for scalar gradient analysis from an experimental view point.

5.4.1 Measurable species for MILD reaction zones

In order to study the adequacy of the conventional chemical markers numerically, LIF signals, S_{CH_2O}, S_{OH}, and S_{CHO}, have to be deduced from the DNS results. The LIF signal is generally related to the local molar concentration of a particular species and local temperature. The relation of the LIF signal, the molar concentration and temperature can be expressed as:

$$S_{CH_2O} \propto [CH_2O]T^{1-\beta}, \;\; 2.2 \leq \beta \leq 3.0, \tag{5.3}$$

$$S_{OH} \propto [OH]T^{1-\beta}, \;\; -2.0 \leq \beta \leq 1.0, \tag{5.4}$$

$$S_{CHO} \propto [CHO]T^{1-\beta}, \;\; 1.0 \leq \beta \leq 1.5, \tag{5.5}$$

for a temperature range of $1000 \leq T \leq 1800$ K when Boltzmann equilibrium is considered (Paul & Najm, 1998; Najm *et al.*, 1998b; Puri *et al.*, 1992; Cessou & Stepowski, 1996; Schiessl *et al.*, 2004). Here, the square brackets denote molar

concentration of species, and the parameter β can be adjusted by the selection of particular transition used for the measurement. For the present study, the parameter β is set to be 2.6 for CH_2O, zero for OH and 1.25 for CHO signals (Paul & Najm, 1998; Najm *et al.*, 1998b). It is also verified that the choice of β does not change the conclusions of the present work, by eliminating the temperature dependence in equations 5.3–5.5 by setting $\beta = 1$.

Figure 5.7 shows variations of the actual $\omega^*_{c_T}$ and estimated reaction rates across the laminar flames, Flame C, MIFEs A and B, discussed in figure 2.3. The estimated reaction rates are obtained as $\omega^*_{e1} = (S_{\rm OH} \times S_{\rm CH_2O})^*$ and $\omega^*_{e2} = S^*_{\rm CHO}$, where the superscript "*" denotes a normalisation using a global maximum value. The peak locations of the actual $\omega^*_{c_T}$ and estimated $\omega^*_{e1,e2}$ reaction rates are almost identical with a small difference of about $0.06\delta_{th}$ for MIFEs, and about $0.11\delta_{th}$ for the conventional premixed laminar flame. However, the variation of the actual reaction rate across the flame is reproduced only approximately by the estimates, as reported in Fayoux *et al.* (2005). Especially, the non-zero reaction rate on the burnt side is captured by neither of the estimates since both CH_2O and CHO are consumed quickly in the reaction zone. Similar trend of estimates is observed for Perfectly Stirred Reactor (PSR) A explained in section 6.2 in figure 5.7d. Thus, as reported in the previous study for conventional premixed flames (Fayoux *et al.*, 2005), these estimated reaction rate $\omega^*_{e1,e2}$ can identify location of the peak reaction rate for both conventional premixed and MILD combustion in the laminar flames, and this holds for PSR-type phenomena.

Effects of non-uniform mixture (section 2.5) and interacting reaction zones (section 3.3) on estimates $\omega^*_{e1,e2}$ need to be verified. The actual and estimated reaction rate fields, $\omega^*_{c_T}$, ω^*_{e1} and ω^*_{e2}, in the mid x-y plane are respectively shown in figures 5.8(a–c), (d–f) and (g–i). Although similar variations of $\omega^+_{c_T}$ are already shown in section 3.2, $\omega^*_{c_T}$ is shown here for comparative purposes since the normalisation is now different. The estimated reaction rate fields show a reasonable agreement with the actual field for both the conventional premixed and MILD cases, although it is not surprising to see good agreement for the conventional premixed case. Many features of the MILD reaction zones observed in the $\omega^*_{c_T}$ field explained in section 3.2 are reproduced reasonably well by ω^*_{e1} and ω^*_{e2}. There are also some differences observed: for example, the shapes of isolated

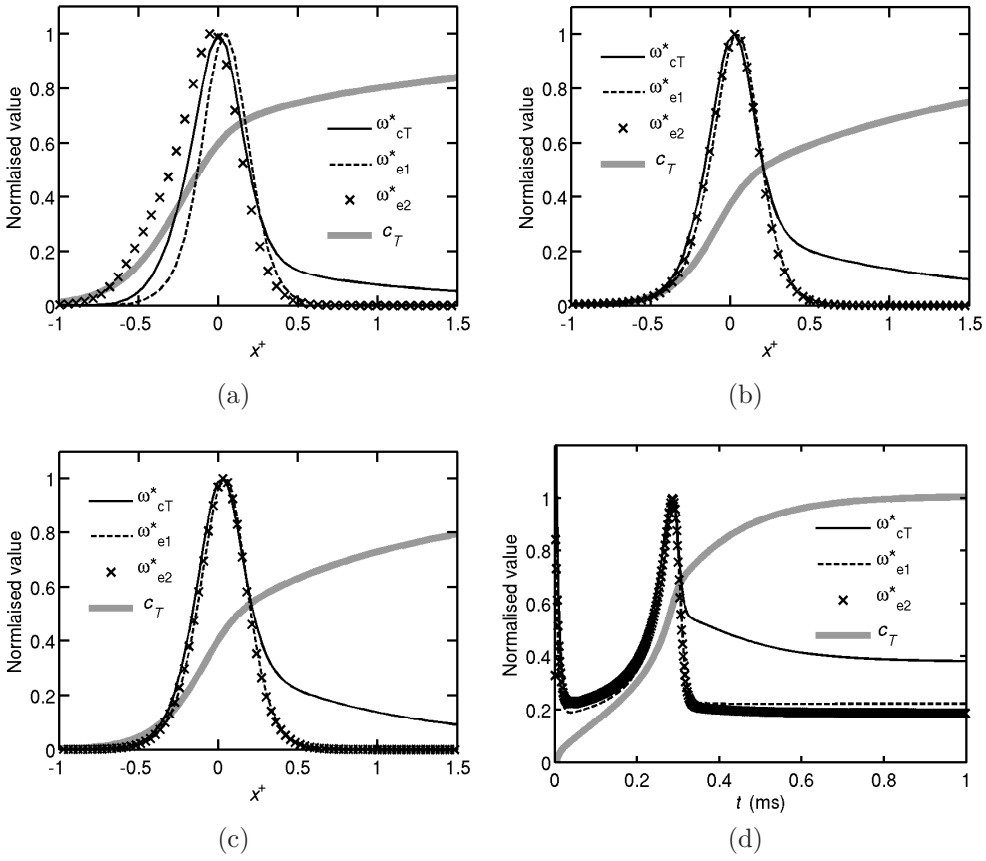

Figure 5.7: Variations of the actual ($\omega^*_{c_T}$: thin black line), and estimated (ω^*_{e1}: dashed line and ω^*_{e2}: $\times$) reaction rates, and c_T (thick grey line) for the respective laminar flames for (a) Case C, (b) Cases A1 and A2, and (c) for Case B1. Similar variations for Perfectly Stirred Reactor (PSR) A proposed in section 6.2 are also shown. The location, $x^+ = 0$, corresponds to the location of peak $\omega^*_{c_T}$, and $x^+ \leq 0$ and $x^+ \geq 0$ correspond to unburnt and burnt sides respectively.

pockets of estimated reaction zones for the Case B1 (figures 5.8f and 5.8i) are not similar to the one in the actual reaction rate field. However, the location of the local maximum reaction rate seems to be well represented by these estimates.

Figure 5.9 shows variations of instantaneous ω^*_{e1} and ω^*_{e2} with $\omega^*_{c_T}$ as a scatter plot for Case B1. The samples are obtained from the mid x-y plane shown in figure 5.8, and this variation is found to be typical for other MILD and conventional premixed cases. The correlation between the actual and estimated values is relatively low for small $\omega^*_{c_T}$ with two distinct branches as shown in figure 5.9. Such trends of $\omega^*_{e1,e2}$ in low reaction rate regions have been already observed in figure 5.7c. However, the agreement of the actual and estimated values is good for high reaction rate ($\omega^*_{c_T} \geq 0.3$). Thus, the estimation of reaction zones using the chemical markers $S_{\mathrm{OH}} \times S_{\mathrm{CH_2O}}$ and S_{CHO} is reasonable for the MILD combustion as well as the conventional premixed combustion.

5.4.2 Measurable species for progress variable and its gradient

The contours of reaction progress variable based on temperature c_T are compared to those estimated using OH LIF signals S^*_{OH}. The estimated progress variable c_{PLIF} is calculated as $c_{\mathrm{PLIF}} = S^*_{\mathrm{OH}}$, where S^*_{OH} varies from zero to unity. The typical results are shown in figure 5.10 for the Cases C and B1. The c_T contours are shown as solid lines while the contours of the estimated progress variable field c_{PLIF} are shown as dashed lines. As one would expect, the c_{PLIF} field reproduces the characteristics of c_T well for the conventional premixed case, except for a small offset. The scatter plot of instantaneous c_T and c_{PLIF} shown in figure 5.11a also suggests that c_T can be reconstructed in most of the domain once local c_{PLIF} is known, since the relationship between instantaneous c_T and c_{PLIF} is monotonic except for $c_{\mathrm{PLIF}} \geq 0.85$. This further confirms that the statistics of c_T and c_{PLIF} is similar to one another for the conventional premixed case.

A typical comparison of c_T and c_{PLIF} shown for a MILD case, Case B, in figures 5.10d–5.10f shows the correlation is not as good as for the conventional premixed case in general. However, a reasonable agreement is observed for $c_T = 0.6$ and $c_{\mathrm{PLIF}} = 0.6$ contours, where the heat release peaks in the respective

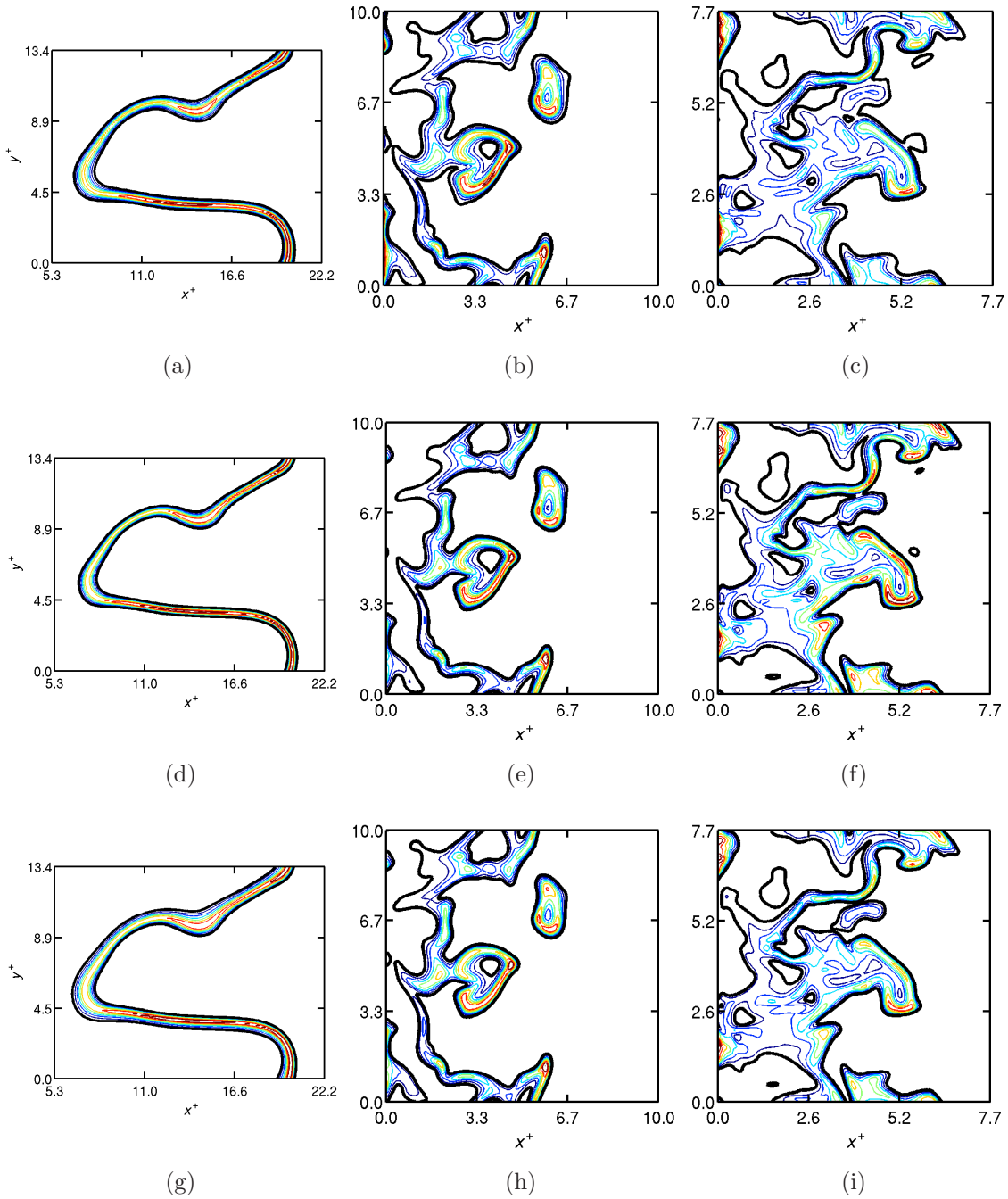

Figure 5.8: Contours of $\omega^*_{c_T}$ (a–c), ω^*_{e1} (d–f), and ω^*_{e2} (g–i) in the mid x-y plane for Case A1 (a, d, g), Case B1 (b, e, h) and Case C (c, f, i). Thick black line:0.2, and thin lines: $0.3, 0.4, \cdots, 0.9$.

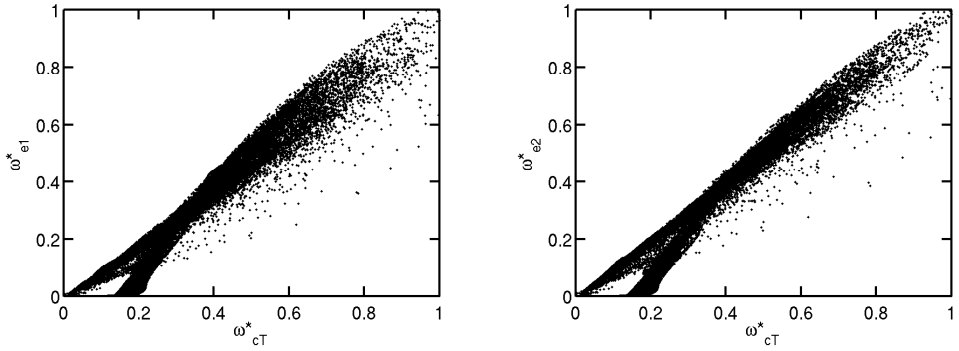

(a) (b)

Figure 5.9: Typical variations of instantaneous (a) ω^*_{e1} and (b) ω^*_{e2} with $\omega^*_{c_T}$ for Case B1. One fourth of all the samples from the same x-y slice as in figure. 5.8 are shown.

canonical laminar flame. For other locations shown in figures 5.10d and 5.10f, there is a close match observed locally between c_T and c_{PLIF} in several locations. The scatter plot in figure 5.11b shows that c_{PLIF} increases with c_T in general. However, the broad distribution of the c_T-c_{PLIF} scatter indicates that S_{OH} is not suitable for the estimation of instantaneous c_T field for MILD combustion.

A close study of figure 5.10 suggests that the c_T and c_{PLIF} contours are almost parallel to one another in predominant regions for the MILD combustion case. Thus, a contour of a particular c_T value can be represented well by a contour of a different c_{PLIF} value. This parallelism suggests that their gradient vectors point in the same direction, which is verified by calculating the PDF of the inner product of the gradient unit vectors based on c_T and c_{PLIF} conditioned on $\omega^*_{c_T}$. These unit vectors are defined as $\boldsymbol{n}_{c_T} = \nabla c_T/|\nabla c_T|$ and $\boldsymbol{n}_{\mathrm{OH}} = \nabla c_{\mathrm{PLIF}}/|\nabla c_{\mathrm{PLIF}}|$. A typical PDF of the inner product conditioned on the reaction rate $\omega^*_{c_T}$, calculated as $P(|\boldsymbol{n}_{\mathrm{OH}}\cdot\boldsymbol{n}_{c_T}||\omega_{c_T}) = P(|\boldsymbol{n}_{\mathrm{OH}}\cdot\boldsymbol{n}_{c_T}|,\omega_{c_T})/P(\omega_{c_T})$, is shown in figure 5.12 for the MILD (Case B1) and conventional premixed cases. The conditional PDF shown for the conventional premixed case peaks near $|\boldsymbol{n}_{c_T}\cdot\boldsymbol{n}_{\mathrm{OH}}| = 1$ as one would expect from the close correlation of c_T and c_{PLIF} shown in figure 5.11. The PDF for Case B1 shown in figure 5.12b is typical for the other MILD combustion cases studied here. The PDF shown for the MILD case also suggests a good alignment

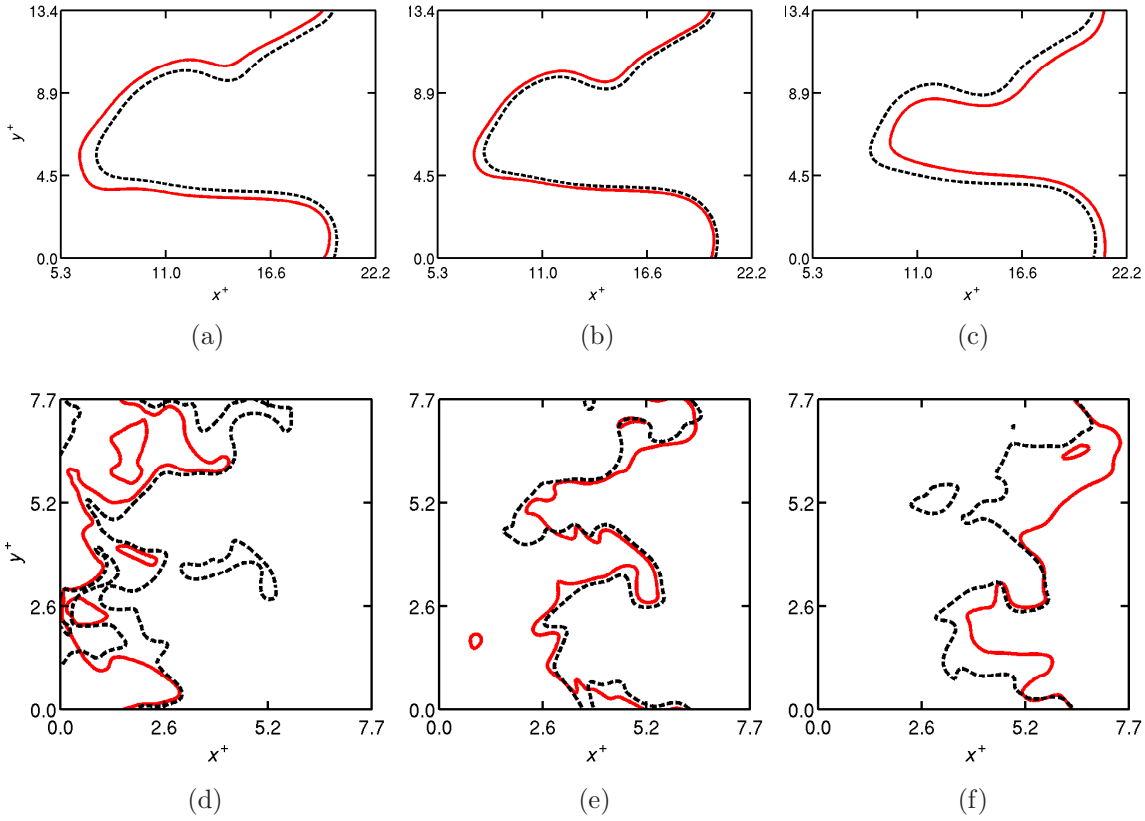

Figure 5.10: Contours of c_T (solid-red line) and c_{PLIF} (dashed line) for Case C (a–c) and Case B1 (d–f) in the same x-y plane as in Fig. 5.8. The contour level is 0.2 (a, d), 0.6 (b, e) and 0.8 (c, f).

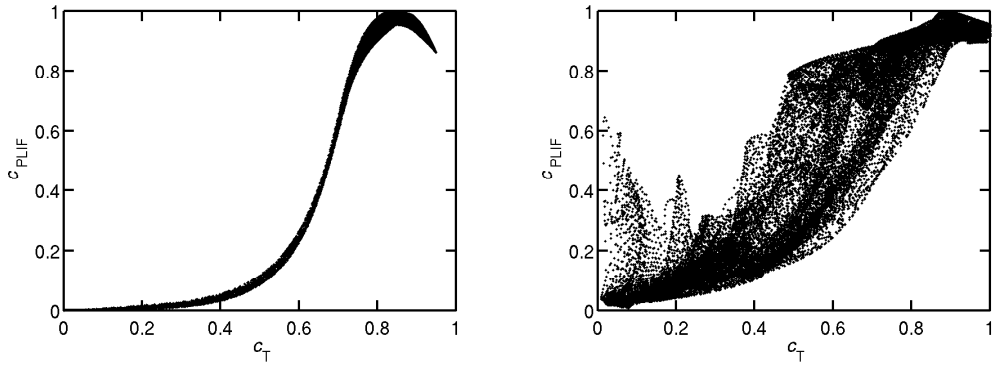

Figure 5.11: Scatter plot of the instantaneous c_T and c_{PLIF} for (a) Case C and (b) Case B1. One fourth of all the samples in the same x-y slice as in figure. 5.10.

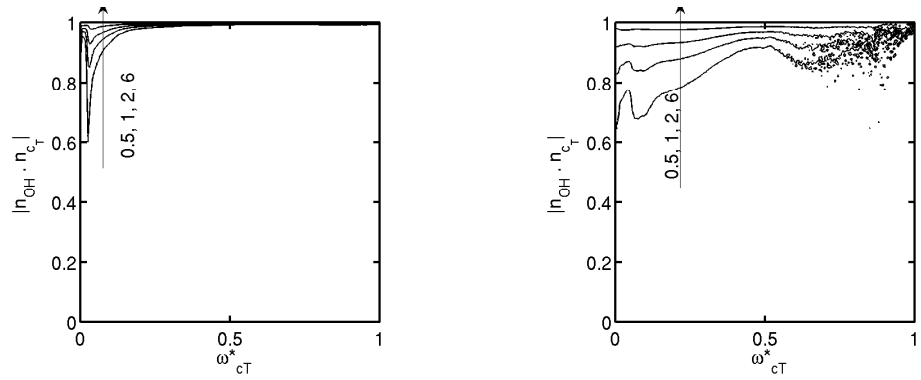

(a) (b)

Figure 5.12: Contours of the conditional PDF of the inner product, $P(|\boldsymbol{n}_{c_T} \cdot \boldsymbol{n}_{\mathrm{OH}}||\omega^*_{c_T})$ for (a) Case C and (b) Case B1. The PDF is constructed using samples from the entire domain and sampling period for each case.

between $\boldsymbol{n}_{c_T}$ and $\boldsymbol{n}_{\mathrm{OH}}$, especially at locations with high heat release rate. The PDF broadens slightly for small $\omega^*_{c_T}$ values, which come predominantly from unburnt and burnt regions of the flame front, as shown in figure 5.7c. Therefore, the orientation of the c_T gradient can be estimated adequately using variation of S^*_{OH} gradient.

5.4.3 Conditional PDF of estimated scalar gradient

The aim in this section is to explain and validate an alternative method to construct a conditional PDF of scalar gradient such that shown in section 5.3, using only two-dimensional measurable fields. In order to construct such a PDF, (1) scalar gradient field is required, and (2) local peak locations of reaction rate have to be accurately identified to calculate normal and tangential vectors. As explained in the previous section, local peak of reaction rate field is well identified using $S_{\mathrm{OH}} \times S_{\mathrm{CH_2O}}$ or S_{CHO}, although its variation, especially in the burnt side, is generally underestimated. The progress variable field cannot be reconstructed using S_{OH} for MILD combustion, but the direction of its gradient is fairly well correlated with ∇S_{OH}. Also, simultaneous PLIF measurements of OH and CH_2O, or OH and CHO are generally possible. Thus, the conditional PDF can be constructed using LIF signals — S_{OH} and $S_{\mathrm{CH_2O}}$, or S_{OH} and S_{CHO} — by employing

standard laser diagnostics such as a simultaneous two-dimensional PLIF of two species. Although the two-dimensionality affects gradient information, the effect is only a factor of $4/\pi = 1.27$ (Hawkes *et al.*, 2011; Chakraborty *et al.*, 2013), which is likely to be negligible when the gradient is plotted in the logarithm scale as in figure 5.5.

First, in order to verify above discussion, the conditional PDF, $P(\psi_i^+|\omega^*)$, is constructed using three-dimensional LIF signals, S_{OH}, $S_{\mathrm{CH_2O}}$ and S_{CHO}, deduced from DNS results. The LIF signals are computed to obtain the 3D estimated reaction rate field, ω_{e1}^* or ω_{e2}^*, and scalar gradient field $\nabla c_{\mathrm{PLIF}}^+$. The estimated fields are then used in the steps described in section 5.3. The estimated conditional PDF based on 3D fields is shown in figure 5.13. The respective laminar flame solution, obtained and normalised in the same manner, is also superimposed onto the constructed PDF. For comparison, the PDFs obtained using actual fields, $\omega_{c_T}^*$ and ∇c_T, are also shown in figures 5.14a–5.14c. These PDFs are basically the same as in figure 5.5, but the normalisation for the reaction rate is different. The PDFs shown in figures 5.14d–5.14f are constructed based on ω_{e1}^* and ∇c_{PLIF}, and figures 5.14g–5.14i are based on ω_{e2}^* and ∇c_{PLIF}. The two branches, clearly appearing in both PDF and laminar flame solution of the conventional premixed case, become less obvious with an increase of dilution level in the MILD cases. For the conventional premixed case, the high probability density regions in the estimated PDF are well followed by the laminar flame solution on a par with the PDF based on the actual fields. In contrast, the estimated PDF for the MILD cases shows broad distribution and agreement between the PDF and laminar flame solution is much less than that shown in the conventional premixed case. Thus, the characteristics of $\omega_{c_T}^*$-∇c_T relation observed in the actual PDF is reproduced reasonably well in the estimated PDF based on three-dimensional fields.

Similar PDFs are constructed using two-dimensional actual and estimated fields, and shown in figure 5.14. Such estimated PDF based on 2D species fields can be obtained through standard laser measurements. The steps described in section 5.3 are repeated to obtain the conditional PDF from 2D subsets of the 3D data. The only difference is in the steps 3 and 4 for the normal and tangential vector calculation. These vectors are obtained simply as $\boldsymbol{n}_1 = (-df_y/ds, df_x/ds)$

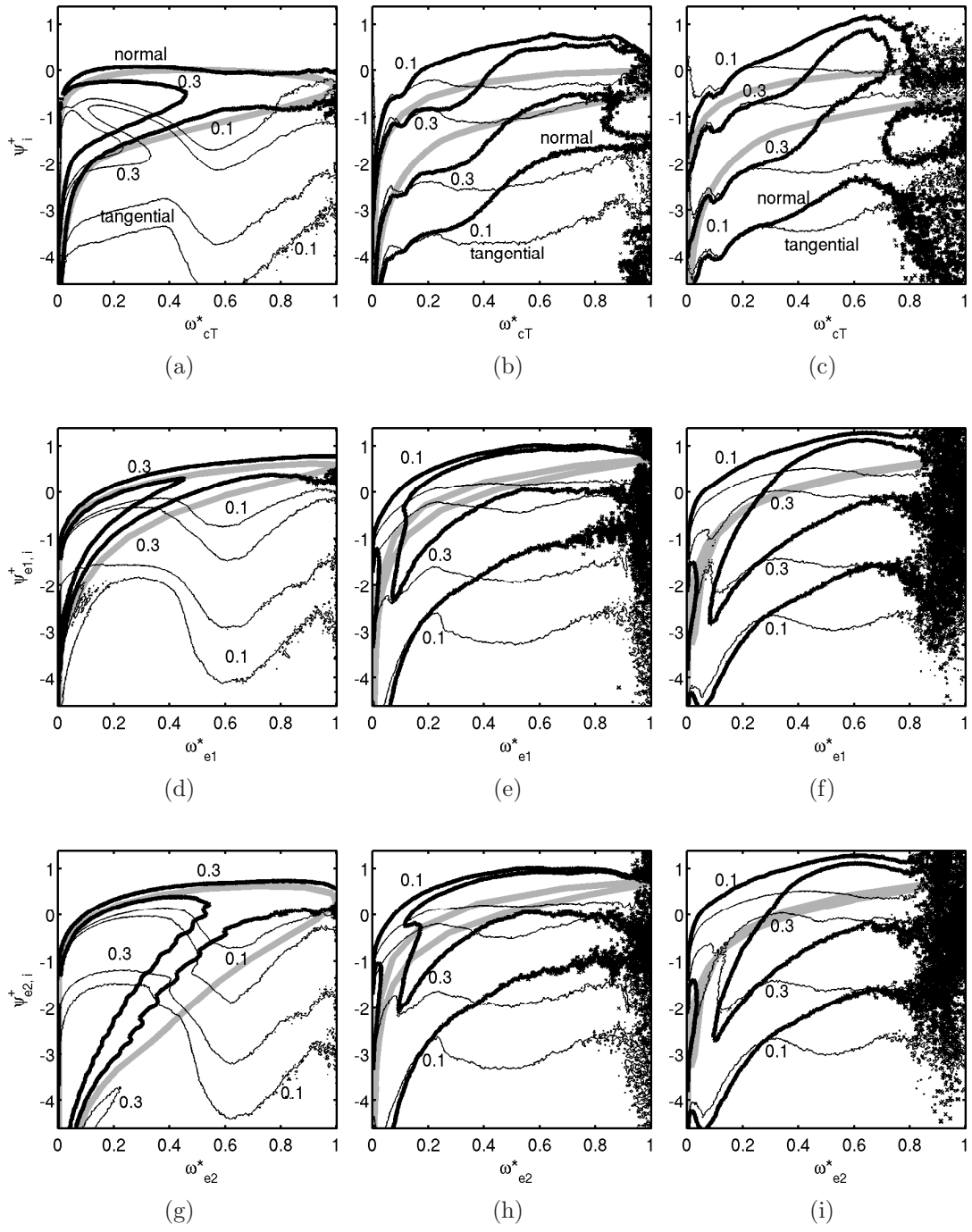

Figure 5.13: The conditional PDF, $P(\psi_i^+|\omega^*)$, of scalar gradient normal component ψ_1^+ (thick line) and tangential component ψ_2^+ (thin line) for the conventional premixed case (a, d, g), Case A2 (b, e, h), and Case B1 (c, f, i). PDFs based on the actual $\omega^*_{c_T}$ and ∇c_T fields (a–c), estimated fields ω^*_{e1} and ∇c_{PLIF} (d–f), and estimated fields ω^*_{e2} and ∇c_{PLIF} (g–i). The grey line is the respective laminar flame solution, $(\psi^+_{\mathrm{lam}}, \omega^*_{c_T})$.

and $\boldsymbol{n}_2 = (df_x/ds, df_y/ds)$ in every 2D (x-y) plane. Despite the effect of two-dimensionality on the gradient results described above, the results seem to be close to the ones obtained using 3D fields shown in figure 5.13. Also, the estimated PDF based on 2D fields reproduce important characteristics observed in the actual conditional PDF in figure 5.5 for both conventional premixed and MILD cases, regardless of the choice of species.

Thus, using conventional PLIF techniques, a similar conditional PDF of scalar gradient can be constructed to study flamelet/non-flamelet characteristics of turbulent combustion, especially for MILD combustion. An analysis based on these PDFs may be more useful for statistical analysis compared to visual examinations of PLIF images. An experimental study on these PDFs would be of interest.

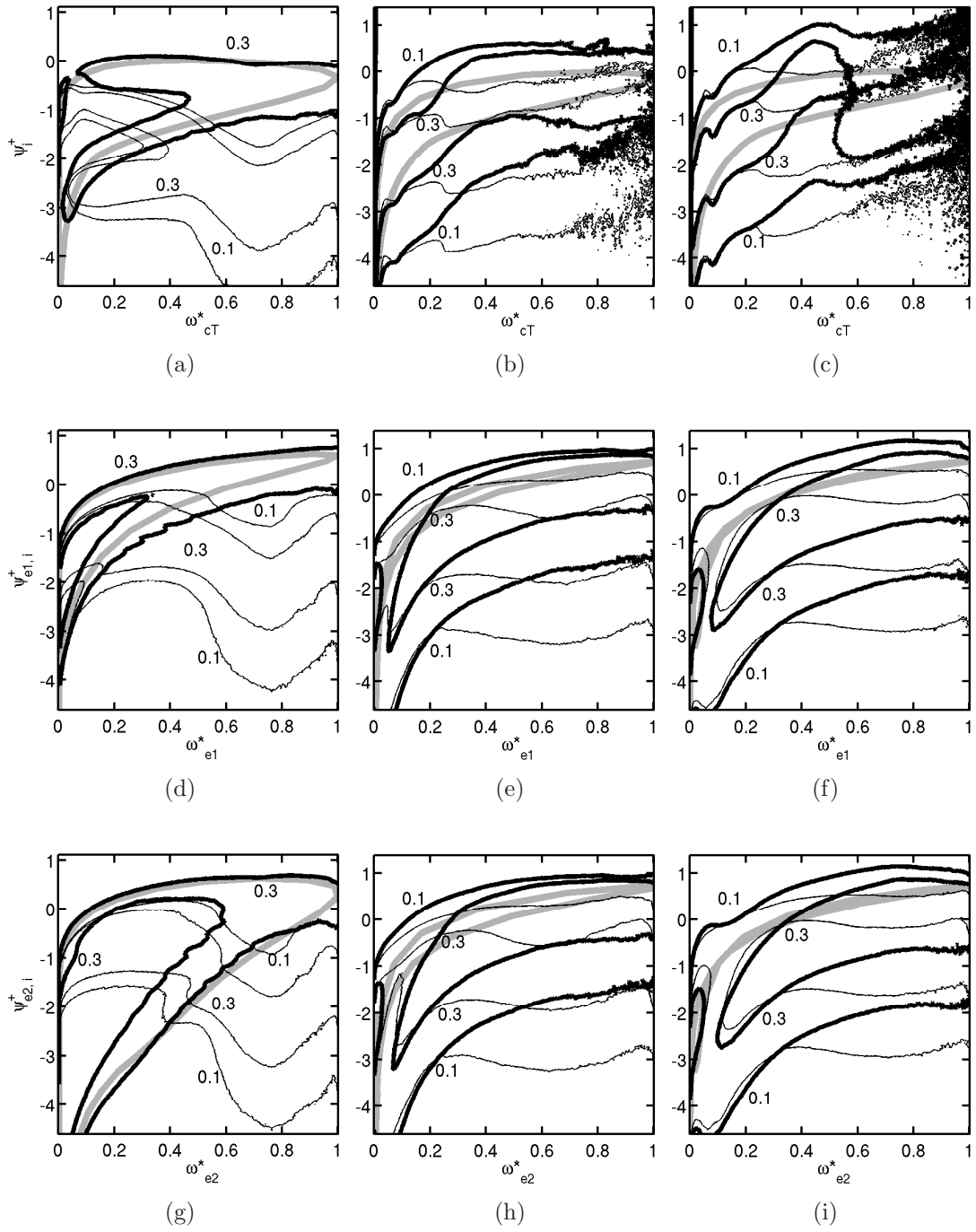

Figure 5.14: The conditional PDF, $P(\psi_i^+|\omega^*)$, of 2D scalar gradient normal component ψ_1^+ (thick line) and tangential component ψ_2^+ (thin line) for the conventional premixed case (a, d, g), Case A2 (b, e, h), and Case B1 (c, f, i). PDFs based on the actual $\omega^*_{c_T}$ and ∇c_T fields (a–c), estimated fields ω^*_{e1} and ∇c_{PLIF} (d–f), and estimated fields ω^*_{e2} and ∇c_{PLIF} (g–i). The grey line is the respective laminar flame solution, $(\psi^+_{\mathrm{lam}}, \omega^*_{c_T})$.

Chapter 6

Modelling of MILD Combustion

6.1 Background and objectives

Most numerical studies of MILD combustion are based on RANS simulations and a few studies are based on LES. For RANS simulations, Eddy Dissipation Concept (EDC) is widely employed to describe distributed reaction zones under MILD conditions to model mean reaction rate (Weber *et al.*, 2000; Orsino *et al.*, 2001; Christo & Dally, 2005; Galletti *et al.*, 2007; Li & Mi, 2011; Aminian *et al.*, 2011). However, EDC was developed to consider the effect of turbulent motion on reaction zone distribution, and so it assumes that distributed reaction zones exist within the fine structure equivalent to the region of turbulence energy dissipation (Magnussen, 1981). Such assumptions may limit the applicability of this mean reaction rate closure for MILD combustion simulations, since the dilution level increases the spatial extent of distributed reaction zones, as shown in figures 3.5–3.7. The deviation of the predicted mean temperature from the experimental results with an increase of the mixture dilution level has been reported in a previous study (Christo & Dally, 2005), suggesting this limitation when EDC is used under high dilution conditions.

The results presented in the present work also suggest that conventional numerical approaches seem to be applicable. For instance, the presumed PDF based on the β-function reasonably represents the PDF of c_T (see section 3.1). Flamelet behaviour is observed in the reaction rate and scalar gradient relation-

ship, although such flamelet-like tendency is weak compared to the conventional premixed case (section 5.3). However, the respective canonical flame based on the laminar flamelet, MIFE, does not fully represent the MILD combustion considered in this work (section 3.4). Thus, a fully representative model reactor is first discussed in the next section, and the model reactor is validated using the DNS results. Afterwards, an a priori assessment is carried out employing the presumed PDF approach to validate the proposed model reactor for a mean and filtered reaction rate closure in the RANS and LES contexts.

6.2 Perfectly Stirred Reactor model

Although the effect of exhaust gas pockets in the initial mixture is partially included in the MILD Flame Elements (MIFEs), the MILD combustion characteristics are not fully represented by the canonical flame as discussed in section 3.4. Thus, the following characteristics need to be taken into account for a fully-representative model reactor, based on the findings discussed in the previous sections.

(1) A MILD mixture consists of both exhaust and fresh gases including radicals and intermediate species (section 3.4).

(2) Thin reaction zones propagating at $\sim S_L$ solely are no longer predominant in MILD combustion due to the reaction zone interactions and autoignition producing distributed reaction zones.

(3) As shown in the previous sections the scalar gradient tends to be smaller for MILD combustion cases, leading to relatively uniform combustion.

Based on the above insights, a one-dimensional laminar flame, which consists of a propagating flame such as Flames A and B (as referenced in section 2.6.1) and MIFEs, may not be suitable in an average sense. MILD combustion consists of volumetric reaction zones which spread out over a large portion of the domain. Another possible way is to treat such MILD reaction zones as Perfectly Stirred Reactors (PSR) having a representative residence time. A tabulated chemistry

Table 6.1: Summary of the mixture properties. Units are Kelvins (K) and milliseconds (ms).

	$X_{CH_4,r}$	$X_{O_2,r}$	$X_{H_2O,r}$	$X_{CO_2,r}$	T_r	T_p	τ_{ign}
PSR A	0.0093	0.0345	0.135	0.064	1500	1667	0.285
PSR B	0.0059	0.0247	0.143	0.068	1500	1610	0.350

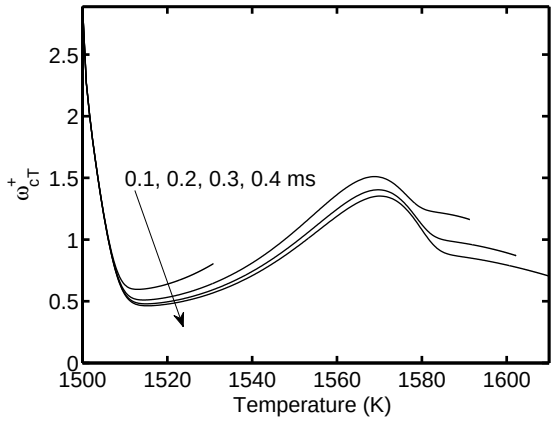

Figure 6.1: Reaction rate variation with temperature for unsteady PSR solution for the mixture in Case B1 with various residence times ranging from 0.1 to 0.4 ms.

involving a PSR has been used in a previous study (Duwig *et al.*, 2008). In the present work, however, the initial diluted reactant mixture composition for PSR is based on the spatial average of the DNS initial species mass fraction field including radicals and intermediate species. Also, only one variable — time t, later converted to c_T — is required for the present PSR model. Other initial parameters are set according to the respective DNS condition, which is shown in table 6.1. Here, PSR A is for DNS Cases A1 and A2, and PSR B is for Case B1.

Based on the initial and inflowing conditions as in table 6.1, the zero-dimensional, unsteady PSR equations are solved for PSRs A and B, using the commercial software COSILAB (COSILAB, 2007). The simulation is continued until the reactor temperature reaches a nearly steady value, which is close to the burnt temperature of the respective DNS result. The present PSR model is similar to the EDC approach, because both assume PSR-type combustion in a certain

volume. However, the present PSR model considers uniform combustion in the volume, $V_{\mathrm{PSR}} \sim \delta_{th}^3$ (see section 3.5), while the EDC model assumes PSR-type combustion in the fine structure equivalent to the volume of turbulence energy dissipation regions, $V_{\mathrm{EDC}} \sim \eta^3$, (Magnussen, 1981). The ratio of these volumes $V_{PSR}/V_{\mathrm{EDC}} \sim (\delta_{th}/\eta)^3 \sim \mathrm{Ka}^{3/2}$, since $\mathrm{Ka} = (\delta_F/\eta)^2 \approx (\delta_{th}/\eta)^2$, and Ka for the present MILD cases is greater than unity (see table 2.2). Thus, the residence time is set to be 0.4 ms which is similar to the flow through time τ_D for the present MILD DNS cases. Note that the choice of residence time does not unduly change the relationship between the reaction rate and temperature variations as seen in figure 6.1. Thus, local regions where PSR-type combustion occurs in a different residence time can also be taken into account sufficiently by the present PSR model.

The variations of conditionally averaged species mass fraction $\langle Y_i|T\rangle$ of the DNS results (Cases A1 and B1) are compared with the solutions of Flames A and B, MIFEs A and B, and PSRs A and B in figure 6.2 for CH_4, H_2O, OH and CO. Note that the conditional average of $\langle Y_i|T\rangle$ for Case A2 is very close to that for Case A1. As discussed in section 3.4, MIFE shows good agreement for major species, but is not sufficient for minor species. The present PSR models, however, show reasonable agreement for both major and minor species mass fraction variations as shown in figure 6.2. This agreement is not unduly affected by the residence time τ_{res} used to compute an unsteady PSR. Figure 6.3 shows a similar comparison between the DNS results $\langle Y_i|T\rangle$ and unsteady PSR solutions where τ_{res} of 0.1, 0.4 and 4.0 ms is used. The mixture for PSR is identical to that used for either PSR A or PSR B. Although, the working temperature increases with an increase of τ_{res}, the variations of Y_i for both major and minor species do not show significant deviation from the respective DNS result. A similar comparison is shown in figure 6.4 for ω_Q, where $\omega_Q = \dot{Q}/c_p$. As is clearly shown, ω_Q variation of Flames A and B does not show good agreement with the DNS values. For MIFE, only qualitative agreement is shown, although it underestimates the reaction rate variation overall. This is because the effects of additional dilution due to the exhaust gas pockets are not fully included in the reactant mixture. Note that strained laminar flames with MIFE mixture are also considered with various strain rates (not shown). However, they do not show adequate predic-

tions in terms of reaction rate. From a physical point of view, this is because the predominant factors in MILD combustion are the phenomena such as convoluted and interacting reaction zones, rather than strain caused by a strong turbulence.

Although a broad scatter distribution of the reaction rate shown in figure 3.14 cannot be represented, the PSR model shows reasonable agreement with the respective DNS case. The peak ω_Q locations predicted by PSR A and B differ only by 15 K and 10 K respectively from the conditionally-averaged variation of the respective MILD DNS cases. The reaction rate at low temperature is significantly large in the PSR result. This significant difference between the DNS and PSR results is due to the boundary conditions; radicals are confined in a relatively small portion to generate an intense reaction rate near the inlet temperature in the DNS, while radical distribution is homogeneous under the PSR boundary conditions. However, given the species mass fraction and reaction rate variations close to DNS results, the PSR models are fully representative for the MILD combustion conditions considered in this study. The broad scatter distribution of the species mass fractions and reaction rate shown in figures 3.13 and 3.14 may be captured by considering additional variable such as c_Y or ξ as in Duwig *et al.* (2008), or by considering a Partially Stirred Reactor (PaSR) using transport PDF methods (Pope, 1985; Chen & Kollmann, 1988). Although, a thorough exploration of possible modelling approaches for MILD combustion is not the aim in the present work, these approaches should be validated using experimental and numerical data sets in the future work.

6.3 A priori assessment for chemical source term

6.3.1 Reynolds averaged reaction rate field

As shown in section 3.1, PDF of c_T can be modelled reasonably well using the β-PDF. The PSR models also show good agreement with DNS results in terms of the conditional average. In this subsection, the β-function and the model reactors, PSRs A and B, are assessed using a presumed PDF method for the reaction rate prediction in the RANS context. Using the presumed PDF P_β, the

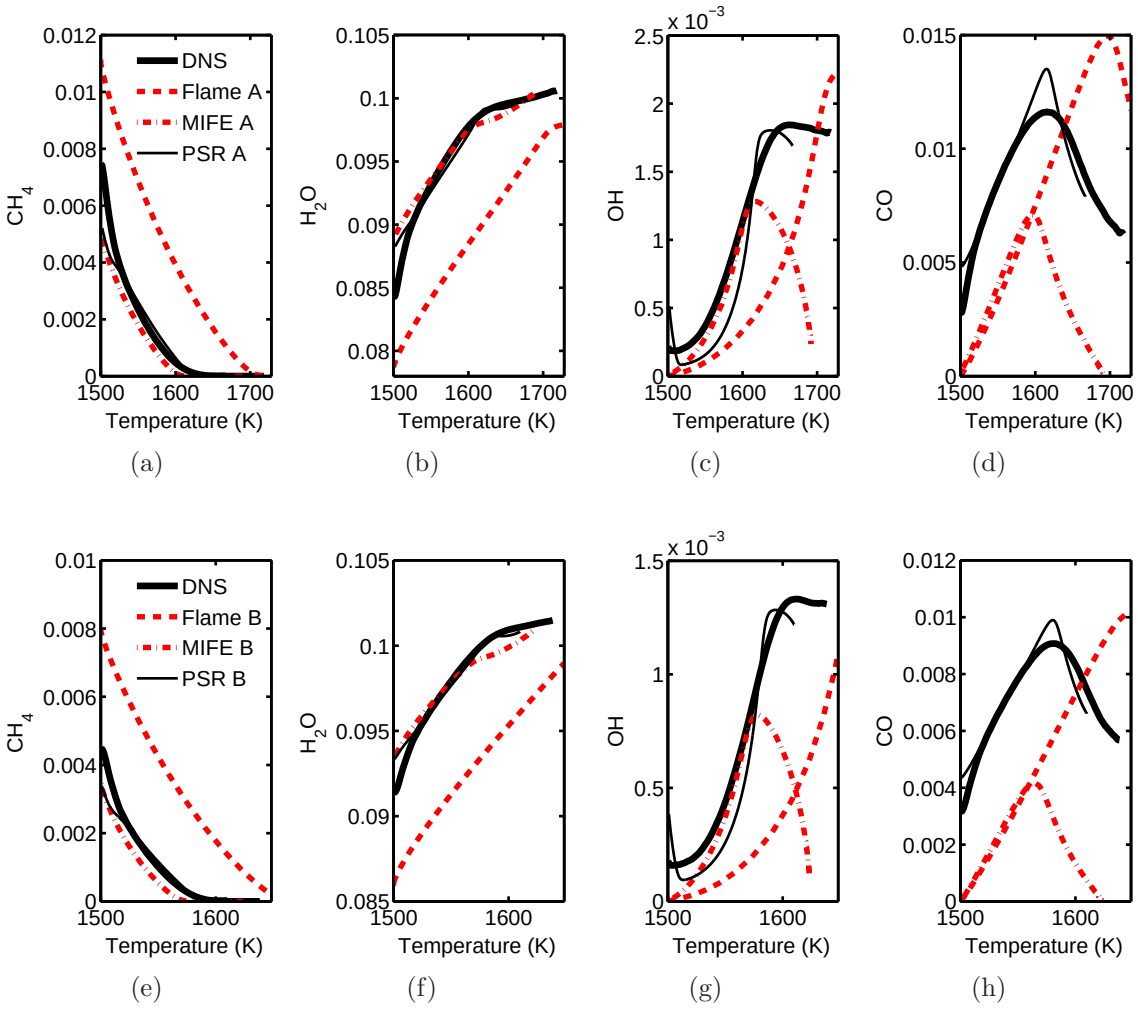

Figure 6.2: Variations of species mass fraction of CH_4 (a, e), H_2O (b, f), OH (c, g), and CO (d, h) for Case A1 (a–d) and Case B1 (e–h). Thick line: DNS result $\langle Y_i|T\rangle$, red dashed line: Flames A and B, red dash-dotted line: MIFEs A and B, and thin solid line: PSRs A and B.

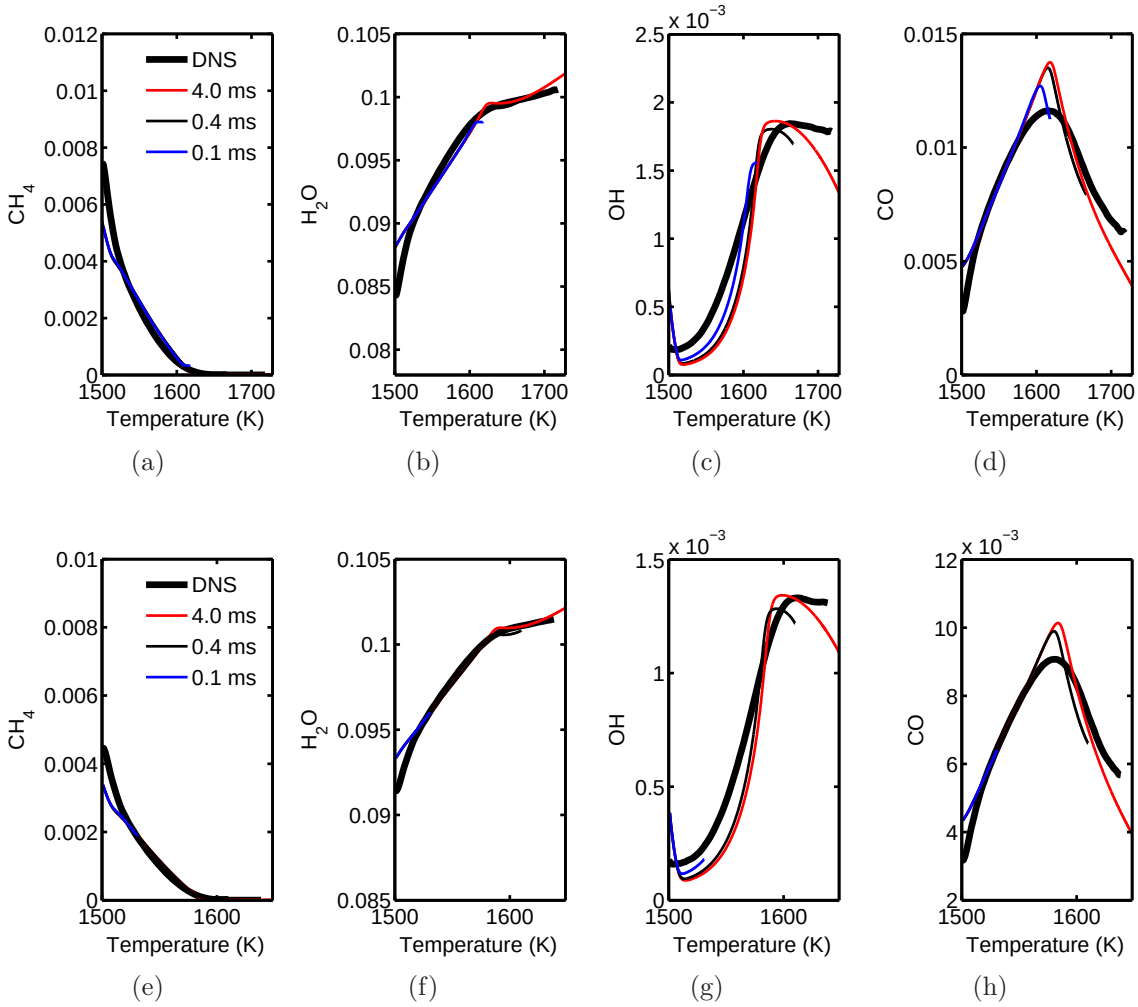

Figure 6.3: Variations of species mass fraction of CH_4 (a, e), H_2O (b, f), OH (c, g), and CO (d, h) for Case A1 (a–d) and Case B1 (e–h). Thick black line: DNS result $\langle Y_i|T\rangle$, thin red line: $\tau_{res} = 4.0$ ms, thin black line: 0.4 ms (PSR A or B), and thin blue line: 0.1 ms. The same mixture as PSR A (a–d) and PSR B (e–h) is used.

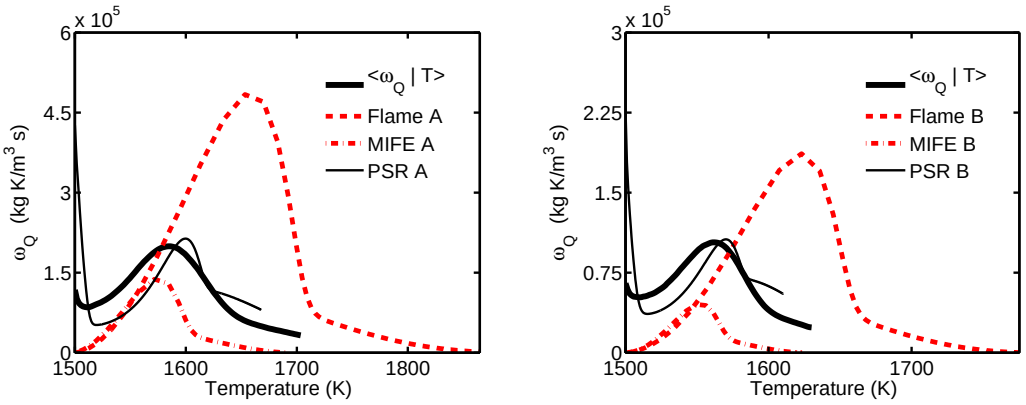

(a) (b)

Figure 6.4: Variation of ω_Q for (a) Case A1 and (b) Case B1. Black thick line: DNS result $\langle \omega_Q | T \rangle$, red dashed line: Flames A and B, red dash-dotted line: MIFEs A and B, and thin solid line: PSRs A and B.

mean reaction rate is modelled as:

$$\bar{\omega}_{c_T,model} = \int_0^1 \omega_L(c) P_\beta(c) dc, \tag{6.1}$$

where $\omega_L(\xi)$ is the reaction rate based on c_T as a function of $\xi = c_T$ obtained from a model reactor, and $P(c)$ is the presumed PDF based on the β-function, which is shown at arbitrary locations in figure 3.2. The exact and modelled mean reaction rate variations, $\bar{\omega}_{c_T}$ and $\bar{\omega}_{c_T,model}$, are shown in figure 6.5 for Cases A1 and B1. Only two canonical reactors, MIFE and PSR, are assessed, since Flames A and B are not representative for the present cases. The mean reaction rate obtained from DNS results shows large values at the upstream region. This clearly shows that the reactant mixture reacts as soon as it enters the (recovered) exhaust gases, as illustrated in figure 2.1. The mean reaction rate variation calculated from the DNS results is captured qualitatively by MIFEs A and B. However, the modelled variations are smaller than the respective DNS results about 2 to 3 times. The PSR models, however, show adequate agreement with the respective DNS case. Such agreement is expected because the solutions of PSRs A and B show the close variations to the conditional averages of reaction rate for the

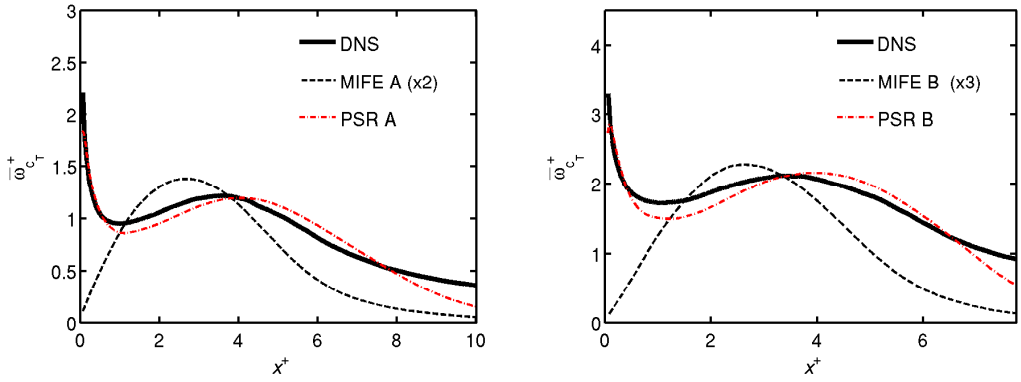

(a) (b)

Figure 6.5: A comparison of the mean $\bar{\omega}_{c_T}$ and predicted $\bar{\omega}_{c_T,model}$ reaction rate variations as a function of c_T for (a) Case A1 and (b) Case B1.

respective DNS case. Also, since PSRs A and B can represent the variations of conditionally averaged mass fractions for both major and minor species, the Reynolds averaged species variation can also be modelled adequately. Therefore the use of conventional β-PDF together with a PSR model can represent the mean fields of MILD combustion under a non-uniform mixture condition adequately.

6.3.2 Filtered reaction rate field

The approach and model reactors considered in section 6.3.1 can be applied to develop a closure for filtered reaction rate for LES. In the LES context, the presumed PDF and the modelled reaction rate can be calculated in the same manner as in the RANS context, but the Reynolds and Favre averages are replaced by LES filters calculated for any field $f(x, y, z)$ respectively as:

$$\langle f(\boldsymbol{x})\rangle^{\mathrm{DNS}} = \int f(\boldsymbol{x'})F(\boldsymbol{x}-\boldsymbol{x'})d\boldsymbol{x'}, \tag{6.2}$$

and

$$[f] = \frac{\langle \rho f\rangle^{\mathrm{DNS}}}{\langle \rho\rangle^{\mathrm{DNS}}}. \tag{6.3}$$

Here, $\langle f\rangle$ and $[f]$ denote filtering and density weighted filtering operations for f, and F is a filter kernel using a Gaussian function. In physical space the kernel

for filter size Δ is written as:

$$F(\boldsymbol{x}-\boldsymbol{x'};\Delta)=\left(\frac{6}{\pi\Delta^2}\right)^{1/2}\exp\left[-\frac{6}{\Delta^2}(\boldsymbol{x}-\boldsymbol{x'})\right]. \tag{6.4}$$

By replacing equations 3.4 and 3.5 respectively with equations 6.2 and 6.3, the same equations for the presumed PDF (equations 3.1–3.3) and for the filtered reaction rate (equation 6.1) can be used as:

$$P_\beta(\xi)=\frac{\xi^{r-1}(1-\xi)^{s-1}}{\Gamma(r)\Gamma(s)/\Gamma(r+s)}, \tag{6.5}$$

$$r=[c_T]\left([c_T]\frac{1-[c_T]}{[c_T''^2]}-1\right),\quad s=r\frac{1-[c_T]}{[c_T]}, \tag{6.6}$$

and

$$\langle\omega_{c_T}\rangle^{\text{model}}=\int_0^1\omega_L(c)P_\beta(c)dc, \tag{6.7}$$

where $[c_T''^2]$ is the fluctuation from the filtered value. The Gaussian filter applied here has the filter size Δ of δ_{th}–$3\delta_{th}$ of the respective MILD case.

Figure 6.6 shows the spatial variations of the filtered $\langle\omega^+_{c_T}\rangle^{\text{DNS}}$ and modelled reaction rate $\langle\omega^+_{c_T}\rangle^{\text{model}}$ for Case B1, where the filter width Δ is set to be δ_{th}, $2\delta_{th}$ and $3\delta_{th}$. The filtered reaction rate is obtained by filtering the DNS results, and the modelled field is based on equation 6.7. The x-y plane shown here is identical to the one shown in figure 3.7a, which is the DNS reaction rate field. The effect of filter widths is clearly seen in figures 6.6a, 6.6c and 6.6e. In the filtered reaction rate field, reaction zone convolutions are apparent for $\Delta=\delta_{th}$, but they are not so clear for $\Delta=2\delta_{th}$ and $3\delta_{th}$. As discussed in sections 3.3 and 4.2, reaction zone interactions and reaction-dominated mixtures tend to occur in relatively small regions, which seem to be filtered out when $\Delta\geq\delta_{th}$ is used. However, patchy behaviour of reaction zones, which is a characteristic of MILD combustion (Dally *et al.*, 2004), still appears for all filter sizes. Although this characteristic and the shape of reaction zones in the upstream regions are not well represented, the magnitude of reaction rate observed in the filtered field is reasonably reproduced by the presumed-PDF model for all the filter sizes tested, as shown in figures 6.6b, 6.6d and 6.6f.

Joint PDF of filtered and modelled reaction rate is shown in figure 6.7 for Case B1 with various filter sizes. This PDF is obtained using samples from the entire sampling period. The diagonal line denotes the perfect agreement between filtered $\langle \omega_{c_T}^{+} \rangle^{\mathrm{DNS}}$ and modelled $\langle \omega_{c_T}^{+} \rangle^{\mathrm{model}}$ reaction rates. As suggested in reaction rate variations in figure 6.6, the joint PDF also shows that a reasonable agreement between filtered and modelled reaction rates for all the filter sizes, and the best agreement is shown for $\Delta = 3\delta_{th}$. A similar joint PDF with a filter size of $3\delta_{th}$ is shown for Cases A1 and A2 in figure 6.8. Although deviation from the diagonal line exists, a large probability density is generally located close to the diagonal lines, suggesting that the present model reactor PSR is strongly representative of MILD combustion.

Instantaneous reaction rate variations (DNS, filtered and modelled) are compared at two instants in figure 6.9. Each reaction rate variation is averaged over the periodic directions. The shape of these variations look similar to the Reynolds averaged reaction rate shown in figure 6.5. The correlation between the filtered and modelled reaction rates appears to be stronger for Case B1 (highest dilution and turbulence level) than Case A2 (lowest dilution and turbulence). The results suggest that the present PSR model works well for combustion under higher dilution conditions where reaction zones are distributed occupying a larger volume, due to reaction zone interactions and turbulence-chemistry interactions.

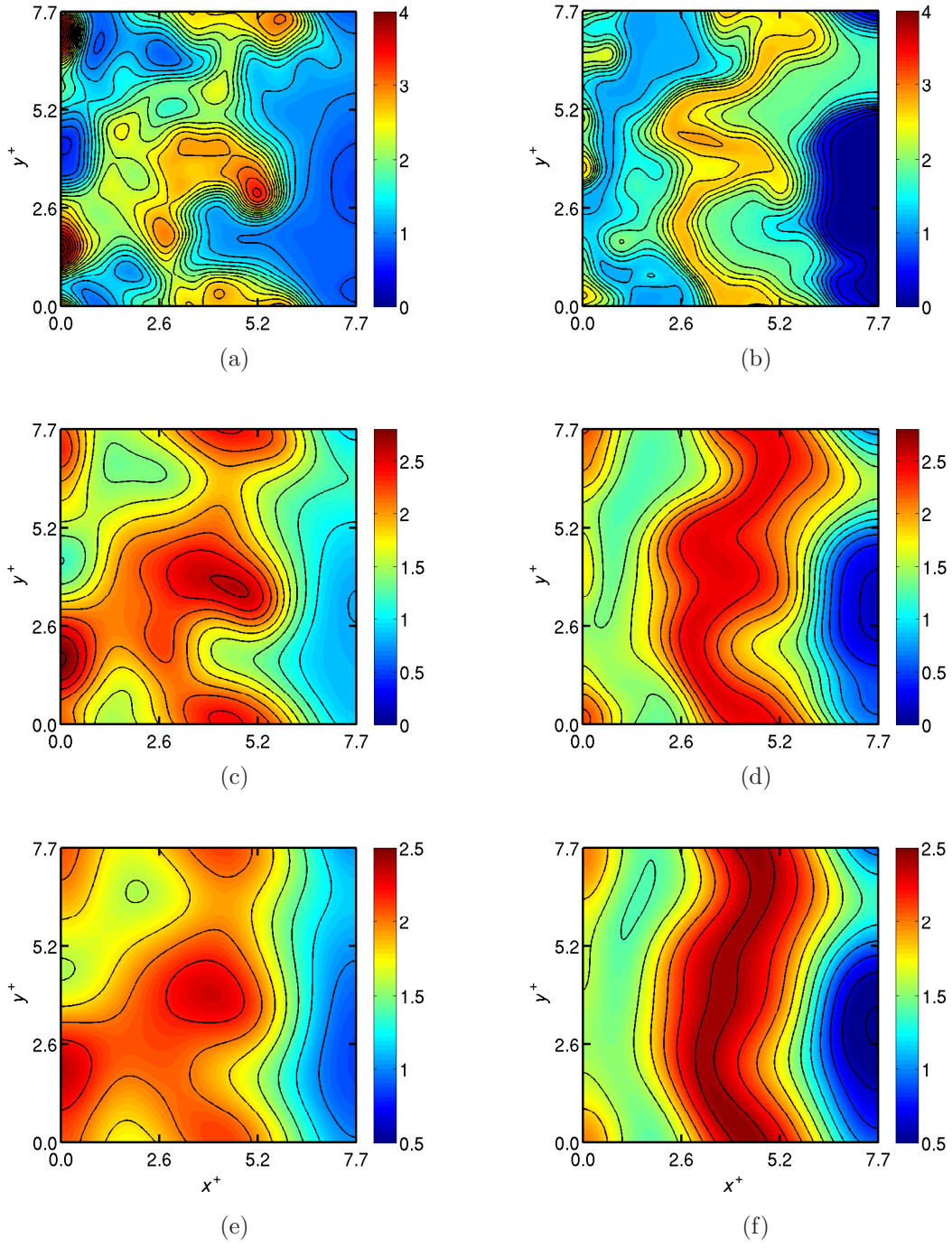

Figure 6.6: A comparison of the filtered $\langle \omega_{c_T}^+ \rangle^{\mathrm{DNS}}$ (a, c, e) and modelled $\langle \omega_{c_T}^+ \rangle^{\mathrm{model}}$ (b, d, f) reaction rate $\bar{\omega}_{c_T}^+$ variations in a mid x-y plane for Case B1 at $t = 1.5\tau_D$ (colour and contour lines). The contour lines show the same level for both filtered and modelled reaction rate fields for comparison. The filter width is set as δ_{th} (a, b), $2\delta_{th}$ (c, d), and $3\delta_{th}$ (e, f).

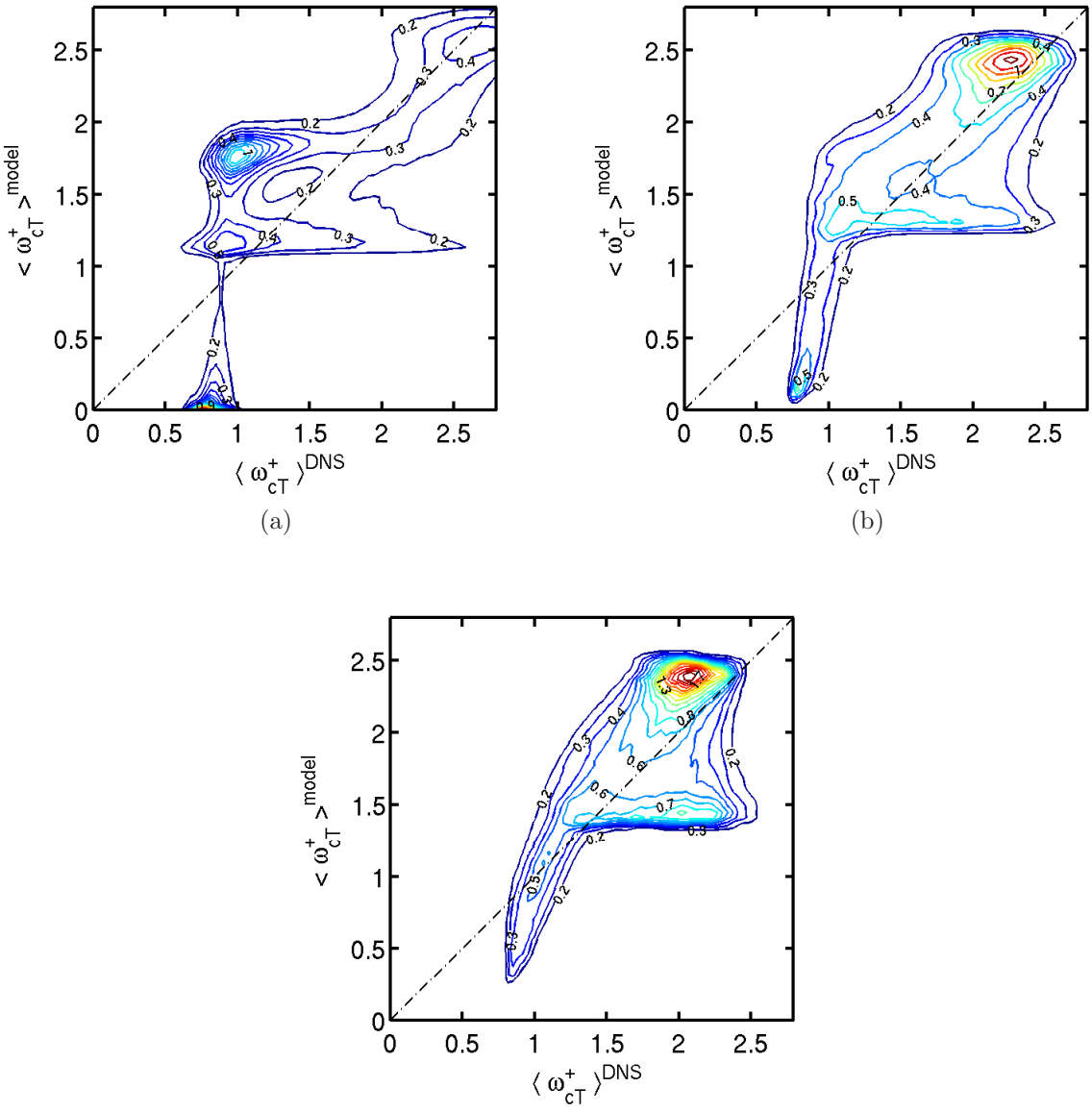

Figure 6.7: Joint PDF of filtered $\langle \omega_{c_T}^{+} \rangle^{\mathrm{DNS}}$ and modelled $\langle \omega_{c_T}^{+} \rangle^{\mathrm{model}}$ reaction rate for Case B1. A perfect correlation between filtered and modelled reaction rates is represented by the diagonal line (dash-dotted). The filter width is set as (a) δ_{th}, (b) $2\delta_{th}$, and (c) $3\delta_{th}$.

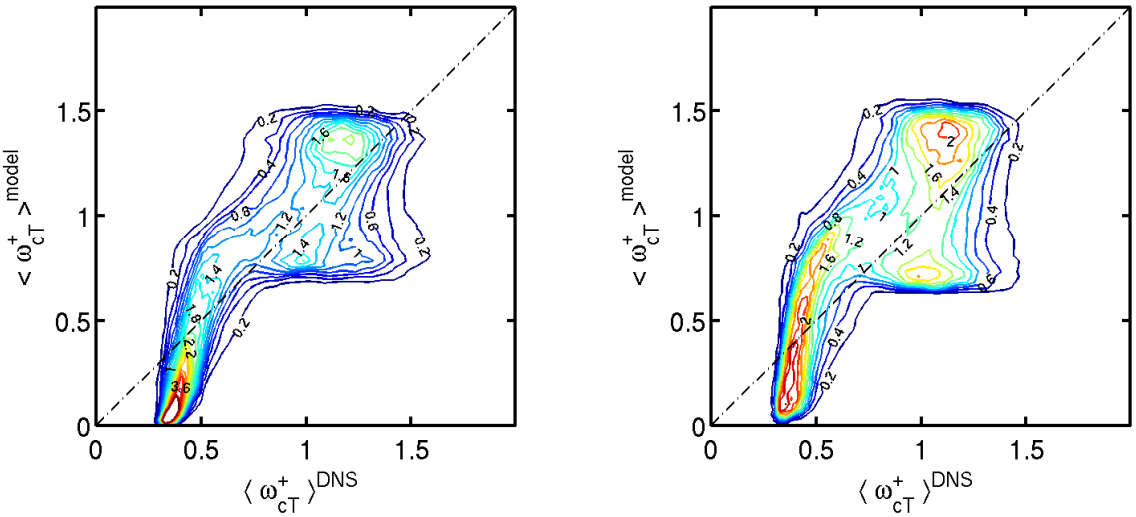

Figure 6.8: Joint PDF of filtered $\langle \omega_{c_T}^{+} \rangle^{\mathrm{DNS}}$ and modelled $\langle \omega_{c_T}^{+} \rangle^{\mathrm{model}}$ reaction rate for (a) Case A1 and (b) Case A2. The filter width is set as $3\delta_{th}$.

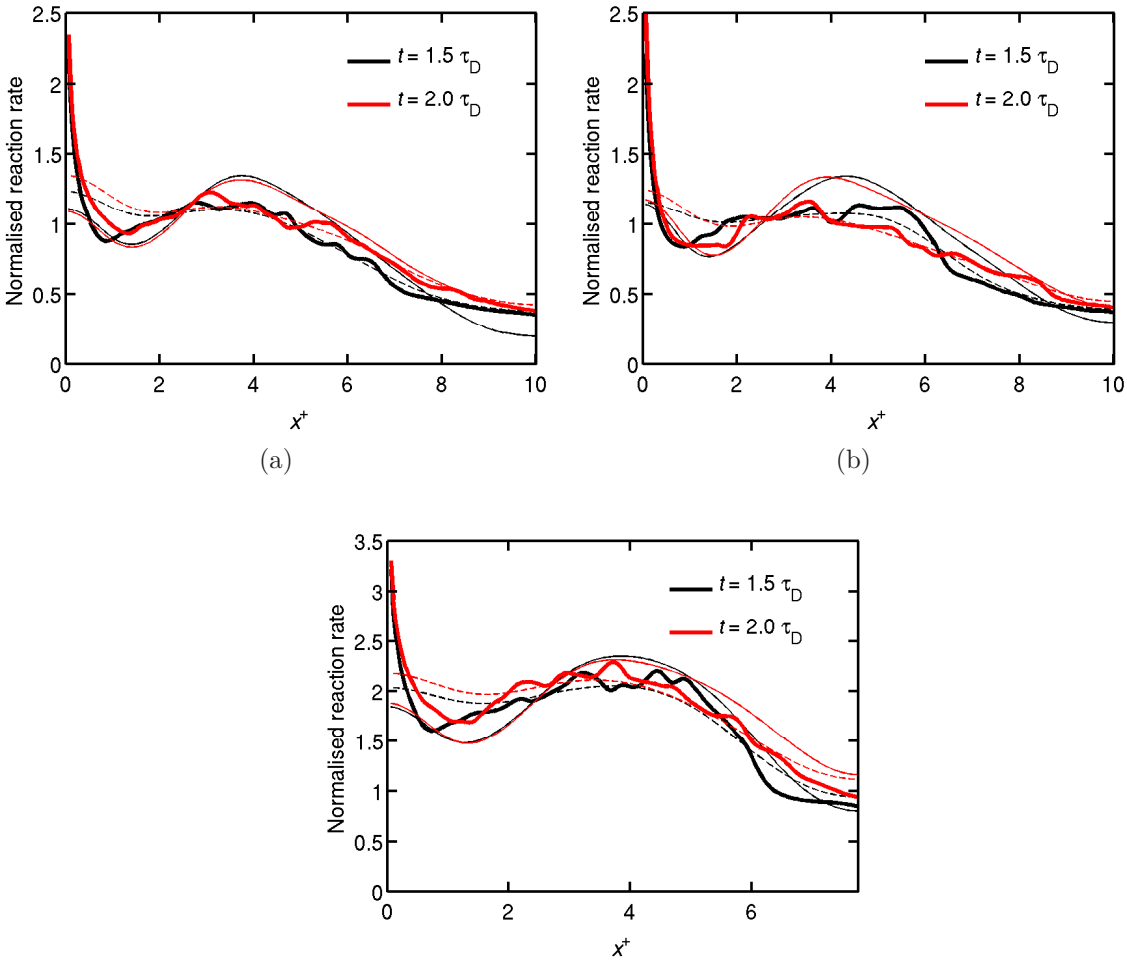

Figure 6.9: One-dimensional variations of the DNS (thick solid lines), filtered $\langle \omega_{c_T}^+ \rangle^{\mathrm{DNS}}$ (dashed lines), and modelled $\langle \omega_{c_T}^+ \rangle^{\mathrm{model}}$ (thin solid lines) reaction rate $\omega_{c_T}^+$ averaged in the periodic directions at $t = 1.5\tau_D$ (black) and $2.0\tau_D$ (red) for (a) Case A1, (b) Case A2, and (c) Case B1. The filter width is set as $3\delta_{th}$.

Chapter 7

Conclusions

The aims of this thesis are to investigate turbulent MILD combustion and its modelling. In order to carry out analysis in detail, DNS of MILD combustion is employed. Typically, a MILD mixture is likely to be inhomogeneous due to short mixing time, although MILD combustion involves with high jet Reynolds number conditions to enhance mixing in practice. The mixture inhomogeneity is included by using the two-stage strategy for the MILD combustion DNS. Also, a skeletal mechanism including non-unity Lewis number effects is employed to describe combustion kinetics. Direct numerical simulation of conventional turbulent premixed flame under a high Da condition is also performed for one case for comparative purposes. In this chapter, the results obtained in previous chapters are presented and summarised. Finally, future work is suggested to close this chapter.

7.1 Preprocessing of inflowing mixture fields for MILD combustion DNS

Construction of initial and inlet mixture fields, which mimics EGR conditions, is carefully processed and the method is presented in chapter 2. The dilution, initial temperature and turbulence conditions are set to represent MILD conditions in the previous experimental studies. These partially premixed fields consisting of exhaust and fresh gas pockets are then fed from the inlet boundary of DNS

combustion domain. Totally three MILD combustion cases and one conventional premixed combustion case are considered. The condition for the conventional premixed case is chosen to represent a classical turbulent premixed flame which has flamelet characteristics, mainly used for comparative purposes.

The features of the simulated MILD combustion cases, such as the uniform temperature field, PDF of normalised temperature and OH radicals, existence of patchy reaction zones, and the contradicting behaviour of OH and temperature fields, are comparable to typical experimental observations. They suggest that the present DNS methodology and conditions are reasonably representative of typical MILD combustion fields in laboratory scale MILD combustors employed in previous experimental studies.

7.2 Reaction zones in MILD combustion

The instantaneous reaction rate field discussed in chapter 3 shows highly convoluted reaction zones, which cause frequent interactions between reaction zones. Such interacting regions appear to contribute to the distributed reaction zones, whose spatial extent increases with the dilution and turbulence levels. Also, the final period of interaction identified using equation 3.8 tends to produce a small scalar gradient with locally thin reaction zones. In order to quantify thin and distributed reaction zone shapes, Minkowski functionals and shapefinders are applied for reaction rate iso-surfaces. Although these methods have originally been developed in the cosmology field, they are sufficiently robust for turbulent combustion study as well. The PDF of shapefinders shows the most probable shapes of MILD reaction zones are pancake like, which classified as shapes between blobs and sheets, while typical reaction zones are sheet like for the conventional combustion. However, the reaction zone shapes in MILD combustion vary widely from blobs to short tubes to pancakes. Several of local MILD reaction zones also locate between sheet and pancake shapes. These morphological characteristics of MILD combustion suggests the existence of non-flamelet like reaction zones, such as autoigniting mixtures, since a propagating flame is usually associated with thin reaction zones.

Various scalar fluxes are studied with the aim of investigations into autoignition and flame-propagation regions. Although the present method identifies reaction dominated and flame-propagation dominated regions but does not distinguish autoigniting regions, it is found that these two regions are entangled closely one another. It is also found that the reaction dominated regions tend to locate in small scalar gradient regions statistically. Similar autoignition characteristics have been reported in previous studies for non-premixed combustion.

Based on the examinations of the reaction rate field, co-existence of thin and distributed reaction zones, reaction zone interactions, reaction dominated regions and flame-propagation dominated regions as well as turbulence-flame interactions seems to have significant effects on flamelet/non-flamelet behaviour of MILD combustion. Such flamelet/non-flamelet characteristics are studied using the PDF of scalar gradient conditioned on the reaction rate, which is proposed in the present study. This PDF allows a direct comparison between the DNS results and the respective laminar flame solution. The results show that MILD combustion has flamelet characteristics although the tendency is weak compared to classical premixed combustion. This is also ensured by studying the relation between the mean reaction rate and mean scalar dissipation rate.

Conventional measurable species for reaction rate estimation are investigated using deduced LIF signals for MILD combustion. LIF signals of species such as OH, CH_2O and CHO are found to be still adequate for MILD combustion to estimate reaction rate field. Although the reaction progress variable cannot be estimated using only OH LIF signals, its gradient direction has strong correlation with the direction of OH PLIF intensity gradient. These estimated reaction zones and scalar gradient directions are used to compute the above conditional PDF of scalar gradient using only measurable species, and compared with the respective laminar flame solution constructed accordingly. The conditional PDF based on two-dimensional deduced LIF fields can reproduce a similar amount of information obtained from the actual PDF, to investigate flamelet/non-flamelet characteristics of MILD combustion. This suggests the same approach can be applied for experimental study for flamelet/non-flamelet behaviour in MILD combustion by employing simultaneous OH and CH_2O PLIF, or OH and CHO PLIF technique.

7.3 Modelling of MILD combustion

Given above results obtained from the DNS data sets, representative model reactors, namely Flames A and B, MIFEs (MILD Flame Elements) A and B, and PSRs A and B are proposed and validated. The first models, Flames A and B, are conventional one-dimensional laminar flamelets used to construct the initial DNS field. The second ones, MIFEs, are similar one-dimensional laminar flames, where the effect of additional dilution due to the existence of exhaust gas pockets in the mixture is taken into account. The third model has a PSR-type configuration to include distributed reaction zones, as well as additional dilution due to exhaust gas pockets. Although PSR-type combustion is also considered in Eddy Dissipation Concept (EDC), the present model assumes PSR-type combustion in a volume, which is larger than the size of typical fine structure considered in EDC approaches. These model reactors are compared with the conditional average of mass fractions of various species and reaction rate using the DNS results, and the PSR-type model is found to be reasonably representative. The representative model reactor is then assessed for the mean and filtered reaction rate closure using a presumed PDF method. The modelled mean/filtered reaction rate variations show good agreement with the DNS results.

7.4 Future work

Generally, most MILD combustion modelling studies are based on non-flamelet approaches such as EDC models, to take the nature of MILD combustion into account. Turbulent combustion models based on EDC assume that the reactants are homogeneously mixed within fine structures corresponding to turbulence energy dissipation regions, whose characteristics dimensions are the same magnitude as the Kolmogorov length scale (Magnussen, 1981). However, as presented in this work, the reaction zones spread out over a substantial volume of the domain, which typically has the dimensions of the same magnitude as δ_{th}^3. According to Christo & Dally (2005), the temperature prediction with the EDC model is less satisfactory under intense dilution conditions ($Y_{O_2} \sim 3\%$). Such deviation

from measured results can be because the portion occupied with distributed reaction zone increases with dilution and turbulence levels due to reaction zones interactions, but EDC does not take this into account. Thus, computation of characteristic residence time in EDC, typically denoted as $\tau^* \sim (\nu/\varepsilon)^{1/2}$, needs to include not only the turbulence effect but also a larger volume occupied by such distributed reaction zones.

In the same way, flamelet approaches such as gradient-based models may work if the effect of reaction zone interactions on scalar gradient is considered, which is suggested by figure 5.2. Also, the validated PSR model appears to work under the present combustion conditions. A similar canonical model needs to be tested thoroughly for other combustion configurations and compared with DNS and/or experimental results.

In the present study, a PSR-type canonical reactor is used in conjunction with the presumed PDF. However, the mixture in the domain is not perfectly stirred as shown in the broad scatter distribution in the T-Y_i space shown in figure 3.13, and local turbulence effects on the scalar mixing has to be taken into account. Therefore, it would be worthwhile to assess the transport PDF method as it can capture PaSR-type combustion (Pope, 1985; Chen & Kollmann, 1988).

It is also interesting to measure OH and CH_2O, or OH and CHO simultaneously in MILD combustion, using PLIF techniques, although measurement of CHO LIF signals may be difficult due to the low signal-to-noise ratio. Using these LIF signals, heat release rate field is constructed to perform visual examinations of MILD reaction zones on par with those performed in the present work. These measured species fields can then be used to construct the conditional PDF of scalar gradient, which is proposed in this work to investigate flamelet/non-flamelet characteristics experimentally.

Appendix A

Skeletal methane-air reaction mechanism

Table 1: Lewis number used for each species (Smooke & Giovangigli, 1991).

	Species	Le
1	CH_4	0.97
2	O_2	1.11
3	H_2O	0.83
4	CO_2	1.39
5	H	0.18
6	O	0.70
7	OH	0.73
8	HO_2	1.10
9	H_2	0.30
10	CO	1.10
11	H_2O_2	1.12
12	HCO	1.27
13	CH_2O	1.28
14	CH_3	1.00
15	CH_3O	1.30
16	N_2	1.00

Table 2: Skeletal methane-air reaction mechanism (Smooke & Giovangigli, 1991). Rate coefficients in the form $k = AT^n \exp(-E/RT)$. Units are moles, cubic centimetres, seconds, Kelvins and calories/mole. The third body efficiencies: $CH_4 = 6.5$, $H_2O = 6.5$, $CO_2 = 1.5$, $H_2 = 1.0$,$CO = 0.75$, $O_2 = 0.4$, and $N_2 = 0.4$. For all other species: 1.0. Fall-off rate coefficient $k_{fall} = 0.0063 \exp(-18000/RT)$.

	REACTION	A	n	E
1f.	$H + O_2 => OH + O$	2.000E+14	0.000	16800.0
1b.	$OH + O => H + O_2$	1.575E+13	0.000	690.0
2f.	$O + H_2 => OH + H$	1.800E+10	1.000	8826.0
2b.	$OH + H => O + H_2$	8.000E+09	1.000	6760.0
3f.	$H_2 + OH => H_2O + H$	1.170E+09	1.300	3626.0
3b.	$H_2O + H => H_2 + OH$	5.090E+09	1.300	18588.0
4f.	$OH + OH => O + H_2O$	6.000E+08	1.300	0.0
4b.	$O + H_2O => OH + OH$	5.900E+09	1.300	17029.0
5.	$H + O_2 + M => HO_2 + M$	2.300E+18	-0.800	0.0
6.	$H + HO_2 => OH + OH$	1.500E+14	0.000	1004.0
7.	$H + HO_2 => H_2 + O_2$	2.500E+13	0.000	700.0
8.	$OH + HO_2 => H_2O + O_2$	2.000E+13	0.000	1000.0
9f.	$CO + OH => CO_2 + H$	1.510E+07	1.300	-758.0
9b.	$CO_2 + H => CO + OH$	1.570E+09	1.300	22337.0
10f.	$CH_4(+M) => CH_3 + H(+M)$	6.300E+14	0.000	104000.0
10b.	$CH_3 + H(+M) => CH_4(+M)$	5.200E+12	0.000	-1310.0
11f.	$CH_4 + H => CH_3 + H_2$	2.200E+04	3.000	8750.0
11b.	$CH_3 + H_2 => CH_4 + H$	9.570E+02	3.000	8750.0
12f.	$CH_4 + OH => CH_3 + H_2O$	1.600E+06	2.100	2460.0
12b.	$CH_3 + H_2O => CH_4 + OH$	3.020E+05	2.100	17422.0
13.	$CH_3 + O => CH_2O + H$	6.800E+13	0.000	0.0
14.	$CH_2O + H => HCO + H_2$	2.500E+13	0.000	3991.0
15.	$CH_2O + OH => HCO + H_2O$	3.000E+13	0.000	1195.0
16.	$HCO + H => CO + H_2$	4.000E+13	0.000	0.0
17.	$HCO + M => CO + H + M$	1.600E+14	0.000	14700.0
18.	$CH_3 + O_2 => CH_3O + O$	7.000E+12	0.000	25652.0
19.	$CH_3O + H => CH_2O + H_2$	2.000E+13	0.000	0.0
20.	$CH_3O + M => CH_2O + H + M$	2.400E+13	0.000	28812.0
16.	$HCO + H => CO + H_2$	4.000E+13	0.000	0.0
17.	$HCO + M => CO + H + M$	1.600E+14	0.000	14700.0
18.	$CH_3 + O_2 => CH_3O + O$	7.000E+12	0.000	25652.0
19.	$CH_3O + H => CH_2O + H_2$	2.000E+13	0.000	0.0
20.	$CH_3O + M => CH_2O + H + M$	2.400E+13	0.000	28812.0
21.	$HO_2 + HO_2 => H_2O_2 + O_2$	2.000E+12	0.000	0.0
22f.	$H_2O_2 + M => OH + OH + M$	1.300E+17	0.000	45500.0
22b.	$OH + OH + M => H_2O_2 + M$	9.860E+14	0.000	-5070.0
23f.	$H_2O_2 + OH => H_2O + HO_2$	1.000E+13	0.000	1800.0
23b.	$H_2O + HO_2 => H_2O_2 + OH$	2.860E+13	0.000	32790.0
24.	$OH + H + M => H_2O + M$	2.200E+22	-2.000	0.0
25.	$H + H + M => H_2 + M$	1.800E+18	-1.000	0.0

Appendix B

Analysis of MILD Flame Element

In the present work, MILD Flame Element (MIFE) is introduced to take account the additional dilution. Figures 1 shows variations of several normalised species mass fractions Y_i^* for Flame C, MIFE A and MIFE B. Here $Y_i^* = (Y_i - Y_{i,\min})/(Y_{i,\max} - Y_{i,\min})$, where $Y_{i,\min}$ and $Y_{i,\max}$ are respectively the minimum and maximum Y_i in the flame solution. Since the distance is normalised using δ_{th}, the variations in the different flames are qualitatively similar for most of the species. However, the variations of CH_2O, which tends to appear before ignition, reflects the dilution level and temperature conditions of the reactant mixture. For Flame C, CH_2O rapidly increases just after H_2O production starts. In contrast, CH_2O starts to be produced before the significant increase of H_2O for MIFE A. This is because the reactant temperature of MIFE A is much higher than the autoignition temperature, and behaviour of the premixed flame becomes relatively close to that of an autoigniting mixture (Sidey *et al.*, 2013). For MIFE B, although CH_2O starts increases before the H_2O production, such a trend is not so strong compared to MIFE A. This is because the dilution level due to products is higher in MIFE B than in MIFE A, but the same reactant temperature as MIFE A is used. If the reactant temperature of MIFE is determined based on the proportion of the burnt gas in the mixture by considering the conservation of enthalpy during the mixing process, the behaviour of MIFE B would approach an autoignition problem compared to MIFE A. Figure 1d is similar species variations of a laminar flame where the same reactant mixture composition as MIFE

B is used but the reactant temperature is increased to 1600 K. As clearly seen in the figure, the CH_2O mass fraction is produced before the flame front. This result further ensures that with an increase of T_r (or possibly with higher dilution with hot products), the behaviour of a laminar flame becomes close to that of an autoignition.

Variations of Y_i^*, c_T, and three terms, $\mathscr{C}^+$, $\mathscr{D}^+$ and $\mathscr{R}^+$, are shown for H_2O and CH_2O for Flame C and MIFE A in figure 2. Here, $\mathscr{C}^+$, $\mathscr{D}^+$ and $\mathscr{R}^+$ are defined from the transport equation of Y_α similar to equation 4.1 as:

$$\frac{\partial \rho Y_\alpha}{\partial t} \underbrace{+ \frac{\partial \rho u_i Y_\alpha}{\partial x_i}}_{\mathscr{C}\text{: convection}} = \underbrace{\frac{\partial}{\partial x_j}\left(\rho D_\alpha \frac{\partial Y_\alpha}{\partial x_j}\right)}_{\mathscr{D}\text{: diffusion}} + \underbrace{\omega_{Y_\alpha}}_{\mathscr{R}\text{: reaction}} . \tag{1}$$

As discussed in above, the variations for H_2O are qualitatively similar between Flame C and MIFE A due to the normalisation, although reaction rate is non-zero and $Y^*_{H_2O}$ continues to increase even in the burnt side for MIFE A. This ensures the slow chemical process under MILD conditions. For the variations of CH_2O, clear differences are observed between Flame C and MIFEs. As described in figure 1, CH_2O is produced in a substantial quantities before temperature increases (compare $Y^*_{CH_2O}$ and c_T variations for each flame in figure 2). The reaction rate $\mathscr{R}^+$ of Y_{CH_2O} in MIFE A is slightly larger than zero in the unburnt side, suggesting the flame behaviour is relatively close to autoignition due to the elevated temperature condition. Such effects of dilution and preheating on chemical species should be investigated in detail, considering the chemical equilibrium and constant enthalpy during the mixing process in future work.

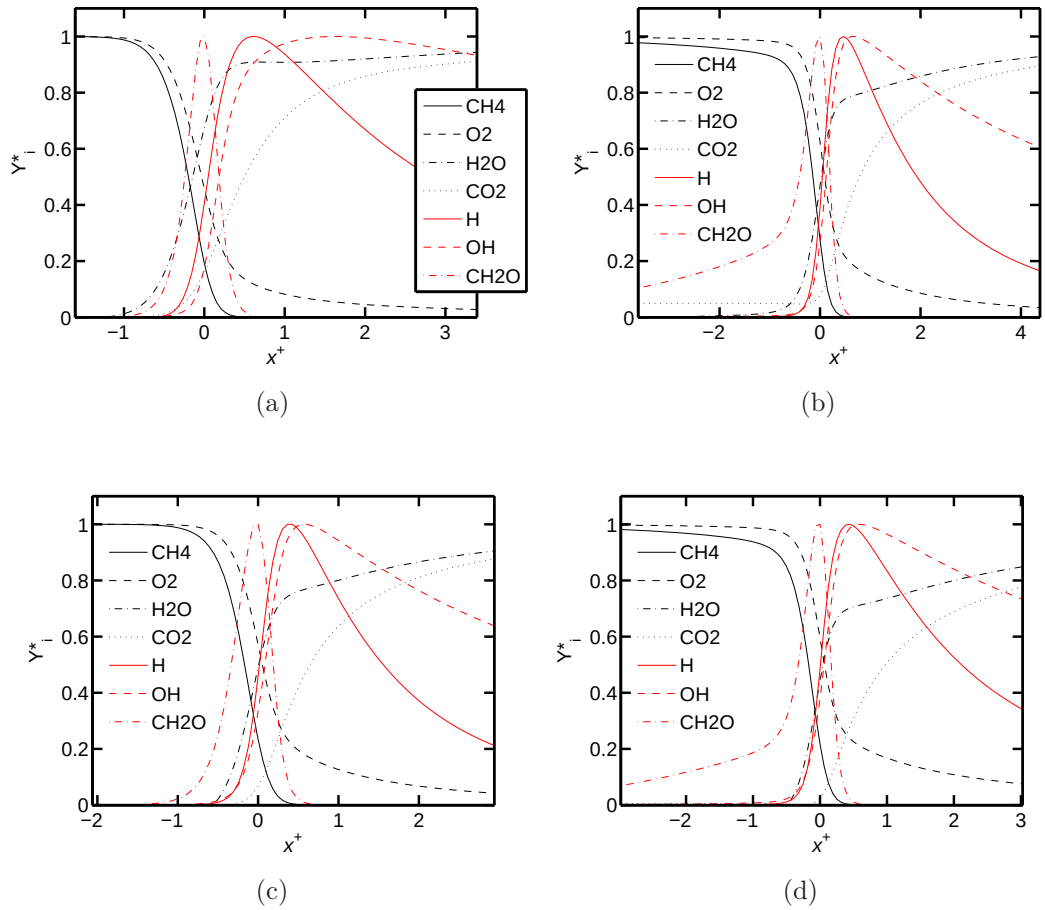

Figure 1: Variations of normalised species mass fraction across the flame. (a) Flame C, (b) MIFE A, (c) MIFE B and (d) MIFE B under the $T_r = 1600$ K condition. The location $x^+ = 0$ corresponds to the peak Y_{CH2O} location.

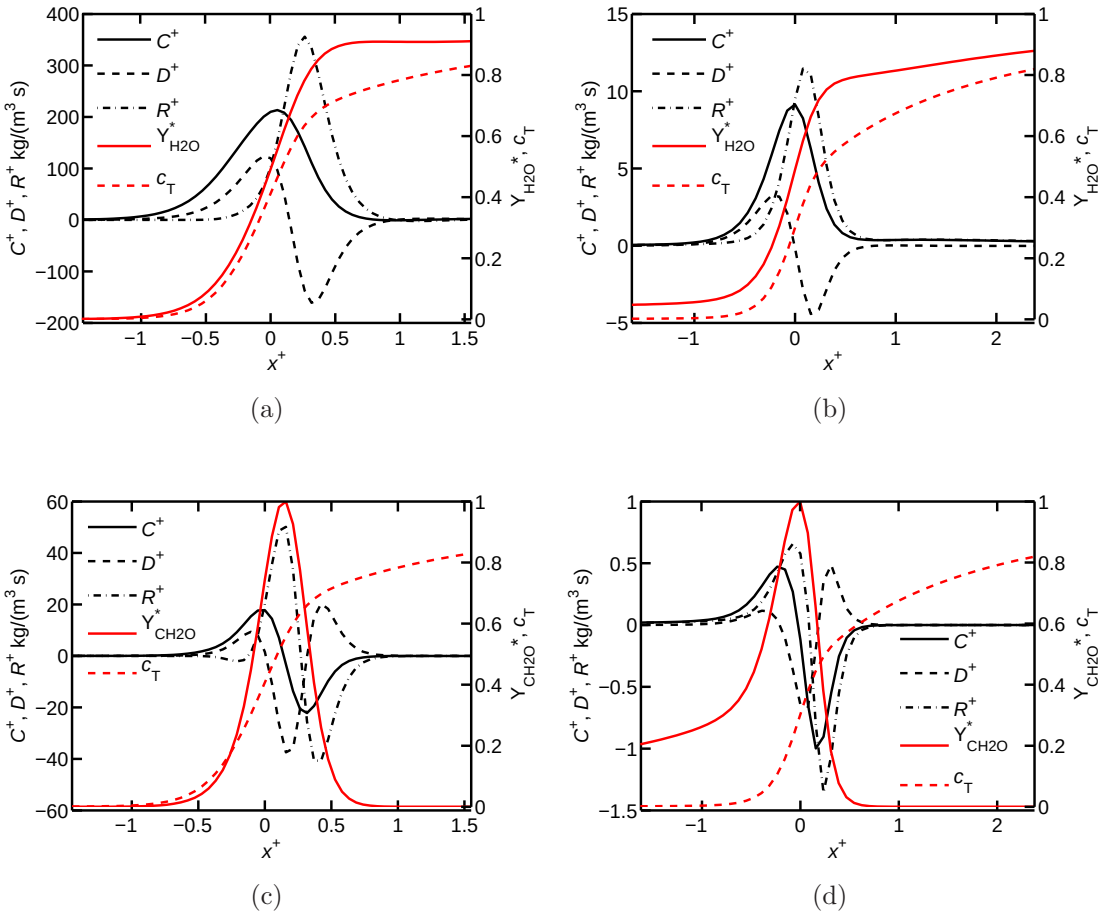

Figure 2: Variations of Y_i^*, c_T, and three terms in equation 1, $\mathscr{C}^+$, $\mathscr{D}^+$ and $\mathscr{R}^+$ of H_2O (a, b) and CH_2O (c, d) for Flame C (a, c) and MIFE A (b, d). The location $x^+ = 0$ corresponds to the peak ∇T location.

Appendix C

Spatial resolution for Morphology analysis

Three simple shapes, a sphere with radius r_s, a cylinder with radius r_c, and an elliptic cylinder with r_{e1} and r_{e2} respectively as minor and major radii are tested to determine the spatial resolution required to obtain accurate shapefinders. Figure 3 shows the variations of P and F for the three test cases as a function of $\Delta\,\kappa_m$, where Δ is numerical resolution (mesh spacing) and κ_m is the maximum curvature calculated as $1/r_s$ for the sphere, $1/r_c$ for the cylinder, and $1/r_{e1}$ for the elliptic cylinder. For large values of $\Delta\,\kappa_m$, the fluctuation is large due to the lack of spatial resolution and $\Delta\,\kappa_m \leq 0.10$ yields P and F within $\pm 3.5\%$ of their actual (theoretical) values. Therefore in this study, any objects having $\Delta\,\kappa_m > 0.10$ are excluded from the calculation.

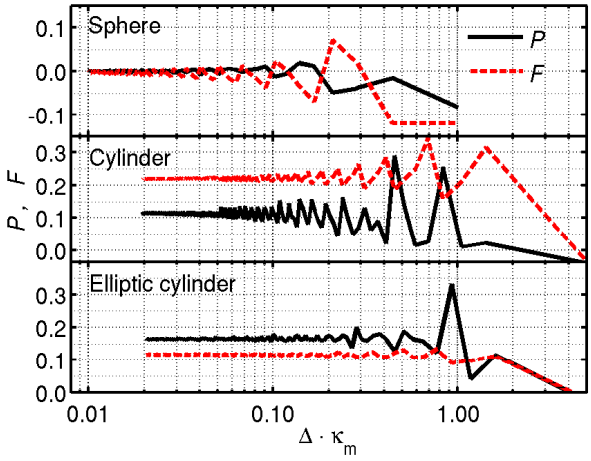

Figure 3: P and F variations for test cases as a function of numerical resolution.

Appendix D

List of Publications

The results of this thesis have been partially published and submitted in the following journal articles:

1. Y. Minamoto and N. Swaminathan, Subgrid scale modelling for MILD combustion, *Proceedings of the Combustion Institute*, submitted, December, 2013.

2. Y. Minamoto, N. Swaminathan, R. S. Cant and T. Leung, Morphology of reaction zones in MILD and premixed combustion, *Combustion and Flame*, submitted, November, 2013.

3. Y. Minamoto and N. Swaminathan, Modelling paradigms for MILD combustion, *International Journal of Advances in Engineering Sciences and Applied Mathematics*, submitted, October, 2013.

4. Y. Minamoto, N. Swaminathan, R. S. Cant and T. Leung, Reaction zones and their structure in MILD combustion, *Combustion Science and Technology*, revised in November, 2013.

5. Y. Minamoto and N. Swaminathan, Scalar gradient behaviour in MILD combustion, *Combustion and Flame*, DOI: 10.1016/j.combustflame.2013.10.005 (2013).

6. Y. Minamoto, T. D. Dunstan, N. Swaminathan and R. S. Cant, DNS of EGR–type turbulent flame in MILD condition, *Proceedings of the Combustion Institute*, 34 (2) 3231–3238 (2013).

and presented in the following conferences:

1. Y. Minamoto and N. Swaminathan, Scalar gradient behaviour in MILD combustion, *Proceedings of the 24th International Colloquium on the Dynamics of Explosions and Reactive Systems*, #27, Taipei, Taiwan, 28 Jul–2 August, 2013.

2. Y. Minamoto and N. Swaminathan, DNS of Turbulent MILD combustion, *Proceedings of JSME-CMD International Computational Symposium*, MS12-4-2, Kobe, Japan, 9–11 October, 2012.

3. Y. Minamoto, T. D. Dunstan and N. Swaminathan, DNS of EGR-type combustion in MILD condition, *Proceedings of the 7th Mediterranean Combustion Symposium*, CD-ROM, Sardinia, Italy, 11–15 September, 2011.

References

Aida, N., Nishijima, T., Hayashi, S., Yamada, H. & Kawakami, T. (2005). Combustion of lean prevaporized fuel-air mixtures mixed with hot burned gas for low-NO_x emissions over and extended range of fuel-air ratios. *Proc. Combust. Inst.*, **30**, 2885–2892. 9

Aminian, J., Galletti, C., Shahhosseini, S. & Tognotti, L. (2011). Key modeling issues in prediction of minor species in diluted-preheated combustion conditions. *Appl. Thermal Eng.*, **31**, 3287–3300. 8, 9, 12, 15, 16, 23, 125

Amzin, S., Swaminathan, N., Rogerson, J.W. & Kent, J.H. (2012). Conditional moment closure for turbulent premixed flames. *Comb. Sci. Technol.*, **184**, 1743–1767. 11

Arndt, C.M., Gounder, J.D., Meier, W. & Aigner, M. (2012). Autoignition and flame stabilization of pulsed methane jets in a hot vitiated coflow studies with high-speed laser and imaging techniques. *Applies Physics B*, **108**, 407–417. 7, 79, 80, 95

Awosope, I., Kandamby, N. & Lockwood, F. (2006). Flameless oxidation modelling: on application to gas turbine combustors. *Journal of the Energy Institute*, **79**, 75–83. 4, 5, 10, 24

Balachandran, R., Ayoola, B., Kaminski, C., Dowling, A. & Mastorakos, E. (2005). Experimental investigation of the nonlinear response of turbulent premixed flames to imposed inlet velocity oscillations. *Combustion and Flame*, **143**, 37 – 55. 110

Barths, H., Hasse, C., Bikas, G. & Peters, N. (2000). Simulation of combustion in direct injection diesel engines using a eulerian particle flamelet model. *Proc. Combust. Inst.*, **28**, 1161–1168. 11

Batchelor, G.K. & Townsend, A.A. (1948). Decay of turbulence in the final period. *Proc. Roy. Soc. Lond. A*, **194**, 527–543. 27

Baum, M., Poinsot, T.J., Haworth, D.C. & Darabiha, N. (1994). Direct numerical simulation of $H_2/O_2/N_2$ flames with complex chemistry in two-dimensional turbulent flows. *J. Fluid Mech.*, **281**, 1–32. 13

Bilger, R.W., Stårner, S.H. & Kee, R.J. (1990). On reduced mechanism for methane-air combustion in nonpremixed flames. *Combust. Flame*, **80**, 135–149. 37

Bilger, R.W., Saetran, L.R. & Krishnamoorthy, L.V. (1991). Reaction in a scalar mixing layer. *J. Fluid Mech.*, **233**, 211–242. 11

Bray, K.N.C. (1979). The interaction between turbulence and combustion. *Proc. Combust. Inst.*, **17**, 223–233. 59, 91, 99, 101

Bray, K.N.C., Libby, P.A. & Moss, J.B. (1985). Unified modelling approach for premixed turbulent combustion–Part I: General formulation. *Combust. Flame*, **61**, 87–102. 11

Burluka, A.A., Gorokhovski, M.A. & Borghi, R. (1997). Statistical model of turbulent premixed combustion with interacting flamelets. *Combust. Flame*, **109**, 173–187. 54

Buschmann, A., Dinkelacker, F., Schäfer, T. & Wolfrum, J. (1996). Measurement of the instantaneous detailed flame structure in turbulent premixed combustion. *Proc. Combust. Inst.*, 437–445. xiii, 35

Cant, R.S. (1999). Direct numerical simulation of premixed turbulent flames. *Phil. Trans. R. Soc. Lond. A.*, **357**, 3583–3604. 13, 14

Cant, R.S. (2012). SENGA2 User Guide. In *Technical Report CUED/A–THERMO/TR67*, Cambridge University Engineering Department. 17, 20, 28

Cant, R.S. & Mastorakos, E. (2008). *An introduction to turbulent reacting flow*. Imperial College Press, London, UK. 12

Cavaliere, A. & de Joannon, M. (2004). Mild combustion. *Prog. Energy Combust. Sci.*, **30**, 329–366. xiii, 3, 4, 5, 6, 7, 8, 9, 10, 24, 32, 56, 79, 80

Cessou, A. & Stepowski, D. (1996). Planar laser induced fluorescence measurement of [oh] in the stabilization stage of a spray jet flame. *Combustion Science and Technology*, **118**, 361–381. 112

Chakraborty, N. & Swaminathan, N. (2007). Influence of the damköhler number on turbulence-scalar interaction in premixed flames. I. Physical insight. *Phys. Fluids*, **19**, 045103. 14

Chakraborty, N. & Swaminathan, N. (2010). Effects of Lewis number on scalar dissipation transport and its modeling in turbulent premixed combustion. *Comb. Sci. Technol.*, **182**, 1201–1240. 14

Chakraborty, N., Kolla, H., Sankaran, R., Hawkes, E.R., Chen, J.H. & Swaminathan, N. (2013). Determination of three-dimensional quantities related to scalar dissipation rate and its transport from two-dimensional measurements direct numerical simulation based validation. *Proc. Combust. Inst.*, 1151–1162. 120

Chen, J.H. (2011). Petascale direct numerical simulation of turbulent combustionfundamental insights towards predictive models. *Proc. Combust. Inst.*, **33**, 99–123. 14

Chen, J.H., Echekki, T. & Kollmann, W. (1999). The mechanism of two-dimensional pocket formation in lean premixed methane-air flames with implications to turbulent combustion. *Combust. Flame*, **116**, 15–48. 56, 86

Chen, J.Y. & Kollmann, W. (1988). PDF modelling of chemical nonequilibrium effects in turbulent nonpremixed hydrocarbon flames. *Proc. Combust. Inst.*, **22**, 645–653. 129, 145

Chen, Y.C., Peters, N., Schneemann, G.A., Wruck, N., Renz, U. & Mansour, M.S. (1996). The detailed flame structure of highly stretched turbulent premixed methane-air flames. *Combust. Flame*, **107**, 223–244. xiii, 35

Christo, F.C. & Dally, B.B. (2005). Modelling turbulent reacting jets issuing into a hot and diluted coflow. *Combust. Flame*, **142**, 117–129. 4, 8, 9, 12, 16, 125, 144

Coelho, P.J. & Peters, N. (2001). Numerical simulation of a Mild combustion burner. *Combust. Flame*, **124**, 503–518. 8, 11, 15

COSILAB (2007). The Combustion Simulation Laboratory Version 2.0.8. Rotexo-Softpredict-Cosilab GmbH & Co. KG, Germany. 29, 127

Dally, B.B., Karpetis, A.N. & Barlow, R.S. (2002). Structure of turbulent non-premixed jet flames in a diluted hot coflow. *Proc. Combust. Inst.*, **29**, 1147–1154. 10, 12, 24

Dally, B.B., Riesmeier, E. & Peters, N. (2004). Effect of fuel mixture on moderate and intense low oxygen dilution combustion. *Combust. Flame*, **137**, 418–431. 6, 7, 8, 9, 10, 11, 15, 16, 24, 49, 54, 80, 95, 134

Darbyshire, O.R. (2011). *Modelling of turbulent stratified flames*. Ph.D. thesis, University of Cambridge, Cambridge, UK. 58

de Joannon, M., Saponaro, A. & Cavaliere, A. (2000). Zero-dimensional analysis of diluted oxidation of methane in rich conditions. *Proc. Combust. Inst.*, **28**, 1639–1646. 4, 5, 6, 15, 32, 41, 45, 54

de Joannon, M., Sabia, P., Tregrossi, A. & Cavaliere, A. (2004). Dynamic behaviour of methane oxidation in premixed flow reactor. *Comb. Sci. Technol.*, **176**, 769–783. 6, 82

de Joannon, M., Cavaliere, A., Faravelli, T., Ranzi, E., Sabia, P. & Tregrossi, A. (2005). Analysis of process parameters for steady operations in methane mild combustion technology. *Proc. Combust. Inst.*, **30**, 2605–2612. 6, 82

Domingo, P. & Vervisch, L. (2007). DNS of partially premixed flame propagating in a turbulent rotating flow. *Proc. Combust. Inst.*, **31**, 1657–1664. 14

Domingo, R., Vervisch, L., Payet, S. & Hauguel, R. (2005). DNS of a premixed turbulent v flame and LES of a ducted flame using a FSD-PDF subgrid scale closure with FPI-tabulated chemistry. *Combust. Flame*, **143**, 566–586. 14

Dunstan, T.D., Swaminathan, N. & Bray, K.N.C. (2012). Influence of flame geometry on turbulent premixed flame propagation: a dns investigation. *J. Fluid Mech.*, **709**, 191–222. 14

Dunstan, T.D., Minamoto, Y., Chakraborty, N. & Swaminathan, N. (2013a). Scalar dissipation rate modelling for Large Eddy Simulation of turbulent premixed flame. *Proc. Combust. Inst.*, **34**, 1193–1201. 59

Dunstan, T.D., Swaminathan, N., Bray, K.N.C. & Kingsbury, N.G. (2013b). Flame interactions in turbulent premixed twin v-flames. *Comb. Sci. Technol.*, **185**, 134–159. 54, 56, 86

Duwig, C., Fuchs, L., Griebel, P., Siewert, P. & Boschek, E. (2007). Study of a confined turbulent jet: Influence of combustion and pressure. *AIAA Journal*, **45**, 624–639. xiii, 35

Duwig, C., Stankovic, D., Fuchs, L., Li, G. & Gutmark, E. (2008). Experimental and numerical study of flameless combustion in a model gas turbine combustor. *Comb. Sci. Technol.*, **180**, 279–295. 8, 13, 127, 129

Duwig, C., Li, B. & Aldén, M. (2012). High resolution imaging of flameless and distributed turbulent combustion. *Combust. Flame*, **159**, 306–316. 6, 7, 8, 9, 15, 32, 49, 110, 112

Einasto, M., Saar, E., Liivamägi, L.J., Einasto, J., Tago, E., Martínez, V.J., Starck, J.L., Müller, V., Heínämäki, P., Nurmi, P., Gramann, M. & Hütsi, G. (2007). The richesst superclusters I. Morphology. *Astron. Astrophys.*, **476**, 697–711. 67

Eswaran, V. & Pope, S.B. (1987). Direct numerical simulations of the turbulent mixing of a passive scalar. *Phys. Fluids*, **31**, 506–520. 27

Fayoux, A., Zhringer, K., Gicquel, O. & Rolon, J. (2005). Experimental and numerical determination of heat release in counterflow premixed laminar flames. *Proc. Combust. Inst.*, **30**, 251 – 257. 110, 113

Frank, J., Kalt, P.A.M. & Bilger, R.W. (1999). Measurements of conditional velocities in turbulent premixed flames by simulataneous oh plif and piv. *Combust. Flame*, **116**, 220–232. 11

Galleti, C., Parente, A. & Tognotti, L. (2007). Numerical and experimental investigation of a Mild combustor burner. *Combust. Flame*, **151**, 649–664. 9, 10, 24

Galletti, C., Parente, A. & Tognotti, L. (2007). Numerical and experimental investigation of a mild combustion burner. *Combust. Flame*, **151**, 649–664. 4, 8, 9, 16, 125

Grout, R.W. (2007). An age extended progress variable for conditioning reaction rates. *Phys. Fluids*, **19**, 105107. 14

Grout, R.W., Swaminathan, N. & Cant, R.S. (2009). Effects of compositional fluctuations on premixed flames. *Proc. Combust. Inst.*, **13**, 823–852. 14

Habisreuther, P., Galeazzo, F.C.C., Prathap, C. & Zarzalis, N. (2013). Structure of laminar premixed flames of methane near the auto-ignition limit. *Combust. Flame*, **10.1016/j.combustflame.2013.06.023**. 29

Hassel, E.P. & Linow, S. (2000). Laser diagnostics for studies of turbulent combustion. *Measurement Science and Technology*, **11**, R37. 7

Hawkes, E.R., Sankaran, R. & Chen, J.H. (2011). Estimates of the three-dimensional flame surface density and every term in its transport equation from two-dimensional measurements. *Proceedings of the Combustion Institute*, **33**, 1447 – 1454. 120

Hayashi, S. & Mizobuchi, Y. (2011). Utilization of hot burnt gas for better control of combustion and emissions. In N. Swaminathan & K.N.C. Bray, eds., *Turbulent premixed flames*, 365–378, Cambridge University Press, Cambridge, UK. 5

Hélie, J. & Trouvé, A. (1998). Turbulent flame propagation in partially premixed combustion. *Proc. Combust. Inst.*, 891–898. 14

Hilbert, R. & Thévenin, D. (2002). Autoignition of turbulent non-premixed flames investigated using direct numerical simulation. *Combust. Flame*, **128**, 22–37. 91

Ihme, M. & See, Y.C. (2012). Les flamelet modeling of a three-stream mild combustor: Analysis of flame sensitivity to scalar inflow conditions. *Proc. Combust. Inst.*, **33**, 1309–1317. 8, 13

Jenkins, K. & Cant, R. (1999). Dns of turbulent flame kernels. In Knight & Sakell, eds., *Proc. Second AFOSR Conf. on DNS and LES*, 192–202, Rutgers University, Kluwer Academic Publishers. 26

Katsuki, M. & Hasegawa, T. (1998). The science and technology of combustion in highly preheated air. *Proc. Combust. Inst.*, 3135–3146. 3, 4, 5, 7, 9, 24, 32, 56, 79

Kee, R.J., Grcar, J.F., Smooke, M. & A.Miller, J. (1985). PREMIX: A fortran program for modeling steady one-dimensional flames. *Sandia National Laboratories*, **SAND85-8240**. 29

Kerscher, M., Schmalzing, J., Retzlaff, J., Borgani, S., Buchert, T., Gottlöber, S., Müller, V., Plionis, M. & Wagner, H. (1997). Minkowski functionals of abell/aco clusters. *Mon. Not. R. Astron. Soc.*, **284**, 73–84. 67

Kiefer, J., Li, Z.S., Seeger, T., Leipertz, A. & Aldén, M. (2009). Planar laser-induced fluorescence of HCO for instantaneous flame front imaging in hydrocarbon flames. *Proc. Combust. Inst.*, **32**, 921–928. 110

Kim, S.H., Huh, K.Y. & Dally, B. (2005). Conditional moment closure modelling of turbulent nonpremixed combustion in diluted hot coflow. *Proc. Combust. Inst.*, **30**, 751–757. 11

Klimenko, A.Y. & Bilger, R.W. (1999). Conditional moment closure for turbulent combustion. *Prog. Energy Combust. Sci.*, **25**, 595–687. 11

Kolla, H., Rogerson, J.W., Chakraborty, N. & Swaminathan, N. (2009). Scalar dissipation rate modelling and its validation. *Comb. Sci. Technol.*, **181**, 518–535. 14, 103

Kolla, H., Rogerson, J.W. & Swaminathan, N. (2010). Validation of a turbulent flame speed model across combustion regimes. *Comb. Sci. Technol.*, **182**, 284–308. 103

Krishnamurthy, N., Paul, P.J. & Blasiak, W. (2009). Studies on low-intensity oxy-fuel burner. *Proc. Combust. Inst.*, **32**, 3139–3146. 4, 5, 15, 41, 45, 54

Kumar, S., Paul, P.J. & Mukunda, H.S. (2002). Studies on a new high-intensity low-emission burner. *Proc. Combust. Inst.*, **29**, 1131–1137. 9

Lammel, O., Schütz, H., Schmitz, G., Lückerath, R., Stöhr, M., Noll, B., Aigner, M., Hase, M. & Krebs, W. (2010). FLOX combustion at high power density and high flame temperatures. *J. Eng. Gas Turbine Power*, **132**, 121503–1. 4, 5

Leung, T., Swaminathan, N. & Davidson, P.A. (2012). Geometry and interaction of structures in homogeneous isotropic turbulence. *J. Fluid Mech.*, **710**, 453–481. xvi, 67, 68, 69

Li, P. & Mi, J. (2011). Influence of inlet dilution of reactants on premixed combustion in a recuperative furnace. *Flow Turbulence Combust.*, **87**, 617–638. 4, 6, 8, 9, 10, 12, 16, 24, 125

Li, Z., Li, B., Sun, Z., Bai, X. & Aldn, M. (2010). Turbulence and combustion interaction: High resolution local flame front structure visualization using

simultaneous single-shot plif imaging of ch, oh, and ch2o in a piloted premixed jet flame. *Combust. Flame*, **157**, 1087 – 1096. 15, 110

Lückerath, R., Meier, W. & Aigner, M. (2008). FLOX combustion at high pressure with different fuel compositions. *J. Eng. Gas Turbine Power*, **130**, 011505–1. 5

Magnussen, B.F. (1981). On the structure of turbulence and a generalized eddy dissipation concept for chemical reaction in turbulent flow. *19th American Institute of Aeronautics and Astronautics Aerospace Science Meeting*, 1–6. 8, 12, 125, 128, 144

Malkeson, S.P. & Chakraborty, N. (2010). A priori direct numerical simulation assessment of algebraic models of variances and dissipation rates in the context of Reynolds-averaged Navier-Stokes simulations for low damköhler number partially premixed combustion. *Comb. Sci. Technol.*, **182**, 960–999. 14

Markides, C.N. & Mastorakos, E. (2005). An experimental study of hydrogen autoignition in a turbulent co-flow of heated air. *Proc. Combust. Inst.*, **30**, 883–891. 79, 80

Mastorakos, E. (2009). Ignition of turbulent non-premixed flames. *Prog. Energy Combust. Sci.*, **35**, 57–97. 8, 80, 91

Mastorakos, E., Taylor, A.M.K.P. & Whitelaw, J.H. (1995). Extinction of turbulent counterflow flames with reactants diluted by hot products. *Combust. Flame*, **102**, 101–114. 7, 79

Mastorakos, E., Baritaud, T.A. & Poinsot, T.J. (1997). Numerical simulation of autoignition in turbulent mixing flows. *Combust. Flame*, **109**, 198–223. 91

Mecke, K.R., Buchert, T. & Wagner, H. (1994). Robust morphological measures for large-scale structure in the universe. *Astron. Astrophys.*, **288**, 697–704. 67

Medwell, P.R. (2007). *Laser diagnostics in MILD combustion*. Ph.D. thesis, The University of Adelaide, Adelaide, Australia. 5, 6, 7, 9, 15, 32, 49, 79, 110, 112

Medwell, P.R., Kalt, P.A.M. & Dally, B.B. (2007). Simultaneous imaging of OH, formaldehyde, and temperature of turbulent nonpremixed jet flames in a heated and diluted coflow. *Combust. Flame*, **148**, 48–61. 6, 7, 8, 15, 16, 79, 80, 95

Medwell, P.R., Kalt, P.A.M. & Dally, B.B. (2008). Imaging of diluted turbulent ehylene flames stabilised on a jet in hot coflow (jhc) burner. *Combust. Flame*, **152**, 100–113. 6, 7, 79

Mi, J., Li, P., Dally, B.B. & Craig, R.A. (2009). Importance of initial momentum rate and air-fuel premixing on moderate or intense low oxygen dilution (MILD) combustion in a recuperative furnace. *Energy and Fuels*, **23**, 5349–5356. 6

Minamoto, Y., Dunstan, T.D. & Swaminathan, N. (2011a). DNS of EGR-type combustion in mild condition. *7th Mediterranean Combustion Symposium*. 15

Minamoto, Y., Fukushima, N., Tanahashi, M., Miyauchi, T., Dunstan, T.D. & Swaminathan, N. (2011b). Effect of flow-geometry on turbulence-scalar interaction in premixed flames. *Phys. Fluids*, **23**, 125107. 14

Minkowski, H. (1903). Volumen und oberfläche. *Math. Ann.*, **57**, 447–495. 65

Mizobuchi, Y., Tachibana, S., Shinjo, J., Ogawa, S. & Takeno, T. (2002). A numerical analysis of the structure of a turbulent hydrogen jet lifted flame. *Proc. Combust. Inst.*, **29**, 2009–2015. 14

Mohamed, H., Bentîcha, H. & Mohamed, S. (2009). Numerical modeling of the effects of fuel dilution and strain rate on reaction zone structure and NOx formation in flameless combustion. *Comb. Sci. Technol.*, **181**, 1078–1091. 4

Mura, A., Tsuboi, K. & Hasegawa, T. (2008). Modelling of the correlation between velocity and reactive scalar gradients in turbulent premixed flames based on DNS data. *Combust. Theory Model.*, **12**, 671–698. 14

Mura, A., Robin, V. & Hasegawa, T. (2009). Small scale features of velocity and scalar fields in turbulent premixed flames. *Flow Turbulence Combust.*, **82**, 339–358. 14

Najm, H.N., Knio, O.M., Paul, P.H. & Wyckoff, P.S. (1998a). A study of flame observables in premixed methane-air flames. *Comb. Sci. Technol.*, **140**, 369–403. 110

Najm, H.N., Paul, P.H., Mueller, C.J. & Wyckoff, P.S. (1998b). On the adequacy of certain experimental observables as measurements of flame burning rate. *Combust. Flame*, **113**, 312–332. 110, 112, 113

Nguyen, Q.V. & Paul, P.H. (1996). The time evolution of a vortex-flame interaction observed via planar imaging of CH and OH. *Proc. Combust. Inst.*, 357–364. 110

Oldenhof, E., Tummers, M.J., van Veen, E.H. & Roekaerts, D.J.E.M. (2010). Ignition kernel formation and lift-off beaviour of jet-in-hot-coflow flames. *Combust. Flame*, **157**, 1167–1178. 79

Oldenhof, E., Tummers, M.J., van Veen, E.H. & Roekaerts, D.J.E.M. (2011). Role of entrainment in the stabilisation of jet-in-hot-coflow flames. *Combust. Flame*, **158**, 1553–1563. 6, 32, 80, 95

Orsino, S., Webber, R. & Bollettini, U. (2001). Numerical simulation of combustion of natural gas with high-temperature air. *Comb. Sci. Technol.*, **170**, 1–34. 8, 9, 12, 16, 125

Özdemir, I.B. & Peters, N. (2001). Characteristics of the reaction zone in a combustor operating at MILD combustion. *Exp. Fluids*, **30**, 683–695. 4, 5, 6, 7, 8, 9, 15, 16, 24, 27, 41, 45, 49, 54, 110

Parente, A., Galletti, C. & Tognotti, L. (2011a). A simplified approach for predicting NO formation in MILD combustion of $CH_4 - H_2$ mixtures. *Proc. Combust. Inst.*, **33**, 3343–3350. 80

Parente, A., Sutherland, J.C., Dally, B.B., Tognotti, L. & Smith, P.J. (2011b). Investigation of the MILD combustion regime via Principal Component Analysis. *Proc. Combust. Inst.*, **33**, 3333–3341. 4

Paul, P.H. & Najm, H.N. (1998). Planar laser-induced fluorescence imaging of flame heat release rate. *Proc. Combust. Inst.*, 43–50. 110, 112, 113

Peters, N. (1986). Laminar flamelets concepts in turbulent combustion. *Proc. Combust. Inst.*, **21**, 1231–1250. 11

Peters, N. (2000). *Turbulent combustion*. Cambridge University Press, Cambridge, UK. xiii, 11, 34, 35, 45

Pfadler, S., Leipertz, A. & Dinkelacker, F. (2008). Systematic experiments on turbulent premixed Bunsen flame including turbulent flux measurement. *Combust. Flame*, **152**, 616–631. xiii, 35

Pfadler, S., Dinkelacker, F., Beyrau, F. & Leipertz, A. (2009). High resolution dual-plane stereo-piv for validation of subgrid scale models in large-eddy simulations of turbulent premixed flames. *Combust. Flame*, **156**, 1552–1564. 11

Pitsch, H. (2006). Large eddy simulation ofturbulent combustion. *Annu. Rev. Fluid Mech.*, **38**, 453–482. 12

Plessing, T., Peters, N. & Wünning, J.G. (1998). Laseroptical investigation of highly preheated combustion with strong exhaust gas recirculation. *Proc. Combust. Inst.*, 3197–3204. 4, 6, 7, 8, 9, 15, 16, 24, 27, 49, 95, 110

Poinsot, T. & Lele, S. (1992). Boundary conditions for direct simulations of compressible viscos flows. *J. Comput. Phys.*, **101**, 104–129. 26

Poinsot, T.J. & Veynante, D. (2005). *Theoretical and numerical combustion, 2nd edn.*. Edwards, Philadelphia, PA. 11, 13, 19, 29, 57, 59

Poinsot, T.J., Veynante, D. & Candel, S. (1991). Quenching processes and premixed turbulent combustion diagrams. *J. Fluid Mech.*, **228**, 561–606. 13, 14

Pope, S.B. (1985). Pdf methods for turbulent reactive flows. *Prog. Energy Combust. Sci.*, **11**, 119–192. 12, 129, 145

Pope, S.B. (2000). *Turbulent flows*. Cambridge University Press, Cambridge, UK. 11, 12

Puri, R., Moser, M., Santoro, R.J. & Smyth, K.C. (1992). Laser-induced fluorescence measurements of oh concentrations in the oxidation region of laminar, hydrocarbon diffusion flames. *Symposium (International) on Combustion*, **24**, 1015 – 1022, twenty-Fourth Symposium on Combustion. 112

Richardson, E.S., Sankaran, R., Grout, R.W. & Chen, J.H. (2010). Numerical analysis of reaction-diffusion effects on species mixing rates in turbulent premixed methane-air combustion. *Combust. Flame*, **157**, 506–515. 14

Richter, M., Collin, R., Nygren, J., Aldén, M., Hildingsson, L. & Johansson, B. (2005). Studies of the combustion process with simultaneous formaldehyde and oh plif in a direct-injected hcci engine. *JSME International Journal Series B Fluids and Thermal Engineering*, **48**, 701–707. 110

Röder, M., Dreier, T. & Schulz, C. (2013). Simultaneous measurement of localized heat-release with OH/CH_2O–LIF imaging and spatially integrated oh chemiluminescence in turbulent swirl flames. *Proceedings of the Combustion Institute*, **34**, 3549–3556. 110

Rogallo, R.S. (1981). Numerical experiments in homogeneous turbulence. *NASA TM*, 81315. 27

Rutland, C.J. & Cant, R.S. (1994). Turbulent transport in premixed flames. *Proceedings of the Summer Program, Centre for Turbulence Research, Stanford University/NASA-Ames*, 75–94. 13

Rutland, C.J. & Ferziger, H. (1991). Simulations of flame-vortex interactions. *Combust. Flame*, **84**, 343–360. 13

Sabia, P., de Joannon, M., Fierro, S., Tregrossi, A. & Cavaliere, A. (2007). Hydrogen-enriched methane Mild combustion in a well stirred reactor. *Experimental Thermal and Fluid Science*, **31**, 469–475. 6, 82

Sahni, V., Sathyaprakash, B.S. & Shandarin, S.F. (1998). Shapefinders: a new shape diagnostic for large-scale structure. *The Astrophysical Journal*, **495**, L1–L5. 67, 68, 69

Sankaran, R., Im, H.G., Hawkes, E.R. & Chen, J.H. (2005). The effects of non-uniform temperature distribution on the ignition of a lean homogeneous hydrogen-air mixture. *Proc. Combust. Inst.*, **30**, 875–882. 27

Schiessl, R., Maas, U., Hoffmann, A., Wolfrum, J. & Schulz, C. (2004). Method for absolute oh-concentration measurements in premixed flames by lif and numerical simulations. *Applied Physics B*, **79**, 759–766. 112

Schmalzing, J. & Buchert, T. (1997). Bevond genus statistics: a unifying approach to the morphology of cosmic structure. *Astrophys. J.*, **482**, L1–L4. 67, 68

Schmalzing, J., Buchert, T., Melott, A.L., Sahni, V., Sathyaprakash, B.S. & Shandarin, S.F. (1999). Disentangling the cosmic web. I. Morphology of isodensity contours. *The Astrophysical Journal*, **526**, 568–578. 67, 68

Schuller, T., Durox, D. & Candel, S. (2003). Self-induced combustion oscillations of laminar premixed flames stabilized on annular burners. *Combust. Flame*, **135**, 525–537. 54

Shandarin, S.F., Sheth, J.V. & Sahni, V. (2004). Morphology of the supercluster-void network in ΛCDM cosmology. *Mon. Not. R. Astron. Soc.*, **353**, 162–178. 67

Sheth, J.V. & Sahni, V. (2005). Exploring the geometry, topology and morphology of large scale structure using Minkowski functionals. *Current Science*, **88**, 1101–1116. 67

Sheth, J.V., Shandarin, S.F. & Sathyaprakash, B.S. (2003). Measuring the geometry and topology of large-scale structure using S U R F G E N: methodology and preliminary results. *Mon. Not. R. Astron. Soc.*, **343**, 22–46. 67, 68

Shim, Y., Tanaka, S., Tanahashi, M. & Miyauchi, T. (2011). Local structure and fractal characteristics of H_2-air turbulent premixed flame. *Proc. Combust. Inst.*, **33**, 1455–1462. 14

Sidey, J., Mastorakos, E. & Gordon, R.L. (2013). Simulations of autoignition and laminar premixed flames in methane-air mixtures diluted with hot products. *Comb. Sci. Technol.*, in press. 149

Smooke, M.D. & Giovangigli, V. (1991). Formulation of the premixed and nonpremixed test problems. In M.D. Smooke, ed., *Reduced kinetic mechanisms and asymptotic approximations for methane-air flames.*, vol. 384, 1–28, Springer Verlag, New York. xxiii, 15, 23, 27, 147, 148

Suzukawa, Y., Sugiyama, S., Hino, Y., Ishioka, M. & Mori, I. (1997). Heat transfer improvement and NOx reduction by highly preheated air combustion. *Energy Convers. Mgmt*, **38**, 1061–1071. 24, 32

Swaminathan, N. & Bilger, R.W. (1997). Direct numerical simulation of turbulent nonpremixed hydrocarbon reaction zones using a two-step mechanism. *Comb. Sci. Technol.*, **127**, 167–196. 13, 14

Swaminathan, N. & Bray, K.N.C. (2005). Effect of dilatation on scalar dissipation in turbulent premixed flames. *Combust. Flame*, **143**, 549–565. 11, 103

Swaminathan, N. & Bray, K.N.C. (2011). *Turbulent premixed flames*. Cambridge University Press, Cambridge, UK. 9, 12, 13, 91

Swaminathan, N., Bilger, R.W. & Cuenot, B. (2001). Relationship between turbulent scalar flux and conditional dilatation in premixed flames with complex chemistry. *Combust. Flame*, **126**, 1764–1779. 54

Tanahashi, M., Fujimura, M. & Miyauchi, T. (1999). Fine scale structure of H_2–air turbulent premixed flames. *1st International Symposium on Turbulence and Shear Flow*, 59–64. 13

Tanahashi, M., Fujimura, M. & Miyauchi, T. (2000). Coherent fine-scale eddies in turbulent premixed flames. *Proc. Combust. Inst.*, **28**, 529–535. 13, 14

Tanahashi, M., Murakami, S., Choi, G.M., Fukuchi, Y. & Miyauchi, T. (2005). Simultaneous CH-OH PLIF and stereoscopic PIV measurements of turbulent premixed flames. *Proc. Combust. Inst.*, **30**, 1665–1672. 110

Tanahashi, M., Taka, S., Shimura, M. & Miyauchi, T. (2008). Ch double-pulsed PLIF measurement in turbulent premixed flame. *Exp Fluids*, **45**, 323–332. 110

Tanaka, S., Shimura, M., Fukushima, N., Tanahashi, M. & Miyauchi, T. (2011). DNS of turbulent swirling premixed flame in a micro gas turbine combustor. *Proc. Combust. Inst.*, **33**, 3293–3300. 14

Trouvé, A. & Poinsot, T. (1994). The evolution equation for the flame surface density in turbulent premixed combustion. *J. Fluid Mech.*, **278**, 1–31. 13, 14, 46

U. S. Energy Information Administration (2010). International energy outlook 2010. *DOE/EIA-0484*. xiii, 1, 2

van Oijen, J.A. (2013). Direct numerical simulation of autoigniting mixing layers in MILD combustion. *Proc. Combust. Inst.*, **34**, 1163–1171. 7, 15, 23, 79

Veynante, D. & Vervisch, L. (2002). Turbulent combustion modelling. *Prog. Energy Combust. Sci.*, **28**, 193–266. 11, 14, 57, 59

Veynante, D., Trouvé, A., Bray, K.N.C. & Mantel, T. (1997). Gradient and counter-gradient scalar transport in turbulent premixed flames. *J. Fluid Mech.*, **332**, 263–293. 11

Weber, R., Orsino, S., Lallemant, N. & Verlaan, A. (2000). Combustion of natural gas with high-temperature air and large quantities of flue gas. *Proc. Combust. Inst.*, **28**, 1315–1321. 8, 9, 12, 16, 125

Wilkin, S.L., Barenghi, C.F. & Shukurov, A. (2007). Magnetic structures produced by the small-scale dynamo. *Phys. Rev. Lett.*, **99**, 134501. 67

Woelk, G. & Wünning, J. (1993). Controlled combustion by flameless oxidation. *Joint Meeting of the British and German Sections of the Combustion Institute, Cambridge, UK*. 3

World Energy Council (2012). World energy perspective: Nuclear energy one year after Fukushima. *ISBN: 978-0-946121-16-8*. 1

Wünning, J.A. (1991). Flameless oxidation with highly preheated air. *Chemie Ingenieur Technik*, **63**, 1243–1245. 3

Wünning, J.A. & Wünning, J.G. (1997). Flameless oxidation to reduce thermal NO-formation. *Prog. Energy Combust. Sci.*, **23**, 81–94. 3, 4, 5, 6, 7, 24, 56, 79

Yoshikawa, I., Shim, Y.S., Nada, Y., Tanahashi, M. & Miyauchi, T. (2013). A dynamic SGS combustion model based on fractal characteristics of turbulent premixed flames. *Proc. Combust. Inst.*, **34**, 1373–1381. 14

Zheng, X.L., Yuan, J. & Law, C.K. (2004). Nonpremixed ignition of H_2/air in a mixing layer with a vortex. *Proc. Combust. Inst.*, **30**, 415–421. 95

Zimont, V.L. & Biagioli, F. (2002). Gradient, counter-gradient transport and their transition in turbulent premixed falmes. *Combust. Theory Model.*, **6**, 79–101. 11